Evolution of coronal magnetic fields

Von der Fakultät für Elektrotechnik, Informationstechnik, Physik
der Technischen Universität Carolo-Wilhelmina
zu Braunschweig
zur Erlangung des Grades einer
Doktorin der Naturwissenschaften
(Dr. rer. nat.)
genehmigte
Dissertation

von Julia Katharina Thalmann
aus Lienz, Österreich

Bibliografische Information der Deutschen Nationalbibliothek

Die Deutsche Nationalbibliothek verzeichnet diese Publikation in der Deutschen Nationalbibliografie; detaillierte bibliografische Daten sind im Internet über `http://dnb.d-nb.de` abrufbar.

1. Referentin oder Referent: Prof. Dr. Karl-Heinz Glaßmeier
2. Referentin oder Referent: Prof. Dr. Sami K. Solanki
eingereicht am: 12. November 2009
mündliche Prüfung (Disputation) am: 12. Februar 2010

ISBN 978-3-942171-41-0

uni-edition GmbH 2010
http://www.uni-edition.de

Printed in Germany

Contents

Summary

In the presented thesis, the explosive phenomena in the solar atmosphere like flares or coronal mass ejections, often related to active regions on the Sun, are aimed to be investigated. For this purpose, a detailed knowledge of the magnetic field in the outer solar atmosphere (the corona) and its coupling with the lower solar atmosphere (the chromosphere and photosphere) is crucial. Well established, direct measurement techniques allow it to routinely measure the magnetic field vector in the photosphere. Difficulties are met, however, in trying to measure the magnetic field vector in the chromosphere and the corona and routine measurements are usually not available. In order to be, nevertheless, able to investigate the magnetic field in these layers, numerical methods have been developed. These methods estimate the magnetic field in the outer solar atmosphere, indirectly, based on measurements routinely made at the photospheric level.

Within this work, we use a numerical model which allows us to approximate the magnetic field in these layers with the so-called "force-free" field approach. This approach assumes that the Lorentz force vanishes, i.e. that the magnetic field and the electric currents are aligned with each other. This is justified in regions where the ratio of the plasma pressure to the magnetic pressure is significantly lower than unity. This is true in large parts of the chromosphere and corona while the photosphere is a region where this assumption is not warrantable. Since we use routine measurements of the photospheric field vector as an input for our numerical method (as lower boundary condition), we have to "preprocess" the photospheric data in order to achieve boundary conditions that are consistent with the force-free assumption. We use the preprocessing algorithm of Wiegelmann et al. (2006) which approximates the physics at a chromospheric level as it transforms an observed, not force-free, photospheric magnetic field to a nearly force-free, chromospheric-like state. It minimizes a functional so that the preprocessed magnetogram suffices the force-free condition in such a way that the optimized boundary condition stays close to the measured photospheric data and is sufficiently smooth. Optionally, chromospheric magnetic field information can be additionally taken into account (Wiegelmann et al. 2008). From these consistent boundary conditions, we are then able to reconstruct potential, linear force-free and nonlinear force-free fields. While potential and linear force-free fields, which only need the longitudinal (line-of-sight) component of the photospheric magnetic field as an input, are capable of reproducing the true coronal magnetic field only to a certain extent, the more general approach of nonlinear force-free fields, which need the full photospheric magnetic field vector as an input, is favorable. Within this work, we use the multigrid-like optimization code of Wiegelmann (2004) to extrapolate the 3D nonlinear force-free coronal magnetic field. It minimizes the volume-integrated force-free and solenoidal condition for the magnetic field vector simultaneously. We also calculate the corresponding potential fields, using a Green's function method after Aly (1989), from the longitudinal

component of the photospheric field. With these prerequisites, we are able to investigate the topology of the 3D coronal magnetic field above solar active regions and to estimate the related physical quantities such as the magnetic energy content, the free magnetic energy (which can partly be released during solar eruptions) and the magnetic energy density (i.e. the amount of stored magnetic energy per unit volume).

In particular, we have investigated the coronal magnetic field associated with the two solar active regions NOAA 10540 and NOAA 10960 both of which were associated with flares and coronal mass ejections. The active region NOAA 10540 launched a large flare while the active region NOAA 10960 only produced two small flares. We were, in particular, interested in the temporal evolution of the magnetic field topology and its associated magnetic energy content in the course of the eruptive events. The 3D coronal magnetic field above active region NOAA 10540 from Jan 18 – 21, 2004 was extrapolated from four photospheric vector magnetograms, measured with the Solar Flare Telescope Vector-Magnetograph of the National Astronomical Observatory of Japan. The 3D coronal magnetic field above active region NOAA 10960 on June 7, 2007 was extrapolated from nine photospheric vector magnetograms, measured with the Synoptic Optical Long-term Investigations of the Sun Vector-Spectro-Magnetograph of the National Solar Observatory.

The outcome of the analysis of these active regions can be summarized as follows. First, magnetic energy accumulates before a flare and part of the excess (free) magnetic energy is released during a flare. Second, a higher amount of free magnetic energy available in an active region leads to larger flares while a smaller amount of free energy powers only smaller flares. Third, the decrease in the magnetic energy of the nonlinear force-free fields is higher than that of the associated potential fields, indicating that the energy release is likely to be more related to the change of the transverse than to that of the longitudinal magnetic field. This implies that the energy storage and energy release are directly related to the field-aligned electric currents in the corona. Fourth, the coronal magnetic fields do not totally relax to a potential field configuration, supporting the theory of magnetic helicity conservation. Fifth, the evolution of the integrated energy density with height indicates that the energy changes due to the flaring activity mainly take place within heights of tens of megameters above the photosphere. Sixth, the computation of iso-surfaces of the absolute magnetic field magnitude supports a proposed, and recently observationally confirmed, implosion scenario for coronal transient phenomena.

Besides the magnetic energy, also the magnetic helicity of the coronal field is often used as a tracer to quantify the topological properties of a magnetic field. As magnetic flux travels from the convection zone until the solar corona, the helicity content of coronal fields may be completely determined by its flow through the photosphere on the one hand and its loss-rate into the solar wind on the other hand. To evaluate the magnetic helicity content of the solar corona, the knowledge of the 3D magnetic vector potential, associated with the 3D magnetic field, is needed. We developed and tested a method to calculate the 3D magnetic vector potential as a physically meaningful quantity. Future application of our method to estimate the helicity content above solar active regions will enable us to compare the calculated amount of helicity with the amount of helicity injected through the solar photosphere and its contribution to the coronal helicity content.

1 Solar magnetic field

1.1 Observations

Localized volumes in the atmosphere of the Sun, which involve strong magnetic fields, frequently give rise to different dynamic and spatially confined phenomena. Such phenomena are, e.g., sunspot groups, faculae, plages, filaments or prominences (when viewed on the solar disk or on the solar limb, respectively) and flares. A localized region of the Sun's surface and atmosphere that displays some or all of these phenomena is often called an "active region" (Murdin 2001). Active regions form when bundles of magnetic field lines emerge from below the photosphere and expand, in form of loop systems, into the solar atmosphere. The magnetic footprint of the atmospheric loop systems on the solar photosphere is observed in form of bipolar magnetic fields. These bipolar magnetic fields represent the locations of positive or negative polarity where magnetic field lines emerge from or re-enter the solar surface, respectively. Each endpoint of an emerged loop represents a separate photospheric element, of opposite polarity. These bipolar magnetic fields are concentrations of strong magnetic fields and, although often complex in structure, they contain on average equal quantities of positive and negative magnetic flux. The overall lifetime of active regions can be up to several months (i.e. much longer than the lifetime of the individual sunspots forming within the active regions and persisting for about two to four weeks), slowly disappearing due to the dissipation of the underlying magnetic field (e.g. Durrant 1988).

In the following, the observational findings regarding the magnetic field in the different layers of the solar atmosphere are discussed. Characteristic magnetic features as observed in the solar photosphere are described in § 1.1.1, that of the chromosphere and corona in § 1.1.2. Solar activity, as appearing in the form of flares and coronal mass ejections, arising from solar active regions with sufficiently complex magnetic configurations, are discussed in § 1.1.3.1 and § 1.1.3.3, respectively. The associated theoretical concepts of how to explain the mechanisms involved in these eruptive phenomena are accordingly pictured in § 1.1.3.2 and § 1.1.3.4. Direct measurement techniques of the solar magnetic field and approaches to infer it indirectly via different model approaches are depicted in § 1.2. Finally, § 1.3 deals with the theoretical view on how the solar magnetic field is generated in the solar interior, briefly outlining existing dynamo models and in § 1.4 a short summary is given.

1.1.1 Photospheric magnetic field

One or more small dark features (magnetic pores), having diameters of some thousands of kilometers with field strengths of about 200 mT – 250 mT, usually precede the emergence of sunspots in a previously undisturbed region of photospheric granulation. Pores have, in contrast to sunpots, no clear penumbra and hence appear like an isolated umbra (Keppens 2001). Interestingly, most of the formed small clusters of pores never develop beyond this stage, disappearing again after a couple of days. Only occasionally, the pores increase in size to evolve into proper sunspots. Sunspots are identified as to be proper if they possess a penumbra. This is a filamentary, inclined field structure of lower magnetic field strength which surrounds the more vertically oriented umbral field of higher magnetic field strength (Title et al. 1993, Lites et al. 1993). The formation process of a sunspot penumbra is difficult to observe since it involves timescales of less than one hour and spacial scales of less than one arcsecond (Leka and Skumanich 1998). Once formed, however, the sizes of proper sunspots vary greatly between extreme cases showing diameters of less than 3000 km or up to 60 000 km (Bray and Loughhead 1964). Given that sunspots grow rapidly after their emergence, they soon reach their maximum size and decay slowly afterwards. Not only the instantaneous size distribution of sunspots but also the distribution of the maximum sunspot sizes have been shown to be of a log-normal shape, i.e. the logarithm of the covered area is normally distributed (Baumann and Solanki 2005). Moreover, the same relative size distribution is found not only for the different phases of a solar cycle but also for various individual cycles (Bogdan et al. 1988). Usually, the magnetic field strength is about 100 mT in a penumbra and about 300 mT (sometimes up to 400 mT) in the center of a sunspot. It is also possible that individually observed large pores which show no signatures of a penumbra (thus appearing as an isolated umbra) are larger than the smallest sunspots, possessing both a penumbra and an umbra. Also, the lifetime of sunspots varies significantly from hours to months for the smallest and largest sunspots, respectively, being linearly correlated to the maximum area covered by a sunspot (Waldmeier 1955, Petrovay and van Driel-Gesztelyi 1997).

After a certain time, however, the sunspots break up and their fragments are subject to transport and distortion by the convective flows in and below the photosphere. Continuously squeezed by granules and swept to the boundaries of supergranular cells, a patchy network of magnetic components is created. This network not only roughly outlines the supergranular cells, it is also detectable in the upper photosphere and even more pronounced at higher altitudes in the solar atmosphere. Magnetic elements have measured field strengths of 100 mT – 150 mT and lifetimes from minutes to hours (Solanki 1993). The difficulty to determine the lifetimes of individual magnetic elements is rooted in their small sizes which are in the order of a few tens of kilometers. Therefore, the analysis of such structures and the associated lifetimes depends on the spacial resolution of the magnetograms used to study them and the ability of different instruments to detect weakest magnetic fluxes. Consequently, Ramsey et al. (1977) and Wang et al. (1985) set quite different lower limits of ten minutes and one hour, respectively, on the lifetimes of small-scale magnetic structures. The magnetic elements represent the opposite-polarity footpoints of small loops which are swept to the edges of the supergranular cells due to convective transport at the solar surface. Since it is there where footpoints of different loops with mixed polarities meet, magnetic elements of opposite flux cancel each other

and disappear. Only at points where several supergranular cells meet accumulations of magnetic elements can be found but also in the interiors of the supergranular cells magnetic features (so-called "internetwork elements") are located.

A quite different behavior is found for sunspot groups which are thought to form due to a successive emergence of many large strands, previously making up a large flux rope beneath the solar surface. Continuously, loops emerge to form spots where they merge together but also loops are produced which end outside of the previously formed spots. However, they are also aligned like the ones passing through the spots so that the magnetic elements at their footpoints are grouped together in two regions of opposite polarity. In other words, the formation of sunspots implies the formation of active regions which typically are of a bipolar magnetic structure (Durrant 1988, Solanki et al. 2006). Outside of sunspots, the magnetic field of active regions is mainly concentrated in more or less discrete features (magnetic elements) forming so-called "faculae" or "plage" regions. Plages are regions of enhanced temperature and density which float in the chromosphere. These regions form before sunspots appear and outlast, for some time, after the sunspots disappeared. Features that are similar in nature but which are observed in the photosphere are called faculae (Murdin 2001). However, the magnetic field in both active regions and the quiet Sun appears as an accumulation of discrete magnetic flux elements, separated by regions with little magnetic flux (called "field-free" regions to a first approximation).

While smaller magnetic features (which only sometimes appear as pores but mostly in the form of magnetic elements) are distributed over the entire solar surface, sunspots are restricted to well-defined zones of latitude on either side of the solar equator. This latitude-dependent distribution is thought to mirror regions which are occupied by strong toroidal fields, previously generated by the internal dynamo process (see § 1.3.2). Plotting the position of the sunspots versus time results in a so-called "butterfly diagram" which shows that two latitude bands on either side of the equator form first at mid-latitudes and then move towards the equator as each cycle progresses (see Fig. 1.1). It takes about 11 years before the first spots of the following cycle show up again at mid-latitudes while sunspots of the present cycle are still observable at near-equatorial latitudes ("Spörer's law"). It is thought that sunspots are manifestations of strong magnetic fields which emerge in form of toroidal flux tubes from the underlying convection zone. Consequently, the locations where magnetic field lines emerge from or re-enter the solar surface are the locations of sunspots with opposite polarity. Because of the emerging flux always appearing in form of a system of magnetic loops, the two intersections of the loop system with the solar surface create a bipolar group of sunspots. In general, the leading spots of a sunspot group are located closer to the equator than the following ones ("Joy's law"). Based on the magnetic classification of sunspots (e.g. McIntosh 1990, 2001), Hale et al. (1919) analyzed 970 sunspots during one solar cycle and proposed the formulation of a sunspot polarity law from which the polarities of spots of any type can be predicted, for either hemisphere and any epoch in the sunspot cycle. They noticed that the preceding and following spots of binary groups were, with few exceptions, of opposite polarity. In the following we call the opposite polarity of leading and following spots in sunspot groups, i.e. the positive/negative or negative/positive polarity of the leading/following spots, the "polarity order". They also found that the corresponding polarity order of such groups in the northern and southern hemisphere was opposite. Investigating the magnetic polarities of sunspot groups during three solar cycles, Hale and Nicholson (1925) were

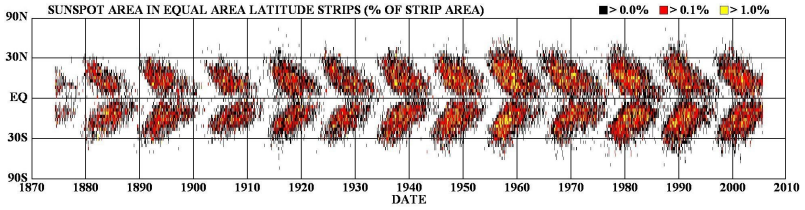

Figure 1.1: Daily observations of sunspot area since 1874, averaged over individual solar rotations. The sunspot area in equal-area latitude strips (vertical axis) is shown as a function of time (horizontal axis). The color code indicates the area covered by a sunspot or a group of sunspots located within a certain latitude strip. (Courtesy of D. Hathaway.)

able to verify the earlier proposed polarity law. They found that out of 2147 spot groups, 61% could be classified as bipolar during the greater part of their existence and that the polarity law applied to about 98% of 1735 groups. Usually, the polarity order in the two hemispheres remains unchanged while a cycle progresses but is reversed in the following cycle (which is usually referred to as "Hale's polarity law"). Thus the full underlying magnetic cycle, i.e. the interval between the appearance of mid-latitude spots of the same magnetic polarity, spans around 22 years.

1.1.2 Chromospheric and coronal magnetic field

The role of magnetic fields in the quiet chromosphere is less obvious than in active regions. Nevertheless, the magnetic flux concentrated along the network and outlining supergranulation cells in photospheric magnetograms, coincides with the chromospheric network as well. Appearing bright in chromospheric radiation, the magnetic elements appear to be larger in size than in the photosphere. This is because the flux tubes are thought to expand due to the decreasing pressure of the surrounding gas with increasing height, until they finally merge with neighboring flux tubes (Durrant 1988). This network can even be traced up into the transition region which separates the lower atmospheric layers, dominated by gravity and gas pressure, from the higher atmospheric layers, dominated by magnetic forces. This, however, led to some confusion since the magnetic network can be observed at heights in the solar atmosphere which lie much above the heights where flux tubes are expected to merge (Hammer 1994).

The transition region is the connection between the hot corona and the cool chromosphere and the energy needed to maintain this transition layer is supplied by a heat flow from the corona (the so-called "back-heating"; Dowdy et al. 1986). The standard magnetic picture of the quiet transition region pictures the magnetic field lines, emerging from the boundaries of supergranules, to fan out rapidly with height to fill the corona (Gabriel 1976). This is consistent with the observation of the transition region's ultraviolet emission which appears to be largely confined to the network defined by the photospheric magnetic field. It successfully reproduces the run of the emission measure with temperature (that is a summary of the temperature structure of the outer solar atmosphere, derived from a select subset of line fluxes) in the hotter part of the transition region, at tempera-

tures of $T \gtrsim 10^5$ K. Also different kinds of back-heating models were able to successfully reproduce the observed run of the emission measure at these temperatures. However, even the approximate behavior of the emission measure in the cooler transition region, at temperatures of $T \lesssim 10^5$ K, was failed to be reproduced by these models (Athay 1981, 1982). This led to the development of a picture of the magnetic transition region, in particular differing from the standard picture in the suggestion that only a few footpoints of large loops and open magnetic regions ("coronal funnels") properly connect to the corona, while the rest of the chromospheric plasma is concentrated in small low-lying loops, closing within the network which are not connected to the corona (Dowdy et al. 1986, Feldman 1998).

The coronal magnetic field appears in two configurations: open or closed. Open magnetic fields have their footpoints in polar regions over most parts of a solar cycle and sometimes (preferentially in periods of magnetic field reversal) originate at low latitudes. These field lines are found to be more or less radial where the field in the underlying photosphere is predominantly unipolar. The open field lines, along which an efficient plasma transport takes place as chromospheric plasma is heated at their footpoints, connect the solar surface with the interplanetary magnetic field. As the coronal plasma is frozen into the magnetic field (i.e. the plasma cannot cross the field lines), regions filled with open field lines allow the plasma to escape from the Sun. This results in regions of reduced plasma density, emitting less radiation than their surrounding, consequently appearing as darker areas and which are therefore called "coronal holes". Analyzing the soft X-ray emission of the Sun, Timothy et al. (1975) found the coronal holes to come in two basic configurations: compact or elongated. The compact features are almost entirely enclosed by fields of opposite polarity and lie predominantly in one hemisphere of the Sun. The elongated holes show a north-south orientation and extend from one pole to mid latitudes in the opposite hemisphere (extending over $\approx 110^\circ - 120^\circ$ of solar latitude). The formation of polar coronal holes takes place around the time of the polar magnetic field reversal and once established they persist for several years. Initially, often irregular shaped holes which are not centered on the pole are observed which, during a longer period of relatively steady growth, develop to holes that are more symmetric about the poles. After reaching, on average, their maximum size during the minimum phase of the solar cycle, they start to decay steadily (Harvey and Recely 2002). Low-latitude coronal holes tend to be situated near the edges of magnetically complex active regions and sometimes active regions even emerge within the coronal holes themselves (Cranmer 2009). Wiegelmann and Solanki (2004) investigated the emissivity of closed loops in equatorial coronal holes and quiet-Sun loops by extrapolating the photospheric, line-of-sight magnetic field, obtained with the Michelson-Doppler Imager on board of the Solar and Heliospheric Observatory (SoHO/MDI; Scherrer et al. 1995), into the corona. Based on the assumption that the temperature of a loop depends on its length and, in particular, that short loops are cooler than long loops, they used a model-based scaling law by Rosner et al. (1978) to convert loop length into temperature. Then they were able to show that the fraction of the considered volume, filled with transition region gas at a temperature of $T = 4 \times 10^5$ K in coronal holes was $\approx 70\%$ of that in the quiet Sun, while this fraction dropped to about 10% at $T = 9 \times 10^5$ K. Therefore, it was concluded that the almost complete absence of closed loops at coronal temperatures in coronal holes yields hardly any emission in lines formed at high temperatures. Over the rest of the solar surface the basic structural component of the corona are regions that mainly contain closed magnetic field lines which are filled

with chromospheric plasma and appear as bright, overdense loops. Most of these loops have both footpoints located in the same active region. However, some appear to link different active regions on the same solar hemisphere while others are found in the form of "transequatorial" loops, connecting active regions on either side of the solar equator. If such closed loops reach heights of more than about one solar radius, they can connect to the heliosphere since the plasma confinement decreases with decreasing magnetic field pressure (e.g. Durrant 1988, Aschwanden 2004).

In the outer layers of the solar atmosphere the magnetic field replaces the gravitational force as the major influence controlling the atmospheric structure. The outer solar atmosphere loses energy in form of radiation and the kinetic and potential energy of the solar wind. Nevertheless, since all magnetic features which expand to the outer solar atmosphere are rooted below the solar photosphere where the magnetic field is frozen into the plasma, (sub)surface motions continue to control the location of the parts of the flux tubes lying below the surface. This naturally implies the flow of electric currents which continuously increases the energy content of the magnetic field above. Part of this energy is instantaneously released on small spatial scales to heat the corona. The rest continues to accumulate until a given magnetic structure becomes unstable and abruptly releases the previously stored magnetic energy in the course of an explosive event (e.g. Durrant 1988, Vršnak 2005).

1.1.3 Explosive phenomena

The plasma in the outer solar atmosphere is dominated by the magnetic fields in the sense that the magnetic energy density is orders of magnitude greater than the thermal, kinetic and gravitational energy density (Forbes 2001). If the changes of the coronal structures take place on length scales comparable to the typical coronal scale height ($\gtrsim 50\,000$ km, as a consequence of the high coronal temperature and light hydrogen gas; see Aschwanden 2004), one can assume the electric currents to be co-aligned with the magnetic field. Thus, the Lorentz force vanishes and the magnetic field is said to be in a "force-free" state. Then the coronal magnetic field can be considered to evolve slowly through a sequence of neighboring force-free equilibria. Due to the subsequent deformation of the magnetic field, electric currents are induced and magnetic energy is consecutively built up so that the stored energy in any force-free field is predominantly of magnetic type. Besides from the shear or twist of existing magnetic fields, the electric currents can also arise from the emergence of new magnetic loops from below the solar surface into an existing coronal magnetic field (Benz 2001). If the magnetic energy content reaches a critical point, an instability may occur so that the system evolves to a new equilibrium state of lower energy and, consequently, that part of the previously stored energy is released (Priest and Forbes 2002). The magnetic energy that is available to be released during the eruptions is called the "free" magnetic energy and represents the energy stored due to the topological reconfigurations of the coronal magnetic field. The amount of free energy in a coronal volume is related to the size of the occurring eruptions and can therefore basically be used as a precursor for the magnitude of the upcoming events.

The large-scale eruptions, as observed in the solar atmosphere, are of three different types: coronal mass ejections (CMEs), prominence eruptions or large two-ribbon flares. These may well occur close in time and thus be associated with each other, indicating the

different manifestations of a joint basic physical process. During CMEs, solar material and magnetic flux are ejected from the lower corona into the interplanetary space on large scales. This thus leads to the opening of magnetic field lines in active regions, observable as the formation of flare ribbons and loops (Priest and Forbes 2002). While large flares are frequently associated with a CME and the eruption of an active-region prominence, most CMEs are not associated with large flares but more than half of all are conjoint with erupting quiescent prominences outside of active regions. In particular, Munro et al. (1979) found for mass ejections associated with near-surface activity that $\approx 40\%$ were associated with flares and more than 70% were associated with an eruptive prominence or filament disappearance (with or without a flare). Gosling et al. (1976) found flare-associated CMEs to move considerably faster through the corona than those associated to eruptive prominences which led them to suggest that flare-associated events are more impulsive. Sheeley et al. (1983) studied the association between CMEs and full-disk X-ray events over about three years of high sunspot activity. They found that the estimated CME probability continuously increased with the X-ray duration of the associated flaring. Analyzing 72 X-ray flares, observed within predefined CME onset windows, Harrison (1995) estimated a probability of $\approx 7\%$, $\approx 15\%$ and $\approx 24\%$ of detecting a CME in association with a B-, C- and M-class flare, respectively (for the solar flare classification based on the measured solar soft X-ray flux see § 1.1.3.1 and Table 1.1).

1.1.3.1 Flares

The localized sudden release of energy within a solar active region, causing a variety of phenomena observable from gamma to radio wavelengths, is called a flare. Large flares often occur above "neutral lines" (that is the line dividing regions of opposite polarity) which are bridged by arcades of loops. In a relaxed state the field lines are directed perpendicular to the neutral line but if, for some reason, the opposite-polarity magnetic field regions move with respect to each other, then the field line footpoints move relative to the neutral line. This is then called a "sheared" configuration where in extreme cases the field lines are oriented nearly parallel with respect to the neutral line. Due to the shear electric currents are induced and, consequently, flares preferentially occur in regions where the electric current has a maximum (Benz 2001). The occurrence rate of flares is also related to the magnetic field strength in given areas on the Sun. Since the magnetic energy is stored faster in strong field regions, preferable flaring locations are sunspot groups while flaring only occasionally occurs in spotless regions. In general, stronger (larger) flares occur when stronger fields are involved, since a higher amount of previously stored free magnetic energy is available to be released (Vršnak 2005). Besides being partly responsible for the heating and large-scale reconfiguration of the solar corona, the largest flares may well affect our Earth. Moreover, the flare-caused disturbances can be immediate, for instance enhancing the ionization of the ionosphere and thus influencing the propagation of radio waves (Benz 2001). However, flaring is not only related to the solar atmosphere in and above, sometimes very complex, active regions. In quiet-Sun regions at the boundary and even in the interior of supergranular cells so-called "microflares" are observed, being about a million times smaller than their active-region relatives. These occur where small-scale magnetic fields build up due to the convective transport of frozen-in magnetic field to the down-draft regions at the surface.

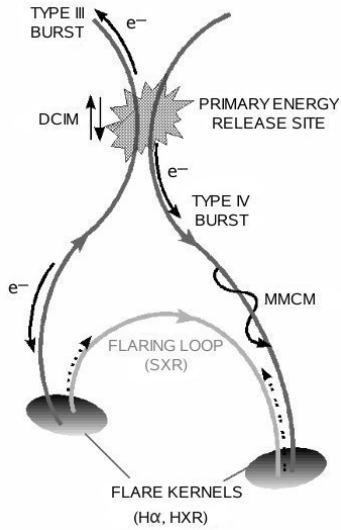

Figure 1.2: Basic processes common to most flares. Interacting magnetic field lines (dark gray solid lines) result in flaring loops (light gray solid line). Electron beams are produced in the primary energy release site and propagate upwards and downwards (black solid arrows). Chromospheric and transition region material is heated and evaporates upwards along the flaring loop (black dashed lines). Adapted from Vršnak (2005).

Being in some cases only a minor part of a large-scale destabilization of the solar corona, a general flare mechanism involves the release of energy in the corona through magnetic reconnection, the acceleration or heating of particles as well as the launch of violent mass motions. The heated and/or accelerated particles propagate from the coronal energy release site downward, encounter the denser material of the chromosphere and lose their energy due to collisions. This in turn, significantly enhances the temperature of the chromospheric material by electron beams and/or thermal conduction (e.g. Fisher 1989). Consequently, the plasma of the chromosphere and transition region is convected upwards so that it expands and adds new, high-temperature plasma to the atmosphere above which is referred to as "chromospheric evaporation" or "ablation" (first suggested by Neupert (1968) to explain the observation of the soft X-ray emission of flares to peak later than the hard X-ray emission). The upward motion of the chromospheric and transition-region plasma not only fills the coronal loops, i.e. the magnetic field lines that connect locations of opposite polarities, but also may continue in form of an expansion of those magnetic loops. Finally, due to radiative losses, the hot and dense plasma rapidly cools (see Fig. 1.2 and e.g. Benz 2001). The outlined scenario is thought to be common to most solar flares and involves a number of energy transport processes. The energy release is assumed to primarily take place in the corona since radio bursts drifting to lower as well as to higher frequencies reveal electron beams propagating upwards and downwards (for a discussion

Soft X-ray flare classification scheme

Flare soft X-ray class	*Peak intensity of flare emission* [Wm^{-2}]
A	$I < 10^{-7}$
B	$10^{-7} \leq I < 10^{-6}$
C	$10^{-6} \leq I < 10^{-5}$
M	$10^{-5} \leq I < 10^{-4}$
X	$10^{-4} \leq I$

Table 1.1: Classification of solar flares according to the GOES soft X-ray brightness in the 0.1 nm – 0.8 nm band. Flare classes are termed by the letter A, B, C, M or X, according to the peak intensity of flare emission on a logarithmic scale.

of flare-associated radio bursts see e.g. Cliver (2001)). This, according to Bastian et al. (1998), supports the assumption of the energy release site in flares to be located somewhere in the lower corona and, in particular, higher in the solar atmosphere than flaring loops emitting soft X-rays (Aschwanden and Benz 1997). These radio bursts are fast-drifting, narrow-band radio fine structures at decimeter to meter wavelengths (denoted as DCIM in Fig. 1.2). Electron beams which escape outwards from the primary energy release site excite type III radio bursts while electrons accelerated downwards along the magnetic field lines stay trapped and excite type IV radio bursts (Vršnak 2005). In strong magnetic fields, electrons with large pitch angles produce emission from millimeter to centimeter wavelengths (denoted as MMCM in Fig. 1.2 and see e.g. Benz 1993). Electrons with small pitch angles penetrate through the magnetic mirrors located near the footpoints of the magnetic loops and hit the dense transition region and chromospheric plasma, exciting line emission of atoms and ions along with hard X-rays. The earlier mentioned chromospheric evaporation represents the establishment of a new hydrostatic equilibrium by the heated chromospheric plasma that starts to expand. Consequently, the closed flaring loops are filled with dense and hot plasma, becoming the source of soft X-ray emission and above these loops a super hot loop top is sometimes observed (Tsuneta et al. 1997, Uchida et al. 2001).

There are several methods to classify solar flares, for instance, in terms of the associated Hα or soft X-ray emission, the related meter-wavelength radio bursts or energetic particle events or the magnetic topology. In the following, only the grouping of flares into classes due to the associated soft X-ray emission is explained in detail since this is the classification scheme we are referring to when describing the flaring activity of active regions later on in this work. For the classification of flares due to the other aforementioned accompanying phenomena we refer to the detailed review by Cliver (2001).

The solar soft X-ray observations in the 0.1 nm – 0.8 nm spectral band of the Geostationary Observational Environmental Satellite (GOES) provide the basis for the soft X-ray flare classification scheme (see Table 1.1 and e.g. Zirin 1988). Flares are classified with a letter (A, B, C, M or X), according to the peak-intensity of the flare emission on a logarithmic where A $\propto 10^{-8}\,Wm^{-2}$, B $\propto 10^{-7}\,Wm^{-2}$, C $\propto 10^{-6}\,Wm^{-2}$, M $\propto 10^{-5}\,Wm^{-2}$ and X $\propto 10^{-4}\,Wm^{-2}$. Additionally, a number acts as a multiplier to indicate the level within each class so that, for example, the most powerful flare ever recorded in soft X-rays on Nov 4, 2003 was classified as an X28 event, according to its peak flux in intensity of $28\times10^{-4}\,Wm^{-2}$.

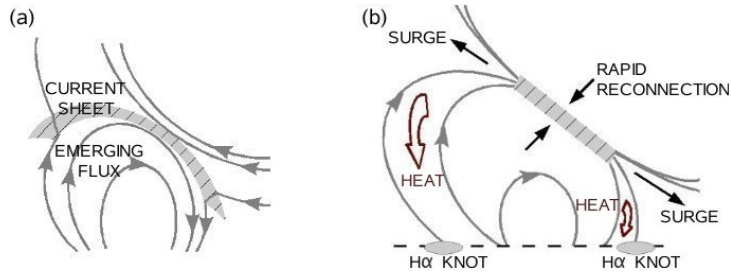

Figure 1.3: Overall picture of an emerging-flux flare. (a) Due to the collision of a newly emerging loop with a preexisting coronal field of opposite polarity a current sheet forms (striped region). (b) Rapid reconnection of field lines is caused by the onset of a resistive microinstability and leads to the conduction of heat (red arrows) and particles to the lower chromosphere. Adapted from Heyvaerts et al. (1977).

1.1.3.2 Flare models

The earlier described basic flaring process represents the heart of flare models and can be incorporated in different flaring scenarios which are constrained by several basic properties as established by various observations. First, the magnetic energy density of the plasma in the outer solar atmosphere is about three orders of magnitude greater than the thermal, kinetic and gravitational energy density (Forbes 2001). Consequently, it is the magnetic energy which is the only source capable of producing the radiative and kinetic energy output associated with a flare. Second, the slow movements of magnetic features in the solar photosphere are, due to the much higher plasma density, unaffected by the occurrence of flares in the low-density coronal plasma above. Third, the timescale in which the thermal and kinetic energy is generated after the onset of flares is only a few minutes which is extremely short for flaring processes which usually involve regions of several tenthousands of kilometers. This implies dynamic velocities from hundreds to thousands of kilometers per second, comparable to the speeds at which slow magneto-acoustic and Alfvén waves, respectively, propagate in the corona (e.g. Nakariakov and Verwichte 2005). The two main flare models are those of interacting magnetic systems (referred to as "interacting-flux" flares) and that of "two-ribbon" flares. The former are directly associated with the reconnection between two or more distinct interacting magnetic systems while the latter involve a pre-flare structure slowly evolving through a series of equilibria, causing a slowly rising filament (arcade) structure to lose its equilibrium and, consequently, to erupt.

A distinct type of interacting-flux flares, associated with emerging flux regions, is usually called an "emerging-flux" flare. There, magnetic flux emerging from below the photosphere presses against an overlying, preexisting field of opposite polarity because of which a current sheet forms. This current sheet grows and a micro-instability develops once a critical threshold is reached. Then, the local resistivity of the plasma might increase so much that the current sheet is rapidly dissipated by the magnetic reconnection between the interacting magnetic systems (see Fig. 1.3 and Heyvaerts et al. (1977) but

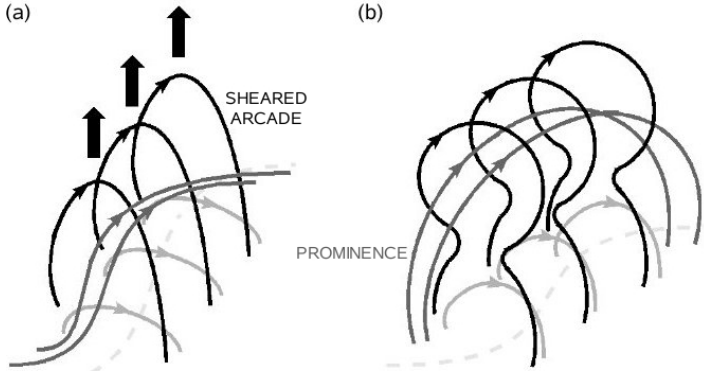

Figure 1.4: Overall picture of a two-ribbon flare. (a) The slow initial rise (black arrows) of the magnetic field lines of a sheared arcade (black solid lines) due to a non-equilibrium is followed by (b) the onset of reconnection below the rising flux tube (dark gray solid lines). The light gray dashed line represents the neutral line, subsequent higher field lines are represented by the subsequent darker color. Adapted from Priest and Forbes (2002).

also e.g. Vršnak (2005)). The reconnection can be caused by emerging or merging motions or can be driven by coalescence instabilities (e.g. Tajima et al. 1987, Kliem 1995). Another type of interacting-flux flares are the so-called "interacting-loop" flares where aligned loops can interact with each other either due to the attraction of longitudinal currents, driving reconnection of azimuthal fields or the reconnection of longitudinal fields. This was shown by Linton et al. (2001) who studied the way how magnetic reconnection occurs, depending on the angles between the magnetic field lines when they come into contact.

Two-ribbon flares involve additional observational constraints in the form of a continuous, low-level emission over a period of several hours after their initial rapid phase and the formation of two bands ("ribbons") of chromospheric emission which slowly propagate away from each other during the evolution of the flares. The preceding evolution of such flares involves, first, a sheared or twisted arcade (containing a prominence) that slowly rises during the pre-flare phase and, second, a rapid eruption (revealing the "flare onset") due to the onset of reconnection below the rising prominence (see Fig. 1.4 and Priest and Forbes (2002) but also e.g. van Ballegooijen and Martens (1989) and Vrsnak et al. (1991)).

1.1.3.3 Coronal mass ejections

Coronal mass ejections (CMEs; originally termed "coronal transients") are thought to contain an erupting filament/prominence (when viewed on the solar disk/on the solar limb, respectively). This implies that a mass up to several billion tons of coronal material at speeds of several hundreds to thousands of kilometers per second is bodily removed from the solar atmosphere (e.g. Gosling et al. 1976). Due to the eruption, magnetic field lines

become open towards the interplanetary space along which material can escape. Although CMEs mainly originate from regions with a closed magnetic field structure, and therefore hardly originate from coronal holes, filaments in the vicinity of coronal holes are often observed to initiate such ejections. Bhatnagar (1996) found that the open magnetic field configuration of coronal holes provides the necessary field structure for reconnection to take place so that a filament eruption can be initiated. In general, the CME activity is related to flaring active regions and to quiet solar regions which contain a filament (van Driel-Gesztelyi et al. 1999). CMEs, therefore, come in two basic flavors: flare-related or associated with a filament/prominence eruption. Consequently, young solar active regions produce mainly the first while the dispersal of active-region magnetic flux results in the dominance of the latter (van Driel-Gesztelyi 2005). Erupting prominences outside of active regions also produce features typical of large flares, like flare ribbons moving apart in time and faint loops ("giant arches", representing the CME counterparts of the flare loops of two-ribbon flares). Compared to the continuous, slower growth of flare loops in time, the CME loops exhibit an upward movement at nearly constant or even increasing rates (Forbes 2000).

Once initiated, the basic CME mechanism involves, first, an acceleration and subsequent expansion. Both are part of the initiation of a CME itself but are also of possible importance for the long-term evolution. Second, it involves drag and distortion which result from the interaction of the CME with the ambient solar wind, co-rotating interaction regions or other CMEs (Forbes et al. 2006). Typically, when CMEs erupt close to the solar limb they are observed as a bright frontal part (the so-called "leading edge"), followed by a darker cavity and a core where the latter is usually even brighter than the leading edge (see Fig. 1.5). When directed towards the Earth, CMEs are recognizable in form of an outflow and an expanding coronal brightness around the Sun (referred to as "halo" CMEs; Howard et al. 1982). Since such events, due to their Earth-directed character, are difficult to analyze the launch of the Solar TErrestrial RElations Observatory (STEREO; Kaiser et al. 2008) spacecrafts represents an advantageous basis to provide estimates of the speed and direction of individual coronal events, based on the observation from two different viewpoints (e.g. Davis et al. 2009). Such "stereoscopic" monitoring has the ability to improve space weather forecasts, not only in the case of Earth-directed eruptions.

When launched in the quiet Sun, the streamer cavity of the ejected structure can be directly seen in white light or soft X-rays which corresponds to weak effects similar to flaring activity as observable in chromospheric Hα images (Hudson et al. 2006). Also related to CMEs is also the disappearance of filaments and the formation of flare ribbons observable in Hα, He I 1083.0 nm and microwave observations. The ribbons produced by erupting prominences outside of solar active regions are often too faint to be observable in Hα but, however, can often be identified in the He I 1083.0 nm line which is more sensitive to chromospheric excitation. At extreme ultraviolet wavelengths, the eruption of a dark filament is usually followed by the formation of an arcade of bright flare loops in its wake, where the post-eruptive arcade is seen in soft X-rays (van Driel-Gesztelyi 2005). The outer edges of the hot soft X-ray loops map the outer edges of the Hα ribbons while the innermost edges of the cool Hα loops, which are formed by a thermal condensation process from the hot loops, map the inner edges of the Hα ribbons (see Fig. 1.5 and Forbes (2000) and references therein). Furthermore, on both sides of the post-eruptive arcade so-

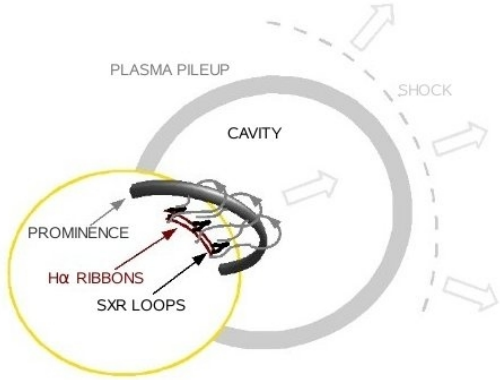

Figure 1.5: Schematic view of the basic features related to CMEs, erupting close to the solar limb (yellow circle). A frontal shock (light gray dashed line) is followed by a cavity. During the filament/prominence eruption Hα flare ribbons (dark red solid lines) and an arcade of giant loops (gray solid lines) are produced. The post-eruptive arcade (black cusp-shaped loops) is observable in form of soft X-ray loops. Adapted from Forbes (2000).

called "dimming regions" are visible as darker regions, e.g. in 19.5 nm images of the Extreme-ultraviolet Imaging Telescope on board the SoHO (SoHO/EIT; Delaboudinière et al. 1995), which indicates that the coronal material may become less dense and/or colder. Referring to these areas of reduced emissivity to as "transient" coronal holes, Rust (1983) interpreted these regions as zones of depleted coronal material. The evidence of these regions to be associated with coronal material escaping along the open field lines, as indicated by Doppler signatures in coronal emission lines, was found by Harra and Sterling (2001). However, not all of the aforementioned features are necessarily visible in all of the observable CMEs. Some ejections may not contain a prominence, others may not be associated with any detectable chromospheric signatures of flare ribbons and some CMEs may not produce an obvious shock wave.

1.1.3.4 CME models

Since there is an absence of strong effects on the photospheric magnetic field, CMEs are thought to involve energy storage and release in the corona (Hudson et al. 2006). Because the energy of CMEs is so high it is unlikely, though not impossible, that they are directly driven by emerging magnetic fields in the photosphere (e.g. Melrose 1995). Therefore, most CME models assume that the energy storage takes place in the coronal magnetic field over a long period of time and that its sudden release is caused by a loss of equilibrium (van Driel-Gesztelyi 2005). The mechanisms resulting in the loss of equilibrium itself might be caused by purely ideal or non-ideal processes (e.g. magnetic reconnection) but do not necessarily involve an energy release. Two mechanisms that trigger solar eruptions are thought to exist. One requires the magnetic energy to be quickly injected into the coronal magnetic field and the other one presumes the energy to be slowly stored in the

coronal magnetic field prior to an eruption. Accordingly, CME models can be divided into two distinct groups, namely "dynamo" or "flux injection" models and "storage" models (Lin et al. 2003, but see also the reviews by Forbes (2000) and Klimchuk (2001)).

Dynamo models (e.g. Sen and White 1972, Heyvaerts 1974, Kan et al. 1983) assume the source of the eruption in a dynamo region in the convection zone. Due to a sudden motion of the plasma in that region, a field-aligned current is produced in a magnetic loop. The increase in the loop current drives the loop outwards, producing an eruptive process. Flux injection models (e.g. Chen 1989, 1996) assume that, e.g., a flux tube which rises from the base of the convection zone results in magnetic flux emergence through the photosphere and the formation of a coronal loop. Correspondingly, a current is injected into the corona which leads to a rapid increase of the energy of the magnetic field. Both models have in common that the injected flux and the associated sudden enhancement of the current (flowing from the convection zone to the corona) necessarily cause photospheric plasma flows (since the photospheric magnetic field is frozen into the plasma). This would lead to the evolution of purely horizontal flows in the case of dynamo models and both upward and horizontal flows in the case of flux injection models. However, such displacements of photospheric material during eruptions have not been observed so far (Lin et al. 2003).

Storage models assume that energy is stored in the coronal magnetic field and once the field loses its equilibrium, an eruption occurs and energy is released. In contrast to dynamo and flux injection models, the continuous emergence of new flux from the convection zone and the movement of footpoints of closed coronal field lines cause the build-up of stresses in the coronal field over a long period of time. Once these stresses exceed a level beyond which a stable equilibrium can not any longer be maintained, the coronal structure erupts. According to Lin et al. (2003), the most successful theoretical storage models are the so-called "sheared arcade", "break-out" and "flux-rope catastrophic" models. Sheared arcade models (e.g. Mikic et al. 1988, Mikic and Linker 1994) assume that a coronal arcade responds to slow photospheric flows, thus to become continuously sheared and hence building up magnetic energy. Once a critical amount of shear is reached the magnetic equilibrium is lost and the arcade expands outward from the Sun so that field lines are opened and a current sheet forms. In the case of finite resistivity, magnetic reconnection occurs at the current sheet which leads, besides others, to the dissipation of energy and to the ejection of a plasmoid. Break-out models, as first proposed by Antiochos et al. (1999), also require magnetic reconnection to trigger the eruption but, in contrast to sheared arcade models, assume the reconnection to take place on top of a low-lying, sheared arcade so that an existing unsheared field above is bodily removed. Flux-rope catastrophic models, as developed by Forbes and Isenberg (1991), assume that the mass flow in the photosphere forces oppositely directed field lines of a flux rope to meet and thus to reconnect. Consequently, magnetic flux and energy is transported quasi-statically into the coronal magnetic field. Once the stresses reach a critical value the flux rope is ejected upward and part of the stored magnetic energy is released.

So far, the observational properties of the magnetic field in the solar atmosphere as well as the role of the solar magnetic field, being the underlying cause of eruptive phenomena, have been discussed. The next chapter will deal with the techniques of how to measure the magnetic field at different heights in the solar atmosphere, using either direct or indirect methods.

1.2 Measurements

1.2.1 Direct measurements

Most widely used methods to estimate the strength of the solar magnetic field are based on the Zeeman effect. This effect reflects the ability of a molecule which possesses a non-vanishing magnetic moment to interact with an external magnetic field (e.g. Herzberg 1950). The Zeeman effect causes a spectral line to split if the line originates from a magnetically sensitive transition and if the line-formation region is embedded in a magnetic field. The splitting is meant in the way that the action of a magnetic field causes any atomic level to split in sublevels spaced equally. Consequently, the energy levels in the atoms split up into sublevels (which are symmetrically distributed around the unperturbed energy level), resulting in the emitted light being split up into differently polarized components (e.g. Condon and Shortley 1970). Basically, the Zeeman effect is made up of two contributions arising from the influence of a magnetic field, one that is proportional to the magnetic field strength ("linear" Zeeman effect) and one which is proportional to its square ("quadratic" Zeeman effect), where the impact of the latter for field strengths found on the Sun is, in general, small compared to the former and is thus neglected.

In the case of weak magnetic fields, the separation between the split components is directly proportional to the square of the wavelength, the magnetic field strength and the Landé factor [1]. Here, "weak" means that the magnetic field is not strong enough to produce energy changes comparable to the separation of the sublevels (Condon and Shortley 1970). It is the ratio of the splitting to the linewidth which determines the ability to detect small splitting effects and, consequently, the Zeeman effect is more significant when probed at longer wavelengths. The splitting itself can be either "normal" or "anomalous", where the former manifests itself in one unshifted (π) and two oppositely directed, displaced (σ) components (together making up a "Zeeman triplet") while the latter shows more than one unshifted and more than two displaced components which, due to the mostly insufficient splitting, can rarely be distinguished (e.g. Stix 2002). If the magnetic field is directed parallel to the line-of-sight, the π-component of the normal Zeeman triplet is absent and the two σ-components are right- and left-handed circularly polarized ("longitudinal" Zeeman effect). In the case of the magnetic field being oriented perpendicular to the line-of-sight, the intensity of the π-component equals the sum of the two σ-components. Then, the π-component is linearly polarized with the electric vector being parallel to the magnetic field if the line is observed in emission and perpendicular to the magnetic field if observed in absorption. The σ-components are linearly polarized, perpendicular to the direction of the π-component ("transversal" Zeeman effect). Last, if the magnetic field is arbitrarily oriented with respect to the line-of-sight, the π- and σ-components will exhibit elliptical and mutually orthogonal polarizations (e.g. Stenflo 1978).

To summarize, the lines corresponding to the Zeeman splitting exhibit certain polarizations. Since the polarization depends on the direction in which an electromagnetic field

[1] The Landé factor is a particular example of a "g-factor", namely for an electron having both a spin and an orbital angular momentum. The g-factor relates the observed magnetic moment of a particle to the appropriate angular momentum quantum number and the appropriate fundamental quantum unit of magnetism (usually the Bohr magneton or nuclear magneton).

is vibrating, it carries information about the magnetic field vector. In particular, the line-of-sight component of the magnetic field can be obtained through the circular polarization via $V \sim B\ \cos\gamma$, where V describes the amount of right- or left-handed circular polarization and γ is the angle between the magnetic field vector and the line-of-sight. The transverse magnetic field can be estimated using the linear polarization with $Q \sim B^2 \sin2\gamma \cos2\varphi$ and $U \sim B^2 \sin2\gamma \sin2\varphi$, where Q describes the amount of linear horizontal or vertical polarization and U the amount of $+45^\circ$ or -45° polarization. Furthermore, φ represents the azimuth of the field vector which evidently implies an 180°-ambiguity in the transverse magnetic field measurements using the Zeeman effect (Raouafi 2005).

In the case of very strong magnetic fields, the line-splitting effect is no longer linearly proportional to the magnetic field. Here, "strong" is a relative measure depending on the magnetic sensitivity of a given spectral line and means that the magnetic field is sufficiently strong to produce energy changes comparable with the separation of the sublevels (Condon and Shortley 1970). Then, the caused line splitting can be large compared to the separation of the spin-orbit system so that the coupling between the orbital and spin angular momenta gets disrupted and the spectral line rearranges (which is referred to as the "Paschen-Back effect"). This is different from the weak-field Zeeman effect in which the magnetic field is not strong enough to disturb the orbit-spin interaction so that the total angular momentum is conserved. However, Maltby (1971) showed that the Paschen-Back splitting of the Li I 670.8 nm resonance lines must be taken into account for sunspot magnetic fields. Using the Zeeman-sensitive He I 1083.0 nm triplet, which allows to determine the magnetic field vector in the upper chromosphere, Socas-Navarro et al. (2004) showed that the Zeeman components are strongly influenced by the Paschen-Back effect, especially for magnetic field strengths of a few tens of mT.

As already mentioned, the splitting of the energy levels into sublevels based on the Zeeman effect is a function of the field strength. If the splitting is small so that the sublevels overlap each other (i.e. that the energy separation does not exceed the energy uncertainty of a level), the superposed wavefunctions of the sublevels may interfere with each other. In particular, this interference occurs in coherent scattering and all polarization signatures caused by this phenomena are called "Hanle effect". If no magnetic field is present, coherent scattering produces linear polarization signals while the presence of a magnetic field causes a reduction of the polarization degree. In the solar photosphere, most of the scattering occurs incoherently so that the polarization resulting from the Hanle effect is very small and therefore difficult to measure. The magnitude of the Hanle effect essentially depends on the ratio of the line splitting to the inverse lifetime of the excited level and is therefore much more sensitive to weak magnetic fields than is the Zeeman effect (Stenflo 1978).

The magnetic field strength in photospheric sunspot umbrae, where the field strength is high, can be well determined by measuring the wavelength separation between the Zeeman components at visible and infrared wavelengths. Far away from sunspots, however, the Zeeman splitting can in general not be seen. This is because the magnetic flux in the quiet Sun is concentrated in small isolated areas with a small filling factor[2]. Therefore, magnetic field measurements based on the Zeeman effect are limited by the difficulty to

[2]The magnetic filling factor is a measure of the fraction of the observed part of the solar surface which is covered by intense magnetic fields. The field strength of magnetic elements increases slowly with increasing filling factor but also with increasing cross-sectional area of the elements (e.g. Solanki et al. 2006).

resolve weak magnetic structures ($\lesssim 5$ mT) and by the cancellation of opposite polarities within the resolution elements (Emonet and Cattaneo 2001, and references therein). Nevertheless, the lines exhibit a polarization pattern due to the present magnetic field. Consequently, the depolarization of spectral lines by turbulent magnetic fields can be detected, allowing measurements in areas of mixed polarities (Stenflo 1982). The Hanle effect, in contrast, does not suffer from this cancellation and is sensitive only to weak magnetic fields. In particular, investigating the signatures of Hanle depolarization, Stenflo et al. (1998) set a range of 0.4 mT – 4 mT for the magnetic field strength of the turbulent magnetic fields which fill about 99 % of the photospheric volume.

Measurements of the chromospheric magnetic field suffer not only from the plasma density being several orders of magnitude lower than that of the photosphere but also from the, on average, lower magnetic field strength. The low plasma density leads to weak emission and absorption signals of the spectral lines, the latter overmore exhibiting a strong contribution from the photosphere. The lower average magnetic field strength additionally weakens the Zeeman signals in the spectral lines for which the interpretation is already hampered by scattering polarization and its modification by the Hanle effect. The Hanle effect, however, finds more favorable conditions in the chromospheric field since, due to the lower plasma density, the collisional rates are smaller and thus scattering becomes coherent. Furthermore, the dominantly radiative energy transport and population imbalances between atomic sublevels, as induced by anisotropic illumination, hamper the measurements and, after all, the assumption of local thermodynamic equilibrium is violated (Wedemeyer-Böhm et al. 2009). However, since the Zeeman effect is more significant at infrared wavelengths, its measurement combined with that of the Hanle effect on the Ca I 850 nm and 854 nm lines as well as the He I 1083 nm line made it possible to infer the magnetic vector above sunspots as well as active regions, respectively (Solanki et al. 2006). For a number of reasons the He I 1083 nm line turned out to be very useful for the quantitative diagnostic of the upper-chromospheric magnetic field related to both sunspots and active-region plages (Rüedi et al. 1994).

The difficulty to determine the magnetic field in the corona is the high temperature of the coronal plasma so that thermal and non-thermal broadening of the emission lines make it much harder to detect the Zeeman splitting. For typical extreme ultraviolet lines with a wavelength of 20 nm in a coronal environment ($B \approx 20$ mT, $T \approx 2$ MK) the ratio of the Zeeman splitting to the thermal broadening is in the range of 10^{-4}. This ratio is even lower at shorter wavelengths (X-rays) but improves for lines at visible and infrared wavelengths (Cargill 2009). As already mentioned, the amount of Zeeman splitting increases with increasing wavelength and hence the measurements should improve using visible and infrared lines (although the latter is restricted to measurements made off the solar limb, sufficiently high above the solar surface). Up to now, using either the Zeeman or the Hanle effect allowed the successful measurement of the magnetic field vector in the hot solar corona above the solar limb in a few cases, based on observations of resonance scattering of the Fe XIV 530.3 nm (Arnaud 1982), the O VI 103.2 nm (Raouafi et al. 2002) or the Fe XIII 1074.7 nm (Lin et al. 2000) spectral line.

Alternatively, the Hanle effect on ultraviolet emission lines can be used to measure the coronal magnetic field but this requires space-based observations. In particular, Trujillo Bueno and Asensio Ramos (2007) used the He I 1083.0 nm multiplet and Raouafi et al. (2009) used the H I Lyα and Lyβ lines to test their ability to probe the coronal magnetic

field. Coronal emission lines at optical frequencies are very faint and extremely broadened due to the low coronal plasma density and the high temperature of emitting ions, respectively. Not only the extraction of very weak signals hampers the success of coronal magnetic field measurements but also the necessary long integration times and the line-of-sight integrated character of the measurements (the latter especially for off-limb observations). Kramar et al. (2006) discussed the associated limitations and pictured the possibility of reconstructing the 3D structure of the coronal magnetic field based on longitudinal Zeeman effect measurements of magnetically sensitive lines, using a tomographic inversion method. Optionally, the gyroresonance emission of strong active-region magnetic fields, originating from electrons gyrating along the coronal magnetic field lines can be measured. Although radio waves at low frequencies are blocked by the atmosphere of the Earth, the gyroresonance emission of few tens of mT can well be measured with ground-based instruments (Cargill 2009).

1.2.2 Indirect estimates

Since several difficulties are met in trying to infer the chromospheric and coronal magnetic field, alternative approaches have been developed which estimate the magnetic field in the upper solar atmosphere based on measurements made on the surface, i.e. at photospheric levels or, individually, at distinct heights in the solar atmosphere.

For instance, the mean parameters of the corona such as the magnetic field strength can be estimated based on measurements of the periods, wavelengths and amplitudes of coronal magnetohydrodynamic (MHD) waves, fed into specific theoretical models of the coronal wave phenomena. Incorporating as many as three modes (Alfvén, slow and fast magnetoacoustic modes with their quite different dispersive, polarization and propagation properties) these "coronal seismology" approaches are very powerful (Roberts et al. 1984). In particular, observed properties of the MHD modes associated with, e.g., active-region loops or open structures have been shown to be in good agreement with the theoretical models (for a detailed review on coronal seismology see e.g. Nakariakov and Verwichte 2005).

Alternatively, the structure of the coronal field can be inferred by extrapolating it from photospheric magnetic field measurements using so-called "force-free" magnetic field models. The term force-free arises from the assumption that the magnetic field is dominating all other forces in the upper chromosphere and big parts of the corona (though this assumption is not valid at photospheric levels and in the solar wind), i.e. that the Lorentz force vanishes. Then, the equilibrium coronal magnetic field can be reconstructed subject to appropriate boundary conditions (for a recent review of existing methods see Wiegelmann 2008). Optionally, "potential field source surface" (PFSS) models or MHD models can be used to extrapolate the global magnetic structure of the solar corona. Neglecting the contribution from transverse magnetic fields (which, however, are of particular importance in active regions), both methods derive the radial magnetic field component from photospheric line-of-sight magnetic field measurements. PFSS models can resolve global structures on spatial scales beyond those that can be handled by the MHD models but cannot directly incorporate time-dependent phenomena. This, however, is unavoidable if, e.g., magnetic reconnection is aimed to be studied (for a comparison of specific models see Riley et al. 2006).

The extrapolation of coronal magnetic fields can also be used in the context of "magnetic stereoscopy" (Wiegelmann and Inhester 2006). Classical geometric stereoscopic reconstruction techniques aim to estimate the 3D magnetic field topology from two (preferentially simultaneously taken) 2D images like, e.g., provided by the STEREO spacecrafts. Therefore, the projected magnetic loops as visible in the 2D images have to be extracted via some feature tracking method and corresponding ones have to be identified (correspondence problem). This introduces a certain ambiguity in the stereoscopic reconstruction since one often encounters multiple coronal loops which overlap each other so that a clear one-to-one correspondence between structures in the two images is not evident. Consequently, the stereoscopic reconstruction is not unique, i.e. the calculated 3D field not only contains the actually existing loops but also additional, unphysical ones (ghost features). Fortunately, the 3D magnetic field lines as calculated from a previously extrapolated force-free magnetic field can be used as a proxy. Once projected onto both 2D stereoscopic images, recognized loops can be compared to the projected force-free field lines and, consequently, corresponding loops precisely associated with each other by minimizing the averaged distance between them (see e.g. Feng et al. 2007).

So far we dealt with the observational properties of the solar magnetic field in the different layers of the solar atmosphere. Also the direct measurement techniques and the indirect (model) methods to derive the magnetic field in the different atmospheric layers have been described. Therefore, it is left to discuss the basic mechanism, assumed to operate below the visible solar surface, which gives rise to the magnetic field.

1.3 Generation mechanism

1.3.1 Magnetohydrodynamics

Magnetohydrodynamics (MHD) describes the dynamics of electrically conducting fluids (liquid or gaseous) which move in a magnetic field. It combines the basic principles of hydrodynamics and electrodynamics in a fluid description. It is capable of depicting how a velocity field across a magnetic field induces electric currents in a conductive fluid, whose magnetic field and associated Lorentz force act back on the velocity. It applies to (at least partially) ionized gases (plasmas) which move at non-relativistic speeds (i.e. the temporal variations are slow) and which are highly collisional. The assumption of the temporal variations to be slow allows it to neglect the displacement current in Ampere's law. Additionally, the fluid is assumed to be globally neutral, which does not mean that the constituents of the fluid are neutral but that there is an approximately even number of positive and negative electric charges present in a given volume at a certain time. In MHD, the equations of fluid dynamics (the mass continuity equation, the momentum equation and the energy equation) are combined with the reduced Maxwell equations

$$\nabla \times \boldsymbol{E} = -\partial_t \boldsymbol{B}, \tag{1.1}$$

$$\nabla \times \boldsymbol{B} = \mu_0 \boldsymbol{J}, \tag{1.2}$$

$$\nabla \cdot \boldsymbol{B} = 0 \tag{1.3}$$

and Ohm's law,

$$\boldsymbol{J} = \sigma (\boldsymbol{E} + \boldsymbol{v} \times \boldsymbol{B}), \tag{1.4}$$

where $\boldsymbol{E}$, $\boldsymbol{B}$ and $\boldsymbol{J}$ represent the electric field, magnetic field and electric current densities, respectively, $\boldsymbol{v}$ is the fluid velocity, μ_0 denotes the permeability of free space and σ the electric conductivity.

The time evolution of the magnetic field can be investigated by inserting Ohm's law (1.4) into Faraday's law (1.1) and eliminating the current density $\boldsymbol{J}$ with the help of Ampère's law (1.2) to gain the MHD induction equation

$$\partial_t \boldsymbol{B} = \nabla \times (\boldsymbol{v} \times \boldsymbol{B}) - \nabla \times (\eta \nabla \times \boldsymbol{B}) \tag{1.5}$$

with $\eta = (\mu_0 \sigma)^{-1}$ being the magnetic diffusivity. The induction equation together with the solenoidal condition (1.3) describes the evolution of the magnetic field $\boldsymbol{B}$, once the velocity field $\boldsymbol{v}$ is known.

If the magnetic diffusivity η is assumed to be spatially constant, (1.5) reduces to

$$\partial_t \boldsymbol{B} = \nabla \times (\boldsymbol{v} \times \boldsymbol{B}) + \eta \, \Delta \boldsymbol{B}. \tag{1.6}$$

Here, the first and second term on the right-hand side describe the induction and diffusion effects, respectively. The relative importance of these two terms is described by the dimensionless magnetic Reynolds number R_m, defined as the ratio of their magnitudes in the form

$$R_m \equiv \frac{| \nabla \times (\boldsymbol{v} \times \boldsymbol{B}) |}{| \eta \, \Delta \boldsymbol{B} |} = \frac{v_c \, l_c}{\eta}, \tag{1.7}$$

where v_c and l_c are the characteristic velocity and length scales of the system, respectively.

Three different domains may be defined according to the relative magnitude of the inductive and diffusive effects. First, if the diffusion dominates the induction then $R_m \ll 1$, which occurs if either v_c or l_c is small or if η is large. Then, the resistivity (that is the inverse of the electric conductivity σ) becomes important in that instabilities may locally increase the effective resistivity of the plasma so that magnetic diffusion can occur quickly ("resistive" MHD). This implies that, in imperfectly conducting fluids, the magnetic field can move through the fluid. Second, when the induction and the diffusion approximately balance each other then $R_m \approx 1$. Third, if the inductive effects dominate the diffusive ones then $R_m \gg 1$, which is considered as domain of "nearly perfect conductivity". Then one deals with the so-called "ideal" MHD which is applicable if the resistive terms are negligible compared to all other terms. This occurs if either v_c or l_c is large or if η is small. It applies only for a limited time for a region of a given size before diffusion becomes too important to be ignored. The "perfect-conductivity" limit, where $R_m \to \infty$ (i.e., $\sigma \to \infty$ or $\eta \to 0$), is the formal limit where $\boldsymbol{B}$ satisfies the frozen-inn condition $\partial_t \boldsymbol{B} = \nabla \times (\boldsymbol{v} \times \boldsymbol{B})$, implying Alfvén's theorem which states the magnetic flux to be conserved across any Lagrangian surface (Moffatt 2002). Then the plasma is said to be "ideal" or "perfectly conducting" and the magnetic field and the plasma move together as an ensemble (e.g. Bellan 2006).

1.3.2 Dynamo theory

Solar dynamo theories have to reproduce the systematic global behavior of solar magnetic field and the associated observable photospheric magnetic patterns since they originate in the solar interior. In particular, this includes the 11-year sunspot cycle, the migration of

the emergence latitudes of sunspots, the polarity rules for sunspot groups, the 22-year magnetic cycle, the reversal of the polar fields at times of sunspot minimum and the modulation of the magnetic field on long time scales (see § 1.1.1 for details).

The basic mechanism of a MHD dynamo aims to picture how a magnetic field can be sustained by electric currents which are induced in a plasma by the motions of the matter. In general, it involves the induction of electric currents from plasma motions across an existing magnetic field where the currents are again a source of the magnetic field. The magnetic field, in turn, influences the velocity field via the Lorentz force so that all these processes are strongly nonlinearly coupled. In particular, a motion $\boldsymbol{v}$ perpendicular to a magnetic field $\boldsymbol{B}$ induces an electric field $\boldsymbol{v}\times\boldsymbol{B}$. This electric field, according to Ohm's law (1.4), drives an electric current and, according to Ampére's law (1.2), produces a magnetic field. The magnetic field with its associated Lorentz force $\boldsymbol{J}\times\boldsymbol{B}$ influences the velocity field to close the system (e.g. Schmitt 1985).

The solution to this highly nonlinear problem needs to show that there exists a velocity field which creates a magnetic field and sustains it against Ohmic losses and, moreover, that the existing forces allow the velocity field to occur. This is called a "hydromagnetic" dynamo problem and implies that both the induction equation (1.6) and the equation of motion for the fluid need to be solved in parallel. Due to the complexity of the problem, the dynamo action of a given velocity field on a weak magnetic field alone is often investigated which is then referred to as a "kinematic" dynamo problem. This means that the problem of the velocity field to be created by the forces and the back reaction of the magnetic field on the velocity field via the Lorentz force is left out of the considerations. The more general class of hydromagnetic dynamo models, however, also incorporates the force due to the magnetic field on the fluid velocity. In any case, an important requirement for a successful dynamo action, based on the magnetic induction equation (1.6), is that the induction term overcomes the diffusion term and, consequently, that the magnetic Reynolds number as introduced in (1.7) is larger than unity (e.g. Solanki et al. 2006).

In the following, the dynamo action of a given velocity field is discussed and hence a kinematic dynamo problem is assumed. Let us furthermore assume, as a first approximation, that the solar magnetic field can be regarded as axisymmetric about the rotation axis of the Sun. This allows the magnetic field to be decomposed into a poloidal (meridional; $\boldsymbol{B}_p$) and a toroidal (azimuthal; $\boldsymbol{B}_t$) component (see Fig.1.6 and e.g. Davidson 2001). The field lines of a poloidal field lie in planes through the rotation axis of the Sun while those of a toroidal field are circular and lie in planes perpendicular to the rotation axis. The poloidal component $\boldsymbol{B}_p$ can be expressed as the curl of a toroidal vector potential $\boldsymbol{A}_t$ so that the decomposition of the total magnetic field $\boldsymbol{B}$ can be written as

$$\boldsymbol{B} = \boldsymbol{B}_p + \boldsymbol{B}_t = \nabla\times\boldsymbol{A}_t + \boldsymbol{B}_t. \tag{1.8}$$

A similar decomposition for the velocity field can be made in the form

$$\boldsymbol{v} = \boldsymbol{v}_p + \boldsymbol{v}_t = \boldsymbol{v}_p + \varpi\,\Omega_t\boldsymbol{e}_\phi \tag{1.9}$$

with $\varpi = r\sin\theta$ and Ω_t being the angular velocity. Substitution into the induction equation (1.6) and separating the poloidal and toroidal components yields two coupled equations of the form

$$\partial_t\boldsymbol{A}_t = \eta\,\Delta\boldsymbol{A}_t + \boldsymbol{v}_p\times(\nabla\times\boldsymbol{A}_t), \tag{1.10}$$

$$\partial_t\boldsymbol{B}_t = \eta\,\Delta\boldsymbol{B}_t + \nabla\times(\boldsymbol{v}_p\times\boldsymbol{B}_t) + \nabla\times(\boldsymbol{v}_t\times\boldsymbol{B}_p), \tag{1.11}$$

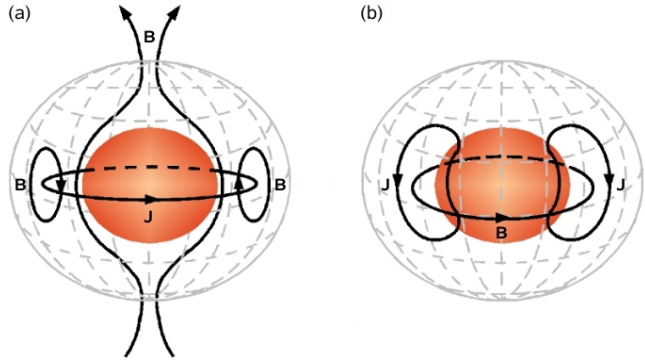

Figure 1.6: Schematic view of the (a) poloidal and (b) toroidal components of an axisymmetric magnetic field $\boldsymbol{B}$, together with the associated electric currents $\boldsymbol{J}$. The poloidal field lines lie in planes through the rotation axis of the Sun while the toroidal field lines lie in planes perpendicular to the rotation axis. The radiative core and the surface of the Sun are represented by the orange sphere and the gray mesh, respectively. Adapted from Davidson (2001).

where the Coulomb gauge ($\nabla \cdot \boldsymbol{A} = 0$) has been used and where $\boldsymbol{v}_t \times \boldsymbol{B}_t = 0$ due to the axisymmetry. Using $\boldsymbol{A}_t = A_t \boldsymbol{e}_\phi$ and $\boldsymbol{B}_t = B_t \boldsymbol{e}_\phi$ in (1.10) as well as (1.11) yields for the ϕ-components

$$\partial_t A_t = \underbrace{\eta\left(\Delta - \frac{1}{\varpi^2}\right) A_t}_{\text{resistive decay}} \underbrace{- \frac{1}{\varpi}\left(\boldsymbol{v}_p \cdot \nabla\right)\left(\varpi A_t\right)}_{\text{advection}}, \tag{1.12}$$

$$\partial_t B_t = \underbrace{\eta\left(\Delta - \frac{1}{\varpi^2}\right) B_t}_{\text{resistive decay}} \underbrace{- \varpi\, \boldsymbol{v}_p \cdot \nabla\left(\frac{B_t}{\varpi}\right)}_{\text{advection}} \underbrace{- B_t\left(\nabla \cdot \boldsymbol{v}_p\right)}_{\text{compression}} + \underbrace{\varpi \boldsymbol{B}_p \cdot \nabla \Omega_t}_{\text{shear}}. \tag{1.13}$$

The only true source term is the shearing term in (1.13) which represents the mechanism creating a toroidal from a poloidal magnetic field. Since there is no comparable source term in (1.12), the poloidal field diffuses away and, consequently, also the generation of the toroidal field stops. This means that the assumed axisymmetric field alone cannot be maintained against Ohmic dissipation (Charbonneau 2005, Cowling 1934, Bullard and Gellman 1954, Cowling 1957, Ivers and James 1988).

Accordingly, a non-axisymmetric mechanism resulting in a source term in (1.12) which could, under solar conditions, create a poloidal from an existing toroidal field is needed. In other words, besides the generation and amplification of toroidal from poloidal fields through differential rotation (referred to as the "Ω-effect"), a flow regenerating the poloidal field is additionally required. Such a mechanism was found in form of the generation of poloidal flux loops from the toroidal fields due to the action of the Coriolis force on convective up- and downflows, forcing them to show an opposite cyclonic character in the two solar hemispheres. A large-scale poloidal field develops through the superposition of a great number of such poloidal loops with its polarity being opposite with respect

to that of the poloidal field which was initially stretched and wound up around the Sun by the differential rotation to create the toroidal field ("Parker loop"; Parker 1955, 1970).

An important step towards developing successful dynamo theories was done by introducing a formal way to incorporate the mechanism proposed by Parker, in the form of the so-called "mean-field" dynamo theory (Steenbeck et al. 1966, Steenbeck and Krause 1966, Krause and Rädler 1980). Within this approach, the magnetic field and the velocity field, as functions of space and time ($\boldsymbol{B} = \boldsymbol{B}(\boldsymbol{x}, t)$, $\boldsymbol{v} = \boldsymbol{v}(\boldsymbol{x}, t)$), are separated into mean slowly varying parts ($\langle \boldsymbol{B} \rangle$, $\langle \boldsymbol{v} \rangle$) and fluctuating, rapidly varying parts ($\boldsymbol{B}'$, $\boldsymbol{v}'$). This decomposition is called the "two-scale" approach so that the magnetic and velocity field can be written as

$$\boldsymbol{B} = \langle \boldsymbol{B} \rangle + \boldsymbol{B}', \qquad \boldsymbol{v} = \langle \boldsymbol{v} \rangle + \boldsymbol{v}'. \tag{1.14}$$

Inserting the decomposition (1.14) into the induction equation (1.6) and applying the Reynolds rules for the averages (see appendix A) then yields

$$\partial_t \langle \boldsymbol{B} \rangle = \eta \, \Delta \langle \boldsymbol{B} \rangle + \nabla \times \Big(\langle \boldsymbol{v} \rangle \times \langle \boldsymbol{B} \rangle \Big) + \nabla \times \mathcal{E}, \tag{1.15}$$

$$\partial_t \boldsymbol{B}' = \eta \, \Delta \boldsymbol{B}' + \nabla \times \Big(\langle \boldsymbol{v} \rangle \times \boldsymbol{B}' + \boldsymbol{v}' \times \langle \boldsymbol{B} \rangle \Big) + \nabla \times \mathcal{G} \tag{1.16}$$

with $\mathcal{E} = \langle \boldsymbol{v}' \times \boldsymbol{B}' \rangle$ being the mean electromotive force and describing the action of the fluctuating parts on the mean magnetic field and $\mathcal{G} = \boldsymbol{v}' \times \boldsymbol{B}' - \langle \boldsymbol{v}' \times \boldsymbol{B}' \rangle$. Since (1.16) indicates that the relation between $\langle \boldsymbol{B} \rangle$ and $\boldsymbol{B}'$ is a linear one, $\mathcal{E}$ can be expressed in the form of a Taylor expansion of the form

$$\mathcal{E}_i = \alpha_{ij} \, \langle B_j \rangle + \beta_{ijk} \, \partial_j \langle B_k \rangle + \ldots, \tag{1.17}$$

where α_{ij} and β_{ijk} are the mean field transport coefficients (being a second-rank and third-rank tensor, respectively). These are functions of the fluctuating velocity field $\boldsymbol{v}'$ only, i.e., independent of $\langle \boldsymbol{B} \rangle$ (e.g. Ossendrijver 2003a). Assuming isotropic turbulence, one can express the cyclonic tensor α_{ij} and the tensor of turbulent diffusivity β_{ijk} as

$$\alpha_{ij} = -\frac{1}{3} \, \delta_{ij} \int_0^\infty \langle \, \boldsymbol{v}'(t) \cdot \big(\nabla \times \boldsymbol{v}'(t - \tau) \big) \, \rangle \, d\tau = \alpha \, \delta_{ij}, \tag{1.18}$$

$$\beta_{ijk} = \frac{1}{3} \, \epsilon_{ijk} \int_0^\infty \langle \, \boldsymbol{v}'(t) \cdot \boldsymbol{v}'(t - \tau) \, \rangle \, d\tau = -\beta \, \epsilon_{ijk}, \tag{1.19}$$

where ϵ_{ijk} is the Levi-Civita tensor [3] and δ_{ij} is the Kronecker-Delta [4]. Thus,

$$\alpha = -\frac{1}{3} \int_0^\infty \langle \, \boldsymbol{v}'(t) \cdot \big(\nabla \times \boldsymbol{v}'(t - \tau) \big) \, \rangle \, d\tau \approx -\frac{\tau_c}{3} \, \langle \, \boldsymbol{v}' \cdot \nabla \times \boldsymbol{v}' \, \rangle, \tag{1.20}$$

$$\beta = \frac{1}{3} \int_0^\infty \langle \, \boldsymbol{v}'(t) \cdot \boldsymbol{v}'(t - \tau) \, \rangle \, d\tau \approx \frac{\tau_c}{3} \, \langle \, \boldsymbol{v}' \cdot \boldsymbol{v}' \, \rangle, \tag{1.21}$$

where τ_c denotes the correlation time of turbulent motions. Furthermore, the quantity $\langle \boldsymbol{v}' \cdot \nabla \times \boldsymbol{v}' \rangle$ represents the mean kinetic helicity of the turbulent motions, described by

[3] With the properties that $\epsilon_{ijk} = 0$ if (i, j, k) are not all different, $\epsilon_{ijk} = +1$ if (i, j, k) are all different and cyclic and $\epsilon_{ijk} = -1$ if (i, j, k) are all different and anti-cyclic.

[4] With the properties that $\delta_{ij} = 0$ if $i \neq j$ and $\delta_{ij} = 1$ if $i = j$.

the scalar product of the velocity $\boldsymbol{v}'$ with its vorticity $\omega' = \nabla \times \boldsymbol{v}'$ (Ossendrijver 2003a). Though very likely not to be true for the solar interior (but nevertheless commonly used in dynamo modelling) is the assumption of isotropic turbulence which yields the tensors α_{ij} and β_{ijk} to become isotropic and representable by a scalar. Then, $\mathcal{E}$ takes the form

$$\mathcal{E} = \alpha \langle \boldsymbol{B} \rangle - \beta \nabla \times \langle \boldsymbol{B} \rangle \tag{1.22}$$

and inserting (1.22) into (1.15) results in the mean-field induction equation

$$\partial_t \langle \boldsymbol{B} \rangle = \nabla \times \Big(\langle \boldsymbol{v} \rangle \times \langle \boldsymbol{B} \rangle + \alpha \langle \boldsymbol{B} \rangle \Big) + \eta_T \, \Delta \langle \boldsymbol{B} \rangle \tag{1.23}$$

with $\eta_T = \eta + \beta$ being the total diffusivity. The physical meaning of α is that it yields a mean electric current parallel or anti-parallel to the original mean magnetic field $\langle \boldsymbol{B} \rangle$. In fact, this leads to the source term lacking in (1.12) for the generation of a poloidal from a toroidal field (called the "convective α-effect"; e.g. Ossendrijver 2003b). In case of cyclonic convection (i.e. an existing correlation between $\boldsymbol{v}'$ and ω'), as brought along by the action of the Coriolis force, this term represents the incorporation of the Parker mechanism into the dynamo formalism (e.g. Solanki et al. 2006). Now, a successful dynamo action can be accomplished by the combination of the generation of a global poloidal field by the α-effect and the regeneration of the toroidal field, either by differential rotation ($\alpha\Omega$-dynamo) or alternatively also by the α-effect itself (α^2-dynamo).

Although being successful in reproducing some of the key observations on the Sun, for instance the periodic field reversal and the polarity rules of sunspot groups, conventional $\alpha\Omega$-dynamos operating in the bulk of the convection zone have some difficulties in reproducing the equatorward migration of the activity zones. Solutions of an $\alpha\Omega$-dynamo propagate from mid-latitudes to the equator only if the product $\alpha \, \partial_r \Omega$ is negative/positive in the northern/southern solar hemisphere. Therefore, for $\alpha\Omega$-dynamos for which α is positive/negative in the northern/southern hemisphere, $\partial_r \Omega < 0$ is required, i.e. an inward increasing radial differential rotation (e.g. Schmitt 1985). This assumption, however, does not match helioseismic observations showing a radial gradient of angular velocity only at the base of the convection zone and, moreover, almost no radial differential rotation in the bulk of the convection zone.

Several models exist to overcome this and other problems, including "overshoot layer" dynamos where the dynamo action is entirely restricted to the overshoot region at the base of the convection zone, "interface" dynamos where the generation regions of toroidal and poloidal fields are spatially separated so that the differential rotation acts in the overshoot layer and the α-effect works throughout the entire convection zone. Currently most promising seem to be the so-called "flux-transport" dynamos, basically being interface dynamos but additionally involving an observationally supported "meridional circulation" which bodily caries the surface magnetic flux toward the poles and some of it down to the bottom of the convection zone and back towards the equator (see Fig. 1.7 and Dikpati and Gilman (2006)). For detailed discussions of the (dis)advantages of different existing dynamo models we refer to Charbonneau (2005) and Solanki et al. (2006).

1.4 Summary

A dynamo action is thought to operate somewhere in the solar convection zone and gives rise to the solar magnetic field. The Sun's differential rotation shears and thus consecu-

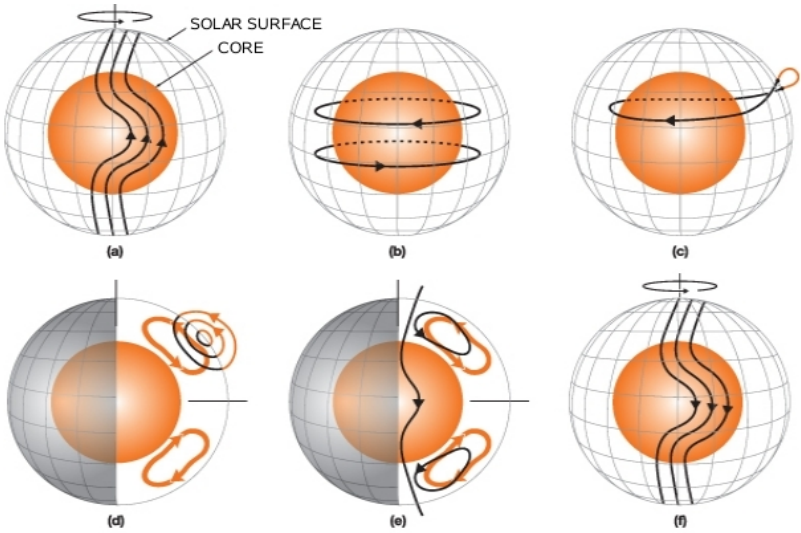

Figure 1.7: Schematic view of a solar flux-transport dynamo. (a) Due to the Sun's differential rotation, a poloidal field (black arrows) is sheared and wound up around the Sun to result in (b) a toroidal field. (c) Is the field strength high enough, bundles of field lines rise to the surface creating sunspots (black dots). (d) Meridional circulation (orange, subsurface circulation) caries the surface magnetic flux toward the poles and some of it down to the bottom of the convection zone and back toward the equator (e). A polarity configuration (f), reversed to that in (a), is produced which can be sheared again to produce a new toroidal field opposite to that in (b). The Sun is represented by the gray mesh and its radiative core by the orange inner sphere. (Courtesy of M. Dikpati.)

tively winds up an existing poloidal field, resulting in a toroidal field. Once strong enough, bundles of toroidal magnetic field lines buoyantly rise through the convection zone and, subject to the Coriolis force, form poloidal flux loops. The superposition of a great number of such poloidal loops emerging into the solar atmosphere from below makes up the large-scale poloidal field, having opposite polarity with respect to that of the poloidal field which was initially wound up. Additionally, a meridional circulation can carry the magnetic field from the equator to the poles but also from the surface to the bottom of the convection zone.

Additionally, due to the systematic twisting of the magnetic field within the convection zone prior to its emergence, kinetic and current helicity is induced which can then in principle be measured on the solar surface and in the atmosphere. Due to the motion of loop footpoints in the photosphere and the corresponding subsequent deformation of the magnetic field in the solar atmosphere, electric currents are introduced to consecutively build up and store magnetic energy. Not only the shear or twist of existing magnetic fields can induce electric currents but also new magnetic loops emerging from below the solar photosphere into a preexisting coronal magnetic field. Once the magnetic energy

content of the coronal field reaches a critical point instabilities in the system, previously in equilibrium, might occur so that preliminary stored magnetic energy is released or converted into other forms of energy.

Unfortunately, direct measurement techniques of the chromospheric and coronal magnetic field are not yet routinely done due to several difficulties. Measurements of the chromospheric magnetic field suffer from its low plasma density leading to weak emission and absorption signals of the spectral lines. This is even more pronounced in the corona due to the even lower plasma density. Additionally, the coronal emission lines are extremely broadened due to the high coronal temperatures so that the detectability of line splittings associated to the magnetic field is hindered. Also the line-of-sight integrated character of coronal observations complicates the interpretation of the magnetic field measurements. To overcome the fact that chromospheric and coronal magnetic field measurements are not yet routinely available, approaches have been developed which extrapolate the measured photospheric magnetic field vector into the corona. Besides other methods, force-free extrapolation techniques can be used to reconstruct the equilibrium coronal magnetic field subject to appropriate boundary conditions. Therefore, the basic assumptions and validity regimes of such extrapolation techniques are discussed in the next chapter.

2 Magnetic field models

Since measurements of the chromospheric and coronal magnetic field based on direct measurements using the Zeeman effect, Hanle effect or the gyroresonance emission are not routinely available, alternative approaches have been developed to estimate the magnetic fields in the upper solar atmosphere. In this chapter, the focus lies on the method of "extrapolating" the force-free coronal magnetic field from routinely measured photospheric (vector)magnetograms.

In the following, the basic principles and assumptions of force-free magnetic field extrapolation methods are discussed in § 2.1. Three distinct classes of magnetic field models, namely potential, linear force-free and nonlinear force-free models arise from these assumptions and are described in § 2.2, § 2.3 and § 2.4, respectively, along with the existing computational methods to solve the related set of equations. The optimization approach to extrapolate the coronal magnetic field for the analysis of solar active regions as used in the presented thesis is discussed in § 2.4.1 and the method to provide consistent boundary conditions to this computational method is outlined in § 2.4.2. Finally, in § 2.5 a short summary is given.

2.1 Basic principles and assumptions

Using the equations of ideal magnetohydrodynamics (MHD), consisting of the continuity equation, the momentum equation and Ampere's law in the limit of negligible electric fields and vanishing electron diffusivity, together with assuming that the plasma is in equilibrium ($\partial_t \approx 0$, i.e. the temporal variations to be slow) and the flows to be insignificant ($\boldsymbol{v}$ small), the plasma of the solar atmosphere can be well described by

$$\nabla \times \boldsymbol{B} = \mu_0 \boldsymbol{J}, \tag{2.1}$$

$$\nabla \cdot \boldsymbol{B} = 0, \tag{2.2}$$

$$\nabla p - \boldsymbol{J} \times \boldsymbol{B} + \rho \boldsymbol{g} = 0, \tag{2.3}$$

where $\boldsymbol{B}$ is the magnetic field strength, $\boldsymbol{J}$ represents the electric current density and $\boldsymbol{g}$ denotes the gravitational acceleration. Furthermore, p and ρ stand for the plasma pressure and density, respectively, and μ_0 is the permeability of free space. Note that the energy equation and the equation of state for the plasma to close the system of equations are omitted here. The set of equations (2.1) – (2.3) basically allows to describe the equilibrium plasma in the solar atmosphere, including the photosphere and corona.

If the considered coronal structures change on length scales comparable to the typical coronal scale height ($\gtrsim 50\,000$ km; Aschwanden 2004) one can assume the acceleration

due to gravitation to be constant. Additionally, if one presumes that the pressure and the magnetic field vary on the same length scale L, normalizing all quantities in (2.3) to typical coronal values takes the form

$$\frac{\beta}{2}\nabla p - \mu_0 \boldsymbol{J}\times\boldsymbol{B} + \frac{\beta}{2}\frac{L}{H}\rho\boldsymbol{g} = 0 \tag{2.4}$$

with

$$\beta = \frac{2\mu_0 p_0}{B_0^2} \tag{2.5}$$

denoting the "plasma-β" (that is the ratio of the normalized plasma pressure p_0 to the normalized magnetic pressure $B_0^2(2\mu_0)^{-1}$) and H representing the pressure scale height. In the context of coronal magnetic field extrapolations, one most commonly assumes that the ratio of the thermal pressure to the magnetic pressure is small (i.e., $\beta \ll 1$), since it is the magnetic field in the corona which dictates the plasma motion. This, according to (2.4), allows to neglect the pressure gradient and gravitational force so that

$$\boldsymbol{J}\times\boldsymbol{B} = 0, \tag{2.6}$$

i.e. that the Lorentz force vanishes and, consequently, that the electric currents can be assumed to be aligned with the magnetic field. Due to the negligibility of nonmagnetic forces the coronal magnetic field is then said to be "force-free". In fact, the solar atmosphere shows a varying pattern of dominance of either the plasma or the magnetic pressure. Vertically, a region of $\beta > 1$ spans from below the photosphere up to the low chromosphere, followed by a region where magnetic forces are dominant ($\beta \ll 1$, including the layers from the mid-chromosphere up to the mid-corona), finally reaching the $\beta \geq 1$ layers of the outer corona and the solar wind.

Already Metcalf et al. (1995) showed that the magnetic field associated with NOAA active region (AR) 7216, as observed on July 3, 1992 with the Mees Solar Observatory/Haleakala Stokes Polarimeter (MSO/HSP; Mickey 1985), could be considered to be force-free only upwards from 400 km above the photosphere. Gary and Alexander (1999) estimated plasma-β values based on photospheric magnetic field observations of NOAA AR 7999, as observed late in Nov and early in Dec 1996, to suggest that the gas pressure becomes important again at heights of about 200 Mm above the photosphere. Later, Gary (2001) addressed the topic of the interchanging dominance of plasma and magnetic pressure throughout the solar atmosphere by modeling the plasma-β above an AR. The used plasma-β model resulted from calculating the ratio of the plasma to the magnetic pressure as a function of height based on a magnetic field and a gas pressure model. The magnetic field model was based on a static potential magnetic field, providing an active-region-like envelope field on which a photospheric field strength of 250 mT (representing a typical umbral field strength) was imposed and in which a correction for the solar wind region was included (to stay consistent with the magnetic field decay in the outer corona). The plasma pressure model was based on a barometric formulation for different temperature regions which not only involved that the plasma densities associated with an AR are higher than the global density but also considered the over-pressure of non-steady loops and high-temperature loops. This modeling revealed that the magnetic forces above the model AR lose their dominance at relatively low heights in the mid-corona between $\approx$200 Mm – 500 Mm above the photosphere (see Fig.2.1 and Gary (2001)).

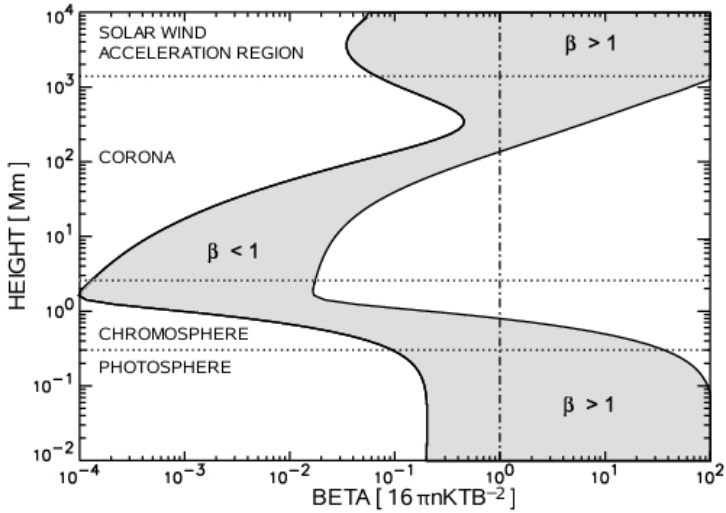

Figure 2.1: Plasma-β model for a solar active region. Outlined in gray is the plasma-β as a function of height in the solar atmosphere for open and closed field lines, originating between a sunspot (right solid black line) and a plage region (left solid black line). Horizontal dashed lines outline the approximate vertical extension of the atmospheric layers. (Courtesy of G. A. Gary.)

To summarize, only for the atmospheric layers from the mid-chromosphere until the mid-corona (at heights between ≈ 0.8 Mm and ≈ 200 Mm above the photosphere) one can regard the solar atmosphere as being almost entirely force-free, so that one is allowed to neglect the pressure gradient and gravitational term in (2.4) with the aforementioned conditions to ensure the validity of (2.6). Once the force-free approximation is justified, however, one finds a proportionality between the electric current density (assumed to be field-aligned) and the magnetic field, equivalent to (2.6), which can be written as

$$\mu_0 \boldsymbol{J} = \alpha_{\mathrm{ff}} \boldsymbol{B}, \tag{2.7}$$

where α_{ff} is the so-called "force-free parameter" which is in general a function of space ($\alpha_{\mathrm{ff}} = \alpha_{\mathrm{ff}}(\boldsymbol{x})$). Generally, for a positive value of α_{ff} the magnetic field spirals outward and counter-clockwise (left-handed; sinistral) for a positive magnetic region and inward and clockwise (right-handed; dextral) for a negative magnetic region. Inserting (2.7) into (2.1), taking its divergence and using (2.2) yields

$$\boldsymbol{B} \cdot \nabla \alpha_{\mathrm{ff}} = 0, \tag{2.8}$$

implying that α_{ff} is constant along field lines but can vary for individual field lines. This, together with (2.2) and (2.7) forms the set equations to be solved for coronal force-free equilibria.

Three different assumptions on the nature of the force-free parameter can be made. First, and representing the most simple of all approximations to the coronal magnetic

field, is that α_{ff} is zero everywhere. Then, from (2.7) it is evident that the electric current density vanishes ($\boldsymbol{J} = 0$) and according to (2.1) that this is also true for the curl of the magnetic field ($\nabla \times \boldsymbol{B} = 0$), while (2.8) is automatically satisfied. Using Helmholtz's theorem[1], one can therefore express the magnetic field by the gradient of a scalar function ϕ which due to (2.2) has to fulfill $\Delta\phi = 0$. Magnetic fields obeying this conditions are said to be "potential" or "current-free". Second, representing a more general approximation, α_{ff} can be assumed to be constant but nonzero everywhere. Precisely, α_{ff} is then presumed to be of the same value for all of the field lines and is in general evaluated by comparing a computed magnetic field configuration with coronal tracers, like loops, simultaneously seen in various spectral lines. Then again, (2.8) is automatically satisfied and due to (2.7) the electric current density is linearly related to the magnetic field so that one deals with so-called "linear force-free" or "constant-α_{ff}" fields. However, the assumption about the force-free parameter α_{ff} of potential and constant-α_{ff} models are far from being true for real solar cases since there it naturally varies from field line to field line. Consequently, a third and most general (most realistic) assumption about the physical nature of α_{ff} is made in the way that the assumed relation between the current density and the magnetic field is no longer linear. Then one cannot reduce the set of equations (2.2), (2.7) and (2.8) further and one deals with so-called "nonlinear force-free" fields. Besides a few existing analytical solutions of nonlinear force-free magnetic fields (e.g. Low 1988, and references therein) one then has to solve the related set of force-free equations numerically.

The first to deal with the meaning of force-free magnetic fields in the context of stellar objects were Lüst and Schlüter (1954) who approximated the magnetic field as a dipole field to derive the solutions to the potential and constant-α_{ff} force-free equations. In particular, it was pointed out that the assumption of the magnetic field being entirely defined by the stellar object itself rather than by any electric current in its surrounding is not well justified and hence one has to seek for more general solutions to the force-free equations than those involving $\nabla \times \boldsymbol{B} = 0$. Chandrasekhar and Kendall (1957) derived a general solution to the linear force-free equations in form of the sum of a poloidal and a toroidal vector field together with discussing its particular properties. A general discussion of the integral properties of the dissipation of magnetic energy and the relaxation towards a minimum energy state have been given by Chandrasekhar and Woltjer (1958) and Woltjer (1958), respectively.

In general, the boundary value problem to be solved for the force-free fields requires the determination of the magnetic field in a given volume (enclosed by a boundary surface ∂V) in terms of the line-of-sight component or the full magnetic field vector on ∂V (in case of potential and linear or nonlinear force-free fields, respectively) such that the field vanishes at infinity. The boundary surface at the bottom of the computational domain, representing the solar photosphere, can be either specified as a sphere or can be identified with a planar surface, depending on the usage of spherical or Cartesian coordinates within

[1]The Helmholtz theorem states that a vector field is uniquely specified if its divergence and curl within a simply connected region and its normal component on the boundary of the volume is given. A vector field for which both its source and circulation densities vanish at infinity may be written as the sum of an irrotational and a solenoidal part (for the formal proof of these two theorems see, e.g., Arfken and Weber 2001). Therefore, the magnetic field $\boldsymbol{B}$ can be written as $\boldsymbol{B} = -\nabla\phi + \nabla \times \boldsymbol{A}$, with ϕ and $\boldsymbol{A}$ denoting the irrotational scalar and solenoidal vector potential, respectively. This, in the case of a potential field (where $\nabla \times \boldsymbol{B} = 0$) reduces to $\boldsymbol{B} = -\nabla\phi$.

the computational method, respectively (Chiu and Hilton 1977). In the following, the numerical approaches to the different force-free cases ($\alpha_{\rm ff} = 0$, $\alpha_{\rm ff} \neq 0$ but constant or $\alpha_{\rm ff} = \alpha_{\rm ff}(\boldsymbol{x})$) are discussed in detail.

2.2 Potential field models

The magnetic scalar potential ϕ is uniquely determinable if ϕ itself or if its normal derivative $\partial_n\phi$ (which is equivalent to the magnetic field component normal to the boundary B_n) is specified on the boundaries and, therefore, one has to solve a Dirichlet or Neumann boundary value problem, respectively. As the line-of-sight component of the magnetic field near the solar disk center is essentially radial it can be used to determine the distribution of magnetic sources which show a straightforward relation to the current-free field above the photosphere. A solution is obtained by solving the Laplace equation for ϕ with the normal magnetic field as a boundary condition and standard methods, using either Green's functions or eigenfunction expansions, for this purpose are existing.

Schmidt (1964) was the first who attempted to express potential (current-free) fields above a semi-infinite plane using a Green's function method. After specifying the normal magnetic field component B_n on a flat lower boundary $\partial V'$ (representing the photosphere), the solution to the Laplace equation in the volume was shown to be given by

$$\phi(\boldsymbol{x}) = \frac{1}{2\pi} \int_{\partial V'} \frac{\partial_n \phi(\boldsymbol{x}')}{|\,\boldsymbol{x} - \boldsymbol{x}'\,|}\, dS' = -\frac{1}{2\pi} \int_{\partial V'} \frac{B_n(\boldsymbol{x}')}{|\,\boldsymbol{x} - \boldsymbol{x}'\,|}\, dS', \tag{2.9}$$

where $B_n(\boldsymbol{x}') = -\partial_n\phi(\boldsymbol{x}')$ with $\partial_n = -\boldsymbol{n}\cdot\nabla$ (where $\boldsymbol{n}$ is the unit vector in the vertical direction) and where the condition for the magnetic potential at $\boldsymbol{x} \to \infty$ is $\phi(\boldsymbol{x}) \to 0$. Then the potential magnetic field components in the upper-half volume $z \geq 0$ can be calculated from the normal component at $z = 0$ and are, in particular, given by $B_i = \partial_{x_i}\phi(x_i)$ with $i = (1, 2, 3)$ and $(x_1, x_2, x_3) = (x, y, z)$. The normal boundary values of $B_n(x', y', 0)$ have to be supplied through the longitudinal (line-of-sight) magnetic field $B_l = B_z(x, y, 0)$ near the solar disk center where the two can be equated and where the curvature of the solar surface can be neglected. Note that in most cases when a Green's function method is used, the approximation of B_n with B_l is assumed to be justified.

To be able to apply this method also to regions considerably far from disk center, Sakurai (1982) extended it to cases where the longitudinal magnetic field component does not necessarily need to be normal to the flat boundary plane. Nevertheless, when considering areas larger than that covered by solar active regions, the curvature of the Sun needs to be taken into account and so Sakurai (1982) also extended the classical Schmidt-method to be able to specify both the longitudinal and the normal component on a spherical boundary surface.

Global magnetic field models based on the extension of the potential theory were first discussed by, e.g., Schatten et al. (1969) and Altschuler and Newkirk (1969) who solved the Green's function in spherical coordinates to get a full spherical solution of the Sun's magnetic field. However, since the force-free assumption does not hold for the solar wind region, an artificial upper boundary (the "source surface", owing a purely radial magnetic field) is usually introduced at a certain distance above the solar surface in such global models. This radial magnetic field is used to approximate, in simplest order, the solar wind and serves as a source for the interplanetary magnetic field.

So far, we discussed potential field models based on the use of Green's functions and we are left with discussing methods using eigenfunction expansions. Since they were mainly developed in the context of linear force-free (constant-$\alpha_{\rm ff}$) fields, they always reveal expressions for the potential field in the limit $\alpha_{\rm ff} \to 0$ and will be therefore discussed in § 2.3. Potential field models have been applied routinely as a quick and easy way to get an overall impression of the general coronal magnetic field topology. When modeling solar active regions, they only require the line-of-sight magnetic field as an input for the numerical procedures but also imply fundamental limitations. Since such models assume that no electric currents are present they are not able to reproduce any topological developments of the coronal magnetic field. Furthermore, they are only to be used for estimating the lowest-energy state corresponding to an observed line-of-sight magnetic field and hence do not provide any estimate for the amount of energy which is built up in a solar active region prior to eruptions and the part of it which could be involved in the reconfiguration of the field. That is because this excess energy is mainly related to the change in the transversal (horizontal) photospheric magnetic field components which a potential field approach (since it only uses the line-of-sight magnetic field information) is not capable of reproducing.

2.3 Linear force-free field models

To overcome the fundamental limitations of potential (current-free) fields one considers the boundary value problem of linear force-free (LFF) fields where $\alpha_{\rm ff}$ is assumed to be constant but nonzero. Taking the curl of (2.7) and using (2.1) and (2.2) yields

$$(\Delta + \alpha_{\rm ff}^2) \, \boldsymbol{B} = 0, \tag{2.10}$$

i.e. $\boldsymbol{B}$ satisfies a Helmholtz equation. In the following, different approaches to solve the LFF boundary value problem, either using Fourier series expansions or Green's functions, are summarized and for an in-depth discussion we refer to the review of Gary (1989).

Nakagawa and Raadu (1972) were first to describe a generalized representation of LFF magnetic fields and to provide (non-unique) solutions of (2.10) using a Fourier series expansion in Cartesian coordinates. In a subsequent work, Nakagawa (1973) formulated a representation of LFF fields in spherical geometry (including the special case $\alpha_{\rm ff} = 0$) but also pointed out that not only the radial magnetic field but also the radial electric current distribution have to be given in order to be able to uniquely determine the magnetic field. Also Seehafer (1978) used a Fourier representation to seek the solution to the set of linear force-free equations in a Cartesian coordinate system. He pointed out that fields being linear force-free in the whole volume outside the Sun neither possess a finite energy content nor can be determined uniquely from the normal photospheric magnetic field component alone. In other words, he found that the consideration of global-scale LFF fields must be restricted to finite volumes. Later, Chiu and Hilton (1977) used Green's function terms to give non-unique analytical expressions for the magnetic field in the half-space $z > 0$ with the limit $\boldsymbol{B} \to 0$ for $z \to \infty$. They also discussed in very detail the difficulties arising from the properties of Green's functions and the physical limitations of observational data.

Comparing the computational speed of the Fourier and the Green's function methods, Alissandrakis (1981) argued that using Fast Fourier Transforms (FFTs) in the series expansion method is about $(N/\log_2 N)^2$ times faster than using a Green's function formulation if one deals with a $N \times N$ array. At the same time, the general problem for methods using FFTs of the computed field being distorted at its edges was discussed. The repetitive nature of the Fourier solutions which causes the effect of "aliasing" gives rise to the need to place a "region of interest" (ROI; that is the true boundary field) into a sufficiently larger array. One therefore places the ROI with a side length of, say, $2L$ into a larger array with a side length of $2L'$ (with $L' > L$), where the points of the larger array which surround the ROI are filled with zeros. Aliasing will cause the original field pattern to be repeated with a spatial period of $P = L'$ so that at the edges of the considered area the original signal will partly be reflected. The wings of these reflections then enter into the solutions for the ROI for $z > 0$ and hence distort the computed field. This effect is more pronounced at the edges $\pm L$ and is more serious for large z and small L'. This gives rise to the question of how large L' (or how small L) should be in order to have negligible distortions at $\pm L$ and Alissandrakis (1981) found that from the choice $L' = L + \pi z$ tolerable errors for B_z arise. Instead of defining a larger array and setting all points except for that corresponding to the ROI to zero, one can alternatively map the ROI that covers a domain, say, $0 \le l_{x_i} \le L_{x_i}$ with $i = (1, 2)$ and $(x_1, x_2) = (x, y)$ into a computational area covering four times that domain, i.e., $-L_{x_i} \le l_{x_i} \le L_{x_i}$. The mapping can be done using $B_z(-x, y, 0) = -B_z(x, y, 0)$ and $B_z(x, -y, 0) = -B_z(x, y, 0)$ or, alternatively, by setting $B_z(-x, y, 0) = B_z(x, y, 0)$ and $B_z(x, -y, 0) = B_z(x, y, 0)$, where the latter readily ensures that the net magnetic flux through the original magnetogram area is balanced. Explicitely, this means that the solution of Nakagawa and Raadu (1972) requires $B_z(0, y, z) = B_z(L_x, y, z)$ and $B_z(x, 0, z) = B_z(x, L_y, z)$ so that the solutions to the LFF equations are periodic with the periods $2L_{x_i}$. Similarly, the more restrictive solution of Seehafer (1978) requires $B_z(0, y, z) = B_z(L_x, y, z) = 0$ and $B_z(x, 0, z) = B_z(x, L_y, z) = 0$ with the solution being periodic with the periods L_{x_i}.

Later, Yan et al. (1991) first proposed a boundary element method to uniquely solve the LFF problem with a finite magnetic energy content and validated their approach by comparing observed magnetograms at a chromospheric level with the corresponding ones calculated from the force-free model. For this purpose, they transformed the boundary value problem into an integral form which allows it to evaluate the magnetic field at every arbitrary point without having to compute it in the entire volume. Independently, Aly (1992) also established the boundary integral representation for finite-energy LFF fields with an unique solution. He also worked out some basic estimates about the behavior of the solutions at infinity and the proof of their stability with respect to changes in the boundary conditions (and therefore with respect to changes in the value of α_{ff}). Moreover, he showed that the energy content of any LFF field is smaller than that of a corresponding open field (with the same normal magnetic field component B_n on the lower boundary). Based on these earlier works, Yan (1995) numerically implemented the boundary integral formulation and applied it to an active-region vector magnetogram. In agreement with earlier works, he showed that the unique solution in the $z > 0$ half-space possesses a finite energy content but also that the uniqueness of the solution does not arise from the availability of the full vector magnetic field at the lower boundary but requires an additionall condition. This additional constraint was imposed by Seehafer (1978) in the form of only considering a half-space column above the solar surface, whereas Yan et al.

(1991) made use of the "Sommerfeld condition", Aly (1992) imposed it in the form of a finite energy content and Yan (1995) in the form of an asymptotic condition, requiring the magnetic field to vanish at infinity.

However, models involving the solution of the set of LFF equations do have some general drawbacks. Chiu and Hilton (1977) pointed out that LFF fields in general have non-unique solutions if only the normal (longitudinal) magnetic field at the photosphere is given. This is because both a potential ($\alpha_{\mathrm{ff}} = 0$) and LFF ($\alpha_{\mathrm{ff}} \neq 0$ but constant) field solution could be generated from the same boundary condition $B_z(x, y, 0)$ since it is independent of the physical structure of the magnetic field. To achieve uniqueness both the normal and tangential component need to be defined on the boundary so that the physical character of the field (as represented by the α_{ff}-parameter) is clearly reflected. They furthermore showed that a necessary requirement for the uniqueness of LFF solutions is that the magnetic flux on the lower boundary is balanced and that this constraint can be used as a condition how to choose the boundary integration limits. Seehafer (1978) and Alissandrakis (1981) showed that in order to achieve a finite energy content, LFF fields (except for $\alpha_{\mathrm{ff}} = 0$) must be considered within finite volumes instead of extending them to infinity. Additionally, α_{ff} has to be smaller than a maximum value, usually proportional to the inverse of the smallest side length of the computational domain (this natural limitation of α_{ff} for general force-free fields has later been demonstrated by Aly 1984). Another fact is that, given either the normal or the transversal magnetic field as a boundary condition, α_{ff} is in general a free parameter. This means that LFF models can be calculated for different values of α_{ff} so that the different solutions can well represent distinct parts of the investigated magnetic field but may not approximate the field very well in other parts. To overcome this, Pevtsov et al. (1995) were the first to vary only α_{ff} for a given method to calculate the LFF field from the same normal boundary field and also to minimize the deviation of the theoretical and measured components of the transversal magnetic field. Consequently, they established a best-fit single value $\alpha_{\mathrm{ff,best}}$ and assumed the corresponding LFF field to represent the given magnetic field configuration best.

Based on the discussion above, it is evident that LFF field models are capable of describing the true coronal magnetic field only to a certain extent. Although producing a higher energy content associated with the magnetic field due to allowing electric currents to be introduced, the assumption of a single value of α_{ff} representative for the whole lower boundary is very doubtful (see § 2.4). If, for example, a field line under ideal conditions is twisted up by localized motions of its photospheric footpoints the configuration departing from its initial potential state will not carry a net current. Consequently, the currents within the force-free field must flow both parallel and anti-parallel with respect to the magnetic field and hence α_{ff} must change its sign which cannot be realized with a constant-α_{ff} assumption. This has been clearly demonstrated by Valori et al. (2005) who intended to reproduce a strongly helical field line using a LFF field and found that neither the twisted loop nor the associated shear could be reproduced using the $\alpha_{\mathrm{ff,best}}$-model.

2.4 Nonlinear force-free field models

In the previous two sections, dealing with potential (current-free) and LFF (constant-α_{ff}) fields, it became clear that a more general approach to approximate the coronal magnetic

field is needed. First, this is based on the fact that the force-free parameter $\alpha_{\rm ff}$ is usually changing in space even inside a given solar active region. The force-free parameter can be estimated by reformulating (2.7) and using the measured transverse photospheric magnetic field $B_t = (B_{x_0}, B_{y_0})$ to gain

$$\alpha_{\rm ff_0} = \frac{\partial_x B_{y_0} - \partial_y B_{x_0}}{B_{z_0}} = \frac{\mu_0 J_{z_0}}{B_{z_0}} \tag{2.11}$$

with J_{z_0} being the vertical current density and B_{z_0} the normal field component on the lower boundary, i.e. a measured vector magnetogram. Here it should be noted that a considerable uncertainty in the accuracy of the transverse field measurements leads to significant errors in the current density estimation. Regions with a weak B_{z_0} result in an even higher uncertainty of the current density calculation and special care has to be taken along polarity inversion lines which have a vanishing normal field component ($B_{z_0} = 0$). Second, potential and LFF fields are inappropriate in reproducing the energy content of the coronal magnetic field accurately since they cannot hold the full magnetic energy content according to their computation from the measured normal (line-of-sight) magnetic field only. From (2.11) it is evident that the electric currents, as induced by the reconfigurations of the transverse magnetic field, play a major role in the energy storage process. It is therefore the excess of magnetic energy over the potential and LFF field energy content that can be either transformed or released during eruptions. Third, potential and LFF fields cannot reproduce the complex magnetic field topology in the solar corona since they do not at all ($\alpha_{\rm ff} = 0$ for potential fields) or only partly ($\alpha_{\rm ff} \neq 0$ but constant for LFF fields) allow the topological deformation of the magnetic field, as represented by the force-free parameter $\alpha_{\rm ff}$.

Nonlinear force-free (NLFF) field models therefore allow $\alpha_{\rm ff}$ to vary from field line to field line, i.e. being a function of space $\alpha_{\rm ff} = \alpha_{\rm ff}(\boldsymbol{x})$. To repeat, these models have to numerically solve the equations

$$\nabla \times \boldsymbol{B} = \alpha_{\rm ff}(\boldsymbol{x})\, \boldsymbol{B}, \tag{2.12}$$

$$\boldsymbol{B} \cdot \nabla \alpha_{\rm ff}(\boldsymbol{x}) = 0 \tag{2.13}$$

simultaneously. Following Neukirch (2005), these equations for $\boldsymbol{B}$ for a given function $\alpha_{\rm ff}(\boldsymbol{x})$ are of elliptic type for which the proper boundary condition is the normal component of the magnetic field on the boundary B_z. These equations for $\alpha_{\rm ff}(\boldsymbol{x})$ for a given $\boldsymbol{B}$ are of hyperbolic type for which $\alpha_{\rm ff}(\boldsymbol{x})$ should only be prescribed on that parts of the boundary on which $B_z > 0$ or $B_z < 0$ (or equivalently, the normal component of the current density $J_z = \mu_0^{-1} \alpha_{\rm ff}(\boldsymbol{x}) B_z$ on those parts). Some methods go further and use the full magnetic field vector $\boldsymbol{B} = (B_x, B_y, B_z)$ as boundary values, giving rise to an ill-posed problem. However, in general it is not clear if solutions to all NLFF boundary value problems exist and in case of existence if they are unique.

The following discussion of existing NLFF field models is focused on its application to approximate the coronal magnetic field in and around solar active regions. Therefore, the solar photosphere (representing the lower boundary) is assumed to be validly approximated by a planar surface. Furthermore, the investigated solar active regions are assumed to be located close to the center of the solar disk and, consequently, that the identification of the normal magnetic field component with the longitudinal (line-of-sight) component

is justified. A number of methods have been developed to solve the set of equations corresponding to NLFF boundary value problems:

- "Vertical integration" methods (Nakagawa 1974, Wu et al. 1985, 1990) use the known photospheric field and its vertical derivatives on the lower boundary to compute the three components of the electric current density. Based on this, expressions for the vertical derivatives of all three magnetic field components are integrated upward in z, i.e. along the line-of-sight for each height. Although easy to implement and being computationally fast the use of such methods seems to be unsuccessful. This is because the particular formulation of the force-free problem is mathematically ill-posed, resulting in an unstable behavior (Cuperman et al. 1990, Amari et al. 1997). For the nonlinear case even regularization techniques cannot prevent the system to amplify unphysical growing modes (Cuperman et al. 1991, Amari et al. 1998, Demoulin et al. 1992). Song et al. (2006) reexamined this method to avoid the introduction of regularizing functions in the way that they transformed the original partial differential equations (ill-posed) into a set of ordinary differential ones (well-posed). Still, it was found that only in the case of strong magnetic fields all of the arising modes are of a decaying nature.

- "Boundary element" methods (Yan and Sakurai 2000, Li et al. 2004, Yan and Li 2006) use a Green's function to reformulate the NLFF problem. The resulting system of linear and nonlinear volume integrals is to be solved using an iterative scheme but since the nonlinear integral equations have to be carried out over the full domain this method is numerically expensive. However, different from other methods it allows to evaluate the magnetic field at every arbitrary point from the boundary data without having to compute it previously in the entire domain. This could be of use if one addresses the computation of the NLFF field only along a given single loop.

- "Grad-Rubin" methods (Sakurai 1981, Amari et al. 1997, 1999, 2006, Wheatland 2004, 2006, 2007), after Grad and Rubin (1958), solve either for the magnetic field, the electric current density or the magnetic vector potential. The NLFF equations are reformulated so that a well-posed boundary problem is addressed. At first, a potential field is computed only from the line-of-sight photospheric magnetic field whose transversal components are then used to compute the photospheric α_{ff}-distribution for one polarity. The field is then iteratively updated for every height in the computational volume until the recalculation does not yield a change in the configuration anymore and thus can be regarded as a stationary state. Recently, Wheatland and Régnier (2009) developed an approach to address the problem of the photospheric measurements being, in general, inconsistent with the force-free assumption by iteratively adjusting the boundary conditions on the solutions until the observed boundary data is best-fitted in a self-consistent way.

- "MHD relaxation" ("evolutionary", "magneto-frictional") methods (Mikic and McClymont 1994, McClymont et al. 1997) do not make use of the NLFF equations directly. They evolve or relax an initial magnetic field that does not satisfy all of the required boundary conditions to a final state where these are fulfilled. Although

ensuring that the magnetic connectivity remains unchanged during the relaxation, it cannot be guaranteed that for a given initial field based on the supplied boundary conditions a force-free equilibrium exists to which the system may relax to. If so, the formation of current sheets can lead to numerical difficulties. Alternative implementations "disturb" the initial potential field by the observed transverse field and subsequently replace the boundary conditions for each iteration step while always relaxing with the use of the same MHD-relaxation scheme. Such "stress and relax" methods either use the magnetic vector potential (Roumeliotis 1996) or directly the magnetic field (Valori et al. 2005).

- "Optimization" methods (Wheatland et al. 2000, Wiegelmann 2004, Inhester and Wiegelmann 2006) minimize the volume-integrated force-free and solenoidal condition simultaneously in pseudo-evolutionary procedures (for an implementation by McTiernan see Schrijver et al. 2006). The magnetic vector field is not necessarily divergence-free during the computation but it is divergence-free once reaching the optimal final state for ideal boundary conditions. In case of non-ideal or inconsistent boundary conditions the resulting field is either not force-free, not solenoidal or both. However, these methods still lack the formal proof to relax to the true force-free state of a magnetic field.

The computational implementation of the latter three methods (Grad-Rubin, magneto-frictional and optimization) in a cubic box in general involves, first, the computation of a start equilibrium to specify the boundary conditions on the unknown lateral and top boundaries (hereafter called the "open" boundaries), second, the replacement of the bottom boundary with the measured vector magnetogram and, third, the iterative minimization of the force-free boundary value problem. The need to use a start equilibrium (mostly in form of a potential field) arises from the necessity to prescribe all six boundaries of the computational box. Clearly, the lower boundary of the box is determined by the measured magnetic field vector and one is left with the need to specify the open boundaries properly. Since assigning to all points on the open boundaries a value of zero would oversimplify the problem, one either can include a variation of the magnetic field on these boundaries or must specify reasonable values there. The way to do so depends on the numerical method used and for the particular choices we refer to the corresponding publications as listed above. For a review of the above listed methods see e.g. Wiegelmann (2008) and for the comparison of the performance of some of them, as carried out during a series of yearly workshops, see Schrijver et al. (2006), Metcalf et al. (2008), Schrijver et al. (2008) and DeRosa et al. (2009). The optimization method is discussed in more detail in § 2.4.1 since this is the method which has been used to calculate the coronal magnetic field in the presented thesis. Before, another requirement for the vector magnetograph data to be used as the lower boundary condition for extrapolation methods, namely that the direction of the measured transverse magnetic field components is truly known, is briefly discussed.

2.4.0.1 180°-ambiguity

As already mentioned, the lower boundary of the computational box is determined by the measured magnetic field vector in the photosphere. Most popular and well-understood for single-height measurements of the solar magnetic field is the Zeeman effect. As discussed

in § 1.2.1, the lines corresponding to the Zeeman splitting exhibit certain polarizations, depending on the direction in which an electromagnetic field is vibrating and thus carrying information about the magnetic field vector. In particular, the line-of-sight component can be obtained through the circular polarization, while the transverse components can be estimated using the linear polarization (e.g. Raouafi 2005). The latter implies that there are for every transverse field vector two possible azimuths which differ by 180° (therefore called the 180°-ambiguity). The observed signal is the same for both an azimuth angle of ψ and $\psi \pm 180°$. This ambiguity must be resolved before the magnetic field data can be used as an input for magnetic field extrapolation methods. Several techniques to do so have been developed and work well for active regions having a potential-field character but difficulties are met when dealing with non-potential active regions (Metcalf 1994, and references therein). Until now, no method is known which could resolve this ambiguity directly using the Zeeman effect and, consequently, further assumptions on the nature of the magnetic field like, e.g. the spatial smoothness or the divergence-freeness have to be made. A number of existing algorithms, typically involving the minimization of a quantity which itself depends on the choice of the azimuth, have been recently tested and compared in Metcalf et al. (2006) by applying them to model vector magnetic field data. In particular, methods which combine the minimization of some measure of the vertical current density with that of an approximation of the divergence were found to be most promising. However, some methods make use of a potential, LFF or a similar model at least as a starting condition and so all issues based on the influence of the boundary conditions to any outcome, as discussed throughout this work, also apply here.

2.4.1 Optimization method

The optimization approach for reconstructing NLFF fields has first been proposed by Wheatland et al. (2000). The minimization of the global departure of an initial field from a force-free and solenoidal state is realized for a vector field $\boldsymbol{B}(\boldsymbol{x}, t)$ within a volume V by minimizing the quantity

$$L = \int_V \Big(B^{-2} \, | \, (\nabla \times \boldsymbol{B}) \times \boldsymbol{B} \, |^2 + | \, \nabla \cdot \boldsymbol{B} \, |^2 \Big) \, d^3x. \tag{2.14}$$

If for ideal conditions L reduces to zero, both $(\nabla \times \boldsymbol{B}) \times \boldsymbol{B}$ and $\nabla \cdot \boldsymbol{B}$ are zero everywhere in V and therefore a force-free field should exist. Using

$$\boldsymbol{\Omega} = B^{-2} \Big((\nabla \times \boldsymbol{B}) \times \boldsymbol{B} - (\nabla \cdot \boldsymbol{B}) \, \boldsymbol{B} \Big), \tag{2.15}$$

the relation (2.14) can be rewritten as

$$L = \int_V B^2 \, \Omega^2 \, d^3x. \tag{2.16}$$

Taking its time derivative along with applying a number of vector identities (see Appendix of Wheatland et al. 2000) yields

$$\frac{1}{2} \frac{dL}{dt} = - \int_V \partial_t \boldsymbol{B} \cdot \boldsymbol{F} \, d^3x \; - \int_{\partial V} \partial_t \boldsymbol{B} \cdot \boldsymbol{G} \, dS, \tag{2.17}$$

where

$$\boldsymbol{F} = \nabla\times(\boldsymbol{\Omega}\times\boldsymbol{B}) - \boldsymbol{\Omega}\times(\nabla\times\boldsymbol{B}) - \nabla(\boldsymbol{\Omega}\cdot\boldsymbol{B}) + \boldsymbol{\Omega}(\nabla\cdot\boldsymbol{B}) + \Omega^2\boldsymbol{B}, \quad (2.18)$$

$$\boldsymbol{G} = \boldsymbol{n}\times(\boldsymbol{\Omega}\times\boldsymbol{B}) - \boldsymbol{n}(\boldsymbol{\Omega}\cdot\boldsymbol{B}). \quad (2.19)$$

Here, $\boldsymbol{n}$ denotes the inward unit normal to the surface ∂V bounding the volume V. If now $\boldsymbol{B}$ is solved according to $\partial_t\boldsymbol{B} = \tau\boldsymbol{F}$, with $\tau > 0$ being an arbitrary function and imposing the boundary condition $\partial_t\boldsymbol{B} = 0$ on ∂V, the evolution of L in (2.17) can be written in the form

$$\frac{dL}{dt} = -2\int_V \tau F^2\, d^3x \quad (2.20)$$

and clearly L decreases since $dL/dt \leq 0$. However, it has to be noted that iteratively solving (2.20) does not ensure that one reaches the global minimum of the functional L. This means that the reached steady state of the evolution may not correspond to the unique (if existing) force-free state in V.

However, the condition $\partial_t\boldsymbol{B} = 0$ on the boundaries ∂V would make it necessary that all three components of $\boldsymbol{B}$ are prescribed there. All of the boundaries, in principle, equally influence the force-free solution inside the domain and for real solar cases one basically never deals with strictly isolated active regions so that field lines starting somewhere on the observed magnetogram (i.e. the bottom boundary of the cubic box) might close somewhere outside the observed region to the solar surface so that they may leave the computational volume through the open boundaries. In this context, Wiegelmann and Neukirch (2003) worked out a way how the assumption of $\partial_t\boldsymbol{B} = 0$ on ∂V could be avoided within the optimization procedure. First, a potential field could be calculated from the normal component of the photospheric field alone and then imposed on the open boundaries as an initial condition. This would be reasonable since it is assumed that potential fields, in general, well represent the coronal magnetic field outside of active regions. However, to allow magnetic flux to leave the computational volume one would not keep the boundary values on the open boundaries fixed but would instead continuously update them, i.e. relax them together with the field inside the box. In other words, since one would deal with $\partial_t\boldsymbol{B} \neq 0$ in (2.17), the surface term would not necessarily vanish and one would extend the iteration by $\partial_t\boldsymbol{B} = \tau\boldsymbol{G}$ on the open boundaries. Consequently, (2.20) would take the form

$$\frac{dL}{dt} = -2\left(\int_V \tau F^2\, d^3x + \int_{\partial V} \tau G^2\, dS\right), \quad (2.21)$$

where the second term on the right-hand side would denote the iteration on the open boundaries. Then, the boundary values would be changed in such a way that L still decreases and the bottom boundary would remain independent of time during the iteration since it is constrained by the photospheric observation.

Since the iterative update of the values on the open boundaries would be computationally expensive, Wiegelmann (2004) developed an alternative way in order to diminish the influence of the open boundaries on the NLFF solution inside the computational volume. He introduced a weighting function $w(x, y, z)$ into (2.14) to explicitly solve

$$L = \int_V w(x,y,z)\left(B^{-2}\,|(\nabla\times\boldsymbol{B})\times\boldsymbol{B}|^2 + |\nabla\cdot\boldsymbol{B}|^2\right) d^3x. \quad (2.22)$$

Note that with the choice $w(x, y, z) = 1$ this is equivalent to the original form of the functional L as introduced by Wheatland et al. (2000). At first, a potential field is calculated from the normal component of the photospheric field alone and then imposed on the open boundaries as an initial condition. Around the "physical" region for which $w(x, y, z) = 1$ (that is the volume of interest including the photosphere at the lower boundary) a finite-size boundary layer to the open boundaries is introduced in which the weighting function $w(x, y, z)$ decreases to zero in form of a cos-profile so that deviations from the force-free state are less severe close to the boundary. In other words, the influence of the assumed potential field on the open boundaries on the solution in the physical region is the lesser the farther away from it and finally has no effect on the open boundaries themselves since there $w(x, y, z) = 0$. The iteration equation, equivalent to (2.17), then becomes (see Appendix of Wiegelmann 2004)

$$\frac{1}{2}\frac{dL}{dt} = -\int_V \partial_t \boldsymbol{B} \cdot \widetilde{\boldsymbol{F}}\, d^3x \; - \int_{\partial V} \partial_t \boldsymbol{B} \cdot \widetilde{\boldsymbol{G}}\, dS \tag{2.23}$$

with

$$\widetilde{\boldsymbol{F}} = w\,\boldsymbol{F} + (\boldsymbol{\Omega}_a \times \boldsymbol{B}) \times \nabla w + (\boldsymbol{\Omega}_b \cdot \boldsymbol{B})\,\nabla w, \tag{2.24}$$

$$\widetilde{\boldsymbol{G}} = w\,\boldsymbol{G}, \tag{2.25}$$

$$\begin{aligned}\boldsymbol{F} = {} & \nabla \times (\boldsymbol{\Omega}_a \times \boldsymbol{B}) - \boldsymbol{\Omega}_a \times (\nabla \times \boldsymbol{B}) \\ & + \nabla (\boldsymbol{\Omega}_b \cdot \boldsymbol{B}) - \boldsymbol{\Omega}_b (\nabla \cdot \boldsymbol{B}) + \left(\Omega_a^2 + \Omega_b^2\right) \boldsymbol{B},\end{aligned} \tag{2.26}$$

$$\boldsymbol{G} = \boldsymbol{n} \times (\boldsymbol{\Omega}_a \times \boldsymbol{B}) - \boldsymbol{n}\,(\boldsymbol{\Omega}_b \cdot \boldsymbol{B}) \tag{2.27}$$

and

$$\boldsymbol{\Omega}_a = B^{-2}\left((\nabla \times \boldsymbol{B}) \times \boldsymbol{B}\right), \tag{2.28}$$

$$\boldsymbol{\Omega}_b = B^{-2}\left((\nabla \cdot \boldsymbol{B})\,\boldsymbol{B}\right). \tag{2.29}$$

Since now the weighting function reduces the effect of the assumed values on the open boundaries on the solution in the volume of interest, again $\partial_t \boldsymbol{B} = 0$ on ∂V can be required. This is because $w(x, y, z) = 0$ on ∂V and hence the surface term of (2.23) is not incorporated directly on the open boundaries. Consequently, the magnetic field inside the computational volume is iterated using $\tilde{F}$ in (2.20), again with the bottom boundary remaining independent of time during the iteration. However, it is nevertheless of advantage to choose a sufficiently large vector magnetogram for which the side boundaries are far away from the central region of interest so that the effect of the open boundaries on the solution is further reduced.

To summarize, the algorithm of Wiegelmann (2004) to compute the NLFF magnetic field inside a cubic numerical box and as used in this work, performs several steps. First, a potential magnetic field is computed from the measured normal component of the magnetic field B_z. For initial (test) cases the Fourier representation after Seehafer (1978) was used but now a Green's function method after Aly (1989) is applied for this purpose. The potential field is then used as the initial (start) configuration and to prescribe the open boundaries. The physical bottom boundary is replaced by the measured vector magnetogram components $\boldsymbol{B}(x, y, z = 0)$. A finite-size boundary layer is introduced to the open

boundaries in which a weighting function $w(x, y, z)$ is defined so that it drops to zero in form of a cos-profile. In this way, the assumption of a potential field around the volume of interest is less severe closer to it. The field inside the box is then iterated according to $\partial_t \boldsymbol{B} = \tau \tilde{F}$ with $\tau > 0$ and according to $\partial_t \boldsymbol{B} = 0$ where $\boldsymbol{B}$ is observed (i.e. on the bottom boundary). This continuous form guarantees that L is monotonically decreasing. In discretized form this is ensured if the iteration (time) step dt is chosen sufficiently small. After each step the code checks if $L(t+dt) < L(t)$. Is this condition not fulfilled, the current iteration step is repeated with dt being reduced by a factor of two. Is the condition fulfilled, dt is slowly increased by a factor of 1.01 so that the time step can become as large as possible with respect to the stability condition. The code stops if $dt \leq dt_0 \times 10^{-7}$ (where dt_0 denotes the time step used at the very beginning of the iterative process) or if $|(L(t) - L(t+dt))/L(t)| < 10^{-4}$ for 100 consecutive iterations.

2.4.1.1 Multi-scale implementation

The optimization code of Wiegelmann (2004) has been extended to use a multi-scale implementation in order to get an optimized initial (start) equilibrium for the NLFF field computation. For this purpose, the solution in the full resolution box (with a dimension of, say, $360 \times 360 \times 200$ grid points) is not directly evaluated but instead the solution on different grids is computed in a series of subsequent extrapolations. One starts with the computation in a smallest cubic box with a coarsest resolution of, say, $90 \times 90 \times 50$ grid points. After iterating the field inside this smallest volume until it reaches a relaxed state, the solution is interpolated onto a larger (finer) grid with, say, $180 \times 180 \times 100$ grid points to be used there as the new start equilibrium. Again, the configuration is iteratively relaxed towards a force- and divergence-free state which is then interpolated onto the full resolution (finest) grid with $360 \times 360 \times 200$ grid points as the new starting equilibrium. The multigrid-like version was first used and described in Metcalf et al. (2008) and was found to converge faster than the version without this multi-scaling but was also found to converge at lower values of L in (2.22). The latter means that a more force- and divergence-free final state can be reached. The faster convergence can be assigned to the fact that the start equilibrium on the largest grid is already more close to the final solution on large scales. Additional parallelization of the code using OpenMP for shared-memory architectures leads to another improvement in the computational speed of the optimization method.

2.4.2 Preprocessing

As already mentioned, one of the basic assumptions of force-free field models is that the plasma-β in the solar atmosphere is considerably lower than unity. This, as discussed in §2.1, is not true for the photosphere in which the available vector magnetograph measurements are performed (see also Fig. 2.1). Thus, nonmagnetic forces can in principle not be neglected and one may find the measured photospheric magnetic field to represent an inconsistent lower boundary condition for the NLFF extrapolation. Therefore, it is unavoidable to apply slight transformations to the observed photospheric data in order to drive them towards being more force-free and chromospheric-like so that they can be used as consistent boundary conditions to the extrapolation method. Such "preprocess-

ing" methods have been developed using either simulated annealing (see Fuhrmann et al. 2007) or incorporating force-free compatibility relations into a minimization procedure (Wiegelmann et al. 2006, 2008). The latter is discussed in detail in § 2.4.2.3 since this is the method we use to gain consistent boundary conditions for our NLFF coronal magnetic field extrapolations. Before, the origin of the aforementioned force-free compatibility relations which are based on the virial theorem extended to the inclusion of magnetic fields is briefly discussed.

2.4.2.1 Virial theorem

The virial theorem has originally been derived in the context of the kinetic theory of gases and the extension to include magnetic fields was done by Chandrasekhar and Fermi (1953). If any force acting on a system is assumed to be constant in time, one can define a total force per unit volume $\boldsymbol{f}$ exerted on the plasma. If the system is assumed also to be in equilibrium so that any kinetic energy vanishes, the constraint as imposed by the virial theorem is

$$\int_V \boldsymbol{f} \cdot \boldsymbol{x}\, d^3x = 0. \tag{2.30}$$

Now, one can separate the forces arising from the magnetic field $\boldsymbol{f}_m$ from those of any other type $\boldsymbol{f}'$. Then, $\boldsymbol{f}_m$ obviously represents the Lorentz force density so that one can write

$$\int_V (\boldsymbol{f}' + \boldsymbol{f}_m) \cdot \boldsymbol{x}\, d^3x = \int_V \boldsymbol{f}' \cdot \boldsymbol{x}\, d^3x + \int_V \left(\frac{1}{\mu_0} (\nabla \times \boldsymbol{B}) \times \boldsymbol{B} \right) \cdot \boldsymbol{x}\, d^3x, \tag{2.31}$$

where $\boldsymbol{J} \times \boldsymbol{B} = \mu_0^{-1} (\nabla \times \boldsymbol{B}) \times \boldsymbol{B}$ and where $\boldsymbol{x}$ denotes the position vector. Since we are concerned with force-free fields here, any force except that exerted by the magnetic field is neglected (i.e., $\boldsymbol{f}' = 0$) and so one is left with evaluating the second term on the right-hand side of (2.31). This leads to the requirement

$$\frac{1}{\mu_0} \int_V B^2\, d^3x = \frac{1}{\mu_0} \int_{\partial V} B^2 (\boldsymbol{x} \cdot \boldsymbol{n})\, dS - \frac{2}{\mu_0} \int_{\partial V} (\boldsymbol{B} \cdot \boldsymbol{x})(\boldsymbol{B} \cdot \boldsymbol{n})\, dS, \tag{2.32}$$

where $\boldsymbol{n}$ denotes the outward normal to the surface (for details see e.g. Marsch 1996). The term on the left hand side of (2.32) is the total magnetic energy which is a positive definite quantity and assumed not to be zero. Consequently, the field on the surface and hence the surface terms on the right-hand side of (2.32) cannot vanish. This means that there must be external forces to balance the outwardly directed pressure due to the total magnetic energy and thus that the virial theorem relates the magnetic field energy in a volume V to the magnetic field value on the surface ∂V. In principle, the virial theorem can therefore be used to estimate the magnetic energy in a given force-free volume based on the knowledge of the magnetic field on its boundary (e.g. Metcalf et al. 2008).

2.4.2.2 Force-free consistency criteria

As shown before, through the magnetic virial theorem one is able to estimate the energy content of a force-free magnetic field based on its values on the volume's bounding surfaces. Since, in general, the magnetic field on the open boundaries is unknown and

only the magnetic field on the lower boundary (the photosphere) is observed, Molodenskii (1969), Molodensky (1974) and Aly (1989) defined conditions in Cartesian geometry what a vector magnetogram has to fulfill in order to be consistent with the assumption of a force-free field. The integral relations and their meaning as derived for force-free fields $\boldsymbol{B}(x, y, z) = (B_x, B_y, B_z)$ are:

1. The net flux through the photospheric boundary S is balanced, i.e.

$$M_0 = \int_S B_z \, dS = 0, \tag{2.33}$$

with $dS = dx\,dy$ at $z = 0$. This clearly needs, at least to a good degree of approximation, to be satisfied for the region under consideration.

2. Force-free fields can, on average, not exert pressure on the photospheric boundary S and cannot induce shear stresses along the x- and y- direction, i.e.

$$M_1 = \int_S B_x B_z \, dS = 0, \tag{2.34}$$

$$M_2 = \int_S B_y B_z \, dS = 0, \tag{2.35}$$

$$M_3 = \int_S \left(B_x^2 + B_y^2 \right) dS - \int_S B_z^2 \, dS = 0. \tag{2.36}$$

3. Force-free fields cannot induce rotational moments along the boundary x-, y- or z-axis, i.e.

$$M_4 = \int_S x \left(B_x^2 + B_y^2 \right) dS - \int_S x B_z^2 \, dS = 0, \tag{2.37}$$

$$M_5 = \int_S y \left(B_x^2 + B_y^2 \right) dS - \int_S y B_z^2 \, dS = 0, \tag{2.38}$$

$$M_6 = \int_S y \left(B_x B_z \right) dS - \int_S x B_y B_z \, dS = 0. \tag{2.39}$$

The relations (2.34) – (2.39) are always fulfilled for potential magnetic fields because of the vanishing electric currents ($\boldsymbol{J} = 0$) which could be created, e.g., by currents at one side of the plane S. However, if currents flow on either side of S both impulse and momentum can be transferred from one side to the other and the distribution of the field in the plane will not satisfy these relations (Molodensky 1974). For completeness, we note that Aly (1984) also derived such compatibility relations which are valid in an arbitrary geometry.

The above integral relations represent moments arising from the magnetic virial theorem and one could in principle additionally take higher-order moments into account. Then also the energy relation (2.32) can be written as

$$\frac{1}{2\mu_0} \int_V B^2 \, d^3x = \frac{1}{\mu_0} \int_S B_z \left(x B_x + y B_y \right) dS \tag{2.40}$$

which means that the total energy content of the field can be approximated through the magnetic field distribution in a certain plane.

2.4.2.3 Classical preprocessing

Based on the force-free consistency criteria described above, Wiegelmann et al. (2006) defined three dimensionless parameters. The introduced flux-balance parameter ϵ_{flux}, the force-balance parameter ϵ_{force} and the torque-balance parameter ϵ_{torque} quantify if an observed photospheric vector magnetogram suffices the flux-balance criterion (2.33), the force-balance criteria (2.34) – (2.36) and the torque-balance criteria (2.37) – (2.39), respectively. Explicitely, they take the form

$$\epsilon_{\text{flux}} = \frac{M_0}{\int_S |B_z| \, dS}, \tag{2.41}$$

$$\epsilon_{\text{force}} = \frac{|M_1| + |M_2| + |M_3|}{\int_S \left(B_x^2 + B_y^2 + B_z^2 \right) dS}, \tag{2.42}$$

$$\epsilon_{\text{torque}} = \frac{|M_4| + |M_5| + |M_6|}{\int_S \sqrt{x^2 + y^2} \left(B_x^2 + B_y^2 + B_z^2 \right) dS} \tag{2.43}$$

and where, ideally, $\epsilon_{\text{force}} = 0$ and $\epsilon_{\text{torque}} = 0$ for an existing force-free field.

The fact that taking a sufficiently flux-balanced, isolated active-region magnetogram (i.e., $\epsilon_{\text{flux}} \ll 1$) may not guarantee that the force-free conditions are fulfilled, i.e. that the magnetogram may not be force-balanced ($\epsilon_{\text{force}} \not\ll 1$) and may not be torque-balanced ($\epsilon_{\text{torque}} \not\ll 1$), led to the development of an iterative method in which a functional

$$L_{\text{pp}} = \sum_{n=1}^{4} \mu_n L_n \tag{2.44}$$

is minimized. The numerical implementation of this functional by Wiegelmann et al. (2006) provides the heart of the preprocessing of photospheric magnetograms and in the prospect of later developed extensions ($n > 4$, as described in § 2.4.2.4) this basic approach is in the following called the "classical" preprocessing. Represented by $n = 1$ and $n = 2$ in (2.44), the initial surface integral relations for ϵ_{force} (2.42) and ϵ_{torque} (2.43) are replaced by summations over all grid nodes p of the bottom (photospheric) surface grid in the form

$$L_1 = \Big(\sum_p B_x B_z \Big)^2 + \Big(\sum_p B_y B_z \Big)^2 + \Big(\sum_p B_z^2 - B_x^2 - B_y^2 \Big)^2, \tag{2.45}$$

$$L_2 = \Big(\sum_p x (B_z^2 - B_x^2 - B_y^2) \Big)^2 + \Big(\sum_p y (B_z^2 - B_x^2 - B_y^2) \Big)^2 + \Big(\sum_p (y B_x B_z - x B_y B_z) \Big)^2. \tag{2.46}$$

An additional condition, represented by $n = 3$ in (2.44) and measuring the nearness of the optimized boundary conditions to the observed data, is introduced in the form

$$L_3 = \sum_p \left(B_x - B_x^{\text{obs}} \right)^2 + \sum_p \left(B_y - B_y^{\text{obs}} \right)^2 + \sum_p \left(B_z - B_z^{\text{obs}} \right)^2, \tag{2.47}$$

where B_x^{obs}, B_y^{obs} and B_z^{obs} denote the truly measured photospheric ($z = 0$) magnetic field vector components. The fourth term of the classical preprocessing method, corresponding to $n = 4$ in (2.44), is defined as

$$L_4 = \sum_p (\Delta B_x)^2 + \sum_p (\Delta B_y)^2 + \sum_p (\Delta B_z)^2, \tag{2.48}$$

where Δ denotes the 2D Laplacian operator (the associated differentiation is done using an usual five-point stencil). Note that since each constraint L_n in (2.44) and as introduced in (2.45) – (2.48) represents a different quantity with different physical units, a weighting factor μ_n for each of it is formally necessary but also allows to give more or less importance to the individual terms.

The aim of the procedure is to minimize all L_n simultaneously so that the modified photospheric vector magnetogram in this way suffices the force- and torque-free condition (which are enforced by (2.45) and (2.46), respectively). Furthermore, (2.47) ensures that the optimized boundary conditions do not deviate too much from the measured photospheric data and additionally, with the help of (2.48), the boundary data is smoothed. The latter is a necessary requirement for the successful performance of the NLFF extrapolation code in which we make use of finite differences but also physically motivated since the magnetic field at the base of the corona clearly shows much smoother structures than at the photospheric levels where the magnetic field measurements are performed. Usually, most weight is given to the force-free and torque-free conditions, followed by the smoothing and the nearness to the actually observed data. Here it should be noted that not the actual weight of the individual terms is of importance but the relative one. The optimal combination of the μ_n is usually found by preprocessing one set of photospheric data from an individual instrument with numerous combinations of different μ_n (see § 2.4.2.4 for details).

Using the known set of analytical, closed force-free solutions by Low and Lou (1990) and adding artificial noise models on it, Wiegelmann et al. (2006) were able to show that applying the NLFF algorithm to the unpreprocessed photospheric-like lower boundary data showed a poor agreement with the original analytical solution while preprocessing the lower boundary data and subsequent extrapolation led to a reasonably good agreement with the analytical model field. This is because the preprocessing routine uses the noisy transverse magnetic field components (B_x and B_y in (2.45) – (2.48) which are for real cases measured with much less accuracy than the normal component B_z) to drive the lower boundary magnetogram towards boundary conditions which are more consistent with the force-free assumption. In addition, Wiegelmann et al. (2006) tested the effect of preprocessing using a real photospheric data set as measured with the Solar Flare Telescope-Vector Magnetograph (SFT-VM; Sakurai et al. 1995) of the National Astronomical Observatory of Japan. The magnetic field extrapolation based on the preprocessed SFT-VM data showed that the optimization code converged at a final value of the functional L by orders of magnitude lower than if applied to the not preprocessed data. The positive effect of preprocessing the photospheric vector magnetograph data prior to its input to different existing NLFF field extrapolation methods was also demonstrated by Metcalf et al. (2008) using a solar-like reference model (see van Ballegooijen et al. 2007, and § 2.4.2.4). This model includes realistic photospheric Lorentz forces and a complex field topology containing a weakly twisted, helical flux rope. In particular, it

was found that some smoothing of the original data is advantageous especially for extrapolation methods involving numerical differentiation and hence that the smoothing term (2.48) should not be disabled by setting $\mu_4 = 0$ in (2.44). It was also shown that trying to reproduce a present flux rope in the solar-like reference model based on the forced, not preprocessed photospheric data was not successful at all but that it was qualitatively replicated when feeding the extrapolation codes with the preprocessed values of the lower boundary.

Despite the relative success of the classical preprocessing, the routine was attempted to be further improved by the inclusion of additional information regarding the chromospheric magnetic field using chromospheric Hα images and the corresponding extension to the classical preprocessing scheme is discussed in the following.

2.4.2.4 Hα-preprocessing

Wiegelmann et al. (2008) extended the preprocessing routine by implementing the idea that the performance of the original classical preprocessing method, as described in § 2.4.2.3, can be improved by taking information about the magnetic field orientation in the chromosphere into account. Such information can be in form of, e.g., chromospheric fibril observations in the Hα 656.3 nm spectral line and the procedure is therefore called "Hα-preprocessing".

Hereby, we incorporate the general assumption that the Hα fibrils are oriented along the horizontal chromospheric magnetic fields to connect the penumbral areas of sunspots with the surrounding plage regions. The involvement of the Hα information is realized with the help of an additional term $\mu_5 L_5$ added to (2.44) in the form

$$L_5 = \sum_p w_{\mathrm{pp}} \left(B_x H_y - B_y H_x \right)^2 = \sum_p w_{\mathrm{pp}} \boldsymbol{B}_\parallel^2 \sin^2\phi \tag{2.49}$$

with

$$\sin\phi = \frac{\boldsymbol{B}_\parallel \times \boldsymbol{H}}{|\boldsymbol{B}_\parallel||\boldsymbol{H}|}, \tag{2.50}$$

where $\boldsymbol{B}_\parallel = (B_x, B_y)$ is the projection of the photospheric magnetic field vector in the image (xy-) plane, ϕ is the angle of the projected magnetic field vector with the Hα fibrils on the xy-plane, $\boldsymbol{H} = (H_x, H_y)$ is the direction of the chromospheric Hα fibrils and $|\boldsymbol{H}|$ is an unit tangent vector to the chromospheric fibrils projected onto the solar photosphere and thus representing the field direction with an 180°-ambiguity (see also § 2.4.0.1). From this, however, no difficulty arises since only the orientation but not the direction of the magnetic field is aimed to be reproduced correctly by the Hα-preprocessing. The space-dependent weighting function $w_{\mathrm{pp}} = w_{\mathrm{pp}}(x, y)$ is not a priori related to the magnetic field strength and can be specified to indicate the confidence level of the detected fibril direction. In regions without reliable Hα signatures one sets $H_x = 0$ and $H_y = 0$ so that only the classic preprocessing terms (2.45) – (2.48) in (2.44) apply. In regions where the observed Hα fibrils are assumed to picture the magnetic field orientation the weighting function w_{pp} can be used to give more or less importance to different parts of the Hα image where $H_x \neq 0$ and/or $H_y \neq 0$ (with the limits $w_{\mathrm{pp}} = 1$ and $w_{\mathrm{pp}} = 0$ for reliable or not trustworth Hα information, respectively).

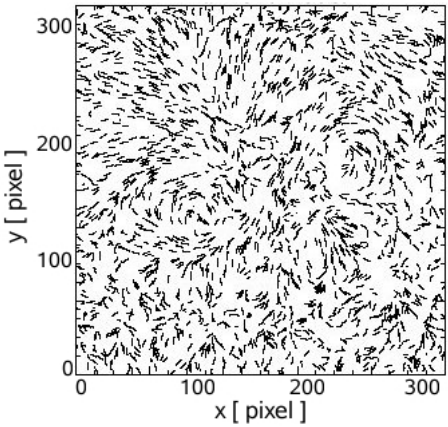

Figure 2.2: Hα fibril model as used within the Hα-preprocessing and as estimated from the solar-like force-free model chromosphere of A. A. van Ballegooijen. The Hα-fibrils are thought to give information about the transverse magnetic field orientation (with an 180°-ambiguity).

The Hα-preprocessing method was tested using the active-region model developed by A. A. van Ballegooijen. For constructing the model, a full-disk photospheric line-of-sight SoHO/MDI magnetogram of Oct 10, 2005 was used which showed the isolated NOAA active region 10814 south of the solar equator. From this photospheric data, as a first step, a potential (current-free; $\alpha_{\rm ff} = 0$) field was computed in spherical coordinates. Corresponding to an observed Hα filament, following the inversion line of active region 10814, a model flux rope (S-shaped, sinistral) was inserted into the calculated 3D potential field configuration (for details see van Ballegooijen (2004) and van Ballegooijen et al. (2007)). The whole system was then relaxed to a NLFF state of equilibrium using a magneto-frictional method (van Ballegooijen et al. 2000, and see also § 2.4) and interpolated onto a rectangular grid. The resulting active-region model is force-free throughout the entire cubic computational domain except within two grid points above the lower boundary. The layer at the bottom of the force-free region (i.e. the layer at the third grid point above the lower boundary of the box) was taken to represent a chromospheric-like solar magnetic field and thus was used to derive the direction vectors for the artificial Hα image (see Fig. 2.2), needed to test the Hα-preprocessing routine. For appropriately testing the effect of including Hα information in the preprocessing method, we first searched for the optimum combination of $\mu_1 - \mu_4$ within the classical scheme (with the initial choice $\mu_5 = 0$). This makes sense, since we need to keep a certain combination of $\mu_1 - \mu_4$ fixed in order to truly investigate the effect of including Hα information by incorporating the L_5-term (2.49) in (2.44) later on. As already mentioned, within the classical preprocessing scheme most weight is given to the force-balance and torque-balance conditions (i.e., $\mu_1 = \mu_2 = \mu_{12} = 1$) and less weight is given regarding the deviation of the optimized boundary conditions from the actually observed data (i.e., $\mu_3 < \mu_{12}$) and to the computationally and physically motivated smoothing (i.e., $\mu_4 < \mu_{12}$).

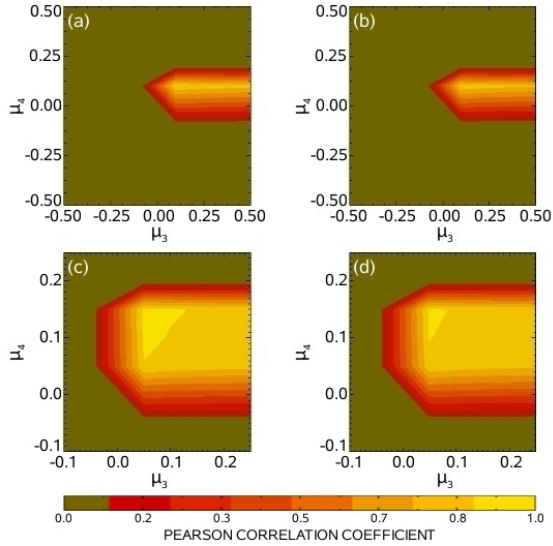

Figure 2.3: Pearson correlation of the classical preprocessed photospheric field with the model chromosphere for the transversal components B_x (left panels) and B_y (right panels) as a function of the combination of different preprocessing parameters μ_3 and μ_4. The local maximum around $\mu_3 = 0.05$ and $\mu_4 = 0.15$ (panels (a) and (b)) was analyzed in more detail (panels (c) and (d)) to find the maximum of the correlation coefficient for both B_x and B_y at $\mu_3 = 0.025$ and $\mu_4 = 0.155$. The color bar indicates the derived values of the correlation coefficient.

To find the best performing combination of μ_3 and μ_4 (while μ_{12} is held fixed) within the classical scheme, about 10^3 combinations of the two parameters were used to preprocess the photospheric model boundary. The relative performance of these parameter combinations were then evaluated by calculating the Pearson correlation coefficient between the preprocessing result and the model chromosphere. This was done only for the transversal components (B_x and B_y) since the correlation of the preprocessed and model-chromospheric normal component (i.e. the line-of-sight component B_z) is in any way higher. Note that this should apply for real solar cases, too since the line-of-sight component of the magnetic field is not affected by the ambiguity problem and since the measurement accuracy of this component is usually higher than that of the transversal components. Out of about 800 combinations of $-5.0 < (\mu_3, \mu_4) < 5.0$ (with step sizes of $\Delta\mu_3 = \Delta\mu_4 = 0.5$ for $-5.0 < (\mu_3, \mu_4) < 5.0$ and $\Delta\mu_3 = \Delta\mu_4 = 0.1$ for $-1.0 \leq (\mu_3, \mu_4) \leq 1.0$) we found a most pronounced local maximum clearly within $-0.5 < (\mu_3, \mu_4) < 0.5$ and therefore, we computed another 100 combinations of $-0.25 \leq (\mu_3, \mu_4) \leq 0.25$ with a reduced step size of $\Delta\mu_3 = \Delta\mu_4 = 0.05$. Hereafter, the local maximum for both transversal magnetic field components B_x and B_y was more precisely localized around $\mu_3 = 0.05$ and $\mu_4 = 0.15$ (see panels (a) and (b) in Fig. 2.3). The region around this local maximum was then analyzed in more detail by using these two values as a new initial guess. Another 100

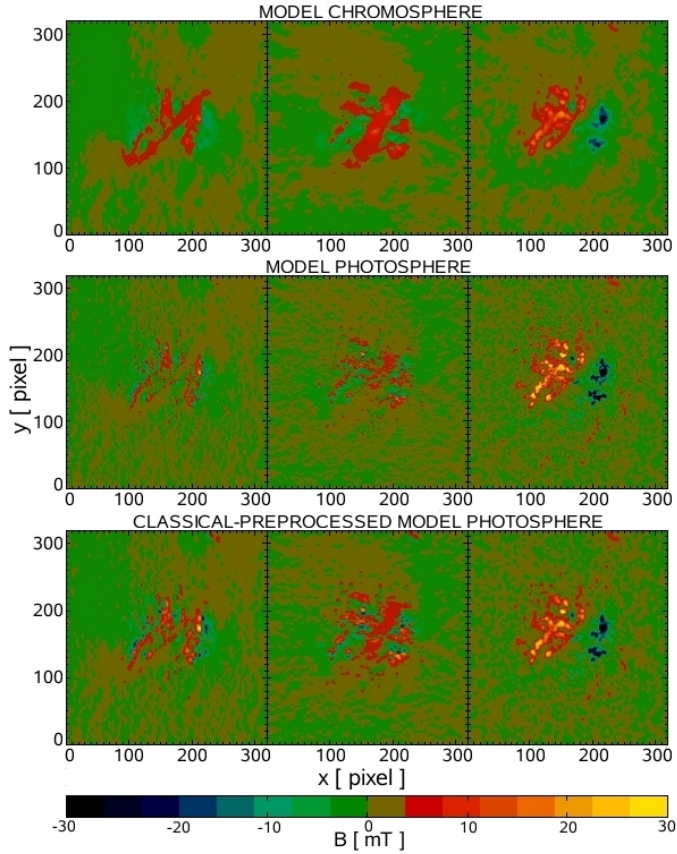

Figure 2.4: Illustrative results of the performance of the classical preprocessing, applied to the not force-free model photosphere of A. A. van Ballegooijen. The top and second row show the force-free model chromospheric and not force-free model photospheric magnetic field, respectively. The third row shows the classical-preprocessed photospheric model data, where the optimum combination of the preprocessing parameters ($\mu_{12} = 1.0$, $\mu_3 = 0.025$ and $\mu_4 = 0.155$) has been used. From left to right, B_x, B_y and B_z are shown. The color bar gives the magnetic field strength in mT.

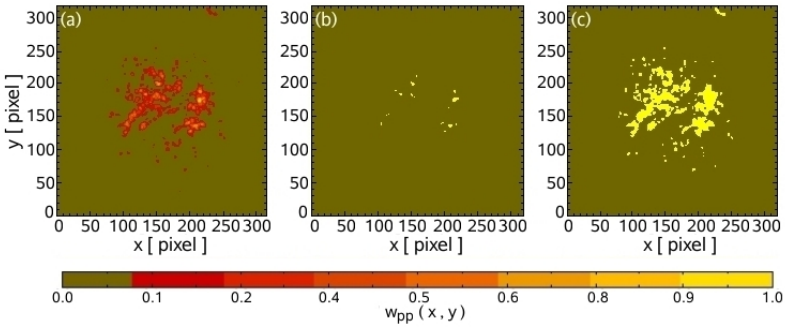

Figure 2.5: Weighting functions $w_{\mathrm{pp}}(x, y)$ used to test the Hα-preprocessing. The different weighting functions w^2_{pp}, w^3_{pp} and w^4_{pp} are shown in panel (a), (b) and (c), respectively. The values of w_{pp}, as indicated by the color bar, control the degree of incorporation of the Hα-fibril information shown in Fig. 2.2.

combinations of μ_3 and μ_4 around this pair, with a reduced step size of $\Delta\mu_3 = \Delta\mu_4 = 0.005$ were then investigated so that the absolute maximum of the correlation coefficients was identified at $\mu_3 = 0.025$ and $\mu_4 = 0.155$, for both B_x and B_y (see panels (c) and (d) in Fig. 2.3, respectively). The resulting classical-preprocessed photospheric magnetic field is shown in the last row of Fig. 2.4. The best-performing combination of μ_3 and μ_4 found in this way was, together with $\mu_{12} = 1.0$, held fixed during the tests regarding the inclusion of Hα information as described in the following.

Equipped with the knowledge of the best-performing combination of $\mu_1 - \mu_4$ within the classical preprocessing scheme we then aimed to find the suitable parameters for including information from the model Hα image (see Fig. 2.2) into the preprocessing. For this purpose, the weighting function $w_{\mathrm{pp}}(x, y)$ in (2.49) has been defined in four different ways. We assumed, first, that every point of our artificial Hα image gives the exact orientation of the chromospheric magnetic field (i.e., $w_{\mathrm{pp}}(x, y) = w^1_{\mathrm{pp}} = 1.0$). Second, we presumed that the magnitude of the underlying photospheric magnetic field $\boldsymbol{B}_{\mathrm{ph}}$ directly indicates the reliability of the overlying chromospheric Hα information to define the corresponding weighting function as $w_{\mathrm{pp}}(x, y) = w^2_{\mathrm{pp}} = \sqrt{(B^2_x + B^2_y + B^2_z)_{\mathrm{ph}}}$ (see panel (a) in Fig. 2.5). Third, we assumed that only points in the Hα image corresponding to regions in the underlying photosphere with a magnetic field magnitude $\geq 50\%$ of the maximum magnitude carry valid Hα information. Therefore, we defined $w_{\mathrm{pp}}(x, y) = w^3_{\mathrm{pp}} = 1.0$ where $w^2_{\mathrm{pp}} \geq 0.5$ and $w_{\mathrm{pp}}(x, y) = w^3_{\mathrm{pp}} = 0.0$ where $w^2_{\mathrm{pp}} < 0.5$ (see panel (b) in Fig. 2.5). Similarly we assumed, fourth, that only points in the Hα image corresponding to regions with magnetic field magnitudes $\geq 10\%$ of the maximum magnitude can be taken as trustworthy to define $w_{\mathrm{pp}}(x, y) = w^4_{\mathrm{pp}} = 1.0$ where $w^2_{\mathrm{pp}} \geq 0.1$ and $w_{\mathrm{pp}}(x, y) = w^4_{\mathrm{pp}} = 0.0$ where $w^2_{\mathrm{pp}} < 0.1$ (see panel (c) in Fig. 2.5). We searched for the optimal values of μ_5 for each of the different weighting functions ($w^1_{\mathrm{pp}} - w^4_{\mathrm{pp}}$) in the range $0.0 < \mu_5 < 2.5$. Initially, we used a step size of $\Delta\mu_5 = 0.05$ and, around the first appearing maximum, we used a reduced step size of $\Delta\mu_5 = 0.005$. We calculated the Pearson correlation coefficient between the chromospheric

reference field and the minimum solution of the preprocessing routine which provided us with the optimal values of μ_5 for the different weighting functions. Precisely, these were $\mu_5 = 1.525$, $\mu_5 = 1.765$, $\mu_5 = 1.880$ and $\mu_5 = 2.115$ for $w_{\rm pp}^1$, $w_{\rm pp}^2$, $w_{\rm pp}^3$ and $w_{\rm pp}^4$, respectively. The Hα-preprocessed photospheric magnetic field, using $w_{\rm pp}^1$, $w_{\rm pp}^2$ and $w_{\rm pp}^3$ is shown in the second, third and fourth row of Fig. 2.6, respectively.

The classical-preprocessed model photosphere, as pictured in the last row of Fig. 2.4, already well reproduces the model chromosphere (as shown in the first row of the same figure). The Hα-preprocessed model photosphere, however, was found to match the reference model chromosphere even better (see the lower three rows of Fig. 2.6). The quality of the classical and Hα-preprocessing was evaluated by testing how well the magnetic field, extrapolated from the preprocessed boundary conditions, agrees with the reference field. Here, with reference field we mean the magnetic field which we extrapolated from the model chromosphere. In particular, beside other quantities, we evaluated the total magnetic energy of an extrapolated field, normalized to a reference field in the form

$$\epsilon_{\rm mag} = \frac{\sum_i \left| \boldsymbol{B}_i^\star \right|^2}{\sum_i \left| \boldsymbol{B}_i \right|^2}, \tag{2.51}$$

where $\boldsymbol{B}_i^\star$ and $\boldsymbol{B}_i$ are the magnetic field vectors at each grid point i. Here, $\boldsymbol{B}^\star$ denotes the 3D magnetic field as extrapolated from the preprocessed data, and $\boldsymbol{B}$ represents the 3D magnetic field, extrapolated from the model chromosphere.

We found that the extrapolations based on the preprocessed fields provide much better results than those obtained by using the unpreprocessed model photosphere. For the classical preprocessing we get the magnetic energy content of the 3D magnetic field correct to within an error of $\approx 3\%$, whereas for unpreprocessed data we get an error of $\approx 35\%$. Taking the chromospheric Hα information into account the result improves with respect to the classical preprocessing so that the magnetic energy is recovered with an accuracy of $\approx 1\%$ or better, even for the cases where we used the chromospheric information only in parts of the entire region (depending on the choice of the weighting function $w_{\rm pp}(x, y)$; for the detailed analysis see Wiegelmann et al. 2008). However, it should be noted here, that in principle one could also vary all μ_n simultaneously and that we therefore cannot exclude that there might exist a combination of $\mu_1 - \mu_5$ resulting in an even better agreement of our preprocessed field and the model chromospheric field. This would, however, not be a suitable way to deal with real data because usually no routine chromospheric vector field measurements exist to test the result. Moreover, it is not possible to provide one optimal parameter set suitable for different vector magnetographs. The optimal combination of the preprocessing parameters has to be carried out for different instruments separately. Nevertheless, we indeed expect that an optimal parameter set for a certain instrument and particular region will also be useful for the preprocessing of other regions of the same kind observed with the same instrument.

In the future, a further improvement of the performance of the preprocessing could be achieved with the help of additional observations, e.g., in the form of line-of-sight chromospheric field measurements as provided by the Synoptic Optical Long-term Investigations of the Sun (SOLIS; Keller et al. 2003a) survey of the National Solar Observatory. These data could be included directly in the L_3-term, either as a certain information or in some weighted combination with the photospheric line-of-sight magnetic field.

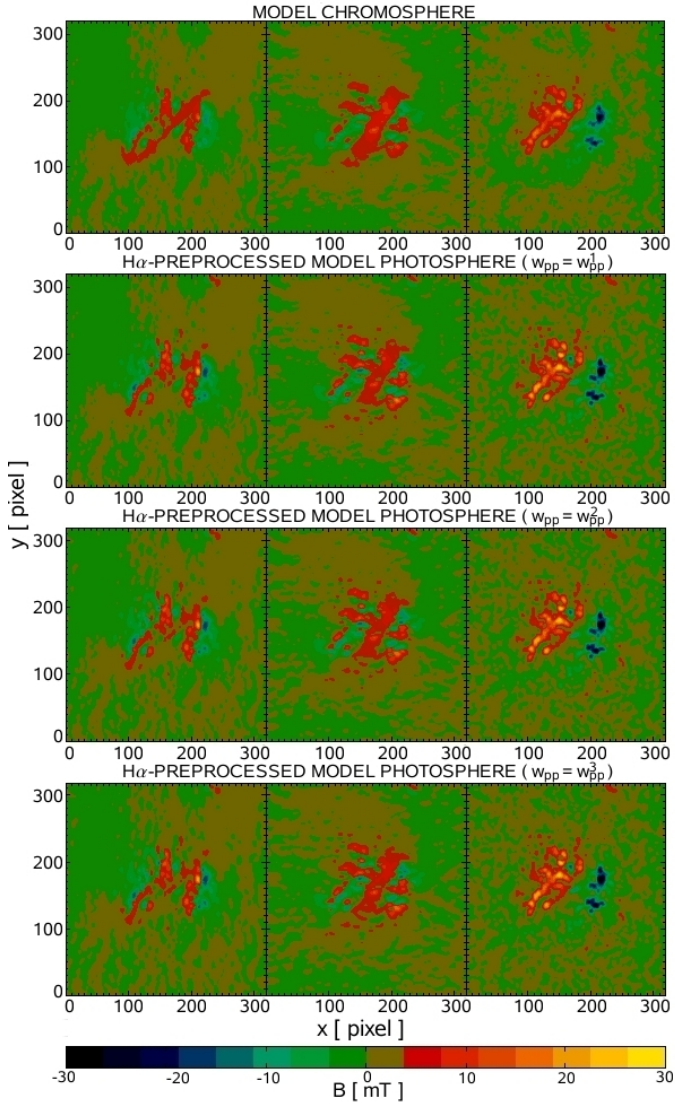

Figure 2.6: Illustrative results of the performance of the Hα-preprocessing, applied to the not force-free model photosphere of A. A. van Ballegooijen. The top row shows the force-free model chromospheric magnetic field. The second, third and fourth row show the result of Hα-preprocessing the photospheric-like data, using w^1_{pp}, w^2_{pp}, w^3_{pp} and w^4_{pp}, respectively. From left to right, B_x, B_y and B_z are shown. The color bar gives the magnetic field strength in mT.

2.5 Summary

Since routine measurements of the chromospheric and coronal magnetic field are usually not available, numerical methods to estimate the magnetic fields in the upper solar atmosphere have been developed and extensively tested. Based on a number of assumptions about the physical conditions in the mid- and upper chromosphere and corona its magnetic field can be calculated using force-free field extrapolation methods. The coronal magnetic field can be approximated either by potential (current-free), linear force-free (constant-α_{ff}) or nonlinear force-free (non-constant-α_{ff}) fields. While potential and constant-α_{ff} fields are only capable of reproducing the true coronal magnetic field (and in particular its magnetic energy content) to a certain extent the more general approach of non-constant-α_{ff} fields is favorable. In contrast to the aforementioned simpler models, these methods need the full photospheric magnetic field vector as the lower boundary condition. In general, as the photosphere is a region in the solar atmosphere where the force-free assumption is known not to be justified, the magnetograms have to be preprocessed in order to achieve a set of boundary conditions compatible with the force-free extrapolation method. For this purpose, a well-tested preprocessing routine can be used to achieve consistent lower boundary conditions in which, optionally, chromospheric magnetic field information in form of the orientation of Hα fibrils or line-of-sight magnetic field measurements can be included.

A number of numerical implementations of the force-free boundary value problem exist and for the presented work an optimization approach is used to extrapolate the 3D magnetic vector from the preprocessed (consistent) photospheric boundary values into the corona. Then, one is able to investigate the 3D coronal magnetic field topology and can estimate the related physical quantities such as the magnetic energy content, the free magnetic energy (which can partly be released during solar eruptions based on the reconfiguration of the magnetic field), the magnetic energy density (that is the stored magnetic energy per unit volume) and also the current and magnetic helicity density.

The next chapter, therefore, deals with the application of our potential and nonlinear force-free models to calculate the coronal magnetic field above two solar active regions. In particular, the temporal evolution of the magnetic energy content, the associated energy density, as well as the magnetic field topology in the course of solar eruptions launched from these active regions are analyzed.

3 Coronal magnetic field above solar active regions

This chapter deals with the application of our potential and nonlinear force-free field models to calculate the coronal magnetic field above solar active regions. A short review of recent applications of force-free techniques to extrapolate the photospheric magnetic field vector into the corona is given in § 3.1. The method used for our own detailed analysis of solar active regions is outlined in § 3.2.1. The results that arose from applying our method to the two solar active regions NOAA 10540 and NOAA 10960 are discussed in detail in § 3.2.2 and § 3.2.3 and have partly been published in Thalmann and Wiegelmann (2008) and Thalmann et al. (2008), respectively. Finally, a short summary is given in § 3.3.

3.1 State of the research

When magnetic flux emerges from below the solar surface and expands into the corona, the coronal magnetic field is destabilized, leading to explosive phenomena such as flares and coronal mass ejections. The free magnetic energy to be released during these events, is believed to be stored in current-carrying coronal magnetic fields that appear twisted or sheared. In general, the energy necessary for such large-scale phenomena is assumed to be stored and released in the corona, although the evolution of the lower lying photosphere certainly has an influence on the available amount of free energy above. To investigate the magnetic field configuration in the solar corona, methods have been developed to derive it from routinely observed photospheric magnetograms.

Coronal magnetic reconstruction techniques have been used in many studies, mainly using the linear force-free (LFF) assumption. For instance, van Driel-Gesztelyi et al. (2000) studied two sigmoid events related to CMEs by matching an extrapolated LFF field with data from the Yohkoh/Soft X-ray Telescope (SXT; Tsuneta et al. 1991). It was noticed that the observed long loops and bright short loops were best characterized by different force-free parameters α_{ff} but also that the LFF extrapolations could not recover the sigmoidal shape exactly since the magnetic twist, which within LFF computations is considered to be homogeneous, is likely to be more concentrated in reality. Tang et al. (2000) used a trial and error method to fit a LFF model with Yohkoh/SXT and NAOJ/SFT Hα data to study a brightening event. Their extrapolated field was found to be potential-like and closely matching the observed large soft X-ray loops around the brightening region. The observed small-scale soft X-ray loops, however, were found to be not oriented along the potential field lines before the brightening. More recently, Mandrini et al. (2005) analyzed the coronal magnetic field around a sigmoidal X-ray bright point. By compar-

ing the model magnetic field lines to coronal loops, observed with the Transition Region And Coronal Explorer (TRACE; Handy et al. 1999), they found the force-free parameter α_{ff} to be higher in the core of the investigated active region (AR) than in the peripheries and the derived values of α_{ff} indicated that the coronal magnetic field configuration was highly non-potential. In both aforementioned cases, the Fast Fourier Transform method as proposed by Alissandrakis (1981) was used to extrapolate the LFF field from the photospheric line-of-sight magnetic field component.

However, as discussed in § 2.3, LFF models cannot fully recover the free magnetic energy to power eruptive processes as it is the excess energy of a LFF field which can partly be transformed into kinetic energy during dynamic events. Therefore, nonlinear force-free (NLFF) field models are needed to be able to describe the magnetic field related to explosive phenomena.

Using one or the other of the existing NLFF field extrapolation methods (see § 2.4), several studies have been concerned with the energy content of the magnetic field above solar ARs. Bleybel et al. (1999, 2002) used the Grad-Rubin-like NLFF field model of Amari et al. (1999) which assumes that the normal component of the magnetic field vanishes on the lateral and top boundaries of the computational box. They estimated the global energy budget of NOAA AR 7912 before and after a long duration C1.6 flare on Oct 14, 1995 and found a decrease in the magnetic energy over the course of the eruption. The post- as well as the pre-flare configuration showed a total magnetic energy content in the order of 10^{25} J. Furthermore, the coronal magnetic field was found not to relax to a constant-α_{ff} LFF state, i.e. still containing nonlinearities and hence not supporting Taylor's relaxation hypothesis (for the formal derivation and a detailed discussion of Taylor's hypothesis see § 4.1.3.1). Analyzing NOAA AR 8151, as visible in Feb 1998 and also using a Grad-Rubin-like method, Régnier et al. (2002) found that the available free magnetic energy was not high enough ($\propto 10^{24}$ J) to produce a large flare. The 3D magnetic configuration of a simultaneously observed Hα filament and X-ray sigmoid has been studied in detail by Régnier and Amari (2004). Their finding of the observed sigmoid to be situated higher in the corona than the observed filament, though having the same orientation, is in agreement with earlier observational and modeling works. Additionally, the electric current density in these structures was found to be opposite. The same AR in its decaying phase was compared with the newly emerged NOAA AR 8210 of May 1998 by Régnier and Priest (2007b) who found the free energy of both ARs to be within the same order of magnitude. Furthermore, they concluded that this amount of energy was high enough to trigger a series of small flares (which have been described in detail by Régnier and Canfield 2006). The same extrapolation method was used to analyze NOAA AR 10486 on Oct 27 and 28, 2003 by Régnier et al. (2005b) where the amount of free energy was estimated as being proportional to 10^{25} J. They also showed that even if the physical meaning of the potential field ($\alpha_{\mathrm{ff}} = 0$) approximation is restricted, the study of the long-term evolution of the potential field energy can be useful to understand the nature of an AR. To get insights into the geometry, topology and connectivity of the magnetic field, however, it was pointed out that NLFF computations are required. The same AR, two days later on Oct 29, 2003 was explored by Metcalf et al. (2005). Applying the magnetic virial theorem to chromospheric vector magnetograms from the Imaging Vector Magnetograph at the Mees Solar Observatory (MSO/IVM; Mickey et al. 1996), they noticed an increase in the free magnetic energy prior to a flare and that part of the final

amount of free energy ($\propto 10^{26}$ J) was sufficient to power an X-class flare. Also Régnier and Priest (2007a) compared the free magnetic energy of two ARs at distinct evolutionary stages as computed with the help of different mathematical approaches. They found that for both, a decaying AR and a newly emerged one, the photospheric distributions of the current density and α_{ff} neither showed any particular patterns nor exhibited any evidence of an organized distribution. For the decaying NOAA AR 8151 higher values of α_{ff} were found, indicating the presence of strong currents in the magnetic configuration, while for the newly emerged NOAA AR 8210 lower α_{ff} values were found, indicating the existence of weak currents. Consequently, as the present electric currents are thought to be responsible for the storage of magnetic energy in the corona, $\approx 40\%$ and $\approx 3\%$ of the total magnetic energy was estimated to having been stored in the decaying and newly emerged AR, respectively. Most recently, Jing et al. (2008) have calculated the shear parameters around the flaring polarity inversion line of NOAA AR 10930 before and after the occurrence of an X3.4 flare based on the extrapolation of observations performed with the Solar Optical Telescope on board Hinode (Hinode/SOT; Kosugi et al. 2007). The comparison of the height variations of the shear parameters in the pre- and post-flare NLFF fields led them to conclude that ≈ 8 Mm seemed to be a critical height below which the non-potentiality of the field increased after the flare. Above this critical height, up to a height of about 70 Mm, the field was found to have relaxed to a more potential state and thus was found to be likely the altitude range in which the energy release had happened. Besides this, various NLFF extrapolation codes were applied to the aforementioned pre- and post-flare Hinode/SOT data, finding a decrease of the free magnetic energy in the order of 10^{25} J, high enough to power the observed X-class flare (Schrijver et al. 2008).

3.2 Applications

3.2.1 Method

As the observed photospheric vector magnetograph data is extracted from magnetic field measurements at a level in the solar atmosphere that is known to be not force-free, the solution to the force-free equations as introduced in § 2.4 may not exist (Gary 2001, Metcalf et al. 1995). The consistency of the observed data with the force-free assumption can be checked with integral relations (see § 2.4.2.2, Molodenskii (1969), Molodensky (1974) and Aly (1989)). These criteria allow dimensionless parameters to be computed that represent an estimate of the total force and torque on the bottom boundary layer, i.e. the observed vector magnetograph data (see § 2.4.2.3 and Wiegelmann et al. (2006)), whose values should be small in order to find a force-free solution in the corona above.

To achieve the consistency of the observed photospheric data with the force-free assumptions, we apply the preprocessing routine as developed by Wiegelmann et al. (2006). As explained in § 2.4.2.3, the procedure minimizes a functional so that the in this way modified photospheric vector magnetogram suffices the force-free and torque-free conditions, that the optimized boundary condition does not deviate too much from the measured photospheric data and that the boundary data is sufficiently smooth. The different involved criteria are individually weighted and as a first step when dealing with real solar data the optimal combination of the weighting parameters has to be carried out. Once found, how-

ever, the preprocessed data provide consistent boundary conditions for a NLFF coronal magnetic field extrapolation. For calculating the NLFF field from these more suitable boundary conditions we use the multigrid-like optimization code of Wiegelmann (2004) which is a modification of the optimization approach originally proposed by Wheatland et al. (2000). It evolves the magnetic field matching the volume-integrated boundary, force-free and divergence-free conditions (for details see § 2.4.1). Besides computing NLFF fields, we also calculate the corresponding potential fields that can be determined from the vertical (line-of-sight) photospheric field alone, using a Green's function method after Aly (1989).

For NLFF field extrapolations, vector magnetograph data are needed near the solar disk center to minimize unavoidable foreshortening effects. If one wants to consider the temporal evolution of the coronal field this, of course, represents a kind of restriction since the observed AR follows the solar rotation. Nevertheless, the observation of the same AR for several consecutive days is important for conclusions about the energy evolution before and after eventual eruptive phenomena. Gary and Hagyard (1990) worked out in detail the problems due to the 180°-ambiguity (see also § 2.4.0.1) and curvature of the Sun associated with off-center magnetograms. For both, a highly non-potential AR close to the solar limb and a quasi-potential AR near the disk center, the azimuthal ambiguity could not be completely resolved by a potential-field acute-angle calculation. Consequently, improper ambiguity resolutions were found to significantly influence the heliographic results and thus the interpretation of the magnetic field structure. Furthermore, they concluded that the curvature of the Sun must be taken into account for regions being located at angles of more than 50° off the solar disk center.

Once extrapolated, we calculate the total magnetic energy content of the 3D magnetic fields by evaluating the volume integral

$$E_m = \frac{1}{2\,\mu_0} \int_V B^2 \, d^3x, \tag{3.1}$$

where $B^2(2\,\mu_0)^{-1}$ is called the magnetic energy density and μ_0 is the magnetic permeability of vacuum. If one substracts the magnetic energy content of an extrapolated potential field E_m^{POT} from that of the corresponding NLFF field E_m^{NLFF} one finds an upper limit for that part of the magnetic energy which can be set free and which is, therefore, called the "free" magnetic energy $\Delta E_{\mathrm{POT}}^{\mathrm{NLFF}} = E_m^{\mathrm{NLFF}} - E_m^{\mathrm{POT}}$. Alternatively, as shown by Régnier and Priest (2007b), one can use the LFF field as a reference field to calculate $\Delta E_{\mathrm{LFF}}^{\mathrm{NLFF}} = E_m^{\mathrm{NLFF}} - E_m^{\mathrm{LFF}}$. To avoid the problems of an unbounded domain, namely the energy being infinite and the field possessing unphysical reversals, they first computed the NLFF field inside a finite domain using the vector potential Grad-Rubin-like method (Amari et al. 1997, 1999). Then they determined the corresponding LFF field by an iterative scheme to find the α_{ff}-value matching the helicity of the NLFF field. Calculating the amount of free magnetic energy in both of the aforementioned ways and comparing the results to the observed eruptive phenomena they concluded that, for their particular method to extrapolate the coronal magnetic fields, $\Delta E_{\mathrm{LFF}}^{\mathrm{NLFF}}$ might give a better estimate. Another way to estimate the coronal energy content is to use the magnetic virial theorem (see § 2.4.2.1, Molodensky (1974) and Aly (1989)). The magnetic energy in the half-space $z > 0$ above the surface

∂V at $z=0$ based on the virial theorem, i.e. following from (2.32), can be written as

$$E_m^{\mathrm{VIR}} = \frac{1}{\mu_0} \int_S \left(x\, B_x + y\, B_y \right) B_z \, dS, \tag{3.2}$$

where S denotes the lower, force-free boundary. Here, besides the assumption of a force-free field, it is additionally assumed that the field falls off sufficiently fast. Note that, in principle, the virial energy can be estimated using all boundaries of a considered volume but that for real solar cases it is only the lower boundary for which the magnetic field is known. An extensive study about the ability of using the magnetic virial theorem for magnetic energy estimations above the photosphere was done by Klimchuk et al. (1992). Based on the vector magnetograph information used in their study, they concluded that the best magnetic energy determinations would be accurate to only $\approx 30\%$ and also that not all instruments can be expected to provide this accuracy. This uncertainty was suspected to be rooted in the noise level of the magnetograms and based on the fact that the solar photosphere is not force-free, as shown by Metcalf et al. (2008), using a solar-like model atmosphere by van Ballegooijen et al. (2007). There, (3.2) was applied to the model photosphere (i.e. the lower boundary of the cubic model atmosphere) and was found to reproduce only about 45% of the true model volume's energy content. When applied to the force-free model chromosphere, however, about 86% of the energy content was reproduced. After applying the preprocessing routine of Wiegelmann et al. (2006) to the model photosphere, to drive the model photosphere to a more chromospheric-like state, the model coronal energy content was reproduced to within about 81%. This showed that the preprocessing of the lower photospheric boundary improves the applicability of the magnetic virial theorem to estimate the coronal energy content.

However, even if the estimation of the coronal magnetic energy content above a solar AR before and after an eruption is reliable to a certain degree, one has to keep in mind that during the processes related to the eruption, part of the coronal magnetic energy is released but another part of it is also transformed into other forms of energy such as kinetic energy or heat. Alternative measures of the topological complexity of magnetic fields are the electric current and the magnetic helicity. The latter has the comfortable property to be almost conserved in resistive MHD since its dissipation time is too long to be relevant for most coronal processes. The practical helicity computation for coronal volumes will therefore be discussed in § 4.

3.2.2 NOAA AR 10540

3.2.2.1 Flare activity

According to the weekly bulletin of the Solar Influence Data Analysis Center's Space Weather Application Pilot Project (SIDC/SWAPP), the flaring activity during the week of Jan 12 – 16, 2004 was low, except for a C3.2 flare showing up on Jan 15 (for the solar flare classification according to the measured peak intensity of the solar soft X-ray flux see § 1.1.3.1). Afterwards the activity increased due to NOAA AR 10540, showing more peaks in the C-level (corresponding to a measured soft X-ray flux between $10^{-6}\,\mathrm{Wm}^{-2}$ and $10^{-5}\,\mathrm{Wm}^{-2}$) and finally producing an M5.0 flare on Jan 17 and an M1.4 flare on Jan 18. The next week, this AR produced a long duration C8.2 flare on Jan 19, accompanied by

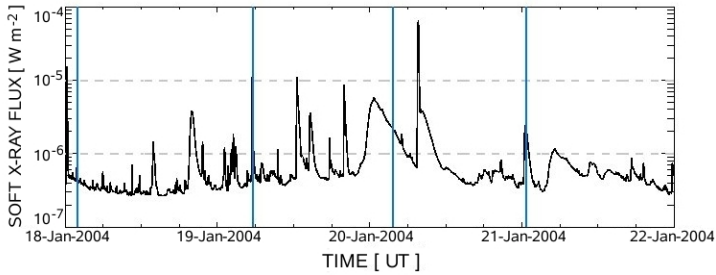

Figure 3.1: GOES solar soft X-ray flux from Jan 18 – 21, 2004, integrated in the wavelength range of 0.1 nm – 0.8 nm. Blue vertical lines indicate when SFT-VM data was available to use.

a full halo CME. Two big prominence eruptions occurred on Jan 21, each leading to a CME, and after that the solar activity dropped to background B-level (corresponding to a measured soft X-ray flux $< 10^{-6}\,\mathrm{Wm}^{-2}$). Two M-class flares launched by AR 10540 are of special interest for the present study. The first, on Jan 19 at 12:40 UT was classified as an M1.0 flare and the second, at 07:43 UT on Jan 20 was categorized as an M6.1 flare, where close in time to the latter a CME showed up first around 08:06 UT (see Fig. 3.1 for the GOES soft X-ray flux of Jan 18 – 22, 2004).

3.2.2.2 NAOJ/SFT Vector Magnetograph

The NAOJ/SFT consists of four telescopes, of which one, a vector magnetograph (20 cm aperture, hereafter SFT-VM) measures the magnetic field vector by using the Zeeman effect on the Fe I 630.3 nm spectral line. The conversion of the observed polarization degrees to the magnetic field strength is based on a model atmosphere by Holweger and Mueller (1974) in which a constant magnetic field is introduced and local thermodynamic equilibrium is assumed. Then, the longitudinal and transverse magnetic field strengths can be related to the circular and linear polarization degrees, respectively. The noise levels of the resulting longitudinal and transverse field strength is about 1 mT and 10 mT, respectively. To remove the 180°-ambiguity of the transversal magnetic field the potential-field acute-angle method is used (see also § 2.4.0.1). It involves the computation of a potential magnetic field from the observed longitudinal field and the subsequent comparison of the computed (model) and observed transverse field. The azimuth which best matches the computed field is then assumed to outline the true direction of the transverse field (for a detailed instrument description see Sakurai et al. 1995).

For the study of NOAA AR 10540 on four subsequent days (from Jan 18 to Jan 21, 2004), at locations that are far enough from the solar limb, one SFT-VM vector magnetogram per day was available with a pixel size of $\approx 1.32''$. The longitudinal magnetic field component of the vector magnetograms of all four days is shown in Fig. 3.2. The SFT-VM vector magnetograms contain a region of $\approx 336'' \times 315''$, i.e. $\approx 241\,\mathrm{Mm} \times 226\,\mathrm{Mm}$ and we display the $x-$, $y-$ and $z-$ component of the photospheric vector magnetic field of Jan 18, 2004 at 01:58 UT in panels (a), (b) and (c) of Fig. 3.3, respectively.

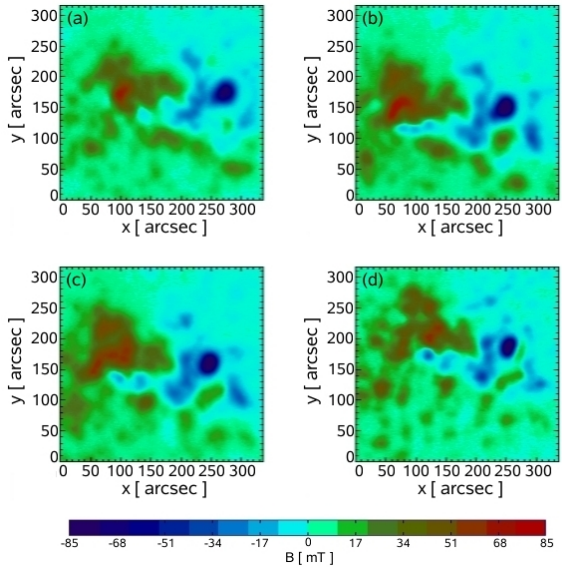

Figure 3.2: Longitudinal photospheric magnetic field component (B_z) of the available SFT-VM vector magnetograms for four subsequent days. Panels (a), (b), (c) and (d) show B_z on Jan 18 at 01:58 UT, Jan 19 at 05:35 UT, Jan 20 at 03:40 UT and Jan 21 at 00:40 UT, respectively. Units are arcseconds and the color bar indicates the magnetic field strength in mT.

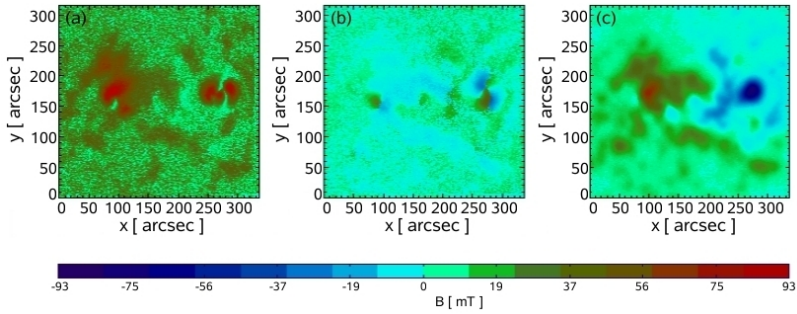

Figure 3.3: Transverse (B_x, B_y) and longitudinal (B_z) photospheric magnetic field components of the available SFT-VM vector magnetogram on Jan 18, 2004 at 01:58 UT. Panels (a), (b) and (c) show B_x, B_y and B_z, respectively. Units are arcseconds and the color bar gives the magnetic field strength in mT.

Force-free consistency of the raw and preprocessed SFT-VM data

Jan 2004		*Raw data*		*Preprocessed data*	
Day	*Time [UT]*	ϵ_{force}	ϵ_{torque}	ϵ_{force}	ϵ_{torque}
18	01:58	0.7341	0.8339	0.0037	0.0018
19	05:35	0.8500	0.9195	0.0037	0.0023
20	03:40	0.8595	0.9534	0.0039	0.0031
21	00:40	0.8804	1.0219	0.0075	0.0051

Table 3.1: Dimensionless force-balance parameter (ϵ_{force}) and the torque-balance parameter (ϵ_{torque}) to quantify the consistency of the observed ("Raw data") and the preprocessed photospheric SFT-VM vector magnetogram data with the force-free assumption.

3.2.2.3 Preprocessing of SFT-VM data

In order to achieve the consistency of the observed vector magnetograms with the assumption of a force-free field, the SFT-VM data need to be preprocessed (see § 2.4.2). Dimensionless parameters are used to quantify whether the observed, photospheric SFT-VM magnetograms suffice the compatibility criteria in order to be used for our NLFF field extrapolations (the force-balance parameter ϵ_{force} and the torque-balance parameter ϵ_{torque} as defined in (2.42) and (2.43) in § 2.4.2.3, respectively). These criteria are sufficiently fulfilled only if $\epsilon_{\text{force}} \ll 1$ and $\epsilon_{\text{torque}} \ll 1$ which, obviously, is not true for the observed SFT-VM data (i.e., $\epsilon_{\text{force}} \not\ll 1$ and $\epsilon_{\text{torque}} \not\ll 1$; see third and fourth column of Table 3.1) and which therefore need to be preprocessed.

When applying our preprocessing routine we need to give respective weights to the individual modifications of the observed, photospheric SFT-VM vector magnetograms. Since Wiegelmann et al. (2006) successfully tested the application of the preprocessing routine to SFT-VM data, we keep the set of weighting parameters used in their study. That means that most weight is given to the force- and torque-balance condition (i.e., $\mu_1 = \mu_2 = 1.0$), that the allowance of the modified boundary conditions to deviate from the measured data is weighted with $\mu_3 = 0.001$ and that the applied smoothing is weighted with $\mu_4 = 0.01$. After applying the preprocessing routine, with this choice of parameters, to the SFT-VM data it can be seen that these modified boundary conditions now well fulfill the consistency criteria (i.e., $\epsilon_{\text{force}} \ll 1$ and $\epsilon_{\text{torque}} \ll 1$; see fifth and sixth column of Table 3.1) so that they can be consistently supplied as lower boundary conditions to the force-free extrapolation code.

3.2.2.4 Global magnetic energy budget

Using the observed SFT-VM vector magnetograms as input data for our analysis, applying the preprocessing routine and magnetic field extrapolation method (see § 2.4.1) gives us a set of potential and NLFF equilibria of the 3D configuration of coronal magnetic field above NOAA AR 10540.

For all four days we find that $E_m^{\text{NLFF}} > E_m^{\text{POT}}$ which means that the potential field contains less magnetic energy than the NLFF field (see third and fourth column of Table 3.2, respectively). The magnetic energy of the potential and NLFF field is slowly build up before the eruptive events and both are on the order of 10^{26} J. However, all the energies

Magnetic energies above NOAA AR 10540

Jan 2004		E_m [$\times 10^{26}$ *J*]			
Day	*Time* [*UT*]	E_m^{POT}	E_m^{NLFF}	$\Delta E_{\mathrm{POT}}^{\mathrm{NLFF}}$	$E_m^{\mathrm{NLFF}}/E_m^{\mathrm{POT}}$
18	01:58	0.80	1.18	0.37	1.46
19	05:35	1.19	1.94	0.71	1.57
20	03:40	1.27	2.20	0.87	1.66
21	00:40	0.86	1.26	0.38	1.42

Table 3.2: Magnetic Energies as calculated from the extrapolated 3D magnetic fields above NOAA AR 10540. E_m^{POT}represents the total magnetic energy of the potential field and E_m^{NLFF}that of the NLFF field. $\Delta E_{\mathrm{POT}}^{\mathrm{NLFF}} = E_m^{\mathrm{NLFF}} - E_m^{\mathrm{POT}}$ gives an upper limit for the free magnetic energy to be set free (see also Fig. 3.4). The ratio $E_m^{\mathrm{NLFF}}/E_m^{\mathrm{POT}}$ indicates the deviation of a NLFF field from a potential state and $E_m^{\mathrm{NLFF}}/E_m^{\mathrm{POT}} = 1.0$ would mean that no free magnetic energy is available to be released or that all of it has been released (see also Fig. 3.5).

go down remarkably after the M6.1 flare on Jan 20, whereas the M1.0 flare on Jan 19 does not seem to have a significant effect on the energy content of the coronal field (see Fig. 3.4). This impression may be due to the low time cadence of the available data (one vector magnetogram per day) as the influence of the M1.0 flare may simply not have been temporarily resolved. The excess energy of a force-free field over the corresponding potential field is an upper limit for the free magnetic energy available for dynamic processes that can be transformed into kinetic energy during flares or CMEs (see § 3.2.1). We find an upper limit for the energy to be set free on the order of $\Delta E_{\mathrm{POT}}^{\mathrm{NLFF}} \propto 10^{25}$ J for all days (see fifth column of Table 3.2), where the largest amount of free energy ($\Delta E_{\mathrm{POT}}^{\mathrm{NLFF}} \approx 8.7 \times 10^{25}$ J) is found before the occurrence of the M6.1 flare and which drops to $\Delta E_{\mathrm{POT}}^{\mathrm{NLFF}} \approx 3.8 \times 10^{25}$ J after it. We also estimated the ratio of the NLFF and potential field's energy content $E_m^{\mathrm{NLFF}}/E_m^{\mathrm{POT}}$ as a relative measure of the available free energy normalized to the potential field (see sixth column of Table 3.2 and Fig. 3.5). Again, we find an increasing trend before the time of the larger M6.1 flare. A maximum of $E_m^{\mathrm{NLFF}}/E_m^{\mathrm{POT}} = 1.66$ is reached before the flare and drops to $E_m^{\mathrm{NLFF}}/E_m^{\mathrm{POT}} = 1.42$ afterwards. In other words, the magnetic field configuration is farthest away from the potential configuration before the occurrence of the M6.1 flare and is closer to it after releasing free magnetic energy during the explosion. However, the magnetic field does not relax to the potential field configuration as this ratio does not reach unity, i.e. the whole amount of available magnetic energy is not set free during the M6.1 flare. This is what one would expect since the state of lowest energy a coronal magnetic field may relax to, given the constraint of helicity conservation, is a LFF field (for the formal proof and a detailed discussion of this so-called Taylor's relaxation theory see § 4.1.3.1). However, again the M1.0 flare does not seem to contribute to a relaxation of the NLFF field towards the potential configuration. In the period of the occurrence of this smaller flare magnetic flux was still emerging, suppressing the influence of the energy release even more during the M1.0 flare.

From a visual inspection of the magnetic field lines within the extrapolation volume, we recognize remarkable changes when comparing the magnetic field structure on the day before the M6.1 flare (which occurred on Jan 20 at 07:43 UT) with that on the day after (see Fig. 3.6). We find that the field lines seem to avoid to close over the central part of NOAA AR 10540 on the day before the flare, i.e. it seems that they avoid to close over

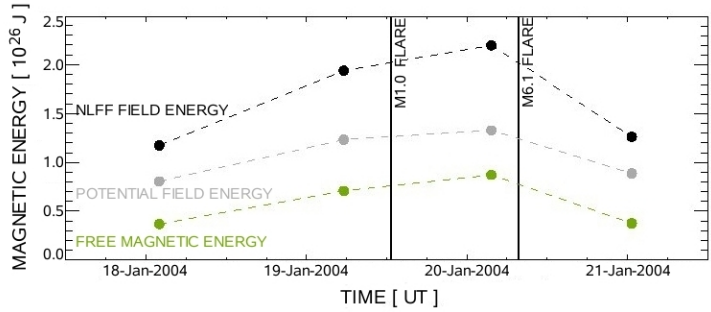

Figure 3.4: Magnetic energies of NOAA AR 10540. The total magnetic energy of the NLFF field, that of the potential field and an upper limit for the free magnetic energy is shown as the top black, middle gray and bottom green curve, respectively (see also Table 3.2). Black vertical lines indicate the two occurring M-class flares.

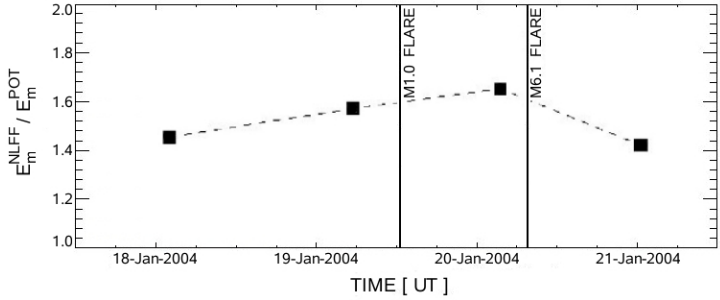

Figure 3.5: Relative energies of NOAA AR 10540, indicating how far the NLFF magnetic field is away from the potential configuration (see also Table 3.2). Black vertical lines indicate the two M-class flares.

the polarity inversion line (see panel (a) of Fig. 3.6). This, however, indicates that there are strong localized currents present and that the magnetic field is highly sheared along the inversion line. This most probably arises due to motions of the field lines footpoints in the photosphere so that they move away from a potential configuration in the period prior to a flare. The low time cadence of the data set (one magnetogram per day), however, does not allow us to follow any footpoint motions for this event and consequently no conclusions about their influence on the coronal energy content can be made. After the flare we recognize that the magnetic field configuration appears more relaxed (i.e., more potential-like) than that of the pre-flare state and the field lines appear to close also over the central area surrounding the inversion line (see panel (b) in Fig. 3.6).

Since flares and CMEs derive their energy from the energy stored locally in the magnetic field, Hudson (2000) stated the conjecture that a flare or a CME must originate in a

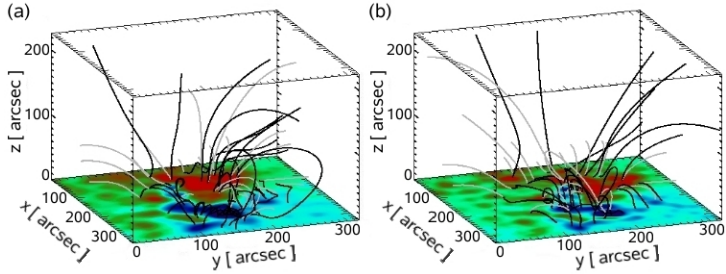

Figure 3.6: Magnetic field line configuration above NOAA AR 10540. Panels (a) and (b) show selected field lines on the day before and after the M6.1 flare (precisely, on Jan 20 at 03:40 UT and Jan 21 at 00:40 UT, respectively) which occurred on Jan 20 at 07:43 UT. Shown are calculated field lines of the potential and NLFF field as gray and black lines, respectively. The color-coded bottoms show the line-of-sight component of the preprocessed photospheric vector magnetograms used as boundary conditions for the extrapolation (see also panels (c) and (d) of Fig. 3.2 for the original SFT-VM data on those days). Units are arcseconds and, for improved visibility, the z-axis is drawn elongated.

magnetic implosion. The site of the implosion was suspected to show the location of pre-flare energy storage and its detection was presumed to be of high priority. Until the present time, however, such implosions had not yet been detected and thus it was assumed that they may occur in form of invisible large-scale flows or on non-observably small spatial scales. From the extrapolated 3D NLFF fields we are, however, able to calculate iso-surfaces (ISs) of equal absolute magnetic field strength and to compare those for the pre- and post-flare configurations. This enables us to show that in the meanwhile the detection and analysis of the coronal implosion scenario with the help of coronal magnetic field extrapolations has become possible. In particular, we computed the IS of $|\boldsymbol{B}_{\mathrm{NLFF}}| = 5\,\mathrm{mT}$, $|\boldsymbol{B}_{\mathrm{NLFF}}| = 10\,\mathrm{mT}$ and $|\boldsymbol{B}_{\mathrm{NLFF}}| = 20\,\mathrm{mT}$ (hereafter IS_5, IS_{10} and IS_{20}, respectively) for the configurations prior to and after the M6.1 flare. When comparing IS_5 before and after the flare we recognize a slightly more pronounced central dip after the flare although, on overall, the IS does not change considerably (see panels (a) and (b) of Fig. 3.7). The change of the IS_{10}, however, shows a higher decrease of the central dip (see panels (c) and (d) of Fig. 3.7) and the IS_{20} shows clear signatures of an implosion, i.e. much less absolute magnetic field strength of $|\boldsymbol{B}_{\mathrm{NLFF}}| = 20\,\mathrm{mT}$ is found after the occurrence of the flare (see panels (e) and (f) of Fig. 3.7).

3.2.2.5 Distribution of the energy density

According to Goff et al. (2007), the M6.1 flare event on Jan 20, 2004 showed a rising soft X-ray emission after 07:32 UT, peaking twice at around 07:37 UT and 07:43 UT, finally decaying until 08:00 UT and followed by the first appearance of a CME around 08:06 UT. A backward extrapolation of the CME projected distance-time profile led them to suggest a starting time between 07:10 UT and 07:25 UT, i.e. the CME had most probably been launched before the onset of the M6.1 flare. They also performed a LFF field extrapolation

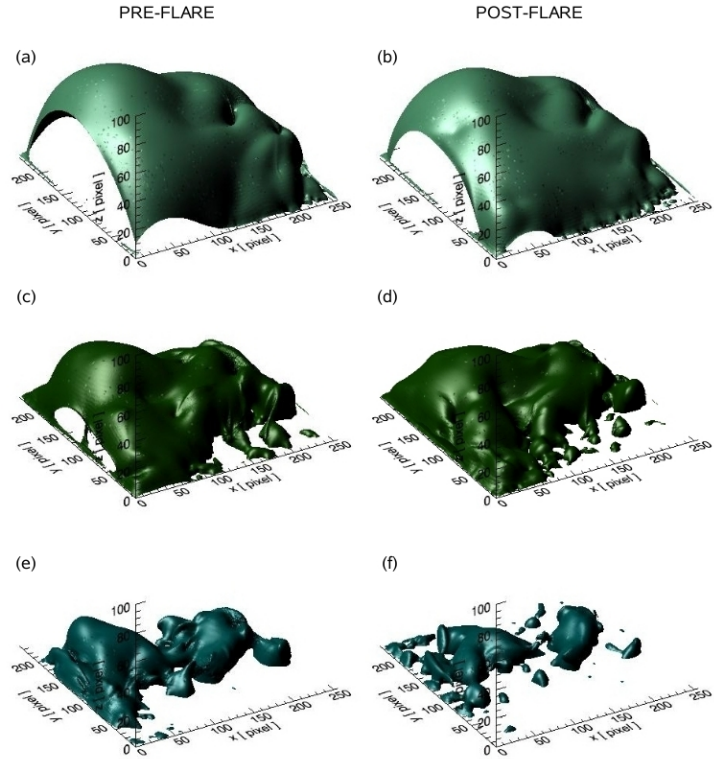

Figure 3.7: Iso-surfaces (ISs) of the absolute NLFF magnetic vector $|\boldsymbol{B}_{\mathrm{NLFF}}|$ in the pre- and post-flare periods (left and right columns, respectively), computed within the entire computational domain. The IS of $|\boldsymbol{B}_{\mathrm{NLFF}}| = 5\,\mathrm{mT}$ before and after the M6.1 flare on Jan 20, 2004 is shown in panels (a) and (b), respectively. The IS of $|\boldsymbol{B}_{\mathrm{NLFF}}| = 10\,\mathrm{mT}$ prior to and after the M6.1 flare is shown in panels (c) and (d), respectively and the IS of $|\boldsymbol{B}_{\mathrm{NLFF}}| = 20\,\mathrm{mT}$ of the pre- and post-eruptive magnetic field is shown in panels (e) and (f), respectively. Units are in pixels and one pixel corresponds to $1.32''$ on the Sun and, for improved visibility, the z-axis is drawn elongated.

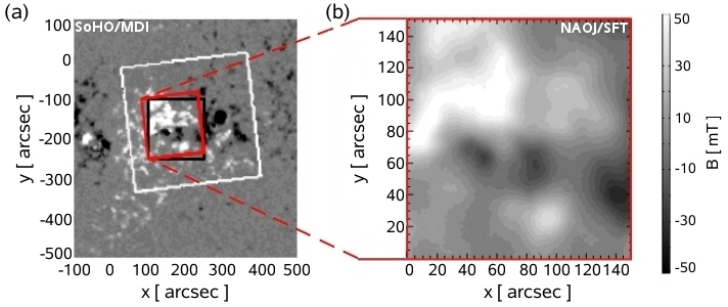

Figure 3.8: Selected subregion of the SFT-VM magnetograms due to the visibility of the flaring activity. Panel (a) shows a SoHO/MDI line-of-sight magnetogram of Jan 20, 2004 (units are arcseconds with respect to the solar disk center). The white square shows the SFT-VM field-of-view and the black outline shows the subfield containing the flaring activity visible in TRACE images as described by Goff et al. (2007). The corresponding subregion in the SFT-VM image is outlined in red and shown blown-up in panel (b) (units are arcseconds). The color bar gives the magnetic field strength in mT.

based on SoHO/MDI data to outline the coronal field configuration on Jan 20 and in the following we take a closer look at the temporal evolution of the energy density, related to the area of flaring activity as described in their study. Therefore, a subregion of the SFT-VM magnetograms was selected (see Fig. 3.8) due to the visibility of the flaring activity related to the M6.1 flare in TRACE images, as discussed by Goff et al. (2007). Based on this SFT-VM subfield, we extracted a subvolume of the 3D NLFF extrapolation domain of $\approx 150'' \times 150'' \times 75''$ (i.e., $\approx 108\,\mathrm{Mm} \times 108\,\mathrm{Mm} \times 54\,\mathrm{Mm}$) and estimated the integrated energy density e as a function of height using

$$e = \int_S u \, dx \, dy, \tag{3.3}$$

where $u = \boldsymbol{B}^2_{\mathrm{NLFF}}/(2\,\mu_0)$ represents the energy density and S denotes the xy-plane at each height z. Along with this, also the change in the energy density Δu was calculated according to

$$\Delta u = u_{i+1} - u_i, \tag{3.4}$$

where u_i denotes the energy density of the previous and u_{i+1} that of the following day. In this way we can get an insight how energy gains or losses are distributed in the coronal volume above the flaring region.

First, we integrated the energy density with the help of (3.3) and displayed it as a function of height above the photosphere in the subvolume (see Fig. 3.9). One recognizes, that highest energy densities appear on Jan 19 and Jan 20 (denoted as e_{19} and e_{20} in Fig. 3.9, respectively). As expected, it seems that the main energy storage takes place before the occurrence of the M6.1 flare on Jan 20 (i.e., $e_{19} \gtrsim e_{21}$ and $e_{20} \gtrsim e_{21}$, where e_{21} represents the integrated energy density on Jan 21) and after this flare was launched, the amount of stored energy goes down remarkably. Besides this, the energy density on

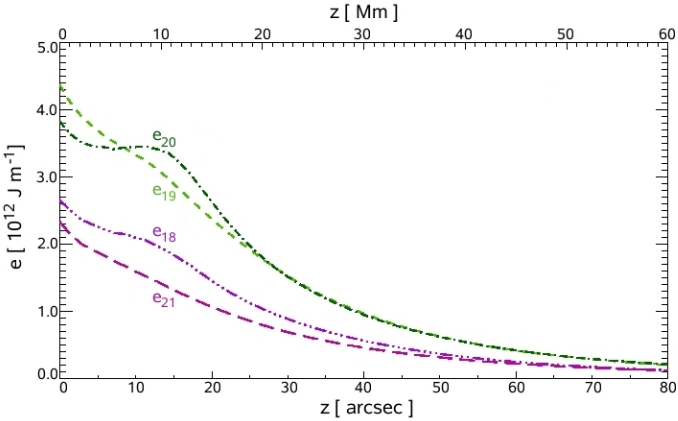

Figure 3.9: Integrated energy density as a function of height in the subvolume for the consecutive days. In particular, e_{18} (violet dashed-triple-dotted line), e_{19} (light green dashed line), e_{20} (dark green dashed-dotted line) and e_{21} (purple long-dashed line) represent the integrated energy density as calculated for the subvolume of Jan 18, Jan 19, Jan 20 and Jan 21, respectively. The lower and upper horizontal axis give the height above the solar photosphere in arcseconds and Mm, respectively.

Jan 18 is higher than on Jan 21 (i.e., $e_{18} \gtrsim e_{21}$, where e_{18} denotes the integrated energy density on Jan 18) as well, meaning that also on the first of the considered days the amount of stored energy is higher than after the M6.1 flare which occurred on the former last day of the data set. Nevertheless, not as much energy is available on Jan 18 to power an explosive event as is on Jan 19 and Jan 20 (i.e., $e_{18} \lesssim e_{19}$ and $e_{18} \lesssim e_{20}$). Especially at the height of $\approx 10'' - 20''$ (i.e., ≈ 7 Mm – 14 Mm) even more energy was stored on Jan 20 than on Jan 19 ($e_{19} < e_{20}$).

Second, we investigated the change of the integrated energy density as a function of height within the subvolume by simply calculating $\Delta e_1 = e_{19} - e_{18}$, $\Delta e_2 = e_{20} - e_{19}$ and $\Delta e_3 = e_{21} - e_{20}$ (see Fig. 3.10). One can see that Δe_1 and Δe_2 are mainly positive (i.e., $e_{18} < e_{19}$ and $e_{19} < e_{20}$, respectively) except that Δe_2 is negative at very low heights of $\lesssim 8''$ (i.e. below ≈ 16 Mm) above the photosphere, whereas Δe_3 is found to be mainly negative (i.e., $e_{20} > e_{21}$). Clearly, as visible in Fig. 3.9 and Fig. 3.10, the absolute values of the integrated energy density decrease with increasing height. However, it cannot be concluded without some doubt that the temporal evolution of the integrated energy density is purely a consequence of the flaring activity since until Jan 20 magnetic flux was still emerging in AR 10540. Finally, in Fig. 3.11 we display the total magnetic energy content calculated from the NLFF field together with the change in the energy density in the extracted subvolumes using (3.4). As found from Fig. 3.10 for the integrated energy densities Δe_1 and Δe_2, we find in panel (a) and (b) of Fig. 3.11 that Δu_1 and Δu_2 are predominantly positive, respectively, especially above a height of $\approx 35''$ (i.e., ≈ 25 Mm). The mainly positive values of Δu_1 and Δu_2 mean that the amount of stored energy in the

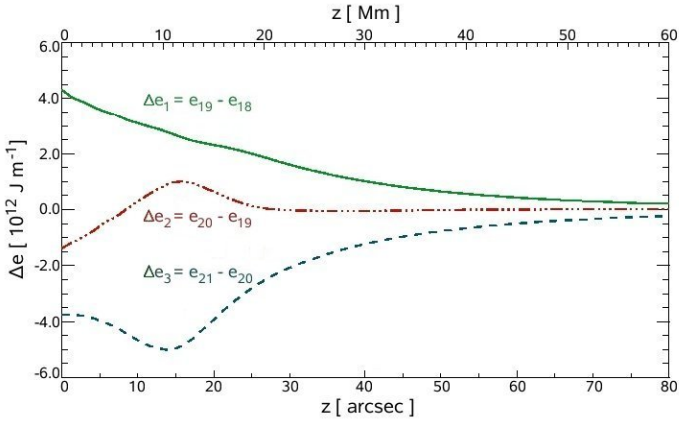

Figure 3.10: Change of the integrated energy density as a function of height in the subvolumes. The change of the integrated energy density between Jan 18 and Jan 19 ($\Delta e_1 = e_{19} - e_{18}$), between Jan 19 and Jan 20 ($\Delta e_2 = e_{20} - e_{19}$) and between Jan 20 and Jan 21 ($\Delta e_3 = e_{21} - e_{20}$) is represented by the green solid, red dashed-triple-dotted and blue dashed line, respectively. The lower and upper horizontal axis give the height above the solar photosphere in arcseconds and Mm, respectively.

considered volume increased until Jan 20 (i.e., $u_{18} \lesssim u_{19}$ and $u_{19} \lesssim u_{20}$). This might be due to the changing magnetic field configuration during the evolution of the upcoming flaring activity. One also finds some small areas of $\Delta u_1 < 0$ (i.e., $u_{18} > u_{19}$) in panel (a), especially below $\approx 15''$ (i.e., ≈ 11 Mm), which are continuously decreasing in size with increasing height. In small parts some magnetic energy seems to be moved around, e.g. by flows corresponding to slow surface motions, or even to be related to the weak C-class flaring on Jan 18. This might also be the reason for the absence of a strong gradient in Δe_1 in Fig. 3.10, showing the change in the integrated energy density as purely positive. However, these small regions of $\Delta u_1 < 0$ as visible in panel (a) of Fig. 3.11 appear in general to be of a positive value in panel (b), i.e. energy was now also stored at low heights so that $\Delta u_2 > 0$. One should notice that the major increase in the energy storage now seems to take place in regions that appeared highly negative in panel (a) which might be related to the flare ribbons as visible in the Hα images described by Goff et al. (2007). Again, the main activity takes place at low heights of $\lesssim 20''$ (i.e., $\lesssim 14$ Mm) above the photosphere but the location of the energy loss (as indicated by the negative values of Δe_2 in Fig. 3.10) cannot be defined clearly. In panel (c) of Fig. 3.11 the change in the energy density appears mostly negative ($\Delta u_3 < 0$, i.e. $u_{20} > u_{21}$ and in agreement with the purely negative values of Δe_3 in Fig. 3.10) which means that the energy density on Jan 21 was lower than on Jan 20. In other words, a considerable amount of energy was released during the M6.1 flare on Jan 20. This might have taken place in the form of converting magnetic energy into other forms of energy by means of, e.g., magnetic reconnection. As found for the previous days, the changes in the amount of stored energy in the considered subvolume take place predominately within a height of $\approx 30''$ (i.e., ≈ 22 Mm) above the photosphere.

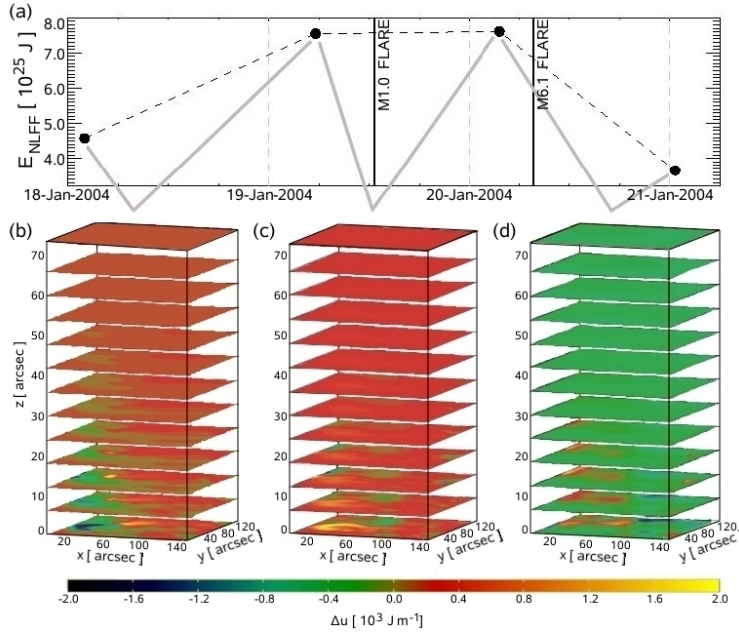

Figure 3.11: Total magnetic energy and change of the energy density within the considered subvolumes. Panel (a) shows the total magnetic energy E_m^{NLFF} of the NLFF field. In the lower three panels the change of the energy density between consecutive days is displayed. The change of the energy density between Jan 18 and Jan 19 ($\Delta u_1 = u_{19} - u_{18}$), between Jan 19 and Jan 20 ($\Delta u_2 = u_{20} - u_{19}$) and between Jan 20 and Jan 21 ($\Delta u_3 = u_{21} - u_{20}$) are shown color-coded in panels (b), (c) and (d), respectively. Units are arcseconds and, for better visibility, the z-axis is drawn elongated.

Also for these subvolumes, we computed the iso-surfaces (ISs) of $|\boldsymbol{B}_{\mathrm{NLFF}}| = 10\,\mathrm{mT}$ and $|\boldsymbol{B}_{\mathrm{NLFF}}| = 20\,\mathrm{mT}$ (hereafter IS_{10} and IS_{20}, respectively) for the configurations prior to and after the M6.1 flare (see Fig. 3.12). Both IS_{10} and IS_{20} show a considerable change and, in particular, IS_{20} indicates the occurrence of a coronal implosion as suggested by Hudson (2000). Recently, Liu et al. (2009) provided observational evidence for the implosion scenario by reporting, for the first time, a contraction of large-scale coronal loops (overlying the flaring AR NOAA 10792 which was associated with a C8.9 flare on July 30, 2005) together with a contraction of an underlying flare loop. The contraction of the overlying coronal loops was interpreted as a manifestation of the release of the free magnetic energy and the consequent decrease of the magnetic pressure in the flaring region. In a further study, Liu and Wang (2009) presented observations of a coronal loop contraction in the wake of a filament eruption which occurred in NOAA AR 9502 on June 15, 2001 in association with an M6-class flare. They suggested that the escape of the filament resulted in the contraction of the overlying coronal loops which can be interpreted as a variant of a coronal implosion.

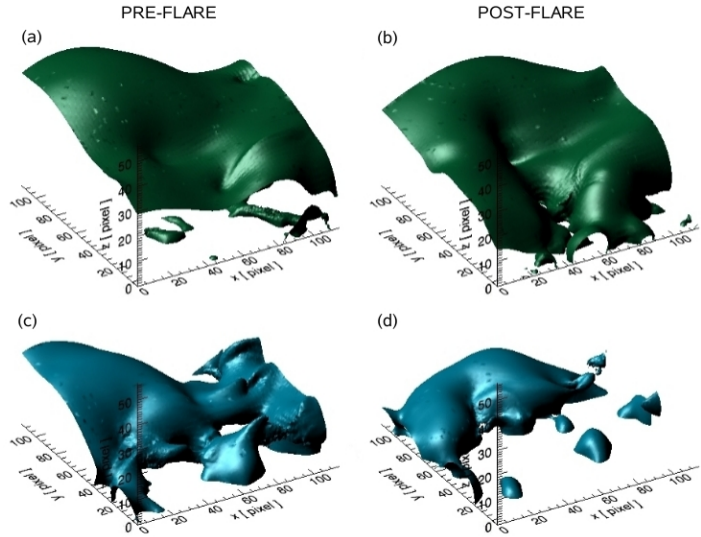

Figure 3.12: Iso-surfaces of equal absolute magnetic field strength in the pre- and post-flare periods computed within the flaring subvolume. The iso-surface for $|\boldsymbol{B}_{\mathrm{NLFF}}| = 10\,\mathrm{mT}$ before and after the M6.1 flare on Jan 20, 2004 is shown in panels (a) and (b), respectively. The iso-surface for $|\boldsymbol{B}_{\mathrm{NLFF}}| = 20\,\mathrm{mT}$ prior to and after the M6.1 flare is shown in panels (c) and (d), respectively. Units are pixels and one pixel corresponds to $1.32''$ on the Sun and, for improved visibility, the z-axis is drawn elongated.

3.2.2.6 Discussion

We investigated the 3D coronal magnetic field configuration related to the flaring activity of NOAA AR 10540 from Jan 18 to Jan 21, 2004. By using a multigrid-like optimization code, we extrapolated the coronal field from photospheric magnetic field measurements as obtained from the SFT-VM. We calculated the energy content of the extrapolated domain for the four consecutive days and estimated the upper limit for the free magnetic energy available to power two M-class flares recorded during this time period (an M1.0 flare on Jan 19 and an M6.1 flare on Jan 20).

We found that the total magnetic energy increased before the M6.1 flare on Jan 20 and decreased afterwards. Before as well as after the flaring activity, the total magnetic energy of the calculated NLFF field was found to be $\propto 10^{26}$ J, which was also true for the potential field. The expectation that the NLFF field energy exceeds that of the potential field could be clearly recovered. Besides this, the drop of the NLFF field's energy was higher than that of the potential field, i.e. the energy release seemed to be related to the change in the transversal magnetic field rather than the normal component of it. This supports the hypothesis that the flare energy was taken from the coronal magnetic field where it had been slowly built up and stored prior to the flare onset. The upper limit of the

free magnetic energy available to be set free was estimated as $\propto 10^{25}$ J which, according to Priest and Forbes (2002), is enough to power a large flare. The first occurring smaller M1.0 flare did not seem to have much influence on the magnetic energy content of the coronal field above NOAA AR 10540. This might be due to the low time cadence of the photospheric vector magnetograph data we used since this smaller event may not have been sufficiently resolved in time. Moreover, magnetic flux was still emerging at this time, additionally reducing any observable effect of the smaller flare. The comparison of the NLFF field and the potential field showed that the ratio of its energy content went down remarkably after the M6.1 flare but did not seem to be responsive to the M1.0 flare. Moreover, the field was not found to relax to the potential configuration since this ratio did not reach unity after the M6.1 flare. This means that not the whole amount of available free magnetic energy was released during this flare.

From a visual inspection of the magnetic field lines within the extrapolation volume, we recognized that the field lines seem to avoid to close over the central part of NOAA AR 10540 on the day before the flare, indicating the presence of strong localized currents. After the flare the magnetic field configuration appeared more potential-like and the field lines also closed over the central area containing the polarity inversion line.

We also investigated the evolution of the integrated energy density with height to be able to restrict the area in which the energy changes due to the flaring activity mainly took place. We found that the major changes in the considered subvolume above the flaring region were restricted to a height of $\lesssim 30''$, i.e. $\lesssim 22$ Mm above the photosphere, varying slightly for the consecutive days. This supports the finding of Jing et al. (2008) who analyzed in detail the height distribution of the magnetic shear in NOAA AR 10930, associated with an X3.4 flare on Dec 13, 2006. They found that the energy release process likely happened at altitudes between 8 Mm and 70 Mm above the photosphere. We also found that the integrated energy density as a function of height was lowest on Jan 21 which can be interpreted such that, since the M6.1 flare had already been launched, previously built-up magnetic energy was released. On all other days, we found a clearly higher amount of energy storage that can be assigned to the change of the magnetic field configuration leading to the upcoming flaring activity, including continuous flux emergence until Jan 20. The change in the integrated energy density showed us that the absolute values of the integrated energy density decreased with increasing height. However, it cannot be stated that its relative values could be purely assigned to the flaring activity since magnetic flux was still emerging until Jan 20. Only the difference in the integrated energy density of the last two days turned out to be purely negative, which also can be attributed to the release of free energy during the M6.1 flare. This was also seen from investigating the change in the energy density itself which appeared to be predominantly negative within the considered subvolume only after the M6.1 flare. Last, the computation of iso-surfaces of the absolute magnetic field magnitude seems to support a proposed implosion scenario during transient coronal events like flares and CMEs (Hudson 2000) which has recently been approved observationally (Liu et al. 2009, Liu and Wang 2009).

The sequence of NLFF equilibria used here has a rather low time cadence of one day. The trend that magnetic energy is quasistatically built up before a flare is, nevertheless, clearly visible. Though noticing a decrease in the energy due to the M6.1 flare, the low time cadence does not allow us to decide which part of this energy drop was related to the sudden release of magnetic energy or to the simultaneous decay of NOAA AR 10540.

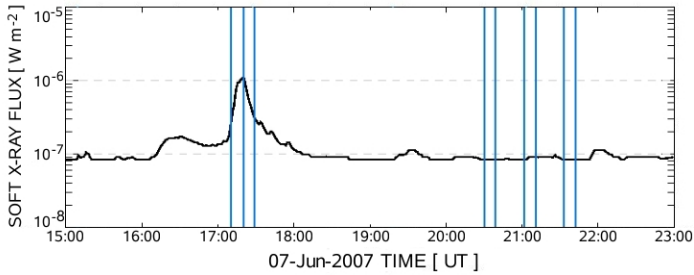

Figure 3.13: GOES solar soft X-ray flux on June 7, 2007, integrated in the wavelength range of 0.1 nm – 0.8 nm. Blue vertical lines indicate when SOLIS-VSM data was available to use.

3.2.3 NOAA AR 10960

3.2.3.1 Flare activity

According to the weekly bulletin of the SIDC/SWAPP, the solar activity during the week of June 4, 2007 was dominated by NOAA AR 10960. An M8.9 flare occurred on June 4 and an M1.0 flare fired off on June 9 (for the solar flare classification according to the measured peak intensity of the solar soft X-ray flux see § 1.1.3.1). Furthermore, 12 C-class flares (corresponding to a measured soft X-ray flux between 10^{-6} Wm^{-2} and 10^{-5} Wm^{-2}) were detected during this week and originated in this group or from its vicinity. The peaks in the measured solar soft X-ray flux indicated only one C1.0 flare on June 7, peaking at 17:20 UT, which is of interest for the present study (see Fig. 3.13 for the GOES solar soft X-ray flux on June 7, 2007).

3.2.3.2 NSO/SOLIS Vector Spectro-Magnetograph

The NSO/SOLIS Vector Spectro-Magnetograph (hereafter SOLIS-VSM) has provided magnetic field observations of the Sun almost continuously since Aug 2003. The instrument is designed to measure the magnetic field vector everywhere on the solar disk using the Fe I 630.2 nm spectral line (Keller et al. 2003b, Henney et al. 2006). In addition, longitudinal magnetic field measurements in the photosphere (using the Fe I 630.15 nm and 630.25 nm spectral lines) and chromosphere (using the Ca II 854.2 nm spectral line) are performed on a daily basis. Quick-look data (JPEG images and FITS files) of the magnetic field vector in and around automatically selected ARs (Georgoulis et al. 2008) are available on-line to the community. The Quick-look data provide estimates of the magnetic field strength, inclination and azimuth which should, because of the high field strength in ARs, be comparable to fully inverted data (which are acquired only once within 24 hours) only differing by a few percent (for details see Henney et al. 2006). The noise level of the resulting longitudinal and transverse field strengths is about 0.1 mT and 5 mT, respectively. The azimuth 180°-ambiguity is solved using the Nonpotential magnetic Field Calculation method (NPFC; Georgoulis 2005) which does not introduce any error in the azimuth or any other quantities. Since, only if the vertical electric current

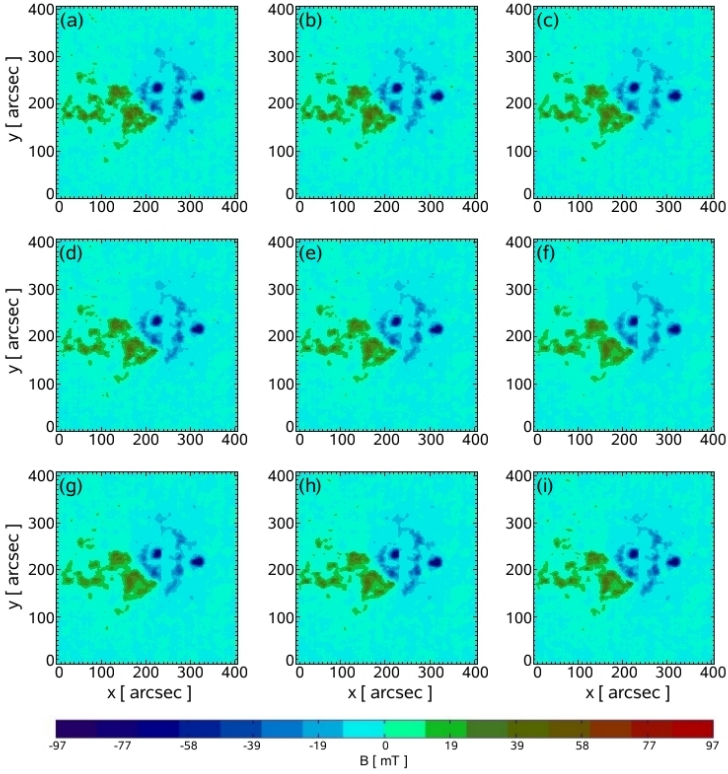

Figure 3.14: Longitudinal photospheric magnetic field component ($\boldsymbol{B}_z$) of the available SOLIS-VSM vector magnetograms on June 07, 2007. In panels (a), (b), (c), (d), (e), (f), (g), (h) and (i) $\boldsymbol{B}_z$ at 17:10 UT, at 17:20 UT, 17:29 UT, 20:30 UT, 20:39 UT, 21:02 UT, 21:11 UT, 21:33 UT and 21:42 UT is shown, respectively. Units are arcseconds and the color bar indicates the magnetic field strength in mT.

density is known a priori, the resolution of the 180°-ambiguity would be a numerically fully determined problem, a minimum-magnitude current density solution is explicitly imposed. Otherwise, the NPFC disambiguation is assumption-free so that the quality of the results depends on the quality of the measurements. The NPFC method first infers the non-potential magnetic field component responsible for the assumed vertical currents and then determines the vertical magnetic field whose potential extrapolation added to the non-potential field best reproduces the observationally inferred horizontal magnetic field.

In the presented study we investigated NOAA AR 10960 during a time period of about five hours on June 7, 2007 at locations that are far enough from the solar limb. In the time period around a C1.0 flare on June 7, three SOLIS-VSM vector magnetograms with a

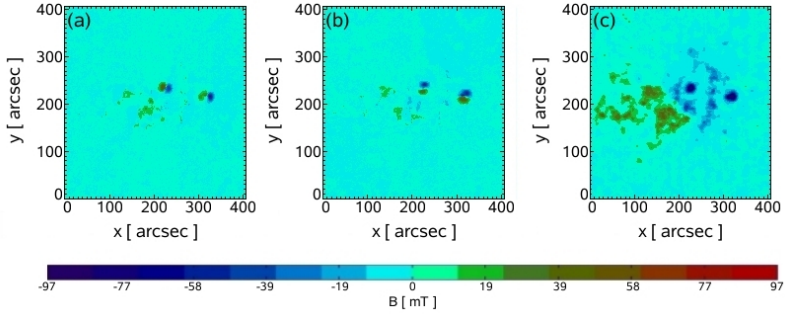

Figure 3.15: Transverse ($\boldsymbol{B}_x$, $\boldsymbol{B}_y$) and longitudinal ($\boldsymbol{B}_z$) photospheric magnetic field components of the available SOLIS-VSM vector magnetogram on June 07, 2007 at 17:10 UT. Panels (a), (b) and (c) show $\boldsymbol{B}_x$, $\boldsymbol{B}_y$ and $\boldsymbol{B}_z$, respectively. Units are arcseconds and the color bar gives the magnetic field strength in mT.

pixel size of $\approx 1.133''$ were available to use. One in the rising phase of the emission, one at the time when the flare peaked and one in its decaying phase (at 17:10 UT, 17:20 UT and 17:29 UT, respectively). We display the corresponding longitudinal magnetic field components of the SOLIS-VSM magnetograms in panels (a), (b) and (c) of Fig. 3.14, respectively. All other magnetic field measurements on June 7, 2007 (between 20:30 UT and 21:42 UT) allowed us to investigate the magnetic field during a period of low solar activity (the corresponding longitudinal magnetic field components are displayed in panels (d) – (i) of Fig. 3.14). The SOLIS-VSM vector magnetograms cover a region of $\approx 400'' \times 400''$, i.e. $\approx 287\,\mathrm{Mm} \times 287\,\mathrm{Mm}$ and we display the $x-$, $y-$ and $z-$ component of the photospheric vector magnetic field on June 7 at 17:10 UT in panels (a), (b) and (c) of Fig. 3.15, respectively.

3.2.3.3 Preprocessing of SOLIS-VSM data

In order to achieve consistency of the observed vector magnetograms with the assumption of a force-free field the SOLIS-VSM data need to be preprocessed (see § 2.4.2). The dimensionless force- and torque-balance parameter $\epsilon_{\mathrm{torque}}$ (as defined in (2.42) and (2.43), respectively, in § 2.4.2.3) quantify if the observed, photospheric SOLIS-VSM magnetograms suffice the criteria to be used for our NLFF field extrapolation. These criteria are sufficiently fulfilled only if $\epsilon_{\mathrm{force}} \ll 1$ and $\epsilon_{\mathrm{torque}} \ll 1$ (ideally, $\epsilon_{\mathrm{force}} = 0$ and $\epsilon_{\mathrm{torque}} = 0$) which, obviously, is not true for the observed SOLIS-VSM vector magnetograms (i.e., $\epsilon_{\mathrm{force}} \not\ll 1$ and $\epsilon_{\mathrm{torque}} \not\ll 1$; see second and third column of Table 3.3) and which therefore need to be preprocessed.

When applying our preprocessing routine we need to give particular weights to the individual modifications of the observed, photospheric SOLIS-VSM vector magnetograms. To repeat, the force- and torque-free condition are weighted with $\mu_1 = \mu_2 = \mu_{12}$, the allowance of the modified boundary conditions to deviate from the measured data is weighted with μ_3 and the applied smoothing is weighted with μ_4. Since within this work,

Force-free consistency of the raw and preprocessed SOLIS-VSM data

June 7, 2007	*Raw data*		*Preprocessed data*	
Time [UT]	ϵ_{force}	ϵ_{torque}	ϵ_{force}	ϵ_{torque}
17:10	0.6352	0.6884	0.0001	0.0002
17:20	0.6372	0.6902	0.0001	0.0002
17:29	0.6400	0.6691	0.0019	0.0033
20:30	0.6490	0.7202	0.0002	0.0015
20:39	0.6606	0.7327	0.0050	0.0069
21:02	0.6453	0.7555	0.0007	0.0011
21:11	0.6775	0.7604	0.0001	0.0004
21:33	0.6298	0.6957	0.0002	0.0003
21:42	0.6277	0.7111	0.0001	0.0003

Table 3.3: Dimensionless force-balance parameter (ϵ_{force}) and the torque-balance parameter (ϵ_{torque}) to quantify the consistency of the observed ("Raw data") and the preprocessed photospheric SOLIS-VSM vector magnetograms with the force-free assumption.

our preprocessing routine has been applied for the first time to SOLIS-VSM data, the optimum combination of these weighting parameters had to be determined first. Since, after minimizing, the final value of our preprocessing functional (2.44) in § 2.4.2.3 might not directly relate to the relative success of the later extrapolation, we decided to seek the optimum preprocessing parameter set while immediately testing the evolution of the associated extrapolation functional. In other words, we run the preprocessing method for a certain combination of $\mu_1 - \mu_4$ and also perform the corresponding extrapolation. For this purpose, i.e. to test the relative performance of the preprocessing, it is not necessary to extrapolate the magnetic field in the entire volume. This is because one can assume that the coronal magnetic field is potential-like at least at heights above $\approx 100''$ (i.e., $\approx 70\,\text{Mm}$). Therefore, we extrapolated the coronal field only up to a height of $\approx 136''$ (i.e., $\approx 98\,\text{Mm}$) which is slightly less than 50% of the height of the final full resolution computational domain. Repeating this procedure for more than 100 combinations of $\mu_1 - \mu_4$, we found the optimum combination as follows. Most weight is given to the force- and torque-balance condition ($\mu_{12} = 1.0$). The allowance of the modified boundary conditions to deviate from the measured data is weighted with $\mu_3 = 10^{-4}$ and the applied smoothing is weighted with $\mu_4 = 1.0$. After applying the preprocessing routine, with this set of parameters, to the SOLIS-VSM data it can be seen that these modified boundary conditions now fulfill the consistency criteria (i.e., $\epsilon_{\text{force}} \ll 1$ and $\epsilon_{\text{torque}} \ll 1$; see fourth and fifth column of Table 3.3) so that they can be consistently supplied to the force-free extrapolation code.

3.2.3.4 Global magnetic energy budget

For all 3D magnetic field configurations considered for NOAA AR 10960, we found that the energy of the extrapolated NLFF field exceeded that of the potential field ($E_m^{\text{NLFF}} > E_m^{\text{POT}}$), both being $\propto 10^{25}\,\text{J}$ (see second and third column of Table 3.4). This was also the case when considering a relative error in the energy estimation of about 0.4% for the potential field (i.e., $E_m^{\text{POT}} \pm 1.2 \times 10^{23}\,\text{J}$) and 1% for the NLFF field (i.e., $E_m^{\text{NLFF}} \pm 3.1 \times 10^{23}\,\text{J}$). Furthermore, the available free magnetic energy was found to be

Magnetic energies above NOAA AR 10960

June 7, 2007	E_m [$\times 10^{25}$ J]			
Time [UT]	E_m^{POT}	E_m^{NLFF}	$\Delta E_{\mathrm{POT}}^{\mathrm{NLFF}}$	$E_m^{\mathrm{NLFF}}/E_m^{\mathrm{POT}}$
17:10	3.130	3.282	0.152	1.049
17:20	3.122	3.272	0.149	1.048
17:29	2.986	3.081	0.095	1.032
20:30	3.024	3.042	0.018	1.006
20:39	3.031	3.127	0.095	1.031
21:02	2.969	3.084	0.116	1.039
21:11	2.938	3.028	0.090	1.031
21:33	2.939	3.125	0.185	1.063
21:42	2.933	3.085	0.152	1.052

Table 3.4: Magnetic Energies as calculated from the extrapolated 3D magnetic fields above NOAA AR 10960. $E_m^{\mathrm{POT}}$and E_m^{NLFF}represent the total magnetic energy of the potential and the NLFF field, respectively. $\Delta E_{\mathrm{POT}}^{\mathrm{NLFF}} = E_m^{\mathrm{NLFF}} - E_m^{\mathrm{POT}}$ gives an upper limit for the free magnetic energy to be set free (see also Fig. 3.16). The ratio $E_m^{\mathrm{NLFF}}/E_m^{\mathrm{POT}}$ indicates the deviation of a NLFF field from a potential state.

10^{23} J $\lesssim \Delta E_{\mathrm{POT}}^{\mathrm{NLFF}} \lesssim 10^{24}$ J (see fourth column of Table 3.4) for which we found a relative error of about 14% (i.e., $\Delta E_{\mathrm{POT}}^{\mathrm{NLFF}} \pm 1.6 \times 10^{23}$ J; for the estimation of the relative error of the calculated energy values see § 3.2.3.5). However, both $E_m^{\mathrm{POT}}$and E_m^{NLFF}were highest in the phase of increasing emission of the C1.0 flare. During the 20 minute time period of the flare (from 17:10 UT to 17:29 UT) the total magnetic energy decreased by $\approx 6\%$ and $\approx 38\%$ of the available free magnetic energy was released (see Fig. 3.16). Although the flare was already declining in intensity at 17:29 UT it still showed a soft X-ray flux of above background B-level (see Fig. 3.13). The next vector magnetogram snapshot was acquired only 3 hours later at 20:30 UT and the free magnetic energy had decreased further, such that $\approx 88.16\%$ of the original amount of free energy had been released. At 20:30 UT, the free magnetic energy was only $\approx 0.6\%$ of the total magnetic energy and consequently the magnetic field was almost potential (see fourth column of Table 3.4). Additionally, we estimated the ratio of the NLFF and potential field's energy content $E_m^{\mathrm{NLFF}}/E_m^{\mathrm{POT}}$ as a relative measure of the available free energy normalized to the potential field (see last column in Table 3.4). This ratio was found to be higher before the C1.0 flare than after it. A minimum of $E_m^{\mathrm{NLFF}}/E_m^{\mathrm{POT}} = 1.006$ was reached at the beginning of a very quiet period around 20:30 UT and increased again afterwards. This can be interpreted as the new accumulation of magnetic energy within the coronal volume. The magnetic field configuration was found to be farthest away from the potential configuration at the end of the investigated sequence. However, the magnetic field did not relax to the potential field configuration (i.e. $E_m^{\mathrm{NLFF}}/E_m^{\mathrm{POT}} \neq 1.0$) which means that not the whole amount of available magnetic energy was set free during the C1.0 flare and, similar to the analysis of the corresponding parameters of NOAA AR 10540, supports the theory that the state of lowest energy a coronal magnetic field may relax to is a LFF field. From Fig. 3.13, we can see that AR10960 showed only background B-level activity (i.e. a measured solar soft X-ray emission $< 10^{-7}$ Wm^{-2}) after around 18:00 UT and almost the entire free magnetic energy may have been released by that time. Unfortunately, no vector magnetograph data was

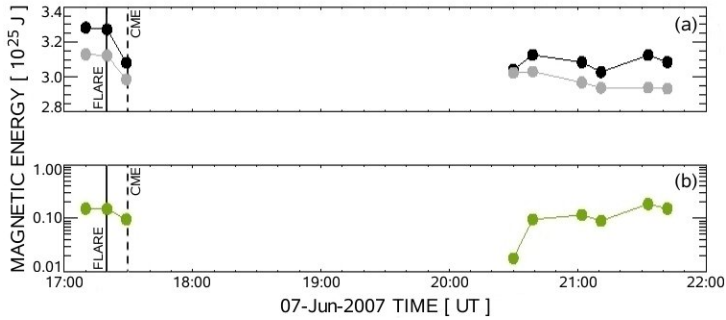

Figure 3.16: Magnetic energies of NOAA AR 10960. Panel (a) shows the total magnetic energy of the NLFF field (black filled circles) and that of the potential field (gray filled circles). Panel (b) shows the upper limit for the free magnetic energy (green filled circles) on a logarithmic scale (see also Table 3.4). Black vertical solid and dashed lines indicate the recorded C1.0 flare and CME, respectively.

available immediately after the declining phase of the C1.0 flare and consequently we were unable to confirm this supposition by analyzing the coronal magnetic field at that time. However, for AR 10960, the maximum excess energy of the NLFF field over the potential field was about 5% during the investigated period. Since this so-called free magnetic energy is thought to represent an upper limit to the available energy to drive eruptive phenomena, consequently only a small C1.0 flare was recorded. No further flares occurred between 20:30 UT and 21:42 UT for which SOLIS-VSM data was available but five C-class flares were recorded about 3 hours later on June 8, 2007 between 01:00 UT and 16:00 UT. However, a significant amount of free magnetic energy accumulated again during the quiet period after 20:30 UT (see fourth column of Table 3.4 and panel (b) of Fig. 3.16) so that the energy content of the coronal magnetic field increased and became, with some fluctuations, comparable to that before the C1.0 flare had occurred.

From a visual inspection of the magnetic field lines within the extrapolation volume, we recognize some changes in the overall magnetic field structure during the C1.0 flare (see Fig. 3.17). We find that the field lines show, on average, their highest vertical extent when the C1.0 flare peaked at 17:20 UT (see panel (b) of Fig. 3.17). Ten minutes earlier, in the increasing phase of the flare, a comparable field structure was found but with a slightly lower vertical extent (see panel (a) of Fig. 3.17). In the declining phase of the flare (nine minutes after the flare peaked) the field line configuration reached its, on average, lowest vertical extent (see panel (c) of Fig. 3.17). However, at 20:30 UT which corresponds to the field configuration of the lowest energy content, the field clearly appears to have restructured showing an even more potential-like topology (see panel (d) of Fig. 3.17).

3.2.3.5 Uncertainty of the magnetic energy estimation

We tested the influence of the noise in the photospheric vector magnetograms to be able to give an estimate of the error in the resulting magnetic energy calculations. Therefore,

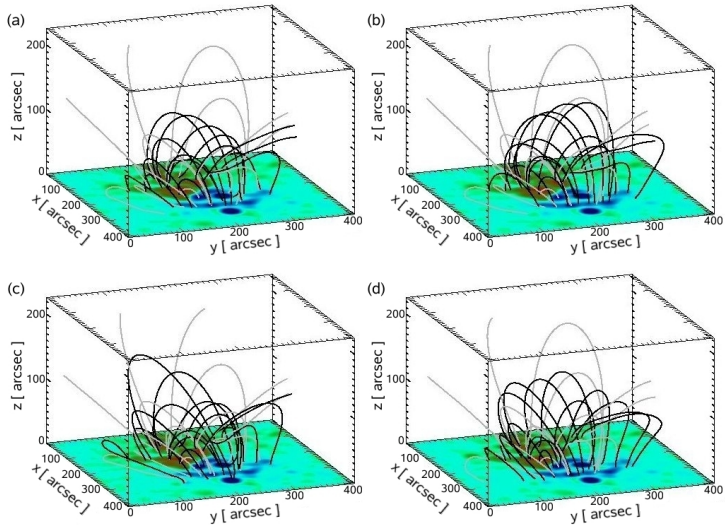

Figure 3.17: Magnetic field line configuration above NOAA AR 10960. Panels (a), (b) and (c) show selected field lines during the C1.0 flare on June 07 at 17:10 UT, 17:20 UT and 17:29 UT, respectively. Panel (d) shows the minimum energy configuration at 21:11 UT. Shown are calculated field lines of the potential and NLFF field as gray and black lines, respectively. The color-coded bottoms show the line-of-sight component of the preprocessed SOLIS-VSM vector magnetograms used as boundary conditions for the extrapolation (see also panels (a), (b), (c) and (g) of Fig. 3.14 for the original SOLIS-VSM data). Units are arcseconds and the z-axis is drawn elongated.

we created noise models, containing normally-distributed, pseudo-random numbers with a mean of zero and a standard deviation of one. To reflect that the longitudinal magnetic field component is, in general, measured with higher accuracy than the transversal ones, we defined the noise models in a way that we added more noise to the transversal components than to the longitudinal component (see columns two to six in Table 3.5 and Fig. 3.18). To repeat, the accuracy of the SOLIS-VSM measurements is about 0.1 mT and 5 mT for the longitudinal and transverse field, respectively. In total we created eight noise models (see Table 3.5) which we added on the original SOLIS-VSM data at 17:10 UT (as shown for noise model no. 2 in Fig. 3.19). After applying the preprocessing and extrapolation methods to this new, noisy vector magnetograms we calculated the energy content of the extrapolated 3D force-free fields and compared it with that of the field as calculated from the SOLIS-VSM vector magnetogram of June 07, 2007 at 17:10 UT without any artificial noise added on it (called noise model no. 0 in Table 3.5).

From the analyzed nine cases, the resulting accuracy of the 3D potential field energy was found to be $E_m^{\mathrm{POT}} = 3.128 \pm 0.013 \times 10^{25}$ J. For the precision of the NLFF field energy we revealed $E_m^{\mathrm{NLFF}} = 3.317 \pm 0.032 \times 10^{25}$ J and for the upper limit of the free magnetic energy we obtained $\Delta E_{\mathrm{POT}}^{\mathrm{NLFF}} = 0.189 \pm 0.026 \times 10^{25}$ J. Correspondingly, our estimates of

Influence of noise on the 3D magnetic energy content

Noise model	*Minimum and maximum noise amplitudes [mT] to be added on* B_x		B_y		B_z		*Magnetic energies* $E_m \times 10^{25}$ J E_m^{POT}	E_m^{NLFF}
0	–	–	–	–	–	–	3.130	3.282
1	-0.304	0.344	-0.386	0.364	-0.374	0.349	3.138	3.325
2	-18.319	18.254	-17.665	17.608	-0.360	0.329	3.158	3.382
3	-0.655	0.685	-0.687	0.6765	-0.302	0.437	3.121	3.318
4	-3.711	3.739	-4.201	3.449	-0.332	0.479	3.121	3.353
5	-1.226	1.249	-1.317	1.880	-0.351	0.331	3.121	3.301
6	-3.823	3.212	-3.485	3.421	-0.364	0.330	3.121	3.287
7	-3.674	3.232	-3.395	4.097	-0.342	0.328	3.121	3.299
8	-4.372	3.104	-3.485	3.421	-0.360	0.324	3.120	3.300

Table 3.5: Effect of artificial noise added to the lower boundary data on the resulting 3D magnetic energies. The minimum and maximum noise amplitudes added on the longitudinal ($\boldsymbol{B}_z$) and transversal ($\boldsymbol{B}_z$, $\boldsymbol{B}_y$) magnetic field components of the original magnetogram for each noise model are listed together with the resulting changes of the potential (E_m^{POT}) and NLFF (E_m^{NLFF}) energies. Noise model no. 0 represents the SOLIS-VSM data at 17:10 UT without any noise added on it.

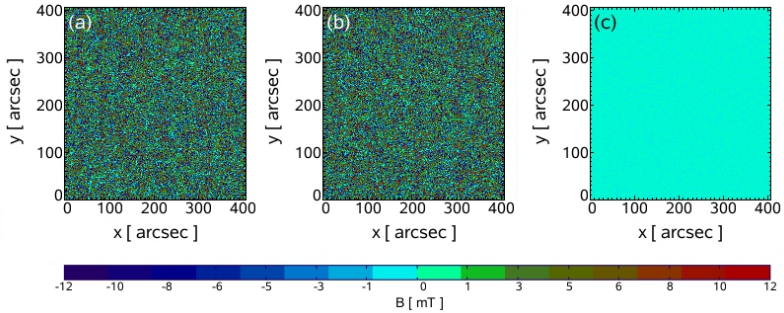

Figure 3.18: Transverse ($\boldsymbol{B}_x$, $\boldsymbol{B}_y$) and longitudinal ($\boldsymbol{B}_z$) components of noise model no. 2 as listed in Table 3.5. Panels (a), (b) and (c) show $\boldsymbol{B}_x$, $\boldsymbol{B}_y$ and $\boldsymbol{B}_z$, respectively. The model creates noise of about ± 20 mT in $\boldsymbol{B}_x$ and $\boldsymbol{B}_y$ and of about ± 0.3 mT in $\boldsymbol{B}_z$. For better visibility regarding the effect of adding the artificial noise, the magnetic field strength is scaled to ±12 mT. Units are arcseconds and the color bar indicates the magnetic field strength in mT.

E_m^{POT}, $E_m^{\mathrm{NLFF}}$and $\Delta E_{\mathrm{POT}}^{\mathrm{NLFF}}$ are accurate to within $\approx 0.4\%$, $\approx 1\%$ and $\approx 13\%$, respectively. Obviously, the potential field energy is not as sensitive to noise in the lower boundary as is the energy of the NLFF field. This is not surprising since the potential field calculation makes use of the longitudinal magnetic field component only.

Here it has to be noted that the error arising from the noise amplitudes in magnetograms is of statistical nature and can therefore be estimated. Besides this, however, additional errors may arise whose magnitudes or influences on the calculated magnetic

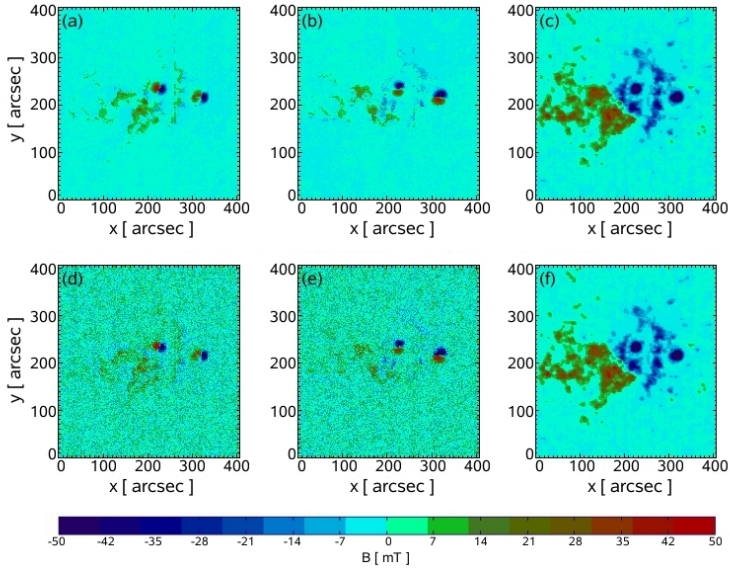

Figure 3.19: Transverse ($\boldsymbol{B}_x$, $\boldsymbol{B}_y$) and longitudinal ($\boldsymbol{B}_z$) components of the SOLIS-VSM data on June 07, 2007 at 17:10 UT with and without artificial noise added on it. Panels (a), (b) and (c) picture the original $\boldsymbol{B}_x$, $\boldsymbol{B}_y$ and $\boldsymbol{B}_z$ magnetic field components, respectively. Panels (d), (e) and (f) show the components after applying noise model no. 2 (see also Fig. 3.18). For better visibility regarding the effect of adding the artificial noise, the magnetic field strength is scaled to ±50 mT. Units are arcseconds and the color bar indicates the magnetic field strength in mT.

energy content of the force-free equilibria, or more generally, on the solution of the force-free equations, carried out inside a 3D box using a numerical extrapolation scheme may not be assessable. These are systematic errors, e.g. arising from the basic assumption of force-freeness in the entire coronal volume under consideration which might only partly or not at all be justified. This is the case, for instance, in the interface region between the photosphere and chromosphere or where magnetic reconnection is under way. Additionally, hardly possible to appraise are the errors introduced by the specific numerical treatment of the "unphysical" boundaries, i.e. the boundaries of a cubic extrapolation box for which no measured magnetic field values exist to be incorporated. In particular, for extrapolations within a numerical box where only the bottom boundary is known, the influence of the unknown lateral and top boundaries (on which reasonable assumptions have to be imposed) on the solution inside the computational volume is hard to estimate.

3.2.3.6 Discussion

We have investigated the coronal magnetic field associated with the NOAA AR 10960 on June 7, 2007 using SOLIS-VSM data. Three vector magnetograms with a time ca-

dence of about ten minutes were available to investigate the magnetic energy content of the coronal magnetic field during a C1.0 flare. Six further snapshots were receivable to analyze a period of low solar activity of about three hours after this flare. Before as well as after the small flare, the magnetic field energy was found to be $E_m^{\mathrm{NLFF}} \approx 3{\times}10^{25}$ J and the NLFF field was estimated to have possessed a free energy of $\Delta E_{\mathrm{POT}}^{\mathrm{NLFF}} \approx 1.5{\times}10^{24}$ J before the occurrence of the flare. As a consequence of the C1.0 flare, the amount of the free magnetic energy reduced by nearly a factor of ten, resulting in an almost potential configuration. The analysis of the six snapshots, acquired within a period of about 70 minutes during a quiet period of 3 – 4 hours after the flare, revealed an increase of the free magnetic energy. Since the estimated free magnetic energy remained only about 5% of the total energy content, no large eruption was produced by NOAA AR 10960. With the help of artificial noise models we were able to estimate the uncertainties of our potential and NLFF energy estimates with $\approx 0.4\%$ and $\approx 1\%$, respectively. Furthermore, the accuracy of the estimated upper limit for the free magnetic energy was found to be $\approx 13\%$.

Additionally, we pictured that the field lines showed, on average, their highest vertical extent when the C1.0 flare peaked and their, on average, lowest vertical extent after the peak time of the flare. At the beginning of a very quiet period and corresponding to the field configuration owing the lowest magnetic energy content, the field showed a more potential-like topology with field lines of a slightly higher extent when compared with the field configuration immediately after the flare.

These results are clearly different from that of the flaring NOAA AR 10540 as observed on Jan 18 – 21, 2004 and analyzed with the help of SFT-VM data of a time cadence of about one day. There, the free energy was $\Delta E_{\mathrm{POT}}^{\mathrm{NLFF}} \approx 66\%$ of the total energy, which was sufficient to power an M6.1 flare. Furthermore, the activity of NOAA AR 10540 was significantly higher than that of NOAA AR 10960 as was the total magnetic energy.

3.3 Summary

We used a multigrid-like optimization code for extrapolating the NLFF coronal magnetic field above two solar ARs. In order to minimize unavoidable foreshortening effects, the investigated ARs and the corresponding vector magnetograph data were selected due to their sufficiently close location to the solar disk center. After checking the consistency of the observed vector magnetograph data with the force-free assumption and subsequent demonstration of its initial inconsistency, we applied a preprocessing routine to gain consistent boundary conditions for the NLFF coronal magnetic field extrapolations. This procedure ensures that the modified photospheric boundary conditions suffice the force-balance and torque-balance condition, that they do not deviate too much from the actually measured photospheric data and that they are sufficiently smooth. Besides computing NLFF fields from this suitable boundary conditions, we also calculated the corresponding potential fields that can be determined from the vertical photospheric field alone.

Despite some differences, in particular in the coronal energy content and the amount of free magnetic energy which can be realeased during solar eruptions, also some common features were found through the investigation of the two ARs and are summarized in the following. Magnetic energy accumulates before a flare and a significant part of the excess energy is released during a flare. A high amount of free magnetic energy available

in an AR leads to large flares while small amounts of free energy power only small flares. Furthermore, the energy decrease in the NLFF field seems to be higher than that of the potential field, i.e. the energy release is likely to be more related to the changes of the transverse magnetic field components than to that of the longitudinal component. This implies that the energy storage and energy release are directly related to the field-aligned electric currents in the corona. Moreover, the coronal magnetic fields do not totally relax to a potential field configuration and the evolution of the energy density with height allows us to assume that the energy changes due to the flaring activity mainly take place within heights in the order of tens of megameters above the photospheric level. The computation of iso-surfaces of equal absolute magnetic field magnitude also seems to support a proposed implosion scenario during transient coronal events like flares and CMEs which has recently been approved observationally.

The sequence of NLFF equilibria to study solar ARs is, in general, based on the availability and quality of vector magnetic field measurements. In case of the SFT-VM (as used for the analysis of NOAA AR 10540 in the presented study) the time cadence is rather low and also is the pixel size (one available vector magnetogram per day and about $1.32''$, respectively). The improved time cadence of one vector magnetogram every ten minutes (occasionally with gaps of two to three hours in between) and a pixel size of about $1.133''$ of the SOLIS-VSM (as used for investigating the coronal magnetic field above NOAA AR 10560 in this work) allow a qualitatively better analysis of the coronal magnetic field in the course of solar eruptions. Investigations of the flare mechanism in great detail, however, require vector magnetic field measurements with an even higher temporal and spacial resolution. Therefore, such measurements, as expected in future from, e.g., the Helioseismic and Magnetic Imager on board of the Solar Dynamics Observatory (SDO/HMI; Graham et al. 2003) with a predicted pixel size of $\approx 0.5''$ and a predicted temporal resolution of ≈ 90 seconds and the corresponding coronal field analysis might allow to establish magnetic field extrapolations as an useful tool to predict solar eruptions.

When estimating physical quantities such as the magnetic energy content and the free magnetic energy of coronal magnetic fields one has to be aware that during the processes related to solar eruptions part of the energy is released but another part of it is transformed into kinetic energy or heat (i.e. the energy is converted back and forth between kinetic and magnetic forms). The next chapter therefore deals with alternative measures of the topology of magnetic fields such as the electric current helicity, the magnetic helicity and, in particular, the advantageous use of the latter due to its comfortable property to be (almost) conserved in (resistive) ideal MHD.

4 Helicity of coronal magnetic fields

In the previous chapters it was emphasized that due to the limited availability of direct chromospheric and coronal magnetic field measurements indirect methods are required. One possibility is the force-free extrapolation of the photospheric magnetic field vector into the corona. As a result, one obtains the 3D coronal magnetic field topology and can estimate the related physical quantities such as the magnetic energy content and the free magnetic energy. During the processes related to solar eruptions, however, part of the coronal magnetic energy is transformed into other forms of energy such as kinetic energy or heat. That is to say, when investigating coronal magnetic fields one has to be aware that the associated energy may be converted back and forth between kinetic and magnetic forms. However, the topology of magnetic fields can also be investigated with the help of the electric current helicity and the magnetic helicity. The electric current helicity (hereafter referred to as current helicity) measures the degree to which the electric currents are aligned with the magnetic field while the magnetic helicity quantifies the shear or twist of a non-potential field. The magnetic helicity has the comfortable property to be (almost) conserved in (resistive) ideal MHD since its dissipation time is too long to be relevant for most coronal processes.

Hereafter, the underlying theoretical concepts of the current helicity are discussed in § 4.1.1 and that of the magnetic helicity in § 4.1.2. The formulation of the magnetic helicity integral for the ideal case in which no field crosses the boundaries of a considered volume is outlined in § 4.1.3 and the necessary formal modifications to apply this concept to coronal volumes are discussed in § 4.1.4. A brief review of recent studies of the coronal magnetic field's helicity based on force-free field extrapolations is given in § 4.2. A method how to calculate the, for the practical computation of the magnetic helicity necessary, 3D vector potential is presented in § 4.3 and the results of testing the developed scheme are discussed in § 4.3.5. Finally, in § 4.4 a brief summary is given.

4.1 Theoretical concepts

The helicity of magnetic fields can be used as a tracer of the topological changes of the coronal magnetic field. One can either investigate the current helicity which gives an estimate of the degree of alignment between the electric currents and the magnetic field or one can evaluate the magnetic helicity which quantifies the contribution of the topological properties of a non-potential field. Generally speaking, the helicity is defined as the dot product of a vector and its curl (the dot product being the so-called helicity density), integrated over a closed volume (Pevtsov 2008).

4.1.1 Current helicity

The current helicity describes the linkage between current channels and can be written as

$$H_c = \mu_0 \int_V \boldsymbol{J} \cdot \boldsymbol{B}\, d^3x = \int_V (\nabla \times \boldsymbol{B}) \cdot \boldsymbol{B}\, d^3x \tag{4.1}$$

with $h_c = \mu_0\, \boldsymbol{J} \cdot \boldsymbol{B}$ being the current helicity density and μ_0 representing the permeability of free space. It can be regarded as a measure of how much $\nabla \times \boldsymbol{B}$ is aligned with $\boldsymbol{B}$, i.e. how much the magnetic field is locally twisted (Démoulin 2007). If the vector magnetic field $\boldsymbol{B}$ is known, the corresponding electric current density $\boldsymbol{J}$ (using $\nabla \times \boldsymbol{B} = \mu_0\, \boldsymbol{J}$) can be calculated and, therefore, (4.1) is directly evaluable. Furthermore, since $\boldsymbol{B}$ is assumed to be a solenoidal field ($\nabla \cdot \boldsymbol{B} = 0$) no gauge freedom for (4.1) arises.

Within the force-free field approximation, the current channels and flux tubes are assumed to coincide. Then, one can relate the magnetic field and the associated currents with $\nabla \times \boldsymbol{B} = \alpha_{\mathrm{ff}}\, \boldsymbol{B}$, where α_{ff} is the force-free field parameter (for details see § 2.1). As already mentioned, the current helicity measures the degree of alignment between the electric currents and the magnetic field and, consequently, for force-free fields this alignment is assumed to be 100%. To repeat, α_{ff} can be chosen as to be zero, constant but non-zero or a function of position, corresponding to potential (current-free; see § 2.2), linear force-free (LFF; see § 2.3) or nonlinear force-free (NLFF; see § 2.4) fields, respectively. Within the force-free approximation one can thus write

$$\alpha_{\mathrm{ff}} = \frac{(\nabla \times \boldsymbol{B}) \cdot \boldsymbol{B}}{B^2} = \frac{\mu_0}{B^2}\, (\boldsymbol{J} \cdot \boldsymbol{B}) = \frac{h_c}{B^2} \tag{4.2}$$

and hence $h_c = \alpha_{\mathrm{ff}}\, B^2$ which can be calculated from vector magnetograph data and which shows that the force-free parameter is proportional to the current helicity density so that it can, in principle, be used as a proxy for the helicity density's estimation (Hagyard and Pevtsov 1999). This, however, needs to be integrated over a specified volume to find the current helicity H_c in that volume and, using (4.2), one can rewrite (4.1) in the form

$$H_c = \int_V \alpha_{\mathrm{ff}}\, B^2\, d^3x \tag{4.3}$$

which implies that the current helicity, based on the force-free field assumption, is of the same sign as the force-free parameter α_{ff} (i.e., both being positive or negative). In the special case of potential fields, (4.2) yields a zero current helicity density and thus a zero current helicity in (4.3). In the case of LFF fields, where α_{ff} is assumed to be constant throughout an entire active region (AR), the current helicity in (4.3) can be further rewritten as

$$H_c = 2\, \mu_0\, \alpha_{\mathrm{ff}}\, E_m^{\mathrm{LFF}} \tag{4.4}$$

with E_m^{LFF} being the total magnetic energy of the 3D LFF field (for the definition of the magnetic energy integral see (3.1) in § 3.2.1). Although the use of LFF fields provides a comfortable way to estimate the current helicity above solar ARs, one has to keep in mind that α_{ff} is, in general, not of the same value throughout an AR. As a result the amount of helicity is likely to be underestimated when using (4.4) for its evaluation (see e.g. Démoulin 2007). The most realistic force-free approximation of the true coronal magnetic field is that of a NLFF field where α_{ff} varies from field line to field line.

4.1.2 Magnetic helicity

The present formalism of the magnetic helicity arose from the first attempts to describe the interaction of electrical circuits and the thus produced magnetic field by Gauss (1833). He defined a measure for the enlacement of two closed or infinitely long curves in the form

$$L_{12} = -\frac{1}{4\pi} \int_{l_1} \int_{l_2} (\, d\boldsymbol{l}_1 \times d\boldsymbol{l}_2 \,) \cdot \frac{\boldsymbol{x}_1 - \boldsymbol{x}_2}{|\, \boldsymbol{x}_1 - \boldsymbol{x}_2 \,|^3}, \tag{4.5}$$

known as the Gauss linking number (GLN). Here, l_1 and l_2 represent two curves and $\boldsymbol{x}_1$ and $\boldsymbol{x}_2$ are points on the curves 1 and 2, respectively. Gauss already noted that this number (i.e., the number of enlacements) remains the same if the two curves are interchanged and, moreover, is left unchanged if l_1 or l_2 are moved without intersecting each other.

Turning this simple relation over to the concept of magnetic field lines, the sum of the GLN over every pair of field lines within a volume gives the magnetic helicity. If there are N distinct flux tubes with the flux ϕ_i (with $i = 1, \ldots, N$) in a closed volume, the total magnetic helicity H_m is given by

$$H_m = \sum_{i=1}^{N} \sum_{j=1}^{N} L_{ij}\, \phi_i\, \phi_j = \sum_{i \neq j} L_{ij}\, \phi_i\, \phi_j + \sum_{i=j} L_{ii}\, \phi_i^2, \tag{4.6}$$

where L_{ij} is the number of windings of field line i through the field line j or vice versa. Then, $N\,(N-1)$ terms for $i \neq j$ arise from the mutual linking of pairs of field lines, N terms for $i = j$ arise from the self linking (twist) of individual field lines and all these terms together make up the total helicity (e.g. Berger 1998, 1999a, Priest 1999).

The different geometrical forms such as the linkage, twist and kink of field lines can change into each other as a magnetic field gets distorted and lead to the storage of magnetic energy. In ideal MHD, every twisting or kinking of magnetic field lines is conserved and, consequently, whatever energy is stored based on the deformation of the field cannot be freed simply by an "untwisting" or "unkinking". Ideally, field lines do not reconnect or pass through each other, hence do not change their topology so that the linking and knotting is preserved, though some energy may be lost, e.g., by converting magnetic into kinetic energy (Berger 1999b). For simple structures, one can count the number of windings of field lines around each other or the twist of individual field lines around themselves in order to determine the contribution to the total helicity. Instead of such simple configurations one will, in general, be confronted with a complex combination of twist and linking, e.g., multiple field lines warping around each other and additionally being highly twisted. However, though the twist and linkage contribute different amounts of helicity, the total helicity does not distinguish between them (see e.g. Hornig and Rastätter 1997). For real cases, one never deals with individual field lines but one considers an infinite number of field lines which concentrate in magnetic flux tubes and fill a volume or surface rather than form simple closed tubes. Then it is already a problem to determine the linkage of two arbitrary flux tubes and, moreover, one would have to sum over an infinite number of pairs of flux tubes. Therefore, the formulation of the linkage of pairs of flux tubes and the twist of individual flux tubes is generalized in order to approximate the helicity in a magnetic volume. Moffatt (1969) was the first to establish a relation between the GLN and the helicity integral in the context of the conservation of linkages of vortex

lines. The magnetic field is considered as a collection of an infinite number ($N \to \infty$) of closed flux tubes, each with infinitesimal flux ($\phi_i \to 0$), to combine (4.5) and (4.6) to a double integral of the form

$$H_m = -\frac{1}{4\pi} \int_V \int_{V'} \left(\frac{\boldsymbol{x} - \boldsymbol{x}'}{|\,\boldsymbol{x} - \boldsymbol{x}'\,|^3} \times \boldsymbol{B}\,(\boldsymbol{x}') \right) \cdot \boldsymbol{B}\,(\boldsymbol{x})\; d^3x'\, d^3x. \tag{4.7}$$

One can then employ the Coulomb-gauge vector potential

$$\boldsymbol{A}(\boldsymbol{x}) = \frac{1}{c} \int_{V'} \frac{\boldsymbol{J}(\boldsymbol{x}')}{|\,\boldsymbol{x} - \boldsymbol{x}'\,|}\, d^3x' \tag{4.8}$$

and make use of $\mu_0\, \boldsymbol{J} = \nabla \times \boldsymbol{B}$ to get, after partial integration,

$$\boldsymbol{A}(\boldsymbol{x}) = -\frac{1}{4\pi} \int_{V'} \frac{\boldsymbol{x} - \boldsymbol{x}'}{|\,\boldsymbol{x} - \boldsymbol{x}'\,|^3} \times \boldsymbol{B}(\boldsymbol{x}')\, d^3x' \tag{4.9}$$

to reduce (4.7) to the form

$$H_m = \int_V \boldsymbol{A} \cdot \boldsymbol{B}\, d^3x = \int_V \boldsymbol{A} \cdot (\nabla \times \boldsymbol{A})\; d^3x \tag{4.10}$$

with $h_m = \boldsymbol{A} \cdot \boldsymbol{B}$ representing the magnetic helicity density (e.g. Berger 1984, 1999a,b, Bellan 1999). Obviously, by redefining $\boldsymbol{A}$ to be $\boldsymbol{A}' = \boldsymbol{A} + \nabla\xi$, with ξ being an arbitrary scalar function one recognizes that still $\boldsymbol{B} = \nabla \times (\boldsymbol{A} + \nabla\xi) = \nabla \times \boldsymbol{A}$. That means that $\boldsymbol{A}$ is undefined with respect to a gauge or, equivalently, that any $\nabla\xi$ can be added to the vector potential without altering the magnetic field since the curl of a gradient is zero. Now, the definition of the magnetic helicity as a gauge-dependent quantity would be not helpful since a gauge has no physical meaning (Bellan 2006). In the following, the gauge-invariant formulation of the magnetic helicity depending on the properties of the considered volume in which it is aimed to be evaluated are therefore discussed.

4.1.3 Magnetic helicity in closed volumes

A volume V which is enclosed by a surface ∂V through which no magnetic field penetrates is called a "magnetically closed" volume. This implies that

$$\boldsymbol{B} \cdot d\boldsymbol{S} = \boldsymbol{B} \cdot \boldsymbol{n}\, dS \;= 0 \;\; \text{on } \partial V, \tag{4.11}$$

where $\boldsymbol{n}$ denotes the outward normal vector on ∂V, dS is a surface element and ∂V can be called an "impermeable" wall. Then, a gauge transform $\boldsymbol{A}' \to \boldsymbol{A} + \nabla\xi$ would yield

$$\delta H_m = \int_V \nabla\xi \cdot \boldsymbol{B}\, d^3x = \oint_{\partial V} \xi\, \boldsymbol{B} \cdot \boldsymbol{n}\, dS \;= 0. \tag{4.12}$$

This shows that, although the magnetic helicity density $\boldsymbol{A} \cdot \boldsymbol{B}$ is a gauge-dependent quantity, the total helicity H_m, as defined in (4.10), in a magnetically closed volume is gauge-independent (Berger 1999a,b). If, additionally, the tangential component of the vector potential $\boldsymbol{A}_t$ on ∂V is fixed, $\boldsymbol{A}$ is unique. The freedom of the gauge selection reflects the freedom of choice of the normal component of the vector potential $\boldsymbol{A}_n$ on ∂V (Jensen and

Chu 1984). However, (4.11) is a very restrictive condition since it limits the application of (4.10) to cases where no magnetic field crosses the boundary. In the MHD case this requires that the normal component of the fluid velocity $\boldsymbol{v}_n$ must vanish at the impermeable wall. Assuming perfect conductivity ($\sigma \to \infty$), Ohm's law reduces to $\boldsymbol{E} = -\boldsymbol{v} \times \boldsymbol{B}$, implying $\boldsymbol{E}_t = -\boldsymbol{v}_n \times \boldsymbol{B} = 0$, meaning that the tangential electric field $\boldsymbol{E}_t$ must vanish on ∂V (since $\boldsymbol{B}$ lies in the plane of the wall). This means that the adoption of an impermeable wall equals that of a conducting wall if $\boldsymbol{B}$ lies in the plane of the wall (Bellan 2006).

4.1.3.1 Helicity relaxation

The quasistatic magnetic field configuration above the photosphere evolves slowly through a sequence of force-free equilibria, induced by material motions in or below the photosphere. Processes like turbulence or instabilities propagate upward from the photosphere, distorting a reached equilibrium and forcing it to perform a slow quasi-static evolution to a neighboring equilibrium (represented by varying photospheric boundary conditions). This subsequent relaxation leads to a minimum magnetic energy state for given photospheric boundary conditions. This minimum energy state in a closed system, subject to the constraint that the magnetic helicity remains constant (i.e., is conserved), can be derived using a Lagrange multiplier ζ to formulate a constrained variational principle of the form

$$\delta E_m - \zeta \, \delta H_m = 0 \tag{4.13}$$

with δE_m (δH_m) being the variation of the magnetic energy (helicity) relative to the minimum magnetic energy (helicity) state (Woltjer 1958, Taylor 1974).

In order to determine the minimum-energy magnetic field $\boldsymbol{B}_{\min}$ for a given helicity, one considers an arbitrary variation of the magnetic field $\boldsymbol{B} = \boldsymbol{B}_{\min} + \delta\boldsymbol{B}$ which satisfies the same boundary conditions as $\boldsymbol{B}_{\min}$. Furthermore, $\boldsymbol{B}$ is assumed to have an associated vector potential $\boldsymbol{A} = \boldsymbol{A}_{\min} + \delta\boldsymbol{A}$ and the magnetic energy associated with $\boldsymbol{B}$ is assumed to be higher than that of $\boldsymbol{B}_{\min}$. If one additionally hypothesizes that the volume V is bounded by a perfectly conducting surface (i.e., to be magnetically closed) so that $\boldsymbol{E}_t = 0$ on ∂V one must, to achieve accordance with the assumption of helicity conservation, also assume the tangential component of the vector potential's variation to vanish at the wall (i.e., $\delta\boldsymbol{A}_t = 0$ on ∂V; Bellan 2006). With these assumptions and using $\delta\boldsymbol{B} = \nabla \times \delta\boldsymbol{A}$ we can rewrite δE_m in (4.13) as

$$\begin{aligned} \delta E_m &= \frac{1}{2\mu_0} \int_V \left(\boldsymbol{B}^2 - \boldsymbol{B}_{\min}^2 \right) d^3x \\ &= \frac{1}{\mu_0} \oint_{\partial V} (\delta\boldsymbol{A} \times \boldsymbol{B}_{\min}) \cdot \boldsymbol{n} \, dS + \frac{1}{\mu_0} \int_V \delta\boldsymbol{A} \cdot (\nabla \times \boldsymbol{B}_{\min}) \, d^3x, \end{aligned} \tag{4.14}$$

where the surface term vanishes in accordance to $\delta\boldsymbol{A}_t = 0$ on ∂V and where we assumed that higher-order variations of $\boldsymbol{A}$ are negligible. Accordingly, we rewrite δH_m in (4.13) as

$$\begin{aligned} \delta H_m &= \int_V (\boldsymbol{A} \cdot \boldsymbol{B} - \boldsymbol{A}_{\min} \cdot \boldsymbol{B}_{\min}) \, d^3x \\ &= \oint_{\partial V} (\delta\boldsymbol{A} \times \boldsymbol{A}_{\min}) \cdot \boldsymbol{n} \, dS + 2 \int_V \delta\boldsymbol{A} \cdot \boldsymbol{B}_{\min} \, d^3x. \end{aligned} \tag{4.15}$$

Inserting (4.14) and (4.15) into (4.13) results in

$$\int_V \delta \boldsymbol{A} \cdot (\nabla \times \boldsymbol{B}_{\rm min} - \zeta \, \boldsymbol{B}_{\rm min}) \, d^3x = 0, \tag{4.16}$$

where we made use of the fact that one can re-define the arbitrary parameter ζ so that it absorbs the factor μ_0 in (4.14) and the factor of two in (4.15). Since the variation $\delta \boldsymbol{A}$ is assumed to be arbitrary within V, the rest of the integrand must vanish and, consequently,

$$\nabla \times \boldsymbol{B}_{\rm min} = \zeta \, \boldsymbol{B}_{\rm min} \tag{4.17}$$

with ζ being spatially uniform (Woltjer 1958, Taylor 1974, Bellan 1999, 2006). This shows that any closed system relaxes by energy dissipation to a force-free field configuration. This may formally explain why the coronal energy content of the NLFF fields above the two analyzed solar ARs (presented in § 3.2.2 and § 3.2.3) does not reduce to that of the corresponding potential field after the occurring flares because the relaxation of a NLFF field to a potential state obviously conflicts with the conservation of its magnetic helicity.

When considering perfectly conducting fluids, the magnetic field is frozen into the plasma and follows its continuous flow. This implies, that the field lines cannot change their topological properties which are therefore conserved for all times. Then, (4.17) only tells that the attained state of minimum magnetic energy is "some" force-free equilibrium. This is because there may exist many subvolumes in the plasma (i.e., many individual flux tubes), bounded by magnetic surfaces for which the corresponding H_m is to be conserved. Because the helicity has to be assumed as constant in each elementary flux tube, in principle, as many Lagrange multipliers as there are flux tubes need to be introduced and the variational principle, allowing for all these extra constraints, does not lead to a force-free field with constant ζ for most initial states. This would be far from being universal and so one considers that real plasmas are never perfectly conducting (Taylor 1974). In plasmas with small but finite resistivity the topological properties are no longer conserved and field lines may reconnect. Though the requirement of helicity conservation for individual field lines would no longer hold, it should still be approximately conserved when considering the entire volume that contains all the field lines. This can be assumed since the topological changes related to individual field lines result only in small changes of the field itself. Consequently, the sum of the helicity over all field lines in the entire volume remains almost unchanged during its evolution to a minimum energy state. If this is true, the final state of minimum energy corresponds to a state with the same value ζ representative for all pairs of field lines (Taylor 1974, Heyvaerts and Priest 1984, Taylor 1986). Now it is clear that ζ, under these conditions, equals the already introduced constant but non-zero force-free parameter $\alpha_{\rm ff}$ of a LFF field so that for subsequent discussions we go back to this notation.

Based on the discussion above, we can write $\nabla \times \boldsymbol{B} = \alpha_{\rm ff} \, \boldsymbol{B} = \alpha_{\rm ff} \, (\nabla \times \boldsymbol{A})$ or, which is equivalent, $\nabla \times (\boldsymbol{A} - \alpha_{\rm ff}^{-1} \, \boldsymbol{B}) = 0$. Uncurling this expression gives $\boldsymbol{A} = \alpha_{\rm ff}^{-1} \, \boldsymbol{B} + \nabla \xi$ with ξ being an arbitrary scalar function that can be added to the $\boldsymbol{A}$ without altering $\boldsymbol{B}$. The volume-integrated (total) magnetic helicity can then be written as

$$H_m = \int_V \left(\alpha_{\rm ff}^{-1} \, \boldsymbol{B} + \nabla \xi \right) \cdot \boldsymbol{B} \, d^3x = \int_V \alpha_{\rm ff}^{-1} \, B^2 \, d^3x + \oint_{\partial V} \xi \, \boldsymbol{B} \cdot \boldsymbol{n} \, dS. \tag{4.18}$$

Since we assumed a magnetically closed volume (i.e., $\boldsymbol{B}\cdot\boldsymbol{n}\,dS = 0$ on ∂V), the surface integral is zero so that for LFF fields (where $\alpha_{\rm ff}$ is assumed to be consant within the considered volume) one can write

$$H_m = 2\,\mu_0\,\alpha_{\rm ff}^{-1}\,E_m^{\rm LFF} \tag{4.19}$$

which means that the magnetic helicity is reversely proportional to $\alpha_{\rm ff}$ and of the same sign (i.e. both being positive or negative; see e.g. Bellan 1999, 2006).

Note that a similar expression was already found for the total current helicity in (4.4) with the difference that it was found to be directly proportional to $\alpha_{\rm ff}$. Thus, in the case of LFF fields and using (4.3) and (4.18) one can establish the relations

$$h_m = \alpha_{\rm ff}^{-2}\,h_c, \tag{4.20}$$

showing that both helicity densities are of the same sign and

$$h_m = \alpha_{\rm ff}^{-1}\,B^2, \tag{4.21}$$

indicating that the magnetic helicity density can be determined by magnetograph data (Hagyard and Pevtsov 1999). Nevertheless, in the most general case of the force-free parameter being a function of position (i.e., $\alpha_{\rm ff} = \alpha_{\rm ff}(\boldsymbol{x})$), the helicity densities h_m and h_c cannot be expected to be simply related since the distribution of $\alpha_{\rm ff}(\boldsymbol{x})$ is a key ingredient in (4.3) and (4.18). Evenmore, as pointed out by Régnier et al. (2005a) and Démoulin (2007), for certain solar configurations h_m and h_c may not be of the same sign.

4.1.4 Magnetic helicity in open domains

In contrast to the previous discussions, the considered volume V is magnetically open (i.e. magnetic field penetrates the boundaries so that $\boldsymbol{B}\cdot d\boldsymbol{S} \neq 0$ on ∂V) if one aims to study the helicity of the solar corona. This is because magnetic flux emerges through the photosphere from below. Even if one were able to count the linkages of flux tubes in the coronal volume, one could not know about the linkage of the flux tubes below the photosphere. This ambiguity in counting the linkage of flux tubes is equivalent to the gauge ambiguity (Bellan 1999). In addition, magnetic field lines have endpoints on the boundaries of the computational volume (representing the considered coronal volume) and hence linking numbers will be undefined. Now, any gauge of the form $\boldsymbol{A}' \rightarrow \boldsymbol{A} + \nabla\xi$ results in $\delta H_m \neq 0$ in (4.12) and H_m will not be invariant with respect to the ambiguous gauge of $\boldsymbol{A}$ and hence will not provide a physically meaningful quantity.

This led to the development of the concept of the "relative" magnetic helicity (Berger and Field 1984, Jensen and Chu 1984). One attempts to measure the helicity inside a volume of interest (VOI) which is generated by currents partly inside and outside of it. Therefore, one defines a volume external to the VOI so that the sum of the two contains no open field lines (Berger 1988). This means that $\boldsymbol{B}\cdot d\boldsymbol{S} = 0$ on the boundary of the external volume but $\boldsymbol{B}\cdot d\boldsymbol{S} \neq 0$ on the interface between the VOI and the external volume. Then an integral over the entire volume (containing the external volume and the VOI) does not fail to count linkages since, by assumption, no open field lines are present (Bellan 1999). This is similar to regarding a magnetic field $\boldsymbol{B}$ to be the sum of a closed field ($\hat{\boldsymbol{B}}$; representing

the VOI) and an open field ($\bar{\boldsymbol{B}}$; representing the external volume) in the form $\boldsymbol{B}=\hat{\boldsymbol{B}}+\bar{\boldsymbol{B}}$, with the special properties $\nabla\times\bar{\boldsymbol{B}}=0$, $\boldsymbol{B}\cdot d\boldsymbol{S}=\bar{\boldsymbol{B}}\cdot d\boldsymbol{S}$ and $\hat{\boldsymbol{B}}\cdot d\boldsymbol{S}=0$ (Kusano et al. 1995). Usually, $\bar{\boldsymbol{B}}$ is called the "vacuum" field and is chosen to be represented by a potential field. If we write the measure of the linking of two fields in the form

$$H_V(\boldsymbol{B}',\boldsymbol{B}'') \equiv \int_V \boldsymbol{A}'\cdot\boldsymbol{B}''\,d^3x, \tag{4.22}$$

where $\boldsymbol{B}'=\nabla\times\boldsymbol{A}'$ and where $\boldsymbol{B}$' and $\boldsymbol{B}$" represent any two divergence-free vector fields, the helicity of the configuration $\boldsymbol{B}=\hat{\boldsymbol{B}}+\bar{\boldsymbol{B}}$ takes the form

$$H_V = H_V(\boldsymbol{B},\boldsymbol{B}) = H_V(\hat{\boldsymbol{B}},\hat{\boldsymbol{B}}) + 2\,H_V(\bar{\boldsymbol{B}},\hat{\boldsymbol{B}}) + H_V(\bar{\boldsymbol{B}},\bar{\boldsymbol{B}}), \tag{4.23}$$

where $H_V(\hat{\boldsymbol{B}},\hat{\boldsymbol{B}})$ measures the self helicity of the closed field and $H_V(\bar{\boldsymbol{B}},\hat{\boldsymbol{B}})$ the mutual helicity between the open and the closed field. Note that the factor of two arises from the fact that $\bar{\boldsymbol{B}}$ is linked with $\hat{\boldsymbol{B}}$ but also vice versa (see § 4.1.2). Both $H_V(\hat{\boldsymbol{B}},\hat{\boldsymbol{B}})$ and $H_V(\bar{\boldsymbol{B}},\hat{\boldsymbol{B}})$ are well-defined quantities, making up together the relative helicity. $H_V(\bar{\boldsymbol{B}},\bar{\boldsymbol{B}})$ is the self helicity of the vacuum field which does not reflect any field linkage and can therefore be omitted (Berger 1999b). The integral formulation for the relative helicity H_{rel} can then be written as

$$H_V = H_{rel} = \int_V \left(\hat{\boldsymbol{A}}\cdot\hat{\boldsymbol{B}} + 2\,\bar{\boldsymbol{A}}\cdot\hat{\boldsymbol{B}}\right) d^3x. \tag{4.24}$$

Since we decomposed the magnetic field $\boldsymbol{B}$ into $\hat{\boldsymbol{B}}$ and $\bar{\boldsymbol{B}}$ and since these are associated to their vector potentials via $\bar{\boldsymbol{B}}=\nabla\times\bar{\boldsymbol{A}}$ and $\hat{\boldsymbol{B}}=\nabla\times\hat{\boldsymbol{A}}$, the total magnetic vector potential can also be decomposed in the form $\boldsymbol{A}=\hat{\boldsymbol{A}}+\bar{\boldsymbol{A}}$. Using this in (4.24) yields

$$\begin{aligned} H_{rel} &= \int_V \left(\boldsymbol{A}-\bar{\boldsymbol{A}}\right)\cdot\hat{\boldsymbol{B}}\,d^3x + \int_V 2\,\bar{\boldsymbol{A}}\cdot\left(\boldsymbol{B}-\bar{\boldsymbol{B}}\right) d^3x \\ &= \int_V \left(\boldsymbol{A}+\bar{\boldsymbol{A}}\right)\cdot\left(\boldsymbol{B}-\bar{\boldsymbol{B}}\right) d^3x \end{aligned} \tag{4.25}$$

which is usually called the "Finn-Antonsen formula" (Berger and Field 1984, Jensen and Chu 1984, Finn and Antonsen 1985). If the gauge potentials $\nabla\xi_A$ and $\nabla\xi_{\bar{A}}$ are added to $\boldsymbol{A}$ and $\bar{\boldsymbol{A}}$, respectively, the change in the relative helicity is

$$\delta H_{rel} = \int_V \nabla\left(\xi_A+\xi_{\bar{A}}\right)\cdot\left(\boldsymbol{B}-\bar{\boldsymbol{B}}\right) d^3x = \oint_{\partial V} \left(\xi_A+\xi_{\bar{A}}\right)\left(\boldsymbol{B}-\bar{\boldsymbol{B}}\right)\cdot\boldsymbol{n}\,dS = 0, \tag{4.26}$$

where we made use of $\boldsymbol{B}\cdot d\boldsymbol{S}=\bar{\boldsymbol{B}}\cdot d\boldsymbol{S}$. According to Jensen and Chu (1984), the boundary condition on $\bar{\boldsymbol{B}}$ can be automatically satisfied by choosing the gauge of $\boldsymbol{A}$ and $\bar{\boldsymbol{A}}$ so that $\boldsymbol{A}\times d\boldsymbol{S}=\bar{\boldsymbol{A}}\times d\boldsymbol{S}$ so that the relative helicity can be written as

$$H_{rel} = \int_V \left(\hat{\boldsymbol{A}}\cdot\hat{\boldsymbol{B}} - \bar{\boldsymbol{A}}\cdot\bar{\boldsymbol{B}}\right) d^3x. \tag{4.27}$$

Also Hornig (2006) considered the total helicity integral (4.10) for magnetic fields which are not closed within a domain. His representation does not require an explicit reference field as the one for the relative helicity integral does. Instead, he constructed an unique expression for the magnetic helicity by giving up the gauge freedom and introducing a gauge condition for $\boldsymbol{A}$ on ∂V which corresponds to the closing of the domain by a topologically unique field.

4.2 Helicity studies based on force-free fields

Based on 3D coronal magnetic field extrapolations, the current and magnetic helicity can be evaluated for an entire computational volume. In the following, the results of some recent work, using force-free extrapolation methods to investigate the coronal magnetic field's helicity, are discussed.

The coronal magnetic helicity associated with the simple bipolar, isolated NOAA AR 7978 between July and Nov 1996 was analyzed by Démoulin et al. (2002). They first computed the LFF (constant-$\alpha_{\rm ff}$) coronal magnetic field using SoHO/MDI line-of-sight magnetic field measurements as the lower boundary condition (assuming a given value of $\alpha_{\rm ff}$) and then compared computed field lines to coronal loops observed with the Yohkoh/SXT. The $\alpha_{\rm ff,best}$-value whose corresponding LFF field computation fitted the coronal loop observations best was found through an iterative process in which LFF fields were calculated using different values of $\alpha_{\rm ff}$. Based on the $\alpha_{\rm ff,best}$-LFF field extrapolations, it was shown that over a time period of about six months the relative magnetic helicity sign corresponded to the southern hemisphere where the AR emerged. With the correspondence of the helicity sign to a particular solar hemisphere we refer to the observationally established "hemispheric sign rule" which (though maybe being more a trend than a rule) manifests itself in the form of predominantly negative/positive helicity patterns in the northern/southern solar hemisphere. Modelling 78 ARs with LFF fields based on SoHO/MDI magnetograms, Nindos and Andrews (2004) found the $\alpha_{\rm ff,best}$-values from fitting the model loops to SoHO/EIT observations of the AR's coronal loops and computed the coronal current helicity from the resulting LFF fields. Averaging all $\alpha_{\rm ff,best}$ of all ARs, they found a higher value than the average photospheric $\alpha_{\rm ff,best}$ derived by Pevtsov et al. (1995) who studied 69 ARs. The source of this difference was suspected to be due to the selection of the considered ARs. They found that the pre-flare value of $\alpha_{\rm ff,best}$ as well as the absolute coronal magnetic helicity of ARs to be smaller when flares without CME association occurred. Also possible changes of the sign of $\alpha_{\rm ff,best}$ and thus of the magnetic helicity due to impulsive variations close to the flare onsets were underlined. Nindos and Andrews (2004) furthermore found that for ARs for which a LFF model was not acceptable, a change of the sign of $\alpha_{\rm ff}$ within an AR occurred more often in those ARs which produced confined flares than in those producing eruptive flares, indicating the presence of magnetic helicity of mixed sign. A large range of $\alpha_{\rm ff}$ values of mixed sign means that a magnetic field is far from a LFF state, though a mixed sign of $\alpha_{\rm ff}$ does not necessarily imply a mixed sign of the magnetic helicity (Démoulin 2007). Using data from the Imaging Vector Magnetograph of the Mees Solar Observatory (MSO-IVM; Mickey et al. 1996), Georgoulis and LaBonte (2007) investigated NOAA AR 8844 and NOAA AR 9165 as observed on Jan 25, 2000 and Sep 15, 2000, respectively, over a period of several hours. While NOAA AR 8844 appeared to be a small, short-lived emerging region NOAA AR 9165 exhibited significant eruptive activity. By calculating the $\alpha_{\rm ff,best}$-LFF field (as found by matching the coronal loops simultaneously observed with the TRACE) they found almost identical average absolute values of $\alpha_{\rm ff,best}$ for both ARs but of different sign (though both ARs were located in the same hemisphere). Moreover, the much larger magnetic flux carried by the eruptive NOAA AR 9165 led to a larger helicity budget compared to that of the non-eruptive NOAA AR 8844. Hence it was concluded that comparing the helicity budget might be a safe way to distinguish between eruptive ARs and such which are not.

The $\alpha_{\rm ff}$- and hence the $\alpha_{\rm ff,best}$-parameter, however, are mostly determined by large scale loops present in an AR. A LFF extrapolation of the coronal magnetic field based on line-of-sight photospheric magnetic field measurements generally approximates shorter (longer) field lines less (more) sheared than they actually are when compared with coronal loop observations. As a result, the amount of helicity present in the solar corona is likely to be underestimated (Démoulin 2007, and references therein) and NLFF field extrapolations are necessary to improve the match of the coronal helicity content.

Using MSO-IVM data, Régnier et al. (2002) analyzed the 3D NLFF (non-constant $\alpha_{\rm ff}$) field of NOAA AR 8151 on Feb 11, 1998. The integrated relative helicity density was found to be positive as was the mean value of $\alpha_{\rm ff}(\boldsymbol{x})$. Since this AR was located in the southern hemisphere this finding supports the hemispheric sign rule. Régnier et al. (2005a) investigated the meaning of the self helicity of the closed field, the mutual helicity between the closed and the open field and the vacuum helicity of NOAA AR 8210 observed on May 1, 1998 using MSO-IVM data. They found that the magnetic configuration of this AR was dominated by the mutual helicity and not by its self helicity. They also showed that, though not gauge invariant, the vacuum helicity is sensitive to the topological complexity of the reference (potential) field. The relative helicity was also estimated using LFF fields with varying $\alpha_{\rm ff}$ from the same boundary conditions as the NLFF computation to compare the result. It was found that the relative helicity computed for the LFF field can be very different in absolute value and sign from that of the NLFF field (Régnier et al. 2005a, and references therein). Régnier and Canfield (2006) analyzed NOAA AR 8210 observed on May 1, 1998 for a period of about five hours with the help of NLFF field extrapolations based on MSO-IVM data. The self helicity of the vacuum (potential) field was found to be nearly constant but non-zero which was suspected to be due to the complex configuration of AR 8210 since for simply connected volumes the self helicity of a potential field is expected to be zero. Its positive value and the apparent location of this AR in the southern hemisphere agrees with the hemispheric sign rule. Furthermore, an injection of negative relative helicity was found before a recorded flare and a decrease of the relative helicity after it. However, a delay of ≈ 20 min was found between the injection of negative helicity and its release after the flare, indicating a delay between the injection into the corona and its associated response. In addition to the two aforementioned ARs, Régnier and Priest (2007b) also analyzed NOAA AR 9077 on July 14, 2000 and NOAA AR 10468 on Oct 27, 2003 as observed with the MSO-IVM. They found a correspondence of the relative magnetic helicity sign, as calculated from extrapolated NLFF fields, with the hemisphere in which the ARs appeared. However, in all of these helicity studies the vector potential Grad-Rubin-like method (Amari et al. 1997, 1999) was used to extrapolate the NLFF coronal magnetic field which assumes for the required boundary conditions on the lateral and top boundaries of the computational box a vanishing normal component of the magnetic field. This seems less realistic than prescribing these boundaries in form of the potential field, as done within our optimization method (see § 2.4.1 and Wiegelmann 2004). Therefore, we aim to calculate the helicity content of coronal magnetic fields extrapolated with our magnetic field model. Since for the calculation of the magnetic helicity the derivation of the 3D magnetic vector potential from the extrapolated magnetic fields is necessary, a recently developed method to do so is presented in the following section.

4.3 Computation of the magnetic vector potential

To evaluate the magnetic helicity content of the solar corona the knowledge of the 3D magnetic field vector and the associated 3D vector potential is needed. The calculation of the 3D coronal magnetic field structure using extrapolation techniques was formally demonstrated in § 2 and its practical application shown in § 3. Hereafter, a newly developed method to derive the vector potential from a given magnetic field is presented.

4.3.1 General formulation of the problem

Permanently, magnetic flux emerges from below through the photosphere into the corona and hence coronal volumes are magnetically open. This, for magnetic field computations within a cubic box, means that magnetic field penetrates all boundaries (i.e., $\boldsymbol{B}\cdot d\boldsymbol{S} \neq 0$). Since the magnetic helicity integral for magnetically open volumes is not invariant with respect to gauge transforms of the associated vector potential (see § 4.1.4) one aims to evaluate the relative helicity, i.e. the helicity with respect to a reference field.

In general, in order to determine the 3D magnetic vector potential $\boldsymbol{A}$ for a given solenoidal ($\nabla\cdot\boldsymbol{B}=0$) vector magnetic field $\boldsymbol{B}$, one has to solve an inhomogeneous partial differential equation (PDE) of the form

$$\nabla \times \boldsymbol{B} = \nabla \times (\nabla \times \boldsymbol{A}) = \nabla(\nabla \cdot \boldsymbol{A}) - \Delta\boldsymbol{A} = \mu_0 \boldsymbol{J}. \tag{4.28}$$

Since the normal magnetic field component on all boundaries ∂V of the considered volume has to be reproduced by the normal component of the vector potential's curl, (4.28) is subject to the boundary requirement

$$\boldsymbol{n} \cdot \boldsymbol{B} = \boldsymbol{n} \cdot (\nabla \times \boldsymbol{A}) \quad \text{on } \partial V. \tag{4.29}$$

Since (4.28) and (4.29) define the curl of $\boldsymbol{A}$ only, i.e. define $\boldsymbol{A}$ up to the gradient of an arbitrary scalar function ξ which could be added to $\boldsymbol{A}$ without altering $\boldsymbol{B}$, one adds the additional constraint $\nabla \cdot \boldsymbol{A} = 0$ (the so-called Coulomb gauge). Then, one also has to provide suitable boundary conditions on $\boldsymbol{A}$ itself which can be achieved by

$$\boldsymbol{n} \times \boldsymbol{A} = 0 \quad \text{on } \partial V \tag{4.30}$$

which defines the tangential component of the gradient of the scalar function ξ on ∂V. We solve the inhomogeneous PDE (4.28) by seeking the special solution of the inhomogeneous equation $\Delta\boldsymbol{A} = -\mu_0 \boldsymbol{J}$ (which takes the electric currents into account) and searching the set of solutions to the homogeneous problem $\Delta\boldsymbol{A}=0$ (which takes the magnetic flux through the boundaries into account). In other words, we calculate the total magnetic vector potential $\boldsymbol{A}$ as the sum of a current-carrying part $\hat{\boldsymbol{A}}$ and a Laplacian part $\bar{\boldsymbol{A}}$ so that $\boldsymbol{A} = \bar{\boldsymbol{A}} + \hat{\boldsymbol{A}}$ (which is equivalent to the decomposition of the magnetic field in the form $\boldsymbol{B} = \bar{\boldsymbol{B}} + \hat{\boldsymbol{B}}$ as introduced in § 4.1.4).

To summarize, our strategy to find the total 3D magnetic vector potential involves, on the one hand, the calculation of the current-carrying part $\hat{\boldsymbol{A}}$ by solving $\Delta\hat{\boldsymbol{A}} = -\mu_0 \boldsymbol{J}$ (which is hereafter called the "inhomogeneous" problem; see § 4.3.2) and, on the other hand, the computation of the Laplacian part $\bar{\boldsymbol{A}}$ by solving $\Delta\bar{\boldsymbol{A}} = 0$ (hereafter named the "homogeneous" problem; see § 4.3.3). Finally, the summation of the two derived parts $\bar{\boldsymbol{A}}$ and $\hat{\boldsymbol{A}}$ gives us the total 3D magnetic vector potential so that $\boldsymbol{B} = \nabla\times\boldsymbol{A} = \nabla\times(\bar{\boldsymbol{A}} + \hat{\boldsymbol{A}})$.

4.3.2 Inhomogeneous problem

The inhomogeneous problem corresponds to find a vector potential $\hat{\boldsymbol{A}}$ in V which takes the electric current density $\boldsymbol{J}$ into account and is of the form

$$\Delta\hat{\boldsymbol{A}} = -\mu_0\,\boldsymbol{J} \tag{4.31}$$

which, using $\nabla\cdot\hat{\boldsymbol{A}}=0$, follows from (4.28). Since $\hat{\boldsymbol{A}}$ is ambiguous with respect to a gauge transform $\hat{\boldsymbol{A}}'=\hat{\boldsymbol{A}}+\nabla\xi$ (with ξ being an arbitrary scalar function), we impose a condition on the tangential component of the vector potential $\hat{\boldsymbol{A}}_t$ on the boundary of the form

$$\boldsymbol{n}\times\hat{\boldsymbol{A}} = 0 \quad \text{on } \partial V. \tag{4.32}$$

A gauge transform $\hat{\boldsymbol{A}}'=\hat{\boldsymbol{A}}+\nabla\xi$ then requires

$$\nabla\cdot\hat{\boldsymbol{A}}' = 0 \quad \rightarrow \quad \Delta\xi = 0 \ \text{ in } V, \tag{4.33}$$

$$\boldsymbol{n}\times\hat{\boldsymbol{A}}' = 0 \quad \rightarrow \quad \boldsymbol{n}\times\nabla\xi = 0 \ \text{ on } \partial V. \tag{4.34}$$

Now, (4.34) is automatically satisfied where $\boldsymbol{n}\parallel\nabla\xi$ on ∂V. On boundaries where $\boldsymbol{n}\perp\nabla\xi$ it is only fulfilled if $\nabla\xi=0$ and hence ξ must be constant on those boundaries. Therefore, and since ξ suffices the Laplace equation (4.33), ξ is constant on ∂V and on the whole of V so that $\hat{\boldsymbol{A}}$ in (4.31) and (4.32) is uniquely specified.

To solve the inhomogeneous problem in a cubic box we consider three scalar Poisson problems for each Cartesian component x_i of the magnetic vector potential, namely

$$\Delta\hat{\boldsymbol{A}}_{x_i} = -\mu_0\,J_{x_i} \tag{4.35}$$

with $i=(1,2,3)$, $(x_1,x_2,x_3)=(x,y,z)$ and J_{x_i} being the Cartesian components of the current density. Then, (4.35) is subject to the mixed Dirichlet/Neumann boundary conditions

$$\hat{\boldsymbol{A}}_{x_i} = 0 \ \text{ where } \boldsymbol{e}_{x_i}\perp\boldsymbol{n}, \tag{4.36}$$

$$\partial_{x_i}\hat{\boldsymbol{A}}_{x_i} = 0 \ \text{ where } \boldsymbol{e}_{x_i}\parallel\boldsymbol{n} \tag{4.37}$$

with $(\boldsymbol{e}_{x_1},\boldsymbol{e}_{x_2},\boldsymbol{e}_{x_3})=(\boldsymbol{e}_x,\boldsymbol{e}_y,\boldsymbol{e}_z)$. These boundary conditions guarantee that the tangential divergence $\nabla_t\cdot\hat{\boldsymbol{A}}_t=0$ vanishes on ∂V and together with $\nabla\cdot\hat{\boldsymbol{A}}=0$ in V ensure the entire divergence-freeness of $\hat{\boldsymbol{A}}$. Since $\boldsymbol{J}$ does not vanish on ∂V the Cartesian components $\hat{\boldsymbol{A}}_{x_i}$ have to satisfy, besides the Neumann condition (4.37), also the Poisson equation

$$\partial^2_{x_i}\hat{\boldsymbol{A}}_{x_i} = -\mu_0\,J_{x_i} \ \text{ where } \boldsymbol{e}_{x_i}\parallel\boldsymbol{n}. \tag{4.38}$$

Clearly, for a Laplace magnetic field $\hat{\boldsymbol{A}}$ vanishes (since $\boldsymbol{J}=0$) so that the vector potential found up to now yields the current-carrying part of the total magnetic field $\boldsymbol{B}$ only.

4.3.3 Homogeneous problem

Seehafer (1978) provided an analytical formulation to derive the potential (Laplacian) field $\bar{\boldsymbol{B}}$. From the Fourier representation of the three Cartesian components $\bar{\boldsymbol{B}}_x$, $\bar{\boldsymbol{B}}_y$ and $\bar{\boldsymbol{B}}_z$ one can explicitly write down the corresponding analytical expressions for $\bar{\boldsymbol{A}}_x$, $\bar{\boldsymbol{A}}_y$ and $\bar{\boldsymbol{A}}_z$. Using Fourier expansions for the magnetic field and the associated vector potential is

advantageous considering the resulting reduced computation time needed for the calculations. However, Fourier methods require the potential magnetic field $\bar{\boldsymbol{B}}$ to be periodic. Since we want to avoid the assumption of periodic boundary conditions within our force-free field calculations, and therefore use the Green's function method after Aly (1989) to calculate the potential field, we developed an alternative numerical method to solve the homogeneous problem in order to find the associated vector potential $\bar{\boldsymbol{A}}$.

For the homogeneous problem we cannot maintain (4.30) anymore but must take magnetic field on the boundaries into account. The Laplacian field $\bar{\boldsymbol{B}}$ satisfies the same normal boundary condition as $\boldsymbol{B}$ on ∂V (i.e., $\boldsymbol{n}\cdot\bar{\boldsymbol{B}} = \boldsymbol{n}\cdot\boldsymbol{B}$) and the tangential magnetic field is explicitly required. To find the solution of the homogeneous problem we thus have to solve

$$\Delta\bar{\boldsymbol{A}} = 0 \tag{4.39}$$

which, using $\nabla\cdot\bar{\boldsymbol{A}} = 0$ and $\boldsymbol{J} = 0$ follows from (4.28), subject to the boundary requirement

$$\boldsymbol{n}\cdot\bar{\boldsymbol{B}} = \boldsymbol{n}\cdot(\nabla\times\bar{\boldsymbol{A}}) \quad \text{on } \partial V. \tag{4.40}$$

Since (4.40) involves derivatives it is not as restrictive as a boundary condition of the form (4.30) and still allows gauge transforms which automatically maintain the boundary conditions (4.40). In particular, a gauge $\bar{\boldsymbol{A}}' = \bar{\boldsymbol{A}} + \nabla\xi$ requires

$$\nabla\cdot\bar{\boldsymbol{A}}' = 0 \quad \rightarrow \quad \Delta\xi = 0 \ \text{ in } V, \tag{4.41}$$

where ξ denotes any scalar Laplace field. A gauge which maintains (4.40) requires similar as in (4.33) that ξ is constant in V. However, since $\nabla\xi$ does not affect $\nabla\times\bar{\boldsymbol{A}}$, ξ is still ambiguous on ∂V. Consequently, $\bar{\boldsymbol{A}}$ in (4.39) and (4.40) is not uniquely fixed so that we additionally have to solve for ξ on the boundaries.

To solve (4.39) and (4.40) in a cubic box we again treat the three Cartesian components x_i (with $i = (1,2,3)$ and $(x_1, x_2, x_3) = (x, y, z)$) of the magnetic vector potential separately and solve the three boundary value Laplace problems

$$\Delta\bar{\boldsymbol{A}}_{x_i} = 0 \tag{4.42}$$

with the mixed Dirichlet/Neumann boundary conditions

$$\bar{\boldsymbol{A}}_{x_i} = \text{given} \quad \text{where } \boldsymbol{e}_{x_i} \perp \boldsymbol{n}, \tag{4.43}$$

$$\partial_{x_i}\bar{\boldsymbol{A}}_{x_i} = 0 \quad \text{where } \boldsymbol{e}_{x_i} \parallel \boldsymbol{n}. \tag{4.44}$$

The boundary condition (4.44) ensures $\nabla_t\cdot\bar{\boldsymbol{A}}_t = 0$ on ∂V and, together with $\nabla\cdot\bar{\boldsymbol{A}} = 0$, the entire divergence-freeness of $\bar{\boldsymbol{A}}$. In this way, the solution of the Laplace equation (4.42) is up to a constant well-defined.

It remains to determine the 2D Cartesian components of $\bar{\boldsymbol{A}}_{x_i}$ on ∂V in (4.43). Therefore, we take advantage of the vanishing 2D divergence on ∂V (i.e., $\nabla_t\cdot\bar{\boldsymbol{A}}_t = 0$) so that we can consider $\bar{\boldsymbol{A}}_t$ on ∂V to be generated by the 2D stream functions of a Laplacian field $\bar{\xi}$. According to (4.40), we thus have to solve a 2D Laplace problem of the form

$$\Delta\bar{\xi} = -\bar{\boldsymbol{B}}\cdot\boldsymbol{n}, \tag{4.45}$$

on each boundary, subject to the Neumann boundary condition

$$\partial_n\bar{\xi} = \sigma_e\,\bar{\boldsymbol{A}}_e, \tag{4.46}$$

where $\bar{\boldsymbol{A}}_e$ are previously unknown constant values of $\bar{\boldsymbol{A}}$ on the edges of each 2D boundary (hereafter we refer to a 2D boundary of our cubic computational domain as to a "face"). We introduce σ_e in order to account for the possibly different orientation which an edge may have with respect to the two faces it is connected to (which can thus have a value of +1 or −1). We not only use the σ_e to ensure that the sum over all four $\bar{\boldsymbol{A}}_e$ (one for each edge of a face) of every face, i.e. $\sum_{e=1}^{4} \sigma_e \bar{\boldsymbol{A}}_e$ yields a proper circulation and equals the total outflow of a face, but also to ensure that the sign of each $\bar{\boldsymbol{A}}_e$ is correct with respect to the face outward normal vector $\boldsymbol{n}$. Once the constant $\bar{\boldsymbol{A}}_e$ on all edges of the computational box are known, we can supply (4.45) with the required Neumann boundary conditions (4.46). After solving (4.45) to calculate the 2D stream function $\bar{\xi}$ on each face, we can determine the tangential components of the vector potential using $\bar{\boldsymbol{A}}_t = -\boldsymbol{n} \times \nabla \bar{\xi}$ so that, explicitly as required in (4.43), we compute

$$\left(\bar{A}_{ij}, \bar{A}_{ik}\right) = \left(-\partial_{x_k} \bar{\xi}, \partial_{x_j} \bar{\xi}\right), \tag{4.47}$$

where (i, j, k) are positive permutations of $(1, 2, 3)$. These values are supposed to be continuous on every edge where two faces join. Implicitly, the in this way constructed $\bar{\xi}$ yields a vanishing 2D divergence $\nabla_t \cdot \bar{\boldsymbol{A}}_t = 0$, or explicitly, $\partial_{x_k} \bar{A}_k + \partial_{x_j} \bar{A}_j = 0$ on every face. Then, following Gauss' (divergence) theorem, $\bar{\boldsymbol{A}}$ also has a vanishing 3D divergence.

4.3.3.1 Calculation of the constant $\bar{A}_e$-values

We choose $\bar{\boldsymbol{A}}_e$ in (4.46) as constant values of the vector potential $\bar{\boldsymbol{A}}$ at the edges of each face of the computational domain and the following discussion is therefore restricted to a purely 2D geometry. We construct $\bar{\boldsymbol{A}}_e$ along the edges of a face in a way that the circulation on each face gives the correct outflow

$$\Phi_f = \int_S \bar{\boldsymbol{B}} \cdot d\boldsymbol{S} = \oint_{\partial S} \bar{\boldsymbol{A}} \cdot d\boldsymbol{l} = \sum_{e=1}^{4} \sigma_e \bar{\boldsymbol{A}}_e L_e \tag{4.48}$$

which the solution for $\bar{\xi}$ in (4.45) delivers correctly due to the boundary condition (4.46). Here, Φ_f denotes the net flux through an individual face, $\sigma_e = \pm 1$ accounts for the orientations of the edges with respect to the particular face and L_e represent the side lengths of a the face. Since we deal with a rectangular grid with all values being defined on the intersections of the grid cells (i.e. at the nodes of the grid and not in the center of the grid cells), we assume the contribution of the magnetic field to the net flux at the corners of a face (that are the pixels at the two ends of each edge) to be 25% and that of the magnetic field along the edges (without the corners) to be 50%. The magnetic field of all other points on the faces (that are all the pixels except that of the corners and on the edges) is assumed to contribute with 100% to a face's net flux. For our cubic computational box we have six faces (2D boundaries) and each of those has four unknowns $\bar{\boldsymbol{A}}_e$ (one for each edge). To repeat, the values of $\bar{\boldsymbol{A}}_e$ on edges where two faces join have to coincide so that in total 12 unknowns have to be determined. From (4.48) six equations arise (one for each face) which, evidently, are not sufficient to determine the 12 unknown values $\bar{\boldsymbol{A}}_e$ uniquely since there exist many possible sets of $\bar{\boldsymbol{A}}_e$ which satisfy (4.48). Therefore, we introduce an additional constraint in order to obtain the unique values of $\bar{\boldsymbol{A}}_e$ so that we minimize, besides (4.48), also $\sum_{e=1}^{12} \bar{\boldsymbol{A}}_e^2$ and the in this way determined set of $\bar{\boldsymbol{A}}_e$ fulfills

the requirement that the total outflow Φ over all faces vanishes (i.e., $\Phi = \sum_{f=1}^{6} \Phi_f = 0$). So far, we constructed a set of edge parameters $\bar{\boldsymbol{A}}_e$ in (4.48) the squared sum of which has to be minimized. A common way to minimize a given function subject to side constraints is to use the method of Lagrangian multipliers. The Lagrangian function corresponding to our particular problem reads as

$$\mathcal{L}\left(\bar{\boldsymbol{A}}_e, \lambda_f\right) = \sum_{e=1}^{12} \bar{\boldsymbol{A}}_e^2 + \sum_{f=1}^{6} \lambda_f \cdot \left(\Phi_f - \sum_{e=1}^{4} \sigma_e \, \bar{\boldsymbol{A}}_e \, L_e\right), \tag{4.49}$$

where λ_f are six Lagrange multipliers. Note that incorporating all six faces of the cubic box in the last term of (4.49) is not necessary. This is because we constructed our problem so that $\Phi = 0$ and we can therefore omit one of the six faces in order not to overdetermine the associated system of equations. Therefore, we decide to leave the top face of the cubic box in the last term of (4.49) aside. This is justified since (although even in case of potential fields a large amount of magnetic flux can cross the boundaries) the coronal magnetic field is strongly decreasing with increasing height. This is because (for flux-balanced magnetograms as lower boundary condition) the strong fields close within low heights so that only little flux is free to leave through the top boundary. Therefore, the requirement of the vanishing total outflow should still be delivered correctly by minimizing

$$\mathcal{L}\left(\bar{\boldsymbol{A}}_e, \lambda_f\right) = \sum_{e=1}^{12} \bar{\boldsymbol{A}}_e^2 + \sum_{f=1}^{5} \lambda_f \cdot \left(\Phi_f - \sum_{e=1}^{4} \sigma_e \, \bar{\boldsymbol{A}}_e \, L_e\right). \tag{4.50}$$

To solve this minimization problem we build the first partial derivatives $\partial_{\bar{\boldsymbol{A}}_e} \mathcal{L}$, arising from the first term on the right-hand side of (4.50) to obtain 12 individual expressions for $\bar{\boldsymbol{A}}_e$ as functions of the Lagrangian multipliers λ_f and the length of the individual edge L_e. Those can be inserted into the five relations for Φ_f which we gain by taking the partial derivatives $\partial_{\lambda_f} \mathcal{L}$, arising from the second term on the right-hand side of (4.50). Accordingly, we obtain a linear system of five equations to be solved for the λ_f. Once the λ_f are found, we insert them back into the 12 relations $\partial_{\bar{\boldsymbol{A}}_e} \mathcal{L}$ to attain the unique values of $\bar{\boldsymbol{A}}_e$. With the knowledge of all the $\bar{\boldsymbol{A}}_e$ we properly specify the Neumann boundary condition (4.46) which we need to provide to the 2D Poisson problems (4.45) on each face of the cubic box.

In the previous sections, the problem of finding the total 3D magnetic vector potential for a given 3D magnetic field has been introduced as the task to find the solutions of homogeneous and inhomogeneous equations, subject to appropriate Dirichlet or Neumann boundary conditions. The solution of these problems is achieved by solving either Poisson or Laplace equations and the numerical implementation is discussed in the following.

4.3.4 Numerical solution of the Poisson and Laplace equations

4.3.4.1 Finite difference formulation

A Poisson problem involving three spatial dimensions is of the form

$$\Delta\Psi(x_1, x_2, x_3) = \partial_{x_1}^2 \Psi + \partial_{x_2}^2 \Psi + \partial_{x_3}^2 \Psi = F(x_1, x_2, x_3), \tag{4.51}$$

where $(x_1, x_2, x_3) = (x, y, z)$, $F(x_1, x_2, x_3)$ is a known function and that is what we formally solve in § 4.3.2. A Laplace problem can be regarded as a special case of (4.51) if $F(x_1, x_2, x_3) = 0$ which is therefore called a "homogeneous" Poisson problem (as technically solved for in § 4.3.3). Note that in the case of a 2D Poisson problem (as is (4.45) in § 4.3.3) only two spatial coordinates are considered, e.g., x_1 and x_2 for the bottom boundary of the computational box with the coordinates $(x_1, x_2, x_3 = 0)$. Then x_3 would not appear in (4.51) and Ψ and F would be a function of x_1 and x_2 only (i.e., $\Psi = \Psi(x_1, x_2)$ and $F = F(x_1, x_2)$). In the following, the formal approximation and numerical implementation of (4.51) is demonstrated.

Using central finite differences, $\Delta\Psi$ in (4.51) at every point (x_1, x_2, x_3) inside a considered volume (except on the boundaries) can be written as

$$\begin{aligned}\Delta\Psi_{x_1,x_2,x_3} &= \frac{\Psi_{x_1+h,x_2,x_3} - 2\,\Psi_{x_1,x_2,x_3} + \Psi_{x_1-h,x_2,x_3}}{h^2} \\ &+ \frac{\Psi_{x_1,x_2+h,x_3} - 2\,\Psi_{x_1,x_2,x_3} + \Psi_{x_1,x_2-h,x_3}}{h^2} \\ &+ \frac{\Psi_{x_1,x_2,x_3+h} - 2\,\Psi_{x_1,x_2,x_3} + \Psi_{x_1,x_2,x_3-h}}{h^2},\end{aligned} \tag{4.52}$$

where we use $\Delta x_1 = \Delta x_2 = \Delta x_3 = h$ as the distance between the individual grid points. After rearranging (4.52) and substitution into (4.51) we find

$$\begin{aligned}\Psi_{x_1,x_2,x_3} &= \frac{1}{6}\Big(\Psi_{x_1+h,x_2,x_3} + \Psi_{x_1-h,x_2,x_3} + \Psi_{x_1,x_2+h,x_3} \\ &\quad + \Psi_{x_1,x_2-h,x_3} + \Psi_{x_1,x_2,x_3+h} + \Psi_{x_1,x_2,x_3-h} - h^2 F_{x_1,x_2,x_3}\Big).\end{aligned} \tag{4.53}$$

This means that if $\Psi(x_1, x_2, x_3)$ satisfies the Poisson equation (4.51) it is at any point inside the considered domain (but not on its boundaries) given by the average of the values of Ψ at the surrounding points. Consequently, in 3D the six points surrounding Ψ in a seven-point stencil determine the value of Ψ in the center of the stencil. Note again that in the case of a 2D Poisson problem we would only consider two spatial coordinates, say x_1 and x_2, and x_3 would not appear in (4.52) and (4.53). Furthermore, we would deal with $\Psi = \Psi(x_1, x_2)$ and $F = F(x_1, x_2)$ and a factor of 1/4 instead of 1/6 would appear in (4.53). Accordingly, the four points surrounding $\Psi(x_1, x_2)$ in a five-point stencil would determine the value of Ψ in the center of the stencil.

On the boundaries of a considered domain, however, no seven- or five-point stencils (in 3D and 2D, respectively) exist because the points on the boundaries are only neighbored by five or three points, respectively. On boundaries where we have to incorporate Dirichlet boundary conditions this imposes no problem since $\Psi(x_1, x_2, x_3)$ or $\Psi(x_1, x_2)$, respectively, can simply be specified in form of constant values on those boundaries. For our case, we explicitly impose zeros on the 2D boundaries of our cubic domain according to (4.36) and (4.43). Where we have to impose Neumann boundary conditions, however, we need to specify derivatives. For our particular problem, this implies the specification of first-order partial derivatives on the 2D faces of the 3D domain due to (4.37) and (4.44) and on the edges of the 2D faces because of (4.46) but also the incorporation of second-order partial derivatives on the 2D faces in accordance to (4.38).

There is a choice how to approximate first-order partial derivatives within the finite-difference approximation, namely in form of a forward or backward one-sided finite difference. For a 2D function $\Psi(x_1, x_2)$ the forward and backward difference expression for

the first-order partial derivative with respect to x_1 read $\partial_{x_1}\Psi_{x_1,x_2} \approx h^{-1}(\Psi_{x_1+h,x_2} - \Psi_{x_1,x_2})$ and $\partial_{x_1}\Psi_{x_1,x_2} \approx h^{-1}(\Psi_{x_1,x_2} - \Psi_{x_1-h,x_2})$, respectively, where $h = \Delta x_1$ and which both are first-order accurate. Alternatively, a centered finite-difference approximation of the form $\partial_{x_1}\Psi_{x_1,x_2} \approx (2h)^{-1}(\Psi_{x_1+h,x_2} - \Psi_{x_1-h,x_2})$ is applicable which we favor due to its second-order accuracy and which we use in order to fulfill the Neumann boundary conditions (4.46) on the 2D faces of our computational box. Note that on the two edges of the 2D faces where $x_1 = 0$ and $x_1 = L_x$ (if $0 \le x_1 \le L_{x_1}$ represents the length of the edge in the x_1-direction), Ψ_{x_1-h,x_2} and Ψ_{x_1+h,x_2}, respectively, refer to points outside the 2D face. In a similar way, Ψ_{x_1,x_2-h} and Ψ_{x_1,x_2+h} refer to points outside the face if we wanted to employ the central-difference expression for $\partial_{x_2}\Psi_{x_1,x_2}$ at $x_2 = 0$ and $x_2 = L_y$, respectively (if $0 \le x_2 \le L_{x_2}$ is the extent of the edge in the x_2-direction). Consequently, for such cases we need to introduce a set of fictitious grid points around the considered 2D plane. These fictitious points Ψ' have to be specified at $x_1 = -1$, $x_1 = L_{x_1}+1$, $x_2 = -1$ and $x_2 = L_{x_2}+1$ in a way that the central-difference expression for the derivative gives the required boundary values and that Ψ can still be determined with the help of a five-point stencil on the edges where $x_1 = 0$, $x_1 = L_{x_1}$, $x_2 = 0$ and $x_2 = L_{x_2}$. We introduce such fictitious grid points around the 2D faces of the 3D computational volume to solve the 2D Poisson problems (4.45), subject to the Neumann boundary condition (4.46). We also need to find the relevant finite-difference expressions to simultaneously fulfill the Neumann boundary conditions (4.37) and (4.38) for the inhomogeneous 3D problem (4.35), involving first- and second-order partial derivatives on the boundaries of the 3D box. Fortunately, the combination of these two boundary requirements simplifies the problem to find the appropriate finite-difference terms. To do so, we make use of the first-order accurate forward- and backward-difference expressions of (4.37). For example, according to (4.37), at $x_1 = 0$ we have $\partial_{x_1}\Psi_{x_1,x_2} \approx h^{-1}(\Psi_{x_1,x_2} - \Psi_{x_1-h,x_2}) = 0$, where $h = \Delta x_1$. This implies that $\Psi_{-1,x_2} = h\,\Psi_{0,x_2}$, i.e. that we can immediately specify the value of Ψ at the point outside the 2D face. Hence, we can supply the central-difference expression $\partial_{x_1}\Psi_{x_1,x_2} \approx (2h)^{-1}(\Psi_{x_1+h,x_2} - \Psi_{x_1-h,x_2})$ of (4.38) at $x_1 = 0$ with the previously unknown value of Ψ_{-1,x_2} without the need to introduce a fictitious layer. In a similar way, one formulates the expressions for $\partial_{x_2}\Psi_{x_1,x_2}$ at $x_2 = 0$, for $\partial_{x_1}\Psi_{x_1,x_3}$ where $x_1 = 0$, for $\partial_{x_3}\Psi_{x_1,x_3}$ where $x_3 = 0$, for $\partial_{x_2}\Psi_{x_2,x_3}$ where $x_2 = 0$ and for $\partial_{x_3}\Psi_{x_2,x_3}$ where $x_3 = 0$. Accordingly, we use forward-difference expression of (4.37) to supply the central-difference expressions of (4.38) with the required values where $x_1 = L_{x_1}$, $x_2 = L_{x_2}$, or $x_3 = L_{x_3}$. To approximate the first-order derivatives (4.44), required for solving the 3D homogeneous (Laplacian) problems in (4.42), we use alternative expressions which arise from the polynomial fit to forward or backward differences. These so-called one-sided finite differences are also second-order accurate but instead of defining fictitious points one makes use of the weighted values of the two next points towards the interior of the volume, neighboring a point on a boundary. Explicitely, we are therefore using $\partial_{x_1}\Psi_{x_1,x_2} \approx (2h)^{-1}(\mp 3\Psi_{x_1,x_2} \pm 4\Psi_{x_1+h,x_2} \mp \Psi_{x_1+2h,x_2})$ at $x_1 = 0$ and $x_1 = L_{x_1}$ where the alternating signs of the components correspond to taking the forward difference at $x_1 = 0$ and the backward difference at $x_1 = L_{x_1}$. Similarly, we find the expression for $\partial_{x_2}\Psi_{x_1,x_2}$ at $x_2 = 0$ and $x_2 = L_{x_2}$, for $\partial_{x_1}\Psi_{x_1,x_3}$ at $x_1 = 0$ and $x_1 = L_{x_1}$, for $\partial_{x_3}\Psi_{x_1,x_3}$ at $x_3 = 0$ and $x_3 = L_{x_3}$, for $\partial_{x_2}\Psi_{x_2,x_3}$ at $x_2 = 0$ and $x_2 = L_{x_2}$ and for $\partial_{x_3}\Psi_{x_2,x_3}$ at $x_3 = 0$ and $x_3 = L_{x_3}$.

4.3.4.2 Iterative solution

The Poisson and Laplace equations are a set of m linear equations in k variables which can be represented in matrix form as

$$\mathbf{C}\,\mathbf{v} = \mathbf{s} \tag{4.54}$$

with $\mathbf{C} = (c_{ij})$ being the $m \times m$ matrix of coefficients, $\mathbf{v}$ representing the column vector of variables and $\mathbf{s}$ denoting the column vector of solutions. If $k < m$, the system is said to be over-determined and no solution exists. If $k = m$ and $\mathbf{C}$ is non-singular the system has an unique solution in the m variables. To solve the linear system of equations we use the successive overrelation method (SOR). This is a faster converging variant of the Gauss-Seidel method which takes a weighted average between two successive Gauss-Seidel iterations and which can in matrix terms be written as

$$\mathbf{v}^n = (\,\mathbf{D} - w_{\rm SOR}\,\mathbf{L}\,)^{-1}\,\Big(\,w_{\rm SOR}\,\mathbf{U} + (\,1 - w_{\rm SOR}\,)\,\mathbf{D}\,\Big)\,\mathbf{v}^{n-1} + w_{\rm SOR}\,(\,\mathbf{D} - w_{\rm SOR}\,\mathbf{L}\,)^{-1}\,\mathbf{s}, \tag{4.55}$$

where $\mathbf{D}$, $-\mathbf{L}$ and $-\mathbf{U}$ represent the diagonal, strictly lower-triangular and strictly upper-triangular parts of $\mathbf{C}$, respectively, $w_{\rm SOR}$ is the SOR parameter and n denotes the number of iteration. The sequence of vectors $\mathbf{v}^n$ will converge to a solution $\mathbf{v}$ of (4.54), and hence of (4.55), provided that the spectral radius ρ (that is the magnitude of the largest eigenvalue of a matrix associated with $\mathbf{C}$) is less than unity (Verner and Bernal 1968). This means that convergence is only achieved if and only if the spectral radius of the SOR matrix $(\mathbf{D} - w_{\rm SOR}\,\mathbf{L})^{-1}\,(w_{\rm SOR}\,\mathbf{U} + (1 - w_{\rm SOR})\,\mathbf{D})$ is lower than unity and if so it will converge to the exact solution $\mathbf{v} = \mathbf{C}^{-1}\,\mathbf{s}$ (Hajjafar 2006). In particular, the smaller ρ the more rapid is the convergence and for the SOR method it is therefore desirable to choose $w_{\rm SOR}$ so that ρ is minimal. We have not yet carried out the required calculations for finding the optimum $w_{\rm SOR}$ using the spectral radius of the SOR matrix but a corresponding analysis is planned for the future.

However, the relaxation parameter can be used either to speed up the convergence of a slow-converging process (with the choice $w_{\rm SOR} > 1.0$ for SOR) or to establish convergence of a diverging process (using $w_{\rm SOR} < 1.0$ for a so-called successive under-relaxation). In general, a value $0 < w_{\rm SOR} < 2$ leads to convergence and the particular choice $w_{\rm SOR} = 1.0$ represents a basic Gauss-Seidel algorithm. For the iterative solution of the 3D Poisson and Laplace problems (4.35) and (4.42), respectively, we chose $w_{\rm SOR} = 1.7$ and we use $w_{\rm SOR} = 1.9$ for solving the 2D Poisson problems (4.45). By taking advantage of the triangular form of $(\mathbf{D} - w_{\rm SOR}\,\mathbf{L})$ the elements $\mathbf{v}^n$ can be computed in the form

$$v_i^n = (\,1 - w_{\rm SOR}\,)\,v_i^{n-1} + \frac{w_{\rm SOR}}{c_{ii}}\left(\,s_i - \sum_{j>i} c_{ij}\,v_j^{n-1} - \sum_{j<i} c_{ij}\,v_j^n\right) \tag{4.56}$$

with $i = 1,\ldots,m$. Within our finite-difference approximation the SOR update (4.56) is explicitly written as

$$\Psi^n_{x_1,x_2,x_3} = (\,1 - w_{\rm SOR}\,)\,\Psi^{n-1}_{x_1,x_2,x_3} + w_{\rm SOR}\,\Psi^{\star\,n}_{x_1,x_2,x_3}. \tag{4.57}$$

Here, $\Psi^{n-1}_{x_1,x_2,x_3}$ denotes the Gauss-Seidel update of the previous iteration and $\Psi^{\star\,n}_{x_1,x_2,x_3}$ denotes the Gauss-Seidel update of the current iteration in the form

$$\begin{aligned}\Psi^{\star\,n}_{x_1,x_2,x_3} \;=\; \frac{1}{6}\,\Big(&\Psi^{n-1}_{x_1+h,x_2,x_3} + \Psi^{n}_{x_1-h,x_2,x_3} + \Psi^{n-1}_{x_1,x_2+h,x_3} \\ &+ \Psi^{n}_{x_1,x_2-h,x_3} + \Psi^{n-1}_{x_1,x_2,x_3+h} + \Psi^{n}_{x_1,x_2,x_3-h} - h^2 F_{x_1,x_2,x_3}\Big).\end{aligned} \tag{4.58}$$

The character of the Gauss-Seidel method, making use of computed results as soon as they are available is evident. At every iteration n the already updated values Ψ_{x_1-h,x_2,x_3}, Ψ_{x_1,x_2-h,x_3} and Ψ_{x_1,x_2,x_3-h} are immediately incorporated, assuming that these updated values are closer to the sought-after solution. Note again that in the case of a 2D Poisson problem one would only consider two of the coordinates, say x_1 and x_2, so that x_3 would not appear in (4.58), Ψ and F would only be a function of x_1 and x_2 and a factor of 1/4 instead of 1/6 would appear.

4.3.4.3 Remark on the relative helicity integral

We just discussed how to derive both the current-carrying part $\hat{\boldsymbol{A}}$ and the Laplacian part $\bar{\boldsymbol{A}}$ of the vector potential so that we can simply sum them up to get the total magnetic vector potential $\boldsymbol{A} = \hat{\boldsymbol{A}} + \bar{\boldsymbol{A}}$ of the total magnetic field $\boldsymbol{B}$ in V. We derived the Laplacian part in a way that we involves the correct values $\bar{\boldsymbol{B}}_n = \boldsymbol{B}_n$ on ∂V, though not considering the presence of electric currents. Additionally, we constructed the current-carrying part in a way that it owns the correct electric currents $\boldsymbol{J}$, without incorporating the values of the magnetic field on ∂V (note that $\hat{\boldsymbol{A}}$ was defined to have no tangential components on ∂V and hence does not destroy the boundary condition for $\bar{\boldsymbol{A}}$ if the two are added). Consequently, the calculated 3D vector potential owns the electric currents as well as the correct boundary values. From the way of deriving $\hat{\boldsymbol{A}}$ and $\bar{\boldsymbol{A}}$, one may recognize that we could have avoided to split $\boldsymbol{A}$ if we were using the boundary condition (4.40) instead of (4.32) right from the beginning. However, first of all we are now able to calculate the relative magnetic helicity of a coronal volume according to (4.25) as introduced in § 4.1.4 and, second, this splitting turns out to be convenient due to the following reason. The integral formulation for the relative helicity as the sum of the self helicity of the closed field and the mutual helicity between the vacuum and the closed field has been introduced in (4.24). However, we can now show that

$$\int_V \left(\hat{\boldsymbol{A}} \cdot \bar{\boldsymbol{B}} - \bar{\boldsymbol{A}} \cdot \hat{\boldsymbol{B}} \right) d^3x = \int_V \nabla \cdot \left(\bar{\boldsymbol{A}} \times \hat{\boldsymbol{A}} \right) d^3x = \oint_S \left(\bar{\boldsymbol{A}} \times \hat{\boldsymbol{A}} \right) \cdot d\boldsymbol{S} = 0, \qquad (4.59)$$

since we constructed $\hat{\boldsymbol{A}}$ in a way that $\hat{\boldsymbol{A}}_t = 0$ on ∂V. Consequently, $\bar{\boldsymbol{A}} \cdot \hat{\boldsymbol{B}} = \hat{\boldsymbol{A}} \cdot \bar{\boldsymbol{B}}$ and we can rewrite (4.24) as

$$H_{rel} = \int_V \hat{\boldsymbol{A}} \cdot \left(\boldsymbol{B} + \bar{\boldsymbol{B}} \right) d^3x \qquad (4.60)$$

so that determining the current-carrying part $\hat{\boldsymbol{A}}$ alone would be sufficient to estimate the relative helicity and we could avoid the calculation of $\bar{\boldsymbol{A}}$.

4.3.5 Testing the method

To test our recently implemented method to calculate the 3D vector potential we used, as for the testing of the Hα-preprocessing scheme presented in § 2.4.2.4, the active region model developed by A. A. van Ballegooijen. First, a full-disk photospheric line-of-sight SoHO/MDI magnetogram showing the isolated NOAA AR 10814 was used to compute a 3D potential field in spherical coordinates. Corresponding to an observed Hα filament a model flux rope was inserted into the calculated potential configuration. After relaxing the whole system to a NLFF state using a magneto-frictional method (van Ballegooijen

et al. 2000) a 3D model atmosphere resulted which is force-free throughout the entire domain except within two gridpoints above the lower boundary (van Ballegooijen 2004, van Ballegooijen et al. 2007). We assume the layer at the bottom of the force-free region (i.e. the layer at the third grid point above the lower boundary of the box) to represent a chromospheric-like solar magnetic field. This model chromosphere we used as the lower boundary condition to extrapolate a NLFF field with the help of our optimization code (Wiegelmann 2004) for which we aimed to determine the 3D vector potential. The resulting computational box in Cartesian coordinates, containing the extrapolated NLFF field is of the dimension $320\times320\times256$ pixels and in the following we denote the spatial extensions in the x-, y- and z-directions as $0 \le x \le L_x$, $0 \le y \le L_y$ and $0 \le z \le L_z$, respectively. Furthermore, we call the 2D boundaries of our 3D box the "left", "right", "front", "back", "bottom" and "top" face, referring to the boundaries with the coordinates $(0, y, z)$, (L_x, y, z), $(x, 0, z)$, (x, L_y, z), $(x, y, 0)$ and (x, y, L_z), respectively. In other words, we name the faces based on their apparent position when facing the $(x, 0, z)$-plane of the cubic domain.

We started with solving the 2D Poisson problems (4.45) on each face of the computational box to find the 2D stream functions $\bar{\xi}(x_i, x_j)$ (with $i=(x,y,z)$, $j=(x,y,z)$ and $i \neq j$), determining the tangential components of the Laplacian vector potential $\bar{\boldsymbol{A}}$. According to (4.46), we therefore calculated the unknown constant values $\bar{\boldsymbol{A}}_e$ on each edge of each face. Hence, according to (4.50), we solved the system of linear equations to find five Lagrangian multipliers λ_f (one for each face, excluding the top face). For this purpose, we implemented the "LU matrix decomposition", representing a matrix as the product of a lower triangular and an upper triangular matrix. Remember that within our numerical scheme we simultaneously ensure that the resulting λ_f (and hence the $\bar{\boldsymbol{A}}_e$) balance the outflow through the individual faces and that the total outflow over all faces is numerically zero. We were then able to specify the required Neumann boundary conditions in (4.46) and to supply them to the 2D Poisson problems (4.45) of the form $\Delta\bar{\xi}(x_i, x_j) = -F(x_i, x_j)$, where $F(x_i, x_j)$ denotes the known normal magnetic field component $\bar{\boldsymbol{B}}_n$ of each particular face. As introduced in § 4.3.4.2, we iteratively solve the 2D Poisson problems using a SOR method (as presented for the 3D case in (4.57)). We chose a relaxation factor of $w_{\mathrm{SOR}} = 1.9$ for the presented test case and note again that the retrieval of the optimum w_{SOR} is left as a future task. To follow the performance of the iterative solution of the 2D Poisson problems, we calculated for each iteration n a measure for the maximum update for two consecutive iterations. We took the maximum of the absolute difference between the updated function $\bar{\xi}^n_{x_i,x_j}$ and the update of the previous iteration $\bar{\xi}^{n-1}_{x_i,x_j}$ in the form

$$U^n_{max} = \max\left(\left|\bar{\xi}^n_{x_i,x_j} - \bar{\xi}^{n-1}_{x_i,x_j}\right|^2\right). \tag{4.61}$$

The subscripts x_i and x_j denote the 2D coordinates of every point of one of the six 2D faces. Then, (x_i, x_j) denotes (y, z) for the left and right face, (x, z) for the front and back face and (x, y) for the bottom and top face. Starting from the second iteration (i.e., $n > 1$) we also compared the maximum updates (4.61) of two successive iterations in the form

$$\Delta U^n_{\max} = U^n_{\max} - U^{n-1}_{\max} = \max\left(\left|\bar{\xi}^n_{x_i,x_j} - \bar{\xi}^{n-1}_{x_i,x_j}\right|^2\right) - \max\left(\left|\bar{\xi}^{n-1}_{x_i,x_j} - \bar{\xi}^{n-2}_{x_i,x_j}\right|^2\right) \tag{4.62}$$

and we stopped to iterate once $\Delta U_{\max} < 10^{-4}$.

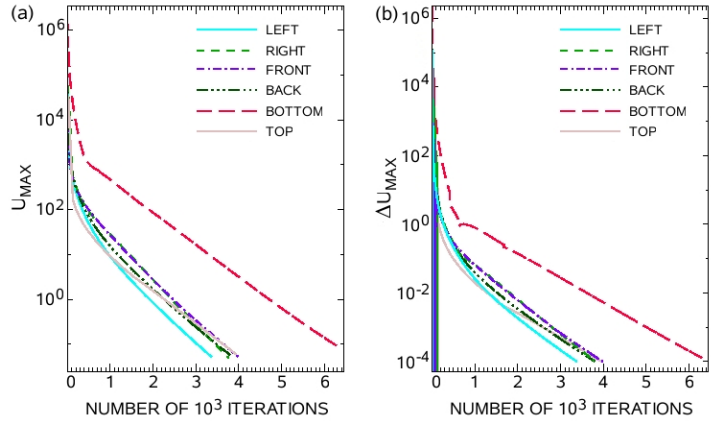

Figure 4.1: Convergence of the iterative solution to the 2D Poisson equation on the six faces of the computational box. Panel (a) shows $U_{\max}$ for every iteration n and (b) shows $\Delta U_{\max}$ for $n>1$. The turquoise solid, light green dashed, violet dashed-dotted, dark green dashed triple-dotted, red long-dashed and rose solid line represent the values corresponding to the iterative solution on the left, right, front, back, bottom and top face, respectively.

The convergence of the iterative solution to the 2D Poisson problems on every face of the cubic computational domain was fast (both $U^n_{\max}$ and $\Delta U^n_{\max}$ decreased by a factor of $\approx 10^4$ during the first ≈ 300 iterations) before a period of less pronounced convergence was reached (where $U^n_{\max}$ and $\Delta U^n_{\max}$ fell by a factor of $\approx 10^4$ during ≈ 5000 iterations; see panel (a) and (b) of Fig. 4.1, respectively). Having a closer look to the values of $\Delta U_{\max}$ during the first 200 iterations (i.e. before the beginning of the steady convergence) we recognized a strong oscillatory behavior of the iterative scheme where big changes occurred (see panel (a) of Fig. 4.2 for the corresponding values of the iterative solution on the left, right and front face and panel (b) of Fig. 4.2 for that on the back, bottom and top face). This might be due to the choice $w_{\mathrm{SOR}} = 1.9$ and a detailed testing of the influence of its choice on the performance of the iterative solution is planned for the future.

To test the solution of the 2D Poisson equation on every face of the computational box we checked, as required for solving (4.45), how well $\Delta\bar{\xi} + \bar{\boldsymbol{B}}_n = 0$ is fulfilled. This sum is qualitatively shown in Fig. 4.3 and the last column of Fig. 4.4 and we display $\bar{\boldsymbol{B}}_n$ and $\Delta\bar{\xi}$ for each face in the left and middle columns of the same figure. To have a corresponding quantitative measure we calculated for each face the maximum value of this sum, namely the maximum of $|\Delta\bar{\xi} + \boldsymbol{B}_n|^2$, which (ideally) should be zero and which we found to be $\propto 10^{-4}$ mT for all of the faces (see the second column of Table 4.1). Since, in general, by solving the 2D Poisson problem on each face we aim to determine the tangential component of the vector potential according to $\bar{\boldsymbol{A}}_t = -\boldsymbol{n} \times \nabla\bar{\xi}$ we additionally need to prove that the tangential divergence $\nabla \cdot \bar{\boldsymbol{A}}_t$ is numerically zero. This is because that is exactly what we assumed for $\bar{\boldsymbol{A}}_t$ in order to be generated by a 2D stream function $\bar{\xi}$ on each of the faces. In particular, as listed in the third column of Table 4.1, we found the

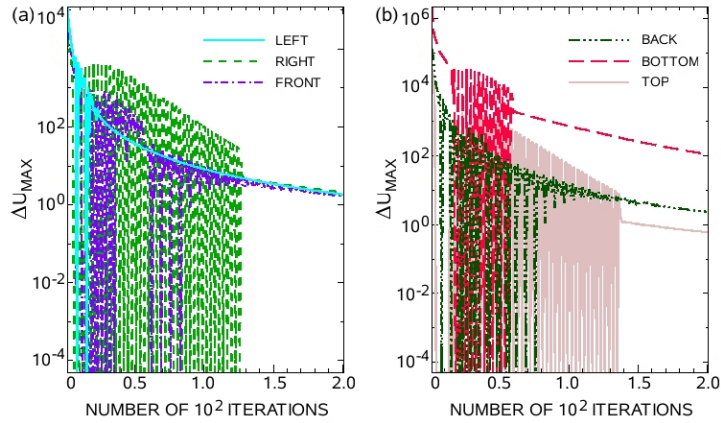

Figure 4.2: Convergence of the Iterative solution to the 2D Poisson equation on the six faces of the cubic computational box within the first 200 iteration steps. Panel (a) shows $\Delta U_{\max}$ for the left, right and front face (represented by the turquoise solid, light green dashed and violet dashed-dotted curves, respectively). Panel (b) shows $\Delta U_{\max}$ for the back, bottom and top face (represented by the dark green dashed triple-dotted, red long-dashed and rose solid line, respectively).

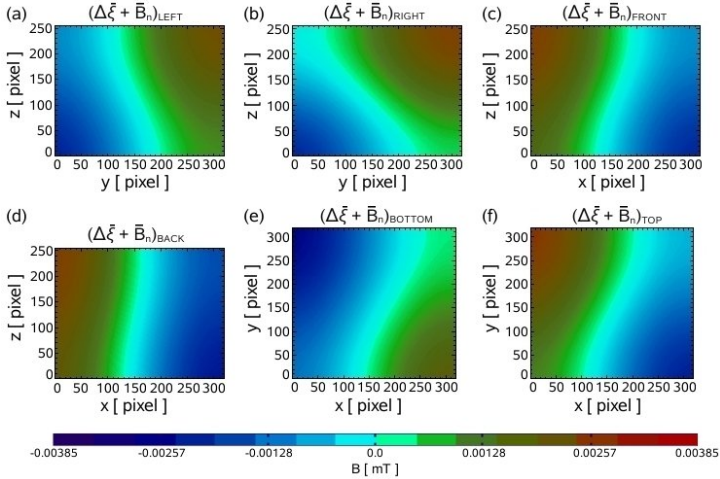

Figure 4.3: Quality of the solution of the 2D Poisson equation on the faces of the computational box. Panels (a), (b), (c), (d), (e) and (f) display $\Delta\bar{\xi}+\bar{\boldsymbol{B}}_n$ for the left, right, front, back, bottom and top face, respectively. Units are pixels and the color bar indicates the field strength in mT.

Absolute performance of the solution to the 2D Poisson problems

Face	$\max\left(\left\lvert \Delta\bar{\xi}+\bar{\boldsymbol{B}}_n \right\rvert^2\right)$ [$\times 10^{-4}$]	$\nabla\cdot\bar{\boldsymbol{A}}_t$ [$\times 10^{-14}$]	$\max\left(\left\lvert \bar{\boldsymbol{B}}_n-\boldsymbol{n}\cdot(\nabla\times\bar{\boldsymbol{A}}_t) \right\rvert^2\right)$
left	5.610	−14.211	1.900
right	5.514	7.105	13.287
front	5.900	0.000	1.734
back	6.405	−10.658	58.555
bottom	8.158	−14.211	441.829
top	6.586	3.553	0.134

Table 4.1: Quality of the solution to the 2D Poisson equation on the faces of the computational domain. The left, right, front, back, bottom and top face correspond to the $(0, y, z)$, (L_x, y, z), $(x, 0, z)$, (x, L_y, z), $(x, y, 0)$ and (x, y, L_z) planes of the box, respectively. All values are given in mT.

Relative performance of the solution to the 2D Poisson problems

Face	$\dfrac{\max\left(\left\lvert \Delta\bar{\xi}+\bar{\boldsymbol{B}}_n \right\rvert^2\right)}{\max\left(\left\lvert \boldsymbol{B}_n \right\rvert^2\right)}$ [$\times 10^{-5}$]	$\dfrac{\max\left(\left\lvert \bar{\boldsymbol{B}}_n-\boldsymbol{n}\cdot(\nabla\times\bar{\boldsymbol{A}}_t) \right\rvert^2\right)}{\max\left(\left\lvert \boldsymbol{B}_n \right\rvert^2\right)}$ [$\times 10^{-3}$]
left	4.778	16.184
right	0.915	22.047
front	15.082	44.308
back	0.216	19.762
bottom	0.001	0.585
top	186.389	38.055

Table 4.2: Quality of the solution to the 2D Poisson equation on the six faces of the cubic computational domain in form of dimensionless numbers. The left, right, front, back, bottom and top face correspond to the $(0, y, z)$, (L_x, y, z), $(x, 0, z)$, (x, L_y, z), $(x, y, 0)$ and (x, y, L_z) planes, respectively.

2D divergence on the six faces $\nabla\cdot\bar{\boldsymbol{A}}_t \approx 10^{-14}$ mT. Finally, we also checked if the resulting $\bar{\boldsymbol{A}}_t$ fulfilled $\bar{\boldsymbol{B}}_n = \boldsymbol{n}\cdot(\nabla\times\bar{\boldsymbol{A}}_t)$ since this is what we imposed as a boundary condition to our 2D Poisson problems. We therefore calculated the maximum of $|\bar{\boldsymbol{B}}_n - \boldsymbol{n}\cdot(\nabla\times\bar{\boldsymbol{A}}_t)|^2$ and the resulting values are listed in the fourth column of Table 4.1. Besides the just discussed quantitative absolute measures, we additionally calculated relative values in form of dimensionless numbers. Therefore, we took the maximum of $|\Delta\bar{\xi} + \boldsymbol{B}_n|^2$ and $|\bar{\boldsymbol{B}}_n - \boldsymbol{n}\cdot(\nabla\times\bar{\boldsymbol{A}}_t)|^2$ for each face and divided the resulting values by the corresponding maximum of $|\boldsymbol{B}_n|^2$ (see the second and third column of Table 4.2, respectively).

Since all of the above mentioned criteria concerning the solution of the 2D Poisson problems on the faces of the computational box were fulfilled sufficiently accurate, we were able to supply the Dirichlet boundary conditions in form of $\bar{\boldsymbol{A}}_t$, as required in (4.43), to the 3D Laplace problems for $\bar{\boldsymbol{A}}$ in (4.42). Together with the Neumann boundary requirements (4.44) we were then able to iteratively solve the homogeneous problems for the three Cartesian components $\bar{\boldsymbol{A}}_x$, $\bar{\boldsymbol{A}}_y$ and $\bar{\boldsymbol{A}}_z$. As before, we checked the performance of the iterative solution by calculating $U_{\max}$ and $\Delta U_{\max}$ similar as introduced in (4.61) and (4.62), respectively, but where we used $\bar{\boldsymbol{A}}_{x_i}(x_i, x_j, x_k)$ instead of $\bar{\xi}(x_i, x_j)$. Here, (x_i, x_j, x_k) denote the 3D coordinates (x, y, z) of every point of the Laplacian part of the 3D vec-

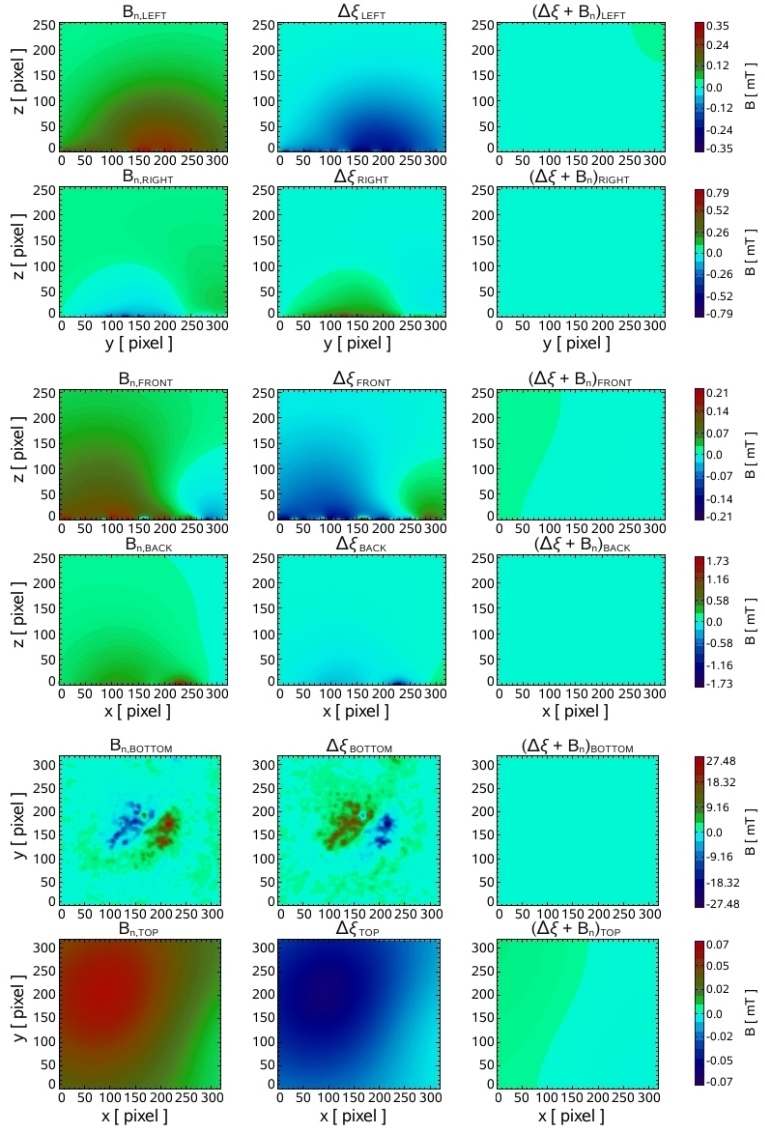

Figure 4.4: Quality of the solution of the 2D Poisson equation on every face of the computational box. From the top to the bottom row, the results for the left, right, front, back, bottom and top face are shown. The left, middle and right columns display $\tilde{\boldsymbol{B}}_n$, $\Delta\tilde{\xi}$ and $\Delta\tilde{\xi}+\tilde{\boldsymbol{B}}_n$, respectively (for the latter see also Fig. 4.3). Units are pixels and the color bars give the magnetic field strength in mT.

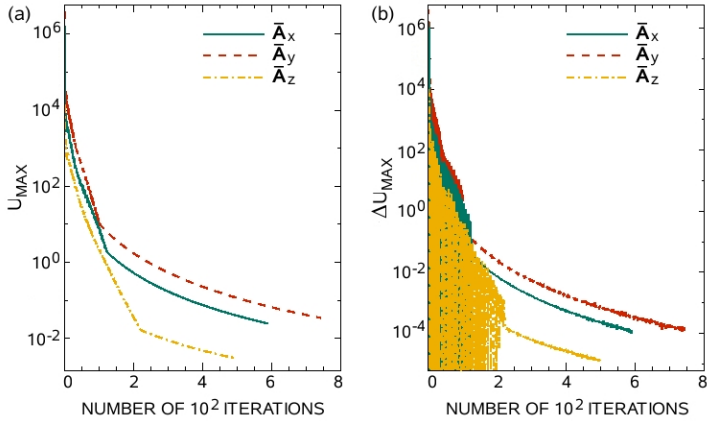

Figure 4.5: Convergence of the solution to the 3D Laplace equation $\Delta \bar{\boldsymbol{A}}_{x_i} = 0$ in the 3D computational volume. Panels (a) and (b) show the calculated values of $U_{\max}$ and $\Delta U_{\max}$, respectively. The three Cartesian components $\bar{\boldsymbol{A}}_x$, $\bar{\boldsymbol{A}}_y$ and $\bar{\boldsymbol{A}}_z$ of the Laplacian part of the magnetic vector potential are represented by the green solid, red dashed and yellow dashed-dotted line, respectively.

tor potential $\bar{\boldsymbol{A}}_x$, $\bar{\boldsymbol{A}}_y$ and $\bar{\boldsymbol{A}}_z$ in the computational box. In a similar way we iteratively solved the 3D Poisson equations for $\hat{\boldsymbol{A}}$ in (4.35) of the inhomogeneous problem subject to the boundary conditions (4.36) – (4.38). We again checked the performance of the iteration by calculating $U_{\max}$ and $\Delta U_{\max}$ similar to (4.61) and (4.62), respectively, but using $\hat{\boldsymbol{A}}_{x_i}(x_i, x_j, x_k)$ instead of $\bar{\xi}(x_i, x_j)$. Again, (x_i, x_j, x_k) denote the 3D coordinates (x, y, z) of every point of $\hat{\boldsymbol{A}}_x$, $\hat{\boldsymbol{A}}_y$ and $\hat{\boldsymbol{A}}_z$ of the current-carrying part of the 3D vector potential. For the iterative solution of the 3D Poisson and Laplace problems we again used the SOR method with $w_{\mathrm{SOR}} = 1.7$ and stopped the iteration once $\Delta U_{\max} < 10^{-4}$.

A fast convergence occurred during the first iterations and a more steady but slower convergence rate was found for the rest of the iterations. In particular, $U_{\max}$ and $\Delta U_{\max}$ decreased by a factor of $\approx 10^5$ for $\bar{\boldsymbol{A}}_x$, $\bar{\boldsymbol{A}}_y$ and $\bar{\boldsymbol{A}}_z$ during the first 100 iterations (see panel (a) and (b) of Fig. 4.5, respectively). Then the convergence was slower where $U_{\max}$ and $\Delta U_{\max}$ declined by a factor of $\approx 10^3$ during about 700 iterations. A similar behavior was found for the three Cartesian components of $\hat{\boldsymbol{A}}$, in particular, $U_{\max}$ and $\Delta U_{\max}$ calculated for for $\hat{\boldsymbol{A}}_x$, $\hat{\boldsymbol{A}}_y$ and $\hat{\boldsymbol{A}}_z$ decreased by a factor of $\approx 10^3$ and $\approx 10^4$, respectively, during the first 50 iterations (see panel (a) and (b) of Fig. 4.6, respectively). Then a period of slower convergence for the next ≈ 500 iterations was encountered during which $U_{\max}$ and $\Delta U_{\max}$ dropped by a factor of $\approx 10^3$. We have not yet performed the necessary study to determine the optimum over-relaxation parameter w_{SOR} which scales with the size of the computational box. Once done, however, an even faster convergence is expected. Additionally, a multigrid-like scheme, similar to that we use to calculate the NLFF fields (see § 2.4.1.1), could be introduced to further increase the computational speed.

After solving the 3D Poisson and Laplace equations for $\hat{\boldsymbol{A}}$ and $\bar{\boldsymbol{A}}$, respectively, we added $\bar{\boldsymbol{A}}$ and $\hat{\boldsymbol{A}}$ to get the total 3D vector potential $\boldsymbol{A}$ and had to test to which extent its

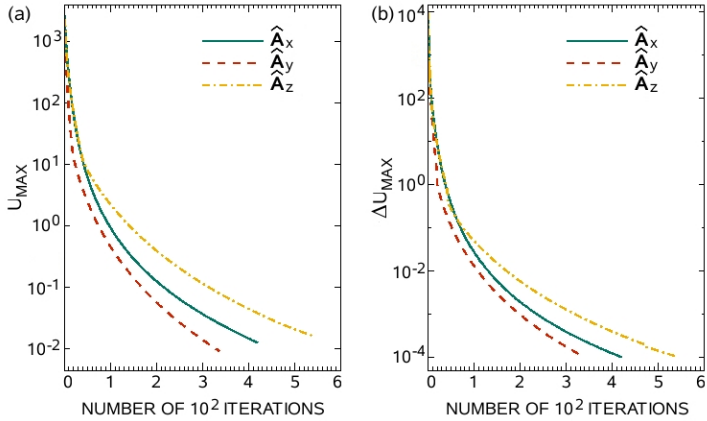

Figure 4.6: Performance of the iterative solution to the 3D Poisson equation $\Delta\hat{\boldsymbol{A}}_{x_i} = J_{x_i}$ in the 3D volume. Panels (a) and (b) show the calculated values of $U_{\max}$ and $\Delta U_{\max}$, respectively. The three Cartesian components $\hat{\boldsymbol{A}}_x$, $\hat{\boldsymbol{A}}_y$ and $\hat{\boldsymbol{A}}_z$ of the current-carrying part of the magnetic vector potential are represented by the green solid, red dashed and yellow dashed-dotted line, respectively.

curl reproduced our input NLFF magnetic field $\boldsymbol{B}$ (see § 4.3.1). Therefore, we calculated the 3D magnetic field associated with the derived 3D vector potential via $\boldsymbol{B}^\star = \nabla\times\boldsymbol{A}$ and compared it to the input field $\boldsymbol{B}$. To quantify the degree of agreement between the two fields, we used some of the metrics developed by Schrijver et al. (2006) which compare local characteristics and the global energy content of 3D vector fields. Note that for the NLFF field extrapolation a finite-size boundary layer to the open boundaries (i.e., the lateral and top boundaries) is introduced which encloses the "physical" region (including the photosphere at the lower boundary). This is supposed to reduce the influence of the assumed potential field on the open boundaries on the NLFF solution inside the physical region. Accordingly, we evaluate all metrics only in the physical region, i.e. we do not incorporate values within the finite-size boundary layer to the lateral and top boundaries (which for the used model force-free field was defined to be 32 pixels wide). In particular, the vector correlation metric is defined as

$$C_{vec} = \frac{\sum_i \boldsymbol{B}_i^\star \cdot \boldsymbol{B}_i}{\sqrt{\sum_i \left|\boldsymbol{B}_i^\star\right|^2 \sum_i \left|\boldsymbol{B}_i\right|^2}}, \tag{4.63}$$

where $\boldsymbol{B}_i^\star$ and $\boldsymbol{B}_i$ are the vectors at each point i and the vector fields are identical if $C_{vec} = 1$. Is $C_{vec} = 0$, the components of the two vector fields are perpendicular to each other everywhere (i.e., $\boldsymbol{B}_i^\star \perp \boldsymbol{B}_i$). For our test case we found $C_{vec} = 0.9849$, i.e. an agreement between the input NLFF field and the one calculated from the curl of the total vector potential of $\approx 98.5\%$. To estimate how well the magnetic energy content of the input field $\boldsymbol{B}$ had been reproduced, we normalized the energy content of $\boldsymbol{B}^\star$ to that of $\boldsymbol{B}$

in the form

$$\epsilon_{\mathrm{mag}} = \frac{\sum_i \left| \boldsymbol{B}_i^{\star} \right|^2}{\sum_i \left| \boldsymbol{B}_i \right|^2}. \tag{4.64}$$

Here we found $\epsilon_{\mathrm{mag}} = 1.05754$, i.e. an relative error in reproducing the magnetic energy of the NLFF field of $\approx 5.8\%$. Last, we checked for the correctness of the implicitly assumed vanishing divergence of the 3D magnetic field and the 3D vector potential. We therefore calculated dimensionless numbers following

$$C_{div}(\boldsymbol{F}) = \frac{\int \left| \nabla \cdot \boldsymbol{F} \right| d^3x}{L^{-1} \int |\boldsymbol{F}| \, d^3x}, \tag{4.65}$$

where L is a characteristic length of the computational domain and $\boldsymbol{F}$ represents any 3D vector field. Particularly, we found $C_{div}(\boldsymbol{B}) = 4.819 \times 10^{-6}$, $C_{div}(\boldsymbol{B}^{\star}) = 4.629 \times 10^{-6}$ and $C_{div}(\boldsymbol{A}) = 0.184$.

4.4 Summary

Based on the magnetic field information one can estimate physical quantities like the magnetic energy and helicity. Since the magnetic energy can be converted back and forth between kinetic and magnetic forms during the processes related to solar eruptions the helicity of the magnetic field, due to its conservation properties, represents an alternative to quantify the topological characteristics of a magnetic field. Based on the the use of the LFF field parameter as a proxy or the analysis of 3D extrapolated force-free fields it has been found that the magnetic field in the solar atmosphere owns a hemispheric trend of handedness and an according trend of helicity. In particular, the finding of predominately negative/positive helicity patterns in the northern/southern solar hemisphere seems to be insensitive to the magnetic field reversal at the end of the solar cycles and some underlying, global mechanism to produce these helicity patterns is thought to exist.

However, any helicity created below the solar surface can be carried into the corona by the emergence of magnetic field through the photosphere. Due to rotational motions in the photosphere itself, the coronal loops can then gain even more helicity. All these processes together then make up the total helicity content of the solar corona. If the coronal magnetic field configuration loses its equilibrium to result in a CME, part of the helicity can be transported into the interplanetary space. This means that the helicity flux from photospheric motions has to balance the variation of the coronal helicity plus the helicity which is carried away by CMEs. Consequently, the processes which transport the helicity to the outer solar atmosphere and finally remove it from the Sun must be at approximately the same rate as its generation in the interior (e.g. Pevtsov 2008). Studies which addressed the question whether the magnetic helicity is mainly injected by horizontal photospheric motions into the corona, e.g. by Démoulin et al. (2002), Green et al. (2002) and Nindos and Zhang (2002), revealed that the coronal helicity and the helicity ejected by CMEs are by orders of magnitude larger than the helicity injected by differential rotation and localized shearing motions. This led to the conclusion that the main source of the coronal helicity must be the emergence of new magnetic flux which has been previously twisted in the convection zone. To summarize, as magnetic flux travels from the convection zone

until the solar corona to be finally ejected from the Sun, its helicity content can be traced and, moreover, the helicity content of coronal fields may be completely determined by its flow through the photosphere on one hand and its loss-rate into the solar wind on the other hand (Berger 1984). From analyzing the helicity carried away by CMEs in comparison to the rate of helicity production by photospheric motions it seems that the main contributor of magnetic helicity injection may either be undetected at photospheric levels or has its origin in sub-photospheric layers (van Driel-Gesztelyi et al. 2003, Démoulin 2007).

To evaluate the magnetic helicity content of the solar corona the knowledge of the 3D magnetic field vector and also that of the associated 3D magnetic vector potential is needed. The ability of indirectly inferring the 3D magnetic field structure in the outer solar atmosphere (for which routine measurements do not exist) with the help of extrapolation techniques and, in particular, for the most realistic estimation of the coronal field in form of NLFF fields is well established. A method to calculate the 3D vector potential has been worked out and its applicability to real solar cases discussed. We presented a method to calculate the 3D vector potential for a given 3D magnetic field as the sum of a Laplacian part and a current-carrying part. Therefore, we decomposed the magnetic vector potential corresponding to the decomposition of the magnetic field as suggested for the calculation of the relative helicity in coronal volumes for a given NLFF field. The basic strategy of finding the 3D magnetic vector potential involves the solution of an inhomogeneous equation, taking the electric currents in the entire computational volume (including the boundaries) into account, and the solution of a homogeneous problem, accounting for the boundary magnetic field of the considered volume. We furthermore imposed the condition of divergence-freeness of both the magnetic field and the associated vector potential.

From estimating the force-free field parameter throughout our computational volumes and comparison with the calculated magnetic helicity, we plan to investigate the relation between them. The application of our method to estimate the helicity content above solar ARs will also enable us to compare it to the amount of helicity injected through the photosphere and its contribution to the coronal helicity content, or alternatively, to estimate the contribution of yet undetected, sub-photospheric sources of the helicity.

5 Conclusions and outlook

Within this work, we used a numerical method to calculate the magnetic field above solar active regions based on vector magnetic field measurements made in the solar photosphere. In particular, we extrapolated the measured photospheric field vector into the chromosphere and corona which, in general, allows it to compensate the lack of routine magnetic field measurements in these atmospheric layers. Our method is based on the force-free assumption, i. e. the adoption that the coronal currents are co-aligned with the magnetic field. Potential (current-free) and nonlinear force-free field models were used to calculate the coronal magnetic field, where the latter represents the currently most sophisticated and most realistic approximation to the true coronal magnetic field.

The analysis of the 3D magnetic field above two solar active regions led to the successful establishment of a clear relation between the amount of available free magnetic energy and the magnitude of observed flares. It was unambiguously demonstrated that nonlinear force-free field extrapolations are a useful tool to investigate the evolution of the associated physical parameters during solar eruptions. Based on the nonlinear force-free field extrapolations we were able to calculate the magnetic energy content, the available free magnetic energy and the distribution of the energy density of the coronal field. This allowed us to demonstrate that magnetic energy is slowly build up during the days before an eruption and that the amount of stored magnetic energy indicates the magnitude of the associated eruption. Furthermore, it was found that not all the stored energy has been released during the explosions, in agreement with existing theories about the relaxation of magnetic fields to configurations of lower energy during solar eruptions. We were also able to localize the height and exact position in the solar atmosphere where the excess energy is stored prior to and released during the eruptions. This is a distinct advantage with respect to coronal observations since they can only indicate the location (projected on the solar surface) of the explosive energy release related to flares but not its height in the corona. Furthermore, the calculation of iso-surfaces of equal absolute magnetic field magnitude allowed us to support a proposed coronal implosion scenario, indicating that the release of free magnetic energy leads to a decrease of the magnetic energy density (and hence the magnetic pressure) in a flaring region.

Despite the relative success of the presented method used to calculate the 3D coronal magnetic field, a successful application of nonlinear force-free field models to real solar data, in general, requires a number of prerequisites. This was concluded by DeRosa et al. (2009) who applied different existing nonlinear force-free codes to data from the Hinode Solar Optical Telescope-SpectroPolarimeter (Hinode/SOT-SP; Kosugi et al. 2007) and where the resulting models showed remarkable differences in the field line configuration and estimates of the free magnetic energy. In the following, the requirements for a successful application of extrapolation techniques to model the coronal magnetic field

are listed. Also, the planned modifications to our codes in order to incorporate them, or rather incorporate them in an optimized manner, are listed together with the possible future applications.

First, large model volumes at high spatial resolution are required which not only accommodate the connectivity within an active region but also the connectivity to the surrounding. This has become clear already in an earlier application of existing extrapolation codes to Hinode/SOT-SP data by Schrijver et al. (2008) and it has been worked out that a vector magnetogram with a small field-of-view (not containing an entire active region and its surrounding) does not provide the necessary magnetic connectivity for an unbiased nonlinear force-free extrapolation. Additionally, a high time cadence is needed in order to be able to investigate the processes during solar eruptions in detail. Already available are ground-based, full-disk and/or active-region scans of the magnetic field vector from the Synoptic Optical Long-term Investigations of the Sun (SOLIS; Keller et al. 2003b) survey with a pixel size of about 1.1 arcseconds and a time cadence of about 10 minutes. Space-borne data from the Helioseismic and Magnetic Imager of the Solar Dynamics Observatory (SDO/HMI; Graham et al. 2003) will have an even higher temporal and spacial resolution. In particular, full-disk vector magnetograms with a pixel size of about 0.5 arcseconds and a time cadence of about 90 seconds will become available from the SDO. With these data, we will be able to study properties such as the magnetic energy, the magnetic helicity (for which we recently developed a method to derive it), current sheet formation and the topology of the pre- and post-eruptive fields in unprecedented detail. We plan not only to carry out nonlinear force-free field extrapolations for active regions with a high resolution but also global spherical extrapolations with a necessarily reduced resolution. For the latter, a method to extrapolate the nonlinear force-free field locally in spherical geometry has been recently developed by Tadesse et al. (2009) and a method to derive the nonlinear force-free field globally has been implemented by Wiegelmann (2007). From these global nonlinear force-free field extrapolations (even though having a lower resolution) we can specify the a priori unknown top and lateral boundary conditions for the higher-resolution active-region computations. In this way we will achieve a consistent connectivity of the local active region magnetic field with the global field structure. Furthermore, our nonlinear force-free models enable us to understand the evolution and transport of the helicity density. For this purpose, a method to calculate the magnetic vector potential associated with the extrapolated force-free magnetic field has been implemented. This allows us to calculate and thus study the temporal evolution of the magnetic helicity as involved in eruptive phenomena. If we find a significant change of the helicity content in our computations this can only mean that the corresponding part has been ejected into the interplanetary space.

Second, the distribution of the magnetic field strength in different heights of the solar atmosphere, as calculated from our force-free field models, could be compared with corresponding radio measurements. As discussed by White (2005), virtually every feature of the solar corona is visible in radio images at some wavelength, based on the emission mechanisms that dominate radio emission. This includes the bremsstrahlung from thermal plasma, the emission from non-relativistic thermal plasma (gyroresonance emission), the emission of gently relativistic electrons (gyrosynchrotron emission) and plasma emission. Radio diagnostics have the advantage of being optically thick so that different layers of the corona can be probed at differend radio frequencies but, unfortunately, they

do not provide absolute height information. On the one hand, by comparing our magnetic field models with gyroresonance radio observations we expect to be able to deliver the missing information about the height of the observed layers in the solar atmosphere. On the other hand, the comparison with radio observations could deliver arguments for a proposed implosion scenario for solar eruptions which we already evidently traced in our coronal model fields. For this purpose, however, simultaneous high-resolution maps at many frequencies (in order to measure a wide range of field strengths) are required.

Third, the preprocessing of the lower-boundary (photospheric) vector field in order to gain boundary conditions consistent with the force-free assumption is necessary. This is because of the basic assumptions of force-free magnetic field models that the magnetic pressure is considerably higher than the thermal pressure in the solar atmosphere. Since this is not true for the photosphere (in which the available vector magnetograph measurements are performed) non-magnetic forces can in principle not be neglected and one would find the photospheric magnetic field to provide an inconsistent lower boundary condition for the force-free extrapolation code. The preprocessing represents the transformation of the observed (not force-free) photospheric field to a (nearly force-free) chromospheric-like field in order to approximate the physics in the solar atmosphere at a chromospheric level. The preprocessing routine developed by Wiegelmann et al. (2006) has been improved by the optional incorporation of magnetic field information with the help of chromospheric Hα images (Wiegelmann et al. 2008) and the preprocessing of photospheric full-disk vector magnetograms, taking the curvature of the Sun into account, has been implemented by Tadesse et al. (2009). A further improvement to reasonably approximate the force-free magnetic field at the base of the corona is planned to be achieved by the supplementary incorporation of routinely measured, chromospheric, line-of-sight magnetic field data, e. g. from SOLIS.

Fourth, the measurement uncertainties in the lower boundary conditions need to be accommodated. This, in particular, concerns the transversal magnetic field measurements which own a much lower level of accuracy than the longitudinal ones. With the help of simultaneously observed coronal images we plan to verify the model magnetic field lines, computed from our nonlinear force-free field extrapolations. In particular, a quantitative measure of the agreement between the magnetic field model and the observed plasma structures can be found by computing the average distances of the plasma loops as visible in 2D coronal images and the 2D projections of the calculated model magnetic field lines. If the distance measure is sufficiently small, the magnetic field model can be assumed to represent a good proxy of the coronal field. Due to errors in the magnetograms, limited information (e. g. if only line-of-sight instead of vector magnetograms are available) or noise, the calculated force-free field lines will deviate from the observed plasma loops. However, as suggested by Wiegelmann et al. (2009), the information of this missmatch is planned to be incorporated for a correction of the magnetic field calculations in form of a distance measure. Since a given coronal image only shows the plasma along a subset of coronal field lines, observations at different wavelengths are required to give a complete distribution of the magnetic field. Such images at a high thermal contrast will soon be available from the Atmospheric Imaging Assembly (AIA) on board the SDO. In particular, simultaneous images at ten different wavelengths corresponding to different chromospheric, transition region and coronal temperatures will be provided.

A Reynolds rules

In general, a two-scale approach (see also § 1.3.2) implies the decomposition of a vector field $\boldsymbol{X}(\boldsymbol{x}, t)$ which is a function of space and time into a mean slowly varying part $\langle \boldsymbol{X} \rangle(\boldsymbol{x}, t)$ and a rapidly fluctuating part $\boldsymbol{X}'(\boldsymbol{x}, t)$. It also implies that an averaging procedure can be defined. This can be either a space, time or an ensemble average. A corresponding volume-averaging operator can be defined as

$$\langle X \rangle = \frac{1}{\lambda^3} \int_V X \, d^3x, \tag{A.1}$$

where the volume averages are computed over some scale λ such that $l \ll \lambda \ll L$, where L and l denote the characteristic length scales on which the slowly varying component $\langle \boldsymbol{X} \rangle$ and the rapidly fluctuating part $\boldsymbol{X}'$ vary, respectively.

According to Krause and Rädler (1980) § 1, the Reynolds rules (after Reynolds (1895) who first proposed it in form of time averaging in the context of turbulent flows) for averaging two arbitrary functions $X(\boldsymbol{x}, t)$ and $Y(\boldsymbol{x}, t)$ are as follows.

1. The average of the sum is the sum of the averages:

$$\langle X + Y \rangle = \langle X \rangle + \langle Y \rangle. \tag{A.2}$$

2. Averaging does not affect constants and vice versa:

$$\langle a X \rangle = a \langle X \rangle, \tag{A.3}$$
$$\langle a \rangle = a, \tag{A.4}$$

   if a is a consant.

Note that these two conditions already imply that the averaging operator is a linear one.

3. Averaging a derivative equals the derivative of the average:

$$\langle \partial_s X \rangle = \partial_s \langle X \rangle, \tag{A.5}$$

   with s being either a space coordinate or time.

4. Averaging products of averages and functions equals products of averages:

$$\langle X \langle Y \rangle \rangle = \langle X \rangle \langle Y \rangle. \tag{A.6}$$

From these four basic requirements to the averaging operator one can derive the following additional properties:

5. From (A.6) follows

$$\langle \langle X \rangle \rangle = \langle X \rangle, \tag{A.7}$$
$$\langle \langle X \rangle \langle Y \rangle \rangle = \langle X \rangle \langle Y \rangle. \tag{A.8}$$

   i.e. that the averages of averages equal the average itself.

6. For $X = \langle X \rangle + X'$ follows from (A.2) and (A.6)

$$\langle X' \rangle = 0, \tag{A.9}$$

   i.e. that the average of the rapidly fluctuating part must vanish.

7. Then, from (A.6) and (A.9) also follows

$$\langle \langle X \rangle Y' \rangle = 0. \tag{A.10}$$

8. And finally, from (A.5) and (A.9) follows

$$\langle \partial_s X' \rangle = 0, \tag{A.11}$$

   with s being either a space coordinate or time.

Bibliography

Alissandrakis, C. E., 1981, On the computation of constant alpha force-free magnetic field, Astron. Astrophys., 100, 197–200

Altschuler, M. D., Newkirk, G., 1969, Magnetic fields and the structure of the solar corona. I. Methods of calculating coronal fields, Sol. Phys., 9, 131–149

Aly, J. J., 1984, On some properties of force-free magnetic fields in infinite regions of space, Astrophys. J., 283, 349–362

Aly, J. J., 1989, On the reconstruction of the nonlinear force-free coronal magnetic field from boundary data, Sol. Phys., 120, 19–48

Aly, J. J., 1992, Some properties of finite energy constant-alpha force-free magnetic fields in a half-space, Sol. Phys., 138, 133–162

Amari, T., Aly, J. J., Luciani, J. F., Boulmezaoud, T. Z., Mikic, Z., 1997, Reconstructing the solar coronal magnetic field as a force-free magnetic field, Sol. Phys., 174, 129–149

Amari, T., Boulmezaoud, T. Z., Maday, Y., 1998, A regularization method for the extrapolationbreak of the photospheric solar magnetic field. I. Linear force-free field, Astron. Astrophys., 339, 252–260

Amari, T., Boulmezaoud, T. Z., Mikic, Z., 1999, An iterative method for the reconstructionbreak of the solar coronal magnetic field. I. Method for regular solutions, Astron. Astrophys., 350, 1051–1059

Amari, T., Boulmezaoud, T. Z., Aly, J. J., 2006, Well posed reconstruction of the solar coronal magnetic field, Astron. Astrophys., 446, 691–705

Antiochos, S. K., DeVore, C. R., Klimchuk, J. A., 1999, A model for solar coronal mass ejections, Astrophys. J., 510, 485–493

Arfken, G. B., Weber, H. J., 2001, Mathematical methods for physicists (5th ed.), San Diego: Harcourt Academic Press

Arnaud, J., 1982, Observed polarization of the Fe XIV 5303 coronal emission line, Astron. Astrophys., 112, 350–354

Aschwanden, M. J., 2004, Physics of the solar corona. An Introduction, Chichester: Praxis Publishing Ltd.

Aschwanden, M. J., Benz, A. O., 1997, Electron densities in solar flare loops, chromospheric evaporation upflows and acceleration sites, Astrophys. J., 480, 825–839

Athay, R. G., 1981, Chromosphere-corona transition region models with magnetic field and fluid flow, Astrophys. J., 249, 340–348

Athay, R. G., 1982, Responses of transition region models to magnetic field geometry and downflow velocities, Astrophys. J., 263, 982–986

Bastian, T. S., Benz, A. O., Gary, D. E., 1998, Radio emission from solar flares, Ann. Rev. Astron. Astrophys., 36, 131–188

Baumann, I., Solanki, S. K., 2005, On the size distribution of sunspot groups in the Greenwich sunspot record 1874-1976, Astron. Astrophys., 443, 1061–1066

Bellan, P. M., 1999, Magnetic helicity and relaxation: Theory, in Helicity in space and laboratory plasmas, (Eds.) M. R. Brown, R. C. Canfield, A. A. Pevtsov, pp. 119–128

Bellan, P. M., 2006, Fundamentals of plasma physics, Cambridge: Cambridge University Press

Benz, A. O. (Ed.), 1993, Plasma astrophysics: Kinetic processes in solar and stellar coronae, vol. 184 of Astrophysics and Space Science Library, Dordrecht, Netherlands: Kluwer Academic Publishers

Benz, A. O., 2001, Solar flare observations, in Encyclopedia of Astronomy and Astrophysics, (Ed.) P. Murdin, Bristol: IOP Publishing and London: Nature Publishing

Berger, M. A., 1984, Rigorous new limits on magnetic helicity dissipation in the solar corona, Geophys. Astrophys. Fluid Dyn., 30, 79–104

Berger, M. A., 1988, An energy formula for nonlinear force-free magnetic fields, Astron. Astrophys., 201, 355–361

Berger, M. A., 1998, Magnetic helicity and filaments, in New perspectives on solar prominences, (Eds.) D. F. Webb, B. Schmieder, D. M. Rust, vol. 150 of Astron. Soc. Pac. Conf. Ser., pp. 102–110

Berger, M. A., 1999a, Introduction to magnetic helicity, Plasma Phys. Control. Fusion, 41, B167–B175

Berger, M. A., 1999b, Magnetic helicity in space physics, in Helicity in space and laboratory plasmas, (Eds.) M. R. Brown, R. C. Canfield, A. A. Pevtsov, pp. 1–9

Berger, M. A., Field, G. B., 1984, The topological properties of magnetic helicity, J. Fluid Mech., 147, 133–148

Bhatnagar, A., 1996, Solar mass ejections and coronal holes, Astrophys. Space Sci., 243, 105–112

Bleybel, A., Amari, T., van Driel-Gesztelyi, L., Leka, K. D., 1999, Nonlinear force-free reconstruction of a flaring active region, in Magnetic fields and solar processes, (Ed.) A. Wilson & et al., vol. 448 of ESA Special Publication, pp. 709–714

Bleybel, A., Amari, T., van Driel-Gesztelyi, L., Leka, K. D., 2002, Global budget for an eruptive active region. I. Equilibrium reconstruction approach, Astron. Astrophys., 395, 685–695

Bogdan, T. J., Gilman, P. A., Lerche, I., Howard, R., 1988, Distribution of sunspot umbral areas: 1917-1982, Astrophys. J., 327, 451–456

Bray, R. J., Loughhead, R. E., 1964, Sunspots, London: Chapman & Hall

Bullard, E., Gellman, H., 1954, Homogeneous dynamos and terrestrial magnetism, Phil. Trans. Roy. Soc., A 247, 213–278

Cargill, P. J., 2009, Coronal magnetism: Difficulties and prospects, Space Sci. Rev., 144, 413–421

Chandrasekhar, S., Fermi, E., 1953, Problems of gravitational stability in the presence of a magnetic field, Astrophys. J., 118, 116–141

Chandrasekhar, S., Kendall, P. C., 1957, On force-free magnetic fields, Astrophys. J., 126, 457–460

Chandrasekhar, S., Woltjer, L., 1958, On force-free magnetic fields, Proc. Nat. Acad. Sci., 44, 285–289

Charbonneau, P., 2005, Dynamo models of the solar cycle, Living Rev. Sol. Phys., 2, 2

Chen, J., 1989, Effects of toroidal forces in current loops embedded in a background plasma, Astrophys. J., 338, 453–470

Chen, J., 1996, Theory of prominence eruption and propagation: Interplanetary consequences, J. Geophys. Res., 101, 27 499–27 520

Chiu, Y. T., Hilton, H. H., 1977, Exact Green's function method of solar force-free magnetic-field computations with constant alpha. I. Theory and basic test cases, Astrophys. J., 212, 873–885

Cliver, E., 2001, Solar flare classification, in Encyclopedia of Astronomy and Astrophysics, (Ed.) P. Murdin, Bristol: IOP Publishing and London: Nature Publishing

Condon, E. U., Shortley, G. H., 1970, The theory of atomic spectra, Cambridge: Cambridge University Press

Cowling, T. G., 1934, The magnetic field of sunspots, Mon. Not. Roy. Astr. Soc., 94, 39–48

Cowling, T. G., 1957, The dynamo maintenance of steady magnetic fields, Quat. J. Mech. Appl. Math., 10, 129–136

Cranmer, S. R., 2009, Coronal holes, Living Rev. Sol. Phys., 6, 3

Cuperman, S., Ofman, L., Semel, M., 1990, Determination of force-free magnetic fields above the photosphere using three-component boundary conditions - Moderately nonlinear case, Astron. Astrophys., 230, 193–199

Cuperman, S., Demoulin, P., Semel, M., 1991, Removal of singularities in the Cauchy problem for the extrapolation of solar force-free magnetic fields, Astron. Astrophys., 245, 285–288

Davidson, P. A., 2001, An introduction to magnetohydrodynamics, Cambridge: Cambridge University Press

Davis, C. J., Davies, J. A., Lockwood, M., Rouillard, A. P., Eyles, C. J., Harrison, R. A., 2009, Stereoscopic imaging of an Earth-impacting solar coronal mass ejection: A major milestone for the STEREO mission, Geophys. Res. Lett., 36, L08 102

Delaboudinière, J., Artzner, G. E., Brunaud, J., Gabriel, A. H., Hochedez, J. F., Millier, F., Song, X. Y., Au, B., Dere, K. P., Howard, R. A., Kreplin, R., Michels, D. J., Moses, J. D., Defise, J. M., Jamar, C., Rochus, P., Chauvineau, J. P., Marioge, J. P., Catura, R. C., Lemen, J. R., Shing, L., Stern, R. A., Gurman, J. B., Neupert, W. M., Maucherat, A., Clette, F., Cugnon, P., van Dessel, E. L., 1995, EIT: Extreme-ultraviolet Imaging Telescope for the SoHO mission, Sol. Phys., 162, 291–312

Démoulin, P., 2007, Recent theoretical and observational developments in magnetic helicity studies, Adv. Space Res., 39, 1674–1693

Demoulin, P., Cuperman, S., Semel, M., 1992, Determination of force-free magnetic fields above the photosphere using three-component boundary conditions. II. Analysis and minimization of scale-related growing modes and of computational induced singularities, Astron. Astrophys., 263, 351–360

Démoulin, P., Mandrini, C. H., van Driel-Gesztelyi, L., Thompson, B. J., Plunkett, S., Kovári, Z., Aulanier, G., Young, A., 2002, What is the source of the magnetic helicity shed by CMEs? The long-term helicity budget of AR 7978, Astron. Astrophys., 382, 650–665

DeRosa, M. L., Schrijver, C. J., Barnes, G., Leka, K. D., Lites, B. W., Aschwanden, M. J., Amari, T., Canou, A., McTiernan, J. M., Régnier, S., Thalmann, J. K., Valori, G., Wheatland, M. S., Wiegelmann, T., Cheung, M. C. M., Conlon, P. A., Fuhrmann, M., Inhester, B., Tadesse, T., 2009, A critical assessment of nonlinear force-free field modeling of the solar corona for active region 10953, Astrophys. J., 696, 1780–1791

Dikpati, M., Gilman, P. A., 2006, Simulating and predicting solar cycles using a flux-transport dynamo, Astrophys. J., 649, 498–514

Dowdy, Jr., J. F., Rabin, D., Moore, R. L., 1986, On the magnetic structure of the quiet transition region, Sol. Phys., 105, 35–45

Durrant, C. J., 1988, The atmosphere of the sun, Bristol: Hilger

Emonet, T., Cattaneo, F., 2001, Small-scale photospheric fields: Observational evidence and numerical simulations, Astrophys. J. Lett., 560, L197–L200

Feldman, U., 1998, On the unresolved fine structures of the solar atmosphere. III. Elemental abundances consideration, Astrophys. J., 507, 974–977

Feng, L., Inhester, B., Solanki, S. K., Wiegelmann, T., Podlipnik, B., Howard, R. A., Wuelser, J., 2007, First stereoscopic coronal loop reconstructions from STEREO SECCHI images, Astrophys. J. Lett., 671, L205–L208

Finn, J. M., Antonsen, T. M., 1985, Magnetic helicity: What is it and what is it good for?, Comm. Plasma Phys. Control. Fusion, 9, 111–126

Fisher, G. H., 1989, Dynamics of flare-driven chromospheric condensations, Astrophys. J., 346, 1019–1029

Forbes, T. G., 2000, A review on the genesis of coronal mass ejections, J. Geophys. Res., 105, 23 153–23 166

Forbes, T. G., 2001, Solar flare models, in Encyclopedia of Astronomy and Astrophysics, (Ed.) P. Murdin, Bristol: IOP Publishing and London: Nature Publishing

Forbes, T. G., Isenberg, P. A., 1991, A catastrophe mechanism for coronal mass ejections, Astrophys. J., 373, 294–307

Forbes, T. G., Linker, J. A., Chen, J., Cid, C., Kóta, J., Lee, M. A., Mann, G., Mikić, Z., Potgieter, M. S., Schmidt, J. M., Siscoe, G. L., Vainio, R., Antiochos, S. K., Riley, P., 2006, CME theory and models, Space Sci. Rev., 123, 251–302

Fuhrmann, M., Seehafer, N., Valori, G., 2007, Preprocessing of solar vector magnetograms for force-free magnetic field extrapolation, Astron. Astrophys., 476, 349–357

Gabriel, A. H., 1976, A magnetic model of the solar transition region, Phil. Trans. Roy. Soc. Lond. A, 281, 339–352

Gary, G. A., 1989, Linear force-free magnetic fields for solar extrapolation and interpretation, Astrophys. J. Suppl. Ser., 69, 323–348

Gary, G. A., 2001, Plasma-beta above a solar active region: Rethinking the paradigm, Sol. Phys., 203, 71–86

Gary, G. A., Alexander, D., 1999, Constructing the coronal magnetic field by correlating parameterized magnetic field lines with observed coronal plasma structures, Sol. Phys., 186, 123–139

Gary, G. A., Hagyard, M. J., 1990, Transformation of vector magnetograms and the problems associated with the effects of perspective and the azimuthal ambiguity, Sol. Phys., 126, 21–36

Gauss, C. F., 1833, Zur mathematischen Theorie der electrodynamischen Wirkungen, in Werke, Band 5, p. 605, Göttingen: Königliche Gesellschaft der Wissenschaften zu Göttingen

Georgoulis, M. K., 2005, A new technique for a routine azimuth disambiguation of solar vector magnetograms, Astrophys. J. Lett., 629, L69–L72

Georgoulis, M. K., LaBonte, B. J., 2007, Magnetic energy and helicity budgets in the active region solar corona. I. Linear force-free approximation, Astrophys. J., 671, 1034–1050

Georgoulis, M. K., Raouafi, N.-E., Henney, C. J., 2008, Automatic active-region identification and azimuth disambiguation of the SOLIS/VSM full-disk vector magnetograms, in Subsurface and atmospheric influences on solar activity, (Eds.) R. Howe, R. W. Komm, K. S. Balasubramaniam, G. J. D. Petrie, vol. 383 of Astron. Soc. Pac. Conf. Ser., pp. 107–114

Goff, C. P., van Driel-Gesztelyi, L., Démoulin, P., Culhane, J. L., Matthews, S. A., Harra, L. K., Mandrini, C. H., Klein, K. L., Kurokawa, H., 2007, A multiple flare scenario where the classic long-duration flare was not the source of a CME, Sol. Phys., 240, 283–299

Gosling, J. T., Hildner, E., MacQueen, R. M., Munro, R. H., Poland, A. I., Ross, C. L., 1976, The speeds of coronal mass ejection events, Sol. Phys., 48, 389–397

Grad, H., Rubin, H., 1958, Hydromagnetic equilibria and force-free fields, in Proc. 2nd Int. Conf. on Peacful Uses of Atomic Energy, vol. 31, pp. 190–197

Graham, J. D., Norton, A., López Ariste, A., Lites, B., Socas-Navarro, H., Tomczyk, S., 2003, The Helioseismic and Magnetic Imager (HMI) on SDO: Full vector magnetography with a filtergraph polarimeter, in Solar polarization, (Eds.) J. Trujillo-Bueno, J. Sanchez Almeida, vol. 307 of Astron. Soc. Pac. Conf. Ser., pp. 131–136

Green, L. M., López fuentes, M. C., Mandrini, C. H., Démoulin, P., Van Driel-Gesztelyi, L., Culhane, J. L., 2002, The magnetic helicity budget of a CME-prolific active region, Sol. Phys., 208, 43–68

Hagyard, M. J., Pevtsov, A. A., 1999, Studies of solar helicity using vector magnetograms, Sol. Phys., 189, 25–43

Hajjafar, A., 2006, Controlled over-relaxation method and the general extrapolation method, Appl. Math. Comput., 174, 188–198

Hale, G. E., Nicholson, S. B., 1925, The law of sunspot polarity, Astrophys. J., 62, 270–300

Hale, G. E., Ellerman, F., Nicholson, S. B., Joy, A. H., 1919, The magnetic polarity of sunspots, Astrophys. J., 49, 153–178

Hammer, R., 1994, The magnetism of the quiet chromosphere and open corona, in Solar magnetic fields, (Eds.) M. Schüssler, W. Schmidt, pp. 347–362

Handy, B. N., Acton, L. W., Kankelborg, C. C., Wolfson, C. J., Akin, D. J., Bruner, M. E., Caravalho, R., Catura, R. C., Chevalier, R., Duncan, D. W., Edwards, C. G., Feinstein, C. N., Freeland, S. L., Friedlaender, F. M., Hoffmann, C. H., Hurlburt, N. E., Jurcevich, B. K., Katz, N. L., Kelly, G. A., Lemen, J. R., Levay, M., Lindgren, R. W., Mathur, D. P., Meyer, S. B., Morrison, S. J., Morrison, M. D., Nightingale, R. W., Pope, T. P., Rehse, R. A., Schrijver, C. J., Shine, R. A., Shing, L., Strong, K. T., Tarbell, T. D., Title, A. M., Torgerson, D. D., Golub, L., Bookbinder, J. A., Caldwell, D., Cheimets, P. N., Davis, W. N., Deluca, E. E., McMullen, R. A., Warren, H. P., Amato, D., Fisher, R., Maldonado, H., Parkinson, C., 1999, The Transition Region And Coronal Explorer, Sol. Phys., 187, 229–260

Harra, L. K., Sterling, A. C., 2001, Material outflows from coronal intensity "dimming regions" during coronal mass ejection onset, Astrophys. J. Lett., 561, L215–L218

Harrison, R. A., 1995, The nature of solar flares associated with coronal mass ejection, Astron. Astrophys., 304, 585–594

Harvey, K. L., Recely, F., 2002, Polar coronal holes during cycles 22 and 23, Sol. Phys., 211, 31–52

Henney, C. J., Keller, C. U., Harvey, J. W., 2006, SOLIS-VSM solar vector magnetograms, in Solar polarization 4, (Eds.) R. Casini, B. W. Lites, vol. 358 of Astron. Soc. Pac. Conf. Ser., pp. 92–95

Herzberg, G., 1950, Molecular spectra and molecular structure. Spectra of diatomic molecules (2nd ed.), New York: Van Nostrand Reinhold

Heyvaerts, J., 1974, Coronal electric currents produced by photospheric motions, Sol. Phys., 38, 419–437

Heyvaerts, J., Priest, E. R., 1984, Coronal heating by reconnection in DC current systems. A theory based on Taylor's hypothesis, Astron. Astrophys., 137, 63–78

Heyvaerts, J., Priest, E. R., Rust, D. M., 1977, An emerging flux model for the solar flare phenomenon, Astrophys. J., 216, 123–137

Holweger, H., Mueller, E. A., 1974, The photospheric barium spectrum: Solar abundance and collision broadening of BA II lines by hydrogen, Sol. Phys., 39, 19–30

Hornig, G., 2006, A universal magnetic helicity integral, arXiv:astro-ph/0606694

Hornig, G., Rastätter, L., 1997, The role of helicity in the reconnection process, Adv. Space Res., 19, 1789–1792

Howard, R. A., Michels, D. J., Sheeley, Jr., N. R., Koomen, M. J., 1982, The observation of a coronal transient directed at Earth, Astrophys. J. Lett., 263, L101–L104

Hudson, H. S., 2000, Implosions in coronal transients, Astrophys. J. Lett., 531, L75–L77

Hudson, H. S., Bougeret, J.-L., Burkepile, J., 2006, Coronal mass ejections: Overview of observations, Space Sci. Rev., 123, 13–30

Inhester, B., Wiegelmann, T., 2006, Nonlinear force-free magnetic field extrapolations: Comparison of the Grad-Rubin and Wheatland-Sturrock-Roumeliotis algorithm, Sol. Phys., 235, 201–221

Ivers, D. J., James, R. W., 1988, Antidynamo theorems for non-radial flows, Geophys. Astrophys. Fluid Dyn., 40, 147–163

Jensen, T. H., Chu, M. S., 1984, Current drive and helicity injection, Phys. Fluids, 27, 2881–2885

Jing, J., Wiegelmann, T., Suematsu, Y., Kubo, M., Wang, H., 2008, Changes of magnetic structure in 3D associated with the X3.4 flare of 2006 December 13, Astrophys. J. Lett., 676, L81–L84

Kaiser, M. L., Kucera, T. A., Davila, J. M., St. Cyr, O. C., Guhathakurta, M., Christian, E., 2008, The STEREO mission: An introduction, Space Sci. Rev., 136, 5–16

Kan, J. R., Akasofu, S., Lee, L. C., 1983, A dynamo theory of solar flares, Sol. Phys., 84, 153–167

Keller, C. U., Harvey, J. W., Giampapa, M. S., 2003a, SOLIS: An innovative suite of synoptic instruments, in Innovative telescopes and instrumentation for solar astrophysics, (Eds.) S. L. Keil, S. V. Avakyan, vol. 4853, pp. 194–204

Keller, C. U., Harvey, J. W., The Solis Team, 2003b, The SOLIS Vector-Spectromagnetograph, in Solar polarization, (Eds.) J. Trujillo-Bueno, J. Sanchez Almeida, vol. 307 of Astron. Soc. Pac. Conf. Ser., pp. 13–22

Keppens, R., 2001, Sunspot pores, in Encyclopedia of Astronomy and Astrophysics, (Ed.) P. Murdin, Bristol: IOP Publishing and London: Nature Publishing

Kliem, B., 1995, Coupled magnetohydrodynamic and kinetic development of current sheets in the solar corona, in Coronal magnetic energy releases, (Eds.) A. O. Benz, A. Krüger, vol. 444 of Lecture notes in physics, pp. 93–114, Berlin: Springer

Klimchuk, J. A., 2001, Theory of coronal mass ejections, in Space weather (Geophys. Monogr.), (Eds.) P. Song, H. Singer, G. Siscoe, vol. 125, pp. 143–157, Washington: Am. Geophys. Union

Klimchuk, J. A., Canfield, R. C., Rhoads, J. E., 1992, The practical application of the magnetic virial theorem, Astrophys. J., 385, 327–343

Kosugi, T., Matsuzaki, K., Sakao, T., Shimizu, T., Sone, Y., Tachikawa, S., Hashimoto, T., Minesugi, K., Ohnishi, A., Yamada, T., Tsuneta, S., Hara, H., Ichimoto, K., Suematsu, Y., Shimojo, M., Watanabe, T., Shimada, S., Davis, J. M., Hill, L. D., Owens, J. K., Title, A. M., Culhane, J. L., Harra, L. K., Doschek, G. A., Golub, L., 2007, The Hinode (Solar-B) mission: An overview, Sol. Phys., 243, 3–17

Kramar, M., Inhester, B., Solanki, S. K., 2006, Vector tomography for the coronal magnetic field. I. Longitudinal Zeeman effect measurements, Astron. Astrophys., 456, 665–673

Krause, F., Rädler, K. H., 1980, Mean-field magnetohydrodynamics and dynamo theory, Oxford: Pergamon Press

Kusano, K., Suzuki, Y., Nishikawa, K., 1995, A solar flare triggering mechanism based on the Woltjer-Taylor minimum energy principle, Astrophys. J., 441, 942–951

Leka, K. D., Skumanich, A., 1998, The evolution of pores and the development of penumbrae, Astrophys. J., 507, 454–469

Li, Z., Yan, Y., Song, G., 2004, Properties of the boundary integral equation for solar non-constant-α force-free magnetic fields, Mon. Not. Roy. Astr. Soc., 347, 1255–1265

Lin, H., Penn, M. J., Tomczyk, S., 2000, A new precise measurement of the coronal magnetic field strength, Astrophys. J. Lett., 541, L83–L86

Lin, J., Soon, W., Baliunas, S. L., 2003, Theories of solar eruptions: A review, New Astron. Rev., 47, 53–84

Linton, M. G., Dahlburg, R. B., Antiochos, S. K., 2001, Reconnection of twisted flux tubes as a function of contact angle, Astrophys. J., 553, 905–921

Lites, B. W., Elmore, D. F., Seagraves, P., Skumanich, A. P., 1993, Stokes profile analysis and vector magnetic fields. VI. Fine-scale structure of a sunspot, Astrophys. J., 418, 928–942

Liu, R., Wang, H., 2009, Coronal implosion and particle acceleration in the wake of a filament eruption, Astrophys. J. Lett., 703, L23–L28

Liu, R., Wang, H., Alexander, D., 2009, Implosion in a coronal eruption, Astrophys. J., 696, 121–135

Low, B. C., 1988, On the hydromagnetic stability of a class of laminated force-free magnetic fields, Astrophys. J., 330, 992–996

Low, B. C., Lou, Y. Q., 1990, Modeling solar force-free magnetic fields, Astrophys. J., 352, 343–352

Lüst, R., Schlüter, A., 1954, Kraftfreie Magnetfelder. Mit 4 Textabbildungen, Zeitschrift fur Astrophysik, 34, 263–282

Maltby, P., 1971, Paschen-Back effect of the Lithium resonance doublet in sunspots, in Solar magnetic fields, (Ed.) R. Howard, vol. 43 of IAU Symposium, pp. 141–147

Mandrini, C. H., Pohjolainen, S., Dasso, S., Green, L. M., Démoulin, P., van Driel-Gesztelyi, L., Copperwheat, C., Foley, C., 2005, Interplanetary flux rope ejected from an X-ray bright point. The smallest magnetic cloud source-region ever observed, Astron. Astrophys., 434, 725–740

Marsch, G. E., 1996, Force-Free magnetic fields. Solutions, topology and applications, Singapore: World Scientific Publishing Co. Pte. Ltd.

McClymont, A. N., Jiao, L., Mikic, Z., 1997, Problems and progress in computing three-dimensional coronal active region magnetic fields from boundary data, Sol. Phys., 174, 191–218

McIntosh, P., 2001, Sunspot classification, in Encyclopedia of Astronomy and Astrophysics, (Ed.) P. Murdin, Bristol: IOP Publishing and London: Nature Publishing

McIntosh, P. S., 1990, The classification of sunspot groups, Sol. Phys., 125, 251–267

Melrose, D. B., 1995, Current paths in the corona and energy release in solar flares, Astrophys. J., 451, 391–401

Metcalf, T. R., 1994, Resolving the 180-degree ambiguity in vector magnetic field measurements: The 'minimum' energy solution, Sol. Phys., 155, 235–242

Metcalf, T. R., Jiao, L., McClymont, A. N., Canfield, R. C., Uitenbroek, H., 1995, Is the solar chromospheric magnetic field force-free?, Astrophys. J., 439, 474–481

Metcalf, T. R., Leka, K. D., Mickey, D. L., 2005, Magnetic free energy in NOAA active region 10486 on 2003 October 29, Astrophys. J. Lett., 623, L53–L56

Metcalf, T. R., Leka, K. D., Barnes, G., Lites, B. W., Georgoulis, M. K., Pevtsov, A. A., Balasubramaniam, K. S., Gary, G. A., Jing, J., Li, J., Liu, Y., Wang, H. N., Abramenko, V., Yurchyshyn, V., Moon, Y.-J., 2006, An overview of existing algorithms for resolving the 180° ambiguity in vector magnetic fields: Quantitative tests with synthetic data, Sol. Phys., 237, 267–296

Metcalf, T. R., Derosa, M. L., Schrijver, C. J., Barnes, G., van Ballegooijen, A. A., Wiegelmann, T., Wheatland, M. S., Valori, G., McTtiernan, J. M., 2008, Nonlinear force-free modeling of coronal magnetic fields. II. modeling a filament arcade and simulated chromospheric and photospheric vector fields, Sol. Phys., 247, 269–299

Mickey, D. L., 1985, The Haleakala Stokes polarimeter, Sol. Phys., 97, 223–238

Mickey, D. L., Canfield, R. C., Labonte, B. J., Leka, K. D., Waterson, M. F., Weber, H. M., 1996, The Imaging Vector Magnetograph at Haleakala, Sol. Phys., 168, 229–250

Mikic, Z., Linker, J. A., 1994, Disruption of coronal magnetic field arcades, Astrophys. J., 430, 898–912

Mikic, Z., McClymont, A. N., 1994, Deducing coronal magnetic fields from vector magnetograms, in Solar active region evolution: Comparing models with observations, (Eds.) K. S. Balasubramaniam, G. W. Simon, vol. 68 of Astron. Soc. Pac. Conf. Ser., pp. 225–232

Mikic, Z., Barnes, D. C., Schnack, D. D., 1988, Dynamical evolution of a solar coronal magnetic field arcade, Astrophys. J., 328, 830–847

Moffatt, H. K., 1969, The degree of knottedness of tangled vortex lines, J. Fluid Mech., 35, 117–129

Moffatt, H. K., 2002, Reflections on magnetohydrodynamics, in Perspectives in fluid dynamics, (Eds.) G. K. Batchelor, H. K. Moffatt, M. G. Worster, pp. 347–391, Cambridge: Cambridge University Press

Molodenskii, M. M., 1969, Integral properties of force-free fields, Soviet Astronomy, 12, 585–588

Molodensky, M. M., 1974, Equilibrium and stability of force-free magnetic field, Sol. Phys., 39, 393–404

Munro, R. H., Gosling, J. T., Hildner, E., MacQueen, R. M., Poland, A. I., Ross, C. L., 1979, The association of coronal mass ejection transients with other forms of solar activity, Sol. Phys., 61, 201–215

Murdin, P., 2001, Encyclopedia of Astronomy and Astrophysics, Bristol: IOP Publishing and London: Nature Publishing

Nakagawa, Y., 1973, A practical representation of the solar magnetic field, Astron. Astrophys., 27, 95–100

Nakagawa, Y., 1974, Dynamics of the solar magnetic field. I. Method of examination of force-free magnetic fields, Astrophys. J., 190, 437–440

Nakagawa, Y., Raadu, M. A., 1972, On practical representation of magnetic field, Sol. Phys., 25, 127–135

Nakariakov, V. M., Verwichte, E., 2005, Coronal waves and oscillations, Liv. Rev. Sol. Phys., 2, 3–65

Neukirch, T., 2005, Magnetic field extrapolation, in Chromospheric and coronal magnetic fields, (Eds.) D. E. Innes, A. Lagg, S. A. Solanki, vol. 596 of ESA Special Publication

Neupert, W. M., 1968, Comparison of solar X-ray line emission with microwave emission during flares, Astrophys. J. Lett., 153, L59–L64

Nindos, A., Andrews, M. D., 2004, The association of big flares and coronal mass ejections: What is the role of magnetic helicity?, Astrophys. J. Lett., 616, L175–L178

Nindos, A., Zhang, H., 2002, Photospheric motions and coronal mass ejection productivity, Astrophys. J. Lett., 573, L133–L136

Ossendrijver, M., 2003a, The solar dynamo: A challenge for theory and observations, in Current theoretical models and future high resolution solar observations: Preparing for ATST, (Eds.) A. A. Pevtsov, H. Uitenbroek, vol. 286 of Astron. Soc. Pac. Conf. Ser., pp. 97–112

Ossendrijver, M., 2003b, The solar dynamo, Astron. Astrophys. Rev., 11, 287–367

Parker, E. N., 1955, Hydromagnetic dynamo models, Astrophys. J., 122, 293–314

Parker, E. N., 1970, The generation of magnetic fields in astrophysical bodies. I. The dynamo equations, Astrophys. J., 162, 665–673

Petrovay, K., van Driel-Gesztelyi, L., 1997, Making sense of sunspot decay. I. Parabolic decay law and Gnevyshev-Waldmeier relation, Sol. Phys., 176, 249–266

Pevtsov, A. A., 2008, What helicity can tell us about solar magnetic fields, J. Astrophys. Astr., 29, 49–56

Pevtsov, A. A., Canfield, R. C., Metcalf, T. R., 1995, Latitudinal variation of helicity of photospheric magnetic fields, Astrophys. J. Lett., 440, L109–L112

Priest, E. R., 1999, Magnetic helicity and relaxation phenomena in the solar corona, in Helicity in space and laboratory plasmas, (Eds.) M. R. Brown, R. C. Canfield, A. A. Pevtsov, pp. 141–156

Priest, E. R., Forbes, T. G., 2002, The magnetic nature of solar flares, Astron. Astrophys. Rev., 10, 313–377

Ramsey, H. E., Schoolman, S. A., Title, A. M., 1977, On the size, structure and strength of the small-scale solar magnetic field, Astrophys. J. Lett., 215, L41–L42

Raouafi, N., Sahal-Bréchot, S., Lemaire, P., 2002, Linear polarization of the O VI lambda 1031.92 coronal line. II. Constraints on the magnetic field and the solar wind velocity field vectors in the coronal polar holes, Astron. Astrophys., 396, 1019–1028

Raouafi, N., Solanki, S. K., Wiegelmann, T., 2009, Hanle effect diagnostics of the coronal magnetic field: A test using realistic magnetic field configurations, in Solar polarization 5, (Ed.) S. V. Berdyugina, K. N. Nagendra, & R. Ramelli, vol. 405 of Astron. Soc. Pac. Conf. Ser., pp. 429–434

Raouafi, N.-E., 2005, Measurement methods for chromospheric and coronal magnetic fields, in Chromospheric and coronal magnetic fields, (Eds.) D. E. Innes, A. Lagg, S. A. Solanki, vol. 596 of ESA Special Publication

Régnier, S., Amari, T., 2004, 3D magnetic configuration of the Hα filament and X-ray sigmoid in NOAA AR 8151, Astron. Astrophys., 425, 345–352

Régnier, S., Canfield, R. C., 2006, Evolution of magnetic fields and energetics of flares in active region 8210, Astron. Astrophys., 451, 319–330

Régnier, S., Priest, E. R., 2007a, Nonlinear force-free models for the solar corona. I. Two active regions with very different structure, Astron. Astrophys., 468, 701–709

Régnier, S., Priest, E. R., 2007b, Free magnetic energy in solar active regions above the minimum-energy relaxed state, Astrophys. J. Lett., 669, L53–L56

Régnier, S., Amari, T., Kersalé, E., 2002, 3D Coronal magnetic field from vector magnetograms: Non-constant-alpha force-free configuration of the active region NOAA 8151, Astron. Astrophys., 392, 1119–1127

Régnier, S., Amari, T., Canfield, R. C., 2005a, Self and mutual magnetic helicities in coronal magnetic configurations, Astron. Astrophys., 442, 345–349

Régnier, S., Fleck, B., Abramenko, V., Zhang, H.-Q., 2005b, Evolution of the magnetic energy budget in AR 10486 from potential and nonlinear force-free models, in Chromospheric and coronal magnetic fields, (Eds.) D. E. Innes, A. Lagg, S. A. Solanki, vol. 596 of ESA Special Publication

Reynolds, O., 1895, On the dynamical theory of incompressible viscous fluids and the determination of the criterion, Phil. Trans. Roy. Soc., A 186, 123–164

Riley, P., Linker, J. A., Mikić, Z., Lionello, R., Ledvina, S. A., Luhmann, J. G., 2006, A comparison between global solar magnetohydrodynamic and potential field source surface model results, Astrophys. J., 653, 1510–1516

Roberts, B., Edwin, P. M., Benz, A. O., 1984, On coronal oscillations, Astrophys. J., 279, 857–865

Rosner, R., Tucker, W. H., Vaiana, G. S., 1978, Dynamics of the quiescent solar corona, Astrophys. J., 220, 643–645

Roumeliotis, G., 1996, The "stress-and-relax" method for reconstructing the coronal magnetic field from vector magnetograph data, Astrophys. J., 473, 1095–1103

Rüedi, I., Solanki, S. K., Livingston, W. C., 1994, Magnetic fields in the upper chromosphere: He I 10830 Å as an almost ideal diagnostic, in Solar magnetic fields, (Eds.) M. Schüssler, W. Schmidt, pp. 363–365

Rust, D. M., 1983, Coronal disturbances and their terrestrial effects, Space Sci. Rev., 34, 21–36

Sakurai, T., 1981, Calculation of force-free magnetic field with non-constant α, Sol. Phys., 69, 343–359

Sakurai, T., 1982, Green's Function methods for potential magnetic fields, Sol. Phys., 76, 301–321

Sakurai, T., Ichimoto, K., Nishino, Y., Shinoda, K., Noguchi, M., Hiei, E., Li, T., He, F., Mao, W., Lu, H., Ai, G., Zhao, Z., Kawakami, S., Chae, J.-C., 1995, Solar flare telescope at Mitaka, Pub. Astron. Soc. Jap., 47, 81–92

Schatten, K. H., Wilcox, J. M., Ness, N. F., 1969, A model of interplanetary and coronal magnetic fields, Sol. Phys., 6, 442–455

Scherrer, P. H., Bogart, R. S., Bush, R. I., Hoeksema, J. T., Kosovichev, A. G., Schou, J., Rosenberg, W., Springer, L., Tarbell, T. D., Title, A., Wolfson, C. J., Zayer, I., MDI Engineering Team, 1995, The solar oscillations investigation - Michelson Doppler Imager, Sol. Phys., 162, 129–188

Schmidt, H. U., 1964, On the observable effects of magnetic energy storage and release connected with solar flares, in The physics of solar flares, (Ed.) W. N. Hess, pp. 107–114

Schmitt, D., 1985, Dynamowirkung magnetostrophischer Wellen, Ph.D. thesis, University of Göttingen

Schrijver, C. J., Derosa, M. L., Metcalf, T. R., Liu, Y., McTiernan, J., Régnier, S., Valori, G., Wheatland, M. S., Wiegelmann, T., 2006, Nonlinear force-free modeling of coronal magnetic fields. I. A quantitative comparison of methods, Sol. Phys., 235, 161–190

Schrijver, C. J., DeRosa, M. L., Metcalf, T., Barnes, G., Lites, B., Tarbell, T., McTiernan, J., Valori, G., Wiegelmann, T., Wheatland, M. S., Amari, T., Aulanier, G., Demoulin, P., Fuhrmann, M., Kusano, K., Regnier, S., Thalmann, J. K., 2008, Nonlinear force-free field modeling of a solar active region around the time of a major flare and coronal mass ejection, Astrophys. J., 675, 1637–1644

Seehafer, N., 1978, Determination of constant alpha force-free solar magnetic fields from magnetograph data, Sol. Phys., 58, 215–223

Sen, H. K., White, M. L., 1972, A physical mechanism for the production of solar flares, Sol. Phys., 23, 146–154

Sheeley, Jr., N. R., Howard, R. A., Koomen, M. J., Michels, D. J., 1983, Associations between coronal mass ejections and soft X-ray events, Astrophys. J., 272, 349–354

Socas-Navarro, H., Trujillo Bueno, J., Landi Degl'Innocenti, E., 2004, Signatures of incomplete Paschen-Back splitting in the polarization profiles of the He I λ 10830 multiplet, Astrophys. J., 612, 1175–1180

Solanki, S. K., 1993, Small-scale solar magnetic fields: An overview, Space Sci. Rev., 63, 1–188

Solanki, S. K., Inhester, B., Schüssler, M., 2006, The solar magnetic field, Rep. Prog. Phys., 69, 563–668

Song, M. T., Fang, C., Tang, Y. H., Wu, S. T., Zhang, Y. A., 2006, A new and fast way to reconstruct a nonlinear force-free field in the solar corona, Astrophys. J., 649, 1084–1092

Steenbeck, M., Krause, F., 1966, Erklärung stellarer und planetarer Magnetfelder durch einen turbulenzbedingten Dynamomechanismus, Z. Naturforschung, A 21, 1285–1296

Steenbeck, M., Krause, F., Rädler, K., 1966, Berechnung der mittleren Lorentz-Feldstärke $\boldsymbol{v}' \times \boldsymbol{B}'$ für ein elektrisch leitendes Medium in turbulenter, durch Coriolis-Kräfte beeinflußter Bewegung, Z. Naturforschung, A 21, 369–376

Stenflo, J. O., 1978, The measurement of solar magnetic fields, Rep. Prog. Phys., 41, 865–907

Stenflo, J. O., 1982, The Hanle effect and the diagnostics of turbulent magnetic fields in the solar atmosphere, Sol. Phys., 80, 209–226

Stenflo, J. O., Keller, C. U., Gandorfer, A., 1998, Differential Hanle effect and the spatial variation of turbulent magnetic fields on the Sun, Astron. Astrophys., 329, 319–328

Stix, M., 2002, The sun: An introduction, Berlin: Springer

Tadesse, T., Wiegelmann, T., Inhester, B., 2009, Nonlinear force-free coronal magnetic field modelling and preprocessing of vector magnetograms in spherical geometry, Astron. Astrophys., 508, 421–432

Tajima, T., Sakai, J., Nakajima, H., Kosugi, T., Brunel, F., Kundu, M. R., 1987, Current loop coalescence model of solar flares, Astrophys. J., 321, 1031–1048

Tang, Y. H., Li, Y. N., Fang, C., Aulanier, G., Schmieder, B., Demoulin, P., Sakurai, T., 2000, Hα and soft X-ray brightening events caused by emerging flux, Astrophys. J., 534, 482–489

Taylor, J. B., 1974, Relaxation of toroidal plasma and generation of reverse magnetic fields, Phys. Rev. Lett., 33, 1139–1141

Taylor, J. B., 1986, Relaxation and magnetic reconnection in plasmas, Rev. Mod. Phys., 58, 741–763

Thalmann, J. K., Wiegelmann, T., 2008, Evolution of the flaring active region NOAA 10540 as a sequence of nonlinear force-free field extrapolations, Astron. Astrophys., 484, 495–502

Thalmann, J. K., Wiegelmann, T., Raouafi, N.-E., 2008, First nonlinear force-free field extrapolations of SOLIS/VSM data, Astron. Astrophys., 488, L71–L74

Timothy, A. F., Krieger, A. S., Vaiana, G. S., 1975, The structure and evolution of coronal holes, Sol. Phys., 42, 135–156

Title, A. M., Frank, Z. A., Shine, R. A., Tarbell, T. D., Topka, K. P., Scharmer, G., Schmidt, W., 1993, On the magnetic and velocity field geometry of simple sunspots, Astrophys. J., 403, 780–796

Trujillo Bueno, J., Asensio Ramos, A., 2007, Influence of atomic polarization and horizontal illumination on the stokes profiles of the He I 10830 Å multiplet, Astrophys. J., 655, 642–650

Tsuneta, S., Acton, L., Bruner, M., Lemen, J., Brown, W., Caravalho, R., Catura, R., Freeland, S., Jurcevich, B., Owens, J., 1991, The soft X-ray telescope for the SOLAR-A mission, Sol. Phys., 136, 37–67

Tsuneta, S., Masuda, S., Kosugi, T., Sato, J., 1997, Hot and superhot plasmas above an impulsive flare loop, Astrophys. J., 478, 787–798

Uchida, Y., Wheatland, M. S., Haga, R., Yoshitake, I., Melrose, D., 2001, YOHKOH/HXT evidence for a hyperhot loop-top source in the pre-impulsive phase of a loop flare, Sol. Phys., 202, 117–130

Valori, G., Kliem, B., Keppens, R., 2005, Extrapolation of a nonlinear force-free field containing a highly twisted magnetic loop, Astron. Astrophys., 433, 335–347

van Ballegooijen, A. A., 2004, Observations and modeling of a filament on the Sun, Astrophys. J., 612, 519–529

van Ballegooijen, A. A., Martens, P. C. H., 1989, Formation and eruption of solar prominences, Astrophys. J., 343, 971–984

van Ballegooijen, A. A., Priest, E. R., Mackay, D. H., 2000, Mean-field model for the formation of filament channels on the sun, Astrophys. J., 539, 983–994

van Ballegooijen, A. A., Deluca, E. E., Squires, K., Mackay, D. H., 2007, Modeling magnetic flux ropes in the solar atmosphere, J. Atmosph. Solar-Terr. Phys., 69, 24–31

van Driel-Gesztelyi, L., 2005, CMEs and magnetic helicity, in Solar magnetic phenomena, (Eds.) A. Hanslmeier, A. Veronig, M. Messerotti, vol. 320 of Astrophysics and Space Science Library, pp. 57–85

van Driel-Gesztelyi, L., Mandrini, C. H., Thompson, B., Plunkett, S., Aulanier, G., Démoulin, P., Schmieder, B., de Forest, C., 1999, Long-term magnetic evolution of an AR and its CME activity, in Third Advances in Solar Physics Euroconference: Magnetic fields and oscillations, (Eds.) B. Schmieder, A. Hofmann, J. Staude, vol. 184 of Astron. Soc. Pac. Conf. Ser., pp. 302–306

van Driel-Gesztelyi, L., Manoharan, P. K., Démoulin, P., Aulanier, G., Mandrini, C. H., Lopez-Fuentes, M., Schmieder, B., Orlando, S., Thompson, B., Plunkett, S., 2000, Initiation of CMEs: The role of magnetic twist, Journal of Atmospheric and Solar-Terrestrial Physics, 62, 1437–1448

van Driel-Gesztelyi, L., Démoulin, P., Mandrini, C. H., 2003, Observations of magnetic helicity, Adv. Space Res., 32, 1855–1866

Verner, J. H., Bernal, M. J. M., 1968, On generalizations of the theory of consistent orderings for successive over-relaxation methods, Num. Math., 12, 215–222

Vrsnak, B., Ruzdjak, V., Rompolt, B., 1991, Stability of prominences exposing helical-like patterns, Sol. Phys., 136, 151–167

Vršnak, B., 2005, Solar flares - Observations and theory, in Solar magnetic phenomena, (Eds.) A. Hanslmeier, A. Veronig, M. Messerotti, vol. 320 of Astrophysics and Space Science Library, pp. 27–56

Waldmeier, M., 1955, Ergebnisse und Probleme der Sonnenforschung (2. erweiterte Auflage), Leipzig: Akademischer Verlag, Geest & Portig

Wang, J., Zirin, H., Shi, Z., 1985, The smallest observable elements of magnetic flux, Sol. Phys., 98, 241–253

Wedemeyer-Böhm, S., Lagg, A., Nordlund, Å., 2009, Coupling from the photosphere to the chromosphere and the corona, Space Sci. Rev., 144, 317–350

Wheatland, M. S., 2004, Parallel construction of nonlinear force-free fields, Sol. Phys., 222, 247–264

Wheatland, M. S., 2006, A fast current-field iteration method for calculating nonlinear force-free fields, Sol. Phys., 238, 29–39

Wheatland, M. S., 2007, Calculating and testing nonlinear force-free fields, Sol. Phys., 245, 251–262

Wheatland, M. S., Régnier, S., 2009, A self-consistent nonlinear force-free solution for a solar active region magnetic field, Astrophys. J. Lett., 700, L88–L91

Wheatland, M. S., Sturrock, P. A., Roumeliotis, G., 2000, An optimization approach to reconstructing force-free fields, Astrophys. J., 540, 1150–1155

White, S. M., 2005, Radio measurements of coronal magnetic fields, in Chromospheric and coronal magnetic fields, (Ed.) D. E. Innes, A. Lagg, & S. A. Solanki, vol. 596 of ESA Special Publication

Wiegelmann, T., 2004, Optimization code with weighting function for the reconstruction of coronal magnetic fields, Sol. Phys., 219, 87–108

Wiegelmann, T., 2007, Computing nonlinear force-free coronal magnetic fields in spherical geometry, Sol. Phys., 240, 227–239

Wiegelmann, T., 2008, Nonlinear force-free modeling of the solar coronal magnetic field, J. Geophys. Res. (Space Phys.), 113, A03S02

Wiegelmann, T., Inhester, B., 2006, Magnetic stereoscopy, Sol. Phys., 236, 25–40

Wiegelmann, T., Neukirch, T., 2003, Computing nonlinear force free coronal magnetic fields, Nonl. Proc. Geophys., 10, 313–322

Wiegelmann, T., Solanki, S. K., 2004, Why are coronal holes indistinguishable from the quiet Sun in transition region radiation?, in SOHO 15 Coronal Heating, (Ed.) R. W. Walsh, J. Ireland, D. Danesy, & B. Fleck, vol. 575 of ESA Special Publication, pp. 35–40

Wiegelmann, T., Inhester, B., Sakurai, T., 2006, Preprocessing of vector magnetograph data for a nonlinear force-free magnetic field reconstruction, Sol. Phys., 233, 215–232

Wiegelmann, T., Thalmann, J. K., Schrijver, C. J., Derosa, M. L., Metcalf, T. R., 2008, Can we improve the preprocessing of photospheric vector magnetograms by the inclusion of chromospheric observations?, Sol. Phys., 247, 249–267

Wiegelmann, T., Inhester, B., Feng, L., 2009, Solar stereoscopy - Where are we and what developments do we require to progress?, Ann. Geophys., 27, 2925–2936

Woltjer, L., 1958, A theorem on force-free magnetic fields, Proc. Nat. Acad. Sci., 44, 489–491

Wu, S. T., Chang, H. M., Hagyard, M. J., 1985, On the numerical computation of nonlinear force-free magnetic fields, NASA Conference Publication, 2374, 17–48

Wu, S. T., Sun, M. T., Chang, H. M., Hagyard, M. J., Gary, G. A., 1990, On the numerical computation of nonlinear force-free magnetic fields, Astrophys. J., 362, 698–708

Yan, Y., 1995, The 3D Boundary element formulation of linear force-free magnetic fields with finite energy content in semi-infinite space, Sol. Phys., 159, 97–113

Yan, Y., Li, Z., 2006, Direct boundary integral formulation for solar non-constant-α force-free magnetic fields, Astrophys. J., 638, 1162–1168

Yan, Y., Sakurai, T., 2000, New boundary integral equation representation for finite energy force-free magnetic fields in open space above the Sun, Sol. Phys., 195, 89–109

Yan, Y., Yu, Q., Kang, F., 1991, A solar magnetic field model and its 3D boundary element method solution, Sol. Phys., 136, 195–198

Zirin, H., 1988, Astrophysics of the Sun, Cambridge: Cambridge University Press

Publications

Teilergebnisse aus dieser Arbeit wurden mit Genehmigung der Fakultät für Elektrotechnik, Informationstechnik und Physik, vertreten durch den Mentor der Arbeit, in folgenden Beiträgen vorab veröffentlicht:

Refereed publications:

- Wiegelmann, T., Thalmann, J. K., Schrijver, C. J., De Rosa, M. L., Metcalf, T. R., 2008, Can we improve the preprocessing of photospheric vector magnetograms by the inclusion of chromospheric observations?, Sol. Phys., 247, 249 - 267
- Thalmann, J. K., Wiegelmann, T., 2008, Evolution of the flaring active region NOAA 10540 as a sequence of nonlinear force-free field extrapolations, Astron. Astrophys., 484, 495 - 502
- Thalmann, J. K., Wiegelmann, T., Raouafi, N.-E., 2008, First nonlinear force-free field extrapolations of SOLIS/VSM data, Astron. Astrophys., 488, L71 - L74
- Thalmann, J. K., Wiegelmann, T., 2009, Magnetic field extrapolation of flaring active regions, Cen. Europ. Astrophys. Bull., 33, 131 - 140

Oral presentations and posters:

- Thalmann, J. K., Wiegelmann, T., Testing of H-alpha preprocessing, NLFFF Consortium Meeting 4, Paris, France, Jun. 12 - 14, 2007. (Oral).
- Wiegelmann, T., Thalmann, J. K., Schrijver, C. J., De Rosa, M. L., Metcalf, T. R., Can we improve the preprocessing of photospheric vectormagnetograms by the inclusion of chromospheric observations?, AGU Fall Meeting, San Francisco, USA, Dec. 10 - 14, 2007. (Poster).
- Thalmann, J. K., Wiegelmann, T., Nonlinear force-free field extrapolation of NOAA active region 10540, AGU Fall Meeting, San Francisco, USA, Dec. 10 - 14, 2007. (Poster).
- Thalmann, J. K., Wiegelmann, T., Evolution of the coronal magnetic field of NOAA active region 10540, EGU Meeting, Vienna, Austria, Apr. 13 - 18, 2008. (Poster).
- Thalmann, J. K., Wiegelmann, T., Magnetic field extrapolation of flaring active regions, NLFFF Consortium Meeting 5, Katlenburg-Lindau, Germany, Jun. 30 - Jul. 2, 2008. (Oral).

- Thalmann, J. K., Wiegelmann, T., Magnetic field extrapolation of flaring active regions, IXth Hvar Astrophysical Colloquium - Solar Minimum Meeting, Hvar, Croatia, Sep. 22 - 26, 2008. (Oral).
- Thalmann, J. K., Wiegelmann, T., Using Solis Vector-SpectroMagnetograph data for coronal magnetic field extrapolations, A Next Generation Coronal Active Region Model Workshop, Philadelphia, USA, Oct. 22 - 23, 2008. (Oral).
- Thalmann, J. K., Wiegelmann, T., Evolution of two flaring active regions with CME association, AGU Fall Meeting, San Francisco, Dec. 15 - 19, 2008. (Poster).

Acknowledgments

This thesis was performed at the Max-Planck-Institute for Solar System Research (MPS) and the International Max Planck Research School (IMPRS) in Katlenburg-Lindau with financial support by DFG-grant WI 3211/1-1.

My thanks go to Dr. Thomas Wiegelmann for the continuous guidance, motivation and support during my entire PhD research. I am grateful also to Dr. Bernd Inhester for his encouragement and patience, especially in the last period of my work. Without the instructive comments and evaluation at every stage of my thesis process, of both of you, this thesis would not have been completed. In addition, I appreciate the other fellow students of our cheerful working group for broadening my perspective through numerous scientific, though entertaining, discussions and also the ongoing technical support by Borut Podlipnik deserves special mention.

Thanks to Dr. Sami Solanki for the helpful discussions, the openness to ideas and for widening my scientific understanding. I also want to express my gratitude to our IMPRS coordinator Dr. Dieter Schmitt. All of your efforts to provide a stimulating and comfortable environment established the fruitful base of this research. Thanks for your ongoing friendly support.

In addition to the aforementioned scientific and technical assistance, I received equally important support from all my fellow graduate students. In particular, I am deeply thankful to Manuela, Silvia and Jean, for supporting me when things were going tough, for the very special moments spending together and most of all for being friends.

Finally and most importantly, I want to thank my beloved family. For always reminding me that it has already been too long that we did not see each other. Most of all, I owe my deepest gratefulness to my wonderful father and my lovely sister. For the wise words, the emotional support and for the faith in me. This thesis is dedicated to you.